Curso 2009/10
CIENCIAS Y TECNOLOGÍAS/8
I.S.B.N.: 978-84-7756-940-4

FRANCISCO MIGUEL MONTENEGRO MONTES

Cuásares emisores en radio con líneas de absorción anchas (Radio-loud Broad Absorption Line Quasars)

Directores
ISMAEL PÉREZ FOURNÓN
KARL-HEINZ MACK
JOSÉ IGNACIO GONZÁLEZ SERRANO

SERVICIO DE PUBLICACIONES
UNIVERSIDAD DE LA LAGUNA

SOPORTES AUDIOVISUALES E INFORMÁTICOS
Serie Tesis Doctorales

Agradecimientos

Firstly, I would like to thank the Instituto de Astrofísica de Canarias (IAC) for holding the international fellowship programme, and for its support during my various visits to La Laguna. It was through this programme that I could have the necessary funds to survive in Bologna during my Ph.D. I am also very grateful to the Istituto Nazionale di Astrofisica (INAF), in particular the Istituto di Radioastronomia (IRA) di Bologna. Despite of the difficult times for research institutions in Italy, they provided me with all the facilities and support that I needed to accomplish this work, including financing for various training and observing trips along these four years. Additional funds for these purposes were provided by the European Commission through its Transnational Access (TNA) programme and RadioNet, as well as by the Spanish Ministerio de Educación y Ciencia.

Thanks also to my thesis supervisors Karl-Heinz Mack, Ignacio González Serrano and Ismael Pérez Fournón for their support and help during these years. It has been a pleasure to work with Karl-Heinz from whom I learnt many things about radioastronomy in general and single-dish observations in particular. He generously helped me with many academic and non-academic matters and made my settling and staying in Bologna much easier. He also supported me with good advice in moments of weakness, knowing how to motivate me to continue until the end. I discovered with pleasure that not all Germans are only "personas serias". Ignacio was an important source of "remote" support and help. His occasional conversations in front of a good beer have always been motivating and revealing. Thanks also to Ismael for taking part in this geographically spread Ph.D. and for his support during my visits to the IAC.

Being part of the "BAL QSO group" has been for me a continuous source of motivation and help while conducting the research that I present in this thesis. I wan to thank all its members: Chris Benn, Ruth Carballo, Ignacio González, Joanna Holt, Florencia Jiménez, Karl-Heinz Mack, Mario Vigotti and also Gabriele Bruni and Emma Salerno who have recently joined the team. Thanks for the excellent meetings at Santander and Bologna that I will remember with fondness in the future. Those nice walks along Avenida de Los Castros and 'El Sardinero' together with the fantastic 'pizza e birra' at Pizzeria *Belle Arti* will inevitably be linked in my mind to these fantastic meetings.

Thanks to the personnel of IRA: scientific staff, computing services and administration. They all helped me a lot and constituted a great environment during my stay at IRA. In particular I want to remember some of my neighbours at the fourth floor: I spent many lunch times at the mensa with Alfredo Gallerani, Roberto Ambrosini and Pietro Bolli. My Italian owes much to the cheerful and heterogeneous conversations with all of them. Alfredo was also patient enough to show me a little more of the misterious world of electronics and offered me help in numerous occasions when my italian was still not good enough.

Thanks to my office-mate Monica Orienti for her patience with my sometimes long Skype phone-calls and for helping us during a long observing run at the 100-m Effelsberg telescope. Nice tee-times were spent together with Alessandra Rossetti, Sergio Mariotti,

Ettore Carretti and Alessandra Zanichelli. Thanks also to Goliardo Tomassetti for showing me some of the stuff in his lab. I picked up from his conversations a couple of interesting radio-amateur experiments that maybe some day I might practise.

I am grateful to Stelio Montebugnoli for generously providing me with accomodation at the observatory of Medicina for several days. I enjoyed giving a hand from time to time in the visitor centre *Marcello Ceccarelli* where I learnt about the history of the observatory since its very beginning. My admiration goes to Stefania Varano whom I saw stoically working in precarious conditions to make from the visitor centre an important node of astronomical outreach in Italy. Thanks also to Barbara Neri for her joy, disponibility and hard work in the organisation of the BAL QSO meetings held at the IRA.

From a more scientific point of view I benefited from some conversations with Mario Vigotti, Franco Mantovani, Roberto Fanti, Carlo Stanghellini, Gianfranco Brunetti and Daniele Dallacasa who also introduced me in the complex but powerful world of the VLBI and, of course, in AIPS. I had the opportunity at IRA to expose and disscuss some of the contents of my work during some of the regular coffee-talks in the Friday afternoons.

A special thanks goes to Ruth Carballo for her patience and dedication which have substatially improved the contents of Chapter 5. From her careful reading came many useful comments and corrections. The spectral ageing analysis on which most of Chapter 6 is based was done making use of the SYNAGE package by Matteo Murgia. Thanks to him for providing me with his software. The reduction of the WSRT data-set presented in Chapter 8 was done in collaboration with Hans-Reiner Klöckner from Oxford University. I am in debt with him for his hospitality and his huge efforts to have the heavy reduction finished on time. Very useful was also his wonderful on-line tutorial[1] about the practical use of AIPS that I had the opportunity to apply in the VLA data reduction of Chapter 5 and the VLBA data reduction of Chapter 7. Some e-mail correspondence with C. Konar was very useful to understand and cross-check my calculations of the magnetic field strengths in Chapter 6. Thanks also to José Acosta who accepted being the internal referee of the thesis at the IAC. He pointed out some details that needed to be corrected or better explained in the final text.

Es mucha la gente a la que he oído mencionar que la consecución de la tesis doctoral es uno de los hitos importantes en la vida de uno. Curiosamente estas palabras solían salir sobre todo de la boca de doctores lo cual por un lado indica que tal opinión está probablemente un poquito sesgada, pero por otra parte esas personas sabían de primera mano de lo que estaban hablando. Llegado a este punto reconozco que estoy de acuerdo con ellos. Para mí la tesis ha supuesto un considerable esfuerzo tanto en lo intelectual como en lo personal y como en todo gran esfuerzo los beneficios sólamente se alcanzan a ver con cierta perspectiva. El beneficio que se ve de forma más inmediata es que uno deja por fin de ser "estudiante" después de pasarse toda la vida estudiando.

[1] `http://www-astro.physics.ox.ac.uk/~hrk/AIPS_TUTORIAL/HRK_AIPS_1.html`

Sin duda gran parte de dicho logro se debe a las personas que antes, durante y al finalizar la tesis brindaron su apoyo incondicional en los momentos clave. Quiero mencionar aquí a algunas de esas personas que me han acompañado en estos movidos años y gracias a las cuales las cosas han sido un poco más sencillas.

Agradezco a Carl Sagan por su dedicación y su obra que me cautivaron en la adolescencia. Gracias en parte a la excitación y motivación que venía implícita en sus palabras es que probablemente me dejé arrastrar poco a poco en el mundo de la astronomía. Más tarde, mis visitas al Planetario de Madrid y a la Agrupación Astronómica de Madrid (AAM) mantuvieron latente mi interés por los astros incluso antes todavía de estudiarlos en la Universidad. Quiero agradecer de manera especial a Manuel Catalán, histórico de la AAM, gracias a quien pude construir mi telescopio de 20 cm.

Mis padres Chari y Juan y mis hermanos Estela y Manolo han estado siempre a mi lado en las decisiones que fuí tomando a lo largo de mi vida académica, aunque ello supusiera tenerme geográficamente cada vez un poco más lejos. Les agradezco de corazón su comprensión y su apoyo incondicional ya que sin ellos esta tesis me hubiera costado cien veces más. Gracias a Nélida y Alberto, mis únicos suegros. Entre ellos y mis padres fueron capaces de organizar de modo impecable una boda intercontinental en mitad de las tesis.

Gracias también a mis compañeros y amigos de Física de la Universidad Complutense de Madrid (UCM) que hicieron agradables unos años de por sí duros. Grapar /QUANTOS> junto a Pablo, Julia, César o Dabidovich fue una de las mejores medicinas para superar los malignos efectos de "endomorfismos superestrella" y otros "paradigmas geométricos". También agradezco a todos mis compañeros y amigos de La Laguna porque fueron unos extraordinarios años en las islas que dieron para mucho. Fueron muchos los momentos para recordar con Aïda, Alejandro, Antonio, Carlos, Evanthia, Gabriel, Isaías, Itahiza, Jorge Quintero y Jorge Pérez, Juan, Miguel, Paola, Pedro, Raquel, Rebecca, Ruymán y Vanessa. Y también agradezco a los profesores del departamento de Astrofísica de la ULL por hacer de la astronomía algo realista y motivador. Quiero mencionar también a Rafael Bachiller y Pere Planesas por prestarse a enseñar radioastronomía en el IAC. Su curso de doctorado me resultó muy útil para no empezar desde cero en Bolonia.

Estoy en deuda con Jorge Pérez, compañero deneboliano, e Ingrid Meschin que me sacaron las papas del fuego en varias ocasiones con los innumerables trámites burocráticos en los estadíos finales de la tesis. Además, ambos hicieron agradables los almuerzos y barraquitos compartidos durante mis visitas a La Laguna.

Finalmente debo agradecer a Ale por un sin número de cosas sin las cuales esta tesis no hubiera sido posible. Ella me ha enseñado a ser un poco más metódico y organizado, lo cual es requisito indispensable para que cualquier tesis llegue a buen puerto. Siempre ha permanecido a mi lado en los momentos de flaqueza, apoyándome con determinación hercúlea y proporcionandome las fuerzas para llegar al final. Gracias por tus ingentes sacrificio y cariño, desde cerca y desde lejos, y sobre todo gracias por ser como eres: *azúcar, pimienta y sal.*

Es mejor encender una luz que maldecir la oscuridad.
— Proverbio árabe

La verdadera ciencia enseña, por encima de todo, a dudar y a ser ignorante.
— Miguel de Unamuno (1864-1936)

Resumen

Esta tesis trata del estudio de los cuásares con líneas de absorción anchas (Broad Absorption Line QSOs, BAL QSOs). Actualmente se desconoce la razón por la que muchos cuásares parecen presentan vientos que pueden ser detectados mediante estas líneas de absorción en una fracción importante de la población de cuásares. Las hipótesis más populares que se barajan para explicar la presencia de estos vientos difieren principalmente en el papel dado a la orientación de estos objetos. En este trabajo nos concentramos en encontrar pistas sobre la naturaleza de los BAL QSOs, mediante la observación con varios telescopios en longitudes de onda radio.

Presentamos observaciones multi-frecuencia de una muestra de 15 BAL QSOs emisores en radio, que cubren un rango entre 74 MHz y 43 GHz. Estas fuentes poseen en la mayoría de los casos un espectro radio convexo cuyo pico se sitúa típicamente entre 1 y 5 GHz (en el sistema observado). Dicho espectro se suele aplanar a frecuencias bajas (MHz) probablemente debido a autoabsorción sincrotrón y cae de forma más empinada a alta frecuencia, aproximadamente a partir de $\nu \gtrsim 20$ GHz. Nuestros mapas con VLA a 22 GHz (con resolución de unos 80 milisegundos de arco) muestran fuentes muy compactas o no resueltas con dimensiones (sin deproyectar) del orden de 1 kpc. Sobre dos tercios de los objetos de la muestra exhiben poca o ninguna polarización at 8.4 GHz, frecuencia a la cual se determinaron límites superiores razonables en la polarización lineal.

Se realizan comparaciones estadísticas entre la distribución de índices espectrales de muestras de BAL QSOs y no BAL QSOs, tanto en el sistema en reposo como en el observado, encontrando que los BAL QSOs tienen espectros más empinados. Sin embargo, restringiendo la comparación sólo a fuentes compactas no se encuentran diferencias significativas entre ambas distribuciones, lo que sugiere que no existe una orientación preferencial para los BAL QSOs. Además, el análisis de la forma espectral, la variabilidad y la polariación de estos objectos muestra que los BAL QSOs radio-emisores comparten varias características con las radio fuentes jóvenes como son las fuentes CSS (Compact Steep Spectrum) o las fuentes GPS (GigaHertz Peaked Spectrum).

También se realiza un análisis de datación espectral y se discuten las diferentes fuentes de error en la determinación de las edades espectrales. Con las restricciones observacionales actuales y asumiendo que tienen lugar condiciones de equipartición de la energía, se determinan edades radiativas de entre 1 y 50.000 años, lo que sugiere que las radio fuentes asociadas a BAL QSOs serían en realidad jóvenes.

Como los BAL QSOs presentan una morfología muy compacta en radio, presentamos observaciones con VLBA de 5 BAL QSOs, a una escala del milisegundo de arco y a frecuencias de 5 y 8.4 GHz. Discutimos la morfología de estos objectos a la escala del parsec y las comparamos con otras observaciones en la literatura. Encontramos una fracción relativamente alta de fuentes no resueltas y no polarizadas que presentan mayormente variabilidad moderada. También se encuentran algunas fuentes con posibles indicaciones de multiples episodios de actividad radio. Ambos descubrimientos favorecen la hipótesis evolutiva para

explicar el orígen de los BAL QSOs.

Para terminar, presentamos un experimento en que se trata de detectar absorción de H I en uno de los radio BAL QSOs más interesantes de nuestra muestra. La consiguiente no detección nos permite estimar un límite superior para la cantidad de hidrógeno neutro en esta fuente.

Summary

This thesis is concerned with Broad Absorption Line Quasars (BAL QSOs). At the moment it is not clear how many quasars host outflows and why these can only be seen in a fraction of the quasar population. The most popular hypotheses proposed to explain this mainly differ in the role given to orientation. In this work, we concentrate on a sample of BAL QSOs showing radio emission at 1.4 GHz and we try to find evidence about the nature of these objects through radio observations with various telescopes.

We present multi-frequency observations of a sample of 15 radio-emitting BAL QSOs, covering a spectral range between 74 MHz and 43 GHz. They display mostly convex radio spectra which typically peak at about 1-5 GHz (in the observer's rest-frame), flatten at MHz frequencies, probably due to synchrotron self-absorption, and become steeper at high frequencies, i.e., $\nu \gtrsim 20$ GHz. VLA 22-GHz maps (HPBW ~ 80 mas) show unresolved or very compact sources, with linear projected sizes of ≤ 1 kpc. About 2/3 of this sample look unpolarised or weakly polarised at 8.4 GHz, a frequency in which reasonable upper limits could be obtained for polarised intensity. Statistical comparisons have been made between the spectral index distributions of samples of BAL and non-BAL QSOs, both in the observed and the rest-frame, finding steeper spectra among non-BAL QSOs. However constraining this comparison to compact sources results in no significant differences between both distributions. This comparison is consistent with BAL QSOs not being oriented along a particular line of sight. In addition, our analysis of the spectral shape, the variability and polarisation properties shows that radio BAL QSOs share several properties common to young radio sources like Compact Steep Spectrum (CSS) or Gigahertz-Peaked Spectrum (GPS) sources.

A synchrotron ageing analysis has been done and we discuss the different parameters contributing to the uncertainty in the radiative age determination. With the current observational constraints, and the assumption of equipartition conditions, radiative ages have been determined in the range 1-50 kyr, suggesting that the radio brightest components in BAL QSOs would actually be young.

Since BAL QSOs have been found to be associated with extremely compact radio sources, we present VLBA milliarcsecond-scale observations of 5 BAL QSOs at 5.0 and 8.4 GHz. We discuss the pc-scale morphology of these objects and compare them with observations of other radio BAL QSOs in the literature. A relatively high fraction of unresolved, unpolarised sources and indications of restarting radio activity in some of the targets favours the evolutionary hypothesis to explain the origin of radio BAL QSOs.

Finally, we make a detection experiment trying to detect H I in absorption in one of the most interesting radio BAL QSOs in our sample. A non-detection allows us to estimate some upper limits of the contents of H I for this source.

Table of Contents

List of Tables

List of Figures

1

Introduction

The discovery of quasars (QSOs) in the late 50's was considered a revolution in astrophysics for various reasons. Understanding the mechanism that releases such enormous amount of energy was a challenge from a theoretical point of view, but at the same time allowed us to see the Universe much further away than previously imagined. It was also a big success of the newly born radioastronomy, which after years of continuous development, is capable now to provide us with a battery of very powerful and sophisticated telescopes.

It is at present widely accepted that the source of energy in Active Galactic Nuclei (AGN) is of gravitational origin, released through matter accretion onto a massive black hole. This hypothesis can explain the UV continuum emission observed in AGNs (i.e. the so-called big blue bump) and the strong and rapid variability that many AGNs exhibit. But from a theoretical point of view, there are still some details to be better understood about the accretion processes. Neither the details about how these supermassive black holes were formed are clear, nor how they evolve and interact with their host galaxies.

More than four decades of observations at different wavelengths and an intense debate about the interpretation of the results have led to a reasonably accepted sketch of the structure of AGNs. All this information has been summarised into the so-called "unified models". According to these models, the amazingly diverse zoo of active objects composed of radio-loud and radio-quiet QSOs, Seyfert galaxies of types 1 and 2, blazars, broad and narrow line radio galaxies, ultraluminous infrared galaxies (ULIRGS), LINERs, etc., can, to some extent, be unified as a single class of object. All this variety would be just the effect of combining a few ingredients, like a different orientation of the AGN as looked from the Earth, different accretion rates and black hole masses or the presence or absence of non-thermal radio emission in the form of jets.

The formation of relativistic jets is not completely understood but it is likely a combination of the dynamics of the accretion disk and the strong magnetic fields present around the central black hole. Also inherent to the accretion processes seems to be the development of sub-relativistic outflows that carry gas and matter away from the disk, helping the

system to shed angular momentum. The imprint of these matter and gas winds can only be detected in a fraction of the whole population of AGNs, and the Broad Absorption Line (BAL) QSOs are their most spectacular manifestation. These objects are the subject of this thesis and, in particular, the study of the rare class of radio-loud BAL QSOs.

There are several advantages when observing at radio wavelengths. A very important one is that radio emission provides additional diagnostic tools to get extra information that complements observations at other wavelengths, allowing one to probe the AGN environment in a more comprehensive way. In addition, the approximately 10 per cent of radio-loud QSOs can be easily detected with current radiotelescopes, even if they are at huge distances from us. This is mostly because radio emission is hardly absorbed along its travel from the emitting source to the Earth. The powerful machinery in the core of AGNs is responsible for the enormous acceleration of particles up to relativistic speeds, and these energetic particles emit synchrotron radiation that radiotelescopes can detect.

Before starting this work, not much was known about the radio properties of BAL QSOs. Previous findings stated that they were rare and mostly compact radio sources, but nothing was known about the shape of their radio spectra or their polarisation properties, and little about their pc-scale morphology. This thesis has tried to fill this gap for the first time, because all this can be valuable information to understand their origin, and how these BAL QSOs relate to the general population of QSOs.

The structure of the thesis will be as follows:

In Chapter 2 BAL QSOs are described, paying special attention to the observational characteristics of these objects. Following a multiwavelength approach, a brief review of their main properties is summarised, and the main two scenarios that have been proposed to explain the nature of these objects are presented. One of the main goals of this thesis is to find evidence in favour of, or against, any of these models from the observations that we present in Chapters 5 and 7.

Since radio observations constitute the main source of data in this work, Chapter 3 tries to give a brief summary on the main emission mechanisms in the radio regime, a description of the different kinds of compact radio sources and the explanation of the main analysis techniques later applied to our samples of BAL QSOs.

In Chapter 4 the most important samples of BAL QSOs that have been defined by different authors in the past years are shown, given special interest to their selection criteria. In addition, the main sample of radio-emitting BAL QSOs that is the subject of this thesis is defined. Finally, a larger sample of radio BAL QSOs which is now available from the recent releases of the Sloan Digital Sky Survey (SDSS) is also presented. This sample will be the basis for future research and can be used to test some of the conclusions found in this work.

Chapter 5 is focused on the description of the radio spectra and polarisation properties

of radio BAL QSOs. For this scope, multiwavelength radio observations in full polarisation of some of these objects are presented. The shape of their spectra, morphology, variability character and polarisation characteristics are studied and discussed in the framework of the possible scenarios proposed to explain the origin of BAL QSOs.

The radio spectra presented in Chapter 5 will be used in Chapter 6 to estimate the radiative age of these sources, through a syncrotron ageing analysis. These estimates are important to have an approximated idea about the evolutionary status of radio BAL QSOs. The main uncertainties affecting these estimates are pointed out.

In Chapter 7 the pc-scale radio morphology of some of the previously presented radio BAL QSOs is studied through Very Long Baseline Interferometry (VLBI) observations. Major interest is given to finding hints about the orientation of these sources. These high-resolution observations are discussed in the framework of the previous analyses developed in Chapters 5-6 to have an overall picture about the radio sources associated with these BAL QSOs. Our VLBI maps are put together with other similar observations in the literature, with the aim of finding general trends on the morphological classification of radio BAL QSOs.

In Chapter 8 deep observations of H I in absorption against J1624+37 are presented. This radio BAL QSO is one of the most interesting ones in our sample and for this reason this detection experiment was tackled. Even if no significant absorption was found, an upper limit on the contents of H I will be reported for this source.

Finally, Chapter 9 summarises the main conclusions of this thesis.

2

Phenomenology of the BAL phenomenon and interpretations

THE subject of this thesis is the study of a particular subset of QSOs that show what has been called the BAL phenomenon. Since their discovery about 50 years ago (Lynds 1967), there have been many observational and theoretical works with the aim of understanding the role of these objects and their relationship with the population of the, in contrast, so-called "normal" QSOs.

In this chapter BAL QSOs are introduced and a brief summary is presented on some properties of these objects that have been discovered over the years. A comprehensive approach is followed trying to extract some relevant pieces of knowledge from multiwavelength observations, from the X-ray regime to radio frequencies. Finally, an introduction is given to the most popular interpretations of the nature of these objects, specially stressing the two main paradigms: the *orientation* and the *evolutionary* scenarios.

The following chapters will make reference to some of these findings and models, so it is important to state here some of the observational and theoretical bases on which those are supported.

2.1 Absorption features in the UV spectrum

The first Broad Absorption Line QSO with references in the literature is PHL 5200 (z=1.981). It was discovered by Lynds (1967) and, curiously, it had been previously selected as an optical counterpart of the radio source 4C −5.93 (Scheuer & Wills, 1966), even if later it was shown that BAL QSOs are less frequent among radio-emitting sources.

Lynds found several absorbing bands in the optical spectra of PHL 5200, each of them about 100-150 Å wide. These bands were located bluewards of some resonance lines, i.e., N V λ 1240 Å, Si IV λ 1400 Å and C IV λ 1549 Å. He associated these bands with their corresponding emission lines not only by their proximity, but also because he found small

emission-like peaks within the bands, which were located at a precise distance from their emission. These small features were divided in three main groups according to their $\Delta\lambda/\lambda$ ratio, that is, three systems with slightly different redshift were identified, with z=1.9806, z=1.9381 and z=1.9032.

A year later, Burbidge (1968) took another spectrum and found what could be another component at z=1.9502, speculating that this feature might have appeared as a new component since the previous observations. Figure 2.1 shows the spectrum of PHL 5200 taken by Burbidge (1968), in which the different emission and absorption features are marked.

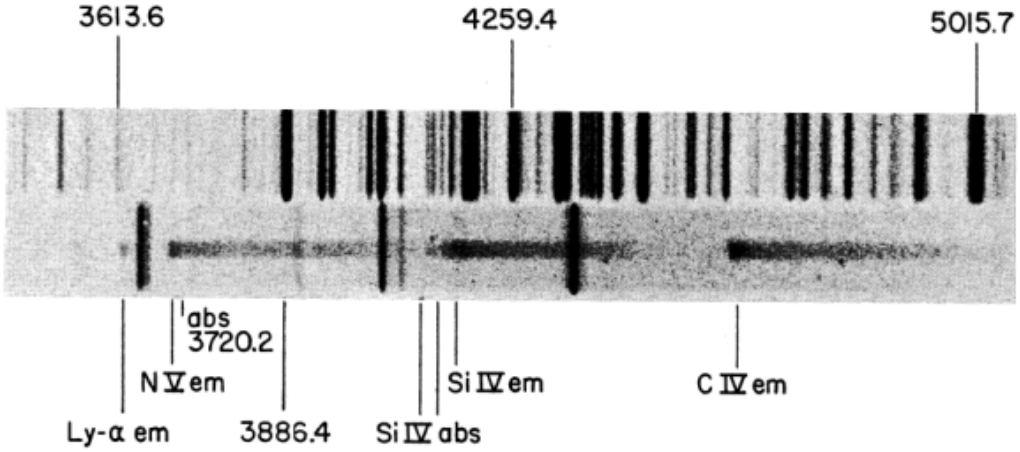

Figure 2.1: Optical spectrum of PHL 5200 (bottom) and reference spectrum (top). The main spectral features in the QSO spectrum have been marked. Extracted from Burbidge (1968).

2.1.1 Broad Absorption Line systems (BALs)

A modern digitised spectrum of PHL 5200 is shown in Figure 2.2. It illustrates many common features found in BAL systems, e.g., high level of ionisation and a smooth profile, being in general the absorption smoother on the blue side and steeper on the red side. The C IV absorption profile looks like a single wide trough, while that in Si IV shows different narrower components. A multi-component absorption is more frequently found in BAL QSOs rather than a single detached trough. In this BAL QSO the absorption extends up to relatively high velocity as measured from the systemic velocity.

At present many authors consider a BAL system as an absorbing feature spanning a velocity width $\gtrsim$ 3,000 km/s, with typical values $\sim$ 10,000 km/s. They trace outflow velocities from about 0 km/s (like in profiles similar to P-Cygni stars) up to $\sim 0.2c$ in the most extreme cases. The blueshifted velocity extremum for an absorbing feature to be considered as a BAL system has been more or less arbitrarily defined as $\gtrsim$ 5,000 km/s

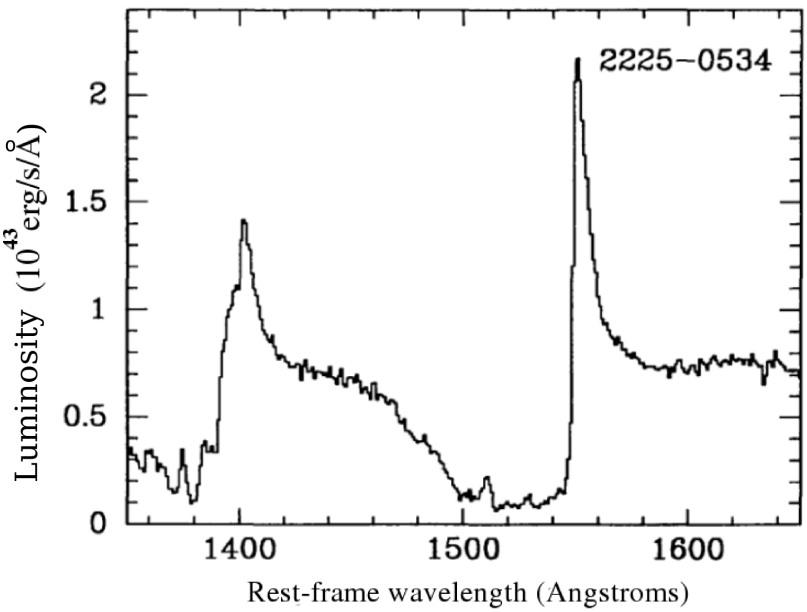

Figure 2.2: Digitised spectrum of PHL 5200. Adapted from Korista et al. (1993).

(Hamann & Murdin, 2000). However, as will be discussed later, there are cases of QSOs for which some of these requirements do not hold and can be classified as *bona-fide* BAL QSOs.

Based on the ionization level of the species where the absorption are present, BALs can be classified into:

- **High-ionisation BALs or HiBALs**: These display absorptions by high-ionisation species. The ionisation potentials[1] to produce these transitions are quite high, which indicates that the gas producing these absorption is in a relatively high state of ionisation. Typical species in which these absorptions are detected are O VI λ 12034 Å, N V λ 1240 Å, Si IV λ 1400 Å or C IV λ 1549 Å, with ionisation potentials of 113.9, 77.5, 34.8 and 37.9 eV, respectively.

- **Low-ionisation BALs or LoBALs**: These display absorptions by both high- and low-ionisation species. The ionisation potentials of the low-ionisation species are smaller, e.g., 7.6 eV for Mg II λ 2799 Å, and 18.8 eV for Al III λ 1857 Å. These transitions occur less frequently than those of HiBALs, showing LoBALs about 1 every 10 BAL QSOs.

- **Low-ionisation BALs with Fe absorptions or FeLoBALs**: These belong to the previous LoBAL category, but show in addition absorption from excited states of Fe II

[1]The ionisation potential is defined as the amount of energy necessary to ionise a certain atom or ion by removing one electron from its least bound orbital.

and/or Fe III. These are a minority class, representing about 1 per cent of the total population of BAL QSOs.

2.1.2 Mini-BALs

In some QSOs there are structures with similar characteristics of BALs, e.g., smooth profiles, wide extensions, similar detachments with respect to the emission line, etc. They have however, intermediate equivalent widths $\lesssim$ 2,000 km/s, smaller than those in BALs but wider than other narrow absorption features. These mini-BALs are less common than BALs since they are found in about 1 per cent of the quasar population (Hamann & Sabra, 2004)

Mini-BALs, like BALs, are certainly associated to quasar outflows. They are quite useful because their narrower velocity widths allows one in some cases to determine the *covering factor* of the absorbing matter and its *optical depth* as a function of velocity. The covering factor, C_f, indicates the fraction of the continuum source covered by the absorber along our line of sight. For instance, the effect of a partial coverage is that some flux remains below the absorbing trough, not reaching the zero intensity. The absorption line intensity is thus a balance between the optical depth of the absorbing material, τ, and the covering factor.

The importance of the study of mini-BALs is that they are often narrow enough to show some doublets or multiplets resolved, while these features might appear blended in the wider BALs. This exceptional peculiarity allows the determination of some physical properties of the BAL winds. An example is shown in Figure 2.3, where the different components identified in a O VI mini-BAL are marked.

Once a doublet has been resolved the procedure to solve for C_f and τ (Barlow & Sargent, 1997) is as follows: since the observed line intensity depends on the effects of C_f and τ, and this is true for both the red and the blue doublet components, the following equations are valid:

$$[I_v]_i = (1 - C_f) + C_f\, e^{-\tau_i}, \quad i = \text{red, blue} \tag{2.1}$$

where I_v is the fraction of absorbed to continuum intensity. From atomic physics, the ratio between the optical depths of the doublet components is known. For instance, in the C IV doublet τ_{red}=$\tau_{blue}/2$, and in this particular case one can derive C_f following Equation 2.2, and then derive τ_{red} replacing C_f in Equation 2.1.

$$C_f = \frac{I_{red}^2 - 2I_{red} + 1}{I_{blue} - 2I_{red} + 1} \tag{2.2}$$

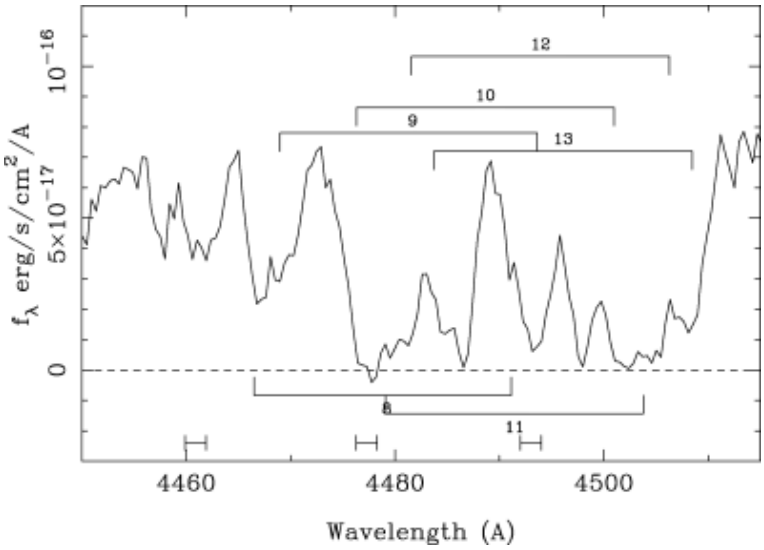

Figure 2.3: Mini-BAL in O VI of the BAL QSO J1624+3758. The ticks indicate the expected positions of the O VI doublet (1031.93, 1037.62 Å) at the redshifts corresponding to various absorbers identified in other ions. The details about the identified components can be found in Benn et al. (2005).

Once the line optical depth has been determined, the column density of the relevant ionised element can be obtained, following Equation 2.3 and integrating in velocity over the absorbing profile.

$$N = \frac{m_e c}{\pi e^2 f \lambda_0} \int \tau_v dv \tag{2.3}$$

This kind of analysis will not be used in this thesis, mainly focused in the radio emission from BAL QSOs. However, it is shown here to stress how powerful it can be to determine the physical conditions in the winds that cause the BAL absorptions, and how these estimates can be used as a reference when interpreting the results coming from radio observations.

This simple approach assumes that the partial coverage is homogeneous, but there is increasing evidence that at least in some cases the absorbing medium can be inhomogeneous, with different fractions of the continuum source being covered by absorbers with different optical depth (Hamann & Sabra, 2004). In any case, the previous equations give a first approximation to the true optical depth, and the homogeneity assumption is supposed not to change the final $e^{-\tau}$ by much more than 10 per cent.

This analysis has been done for several quasars using high-resolution spectra from large ground-based or space telescopes, because it is necessary to have sufficiently high signal-to-noise per resolution element to estimate line depths accurately. Some examples of studies where this kind of observations have been done are listed by Benn et al. (2005).

2.1.3 Narrow Absorption Line systems (NALs)

The absorbing features with smaller widths, typically a few hundred km/s, are known as NALs, but the origin of these systems has to be investigated on a case-by-case basis. The radiation emitted by the continuum source in the AGN can be absorbed at different places on its way towards us. This absorption can be caused by the gas in the surroundings of the central engine and in this case the absorption provides information about physical processes around the AGN, like in BALs or mini-BALs. It is also possible that this absorption is caused by gas within the host galaxy or in a cluster that contains the galaxy. Then the absorption, although being not close to the nucleus, could depend on the physical properties of the AGN. Finally the absorption can just be produced far away from the source, in disks or halos of galaxies or even in single clouds within the intergalactic medium along the line of sight between the source and us. These are known as *intervening* absorbers.

Those NALs with absorption redshifts within ±5000 km/s of the emission redshift are traditionally called *associated* lines, because they likely have an intrinsic origin. The reason is that the number of intervening systems across the line of sight to the quasar seems to decrease when approaching the AGN, the so-called "proximity effect" (Murdoch et al. 1986).

Barlow et al. (1997) pointed out a series of observational characteristics that seem to differentiate intrinsic from intervening absorptions. These are listed in order of decreasing reliability:

- Time variability of the absorbing troughs (Hamann et al. 1995). Associated absorptions present variable line strengths, which require dense, compact regions and thus intense radiation fields for photoionisation. Intervening absorptions, especially those due to intergalactic HI clouds hardly present any variability.

- Partial coverage of the continuum source. Absorbing clouds in the vicinity of the quasar are not supposed to cover completely the emitting nucleus along our line of sight. Intervening absorption systems may have angular sizes larger than the continuum source. Partial coverage has been recently used to classify absorption features in relatively large quasar samples (see e.g., Ganguly et al. 2004, or Misawa et al. 2007).

- High electron density as derived from fine structure lines as a distance indicator when combined with an ionisation level estimate (Morris et al. 1986).

- Increased optical polarisation degree in the lines compared to that in the continuum, as seen in mini-BALs or BALs (Ogle et al. 1999; Schmidt & Hines 1999), and probably due to line resonant scattering (Wang et al. 2007).

- Velocity structure when observed at high resolution, i.e., 10 km/s. In the presence of several components, absorptions by intrinsic lines present smooth line profiles, while intervening systems usually show them as independent components.

- High metallicities. The ionization structure observed in the associated systems is clearly different from that of the intervening ones, indicating that the associated systems are influenced by the strong UV flux from the QSO (D'Odorico et al. 2004).
- High ionisation levels, due to the proximity of the continuum ionising radiation in intrinsic systems.
- Proximity to BALs even if there might be some intervening systems lying by chance close to BALs in particular objects.
- Absorption redshifts close to the emission line redshift (Anderson et al. 1987) are usual in intrinsic absorbers, with evidence of stronger absorptions associated with radio-loud quasars. However, there are also intrinsic NALs due to high velocity outflows (HVOs) which are largely blueshifted with respect to the emission (e.g., Rodriguez Hidalgo et al. 2007)

Like mini-BALs, intrinsic NALs are narrow enough that, in many cases, the two components in a doublet can be resolved, allowing the optical depth and covering factor to be determined independently, in a similar way as explained above.

2.1.4 Metrics to quantify the absorption in BAL QSOs

It was shown that BAL QSOs can be visually recognised by their absorbed spectra, but these absorptions can be quite complex, and their shape and dimensions heterogeneous with different velocity widths, depths of the absorption and detachments from the corresponding emission lines. In order to characterise the population of BAL QSOs according to their absorbed profiles it is necessary to define a numerical quantity to objectively measure these absorptions.

The Balnicity Index

The Balnicity Index (BI, Weymann et al. 1991; see Equation 2.4) has traditionally been used to measure the strength of the absorption due to BAL winds. This index is basically a special equivalent width measure calculated integrating the area below 10 per cent of the continuum level as a function of velocity, in a range starting at 3,000 km/s and extending up to 25,000 km/s bluewards the peak emission. The lower limit of the integral was originally set to avoid absorptions close the emission peak caused by absorbers that were thought to be unrelated to the BAL phenomenon. The constant C in Equation 2.4 is a parameter that can be either 0 or 1, with C being 1 only if there was non-zero contribution to the index during the previous integrated 2000 km/s. This is thus the minimum width considered for a BAL trough, according to this definition.

$$BI = -\int_{3000}^{25000} \left(1 - \frac{f(v)}{0.9}\right) C dv \tag{2.4}$$

The BI is a safe way to select *bona fide* BAL QSOs, because it was designed to avoid several other contaminants, like noise peaks, absorption by intervening systems, etc. However, there are some cases for which the BI is too conservative. For instance, BAL troughs are sometimes present within the first 3,000 km/s from the systemic velocity, or further away than 25,000 km/s. In addition, several objects show the presence of absorbing features narrower than 2,000 km/s but otherwise with similar characteristics of BAL systems, and all these might end up with BI=0.

The Absorption Index

Proposed to partially solve this difficulty, the Absorption Index (AI, Hall et al. 2002; see Equation 2.5) was defined as a less conservative update of the BI. It considers troughs wider than 450 km/s and in this case the integration starts just at the peak emission (v=0) and extends bluewards typically up to 25,000 km/s but this limit can be increased when necessary, trying to avoid contributions from other species (e.g. Si IV when measuring the absorption in C IV).

$$AI = -\int_0^{(25000)} \left(1 - \frac{f(v)}{0.9}\right) C' dv \tag{2.5}$$

Equation 2.6 shows the formal uncertainty of this index, which depends on the spectrum noise $\sigma_{f(v)}$. However, this quantity should be only considered as a formal estimate on the error, because the main source of uncertainty comes from the determination of the continuum level, which is much more difficult to determine quantitatively.

$$\sigma_{AI}^2 = -\int_0^{(25000)} \left(\frac{\sigma_{f(v)}}{0.9}\right)^2 C' dv \tag{2.6}$$

Summarising, the BI is more *reliable*, while the AI is more *complete* for selecting BAL QSOs. Depending on the research interests any of these can be used taking its limitations into account. An illustrative example can be seen in Figure 2.4, where the same absorption is measured using these two different indices.

Other approaches

None of the two mentioned ways of classifying BAL QSOs using the strength of the absorption is entirely satisfactory. It has been shown that pure-AI classifications produce heterogeneous catalogues in which there seem to be different populations of objects (Knigge

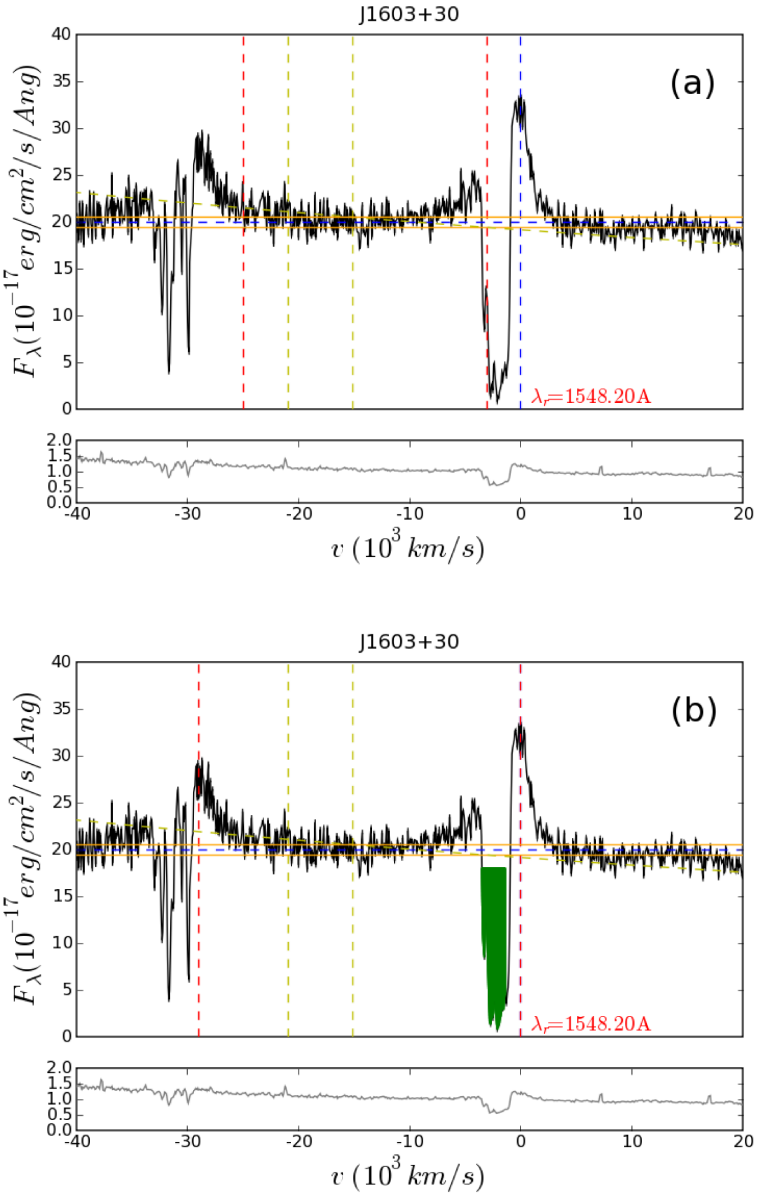

Figure 2.4: Rest-frame UV spectra of SDSS J160354.15+300208.6 showing a BAL system close to the C IV emission line. In the top panel, BI is computed, and the corresponding integration limits are shown as red vertical lines. The vertical yellow lines mark the region used to estimate the continuum level, which is represented as a horizontal stripe. This computation results on BI=0. In the bottom panel AI results on a non-zero contribution (represented by the green area), yielding AI=1495 and σ_{AI}=3.1. The small boxes below each spectra show the spectrum noise, as determined by the SDSS reduction pipeline.

et al. 2008), not always related to the BAL phenomenon. On the other hand, pure-BI classifications produce incomplete catalogues which hamper for instance a precise estimate on

the fraction of QSOs showing the BAL phenomenon.

Some attempts have been made to overcome this difficulty. One approach is to use the BI to classify the most obvious examples, and then visually classify the remaining candidates, having in mind other properties attributed to genuine BAL QSOs like smooth profiles, low variability, partial coverage, etc. This was done for instance by Ganguly et al. (2007) who could make an estimate on the number of "contaminants" present in the AI-based catalogue of SDSS-DR3 QSOs previously compiled by Trump et al. (2006). This brute-force way of classification has the disadvantage of being highly time-consuming when it has to be applied to large samples, and also somewhat subjective. However, it definitely makes a more complete and reliable classification than any of the BI or AI indices alone.

A more recent approach was followed by Knigge et al. (2008) who again used the BI as a first step to classify the most obvious BAL QSOs. Afterwards they refined the classification with a trained neural network (LVQ, Learning Vector Quantization; Kohonen 2001) to classify those limiting cases close to BI=0. The information provided to the neural network was the continuum-subtracted spectrum in a region from 1400 to 1700 Å (rest-frame), thus covering the C IV line. After the network was trained using a subset of previously classified objects, the target sample is thus classified, and those cases for which the network and the BI gave different results were visually inspected to make a final decision.

The Detachment Index

Other indices have been defined to fully characterise the absorbing troughs with the aim of finding correlations with other different QSO characteristics. For instance, Weymann et al. (1991) who defined the already mentioned BI also introduced the so-called Detachment Index (DI). The purpose was to quantify how shifted an absorbing trough is with respect to its associated emission feature. Such a definition is difficult because, as mentioned above, many BAL QSOs can have complex structures with several troughs. A solution can be to select the most prominent through, and then measure the shift of this with respect to the emission peak. Another difficulty is that sometimes the emission peak is not easy to determine precisely because part of the line can already be absorbed by the BAL. The relatively complex recipe proposed by Weymann et al. (1991) is explained in the Appendix B of their work.

2.1.5 Variability of the BAL troughs

BALs are assumed to be associated with plasma outflows in the vicinity of the quasar nucleus, so it is expected that strong physical changes in the velocity, density or geometry of these outflows should be translated into some kind of variability in the BAL structure. Depending on the mechanism driving the changes in the outflow properties, the corresponding BAL variability might be observable on different timescales. For instance, in sufficiently dense winds, variability can be observed on timescales of weeks or even days, and this can be due to changes in the continuum UV flux which, in turn, change the photoionisation

state of the wind.

An example of the variability observed in the C IV and Si IV BALs in the spectrum of quasar CSO 203 can be seen in Figure 2.5. Significant variations are found between the two first observational epochs, distant about 1 year (4 months in the quasar's rest-frame).

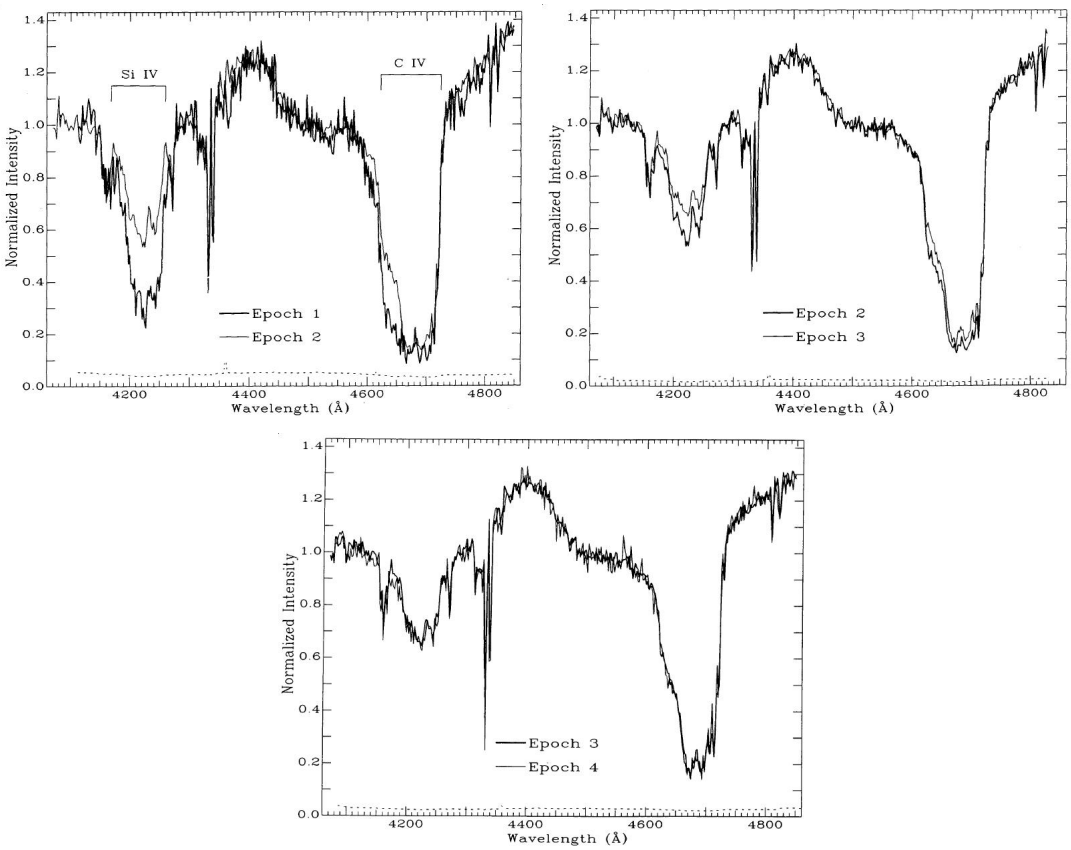

Figure 2.5: Comparison of the different observations of the C IV and Si IV absorptions present in the spectrum of the BAL QSO CSO 203. The interval between epochs 1 and 2 is about 1 year ($\sim$ 4 months in the rest frame), and 2.5 months between epochs 2 and 3 and between epochs 3 and 4 ($\sim$ 24 days in the rest frame). Extracted from Barlow et al. (1992).

Monthly BAL variations seem to be stronger at relatively high detachments from the emission line, which implies higher outflow velocities. For instance, Lundgren et al. (2007) analysed a sample of 36 BAL troughs and found significant time variability on several of them, among which three are highly variable. The latter presented detached BALs covering a velocity range 12,000−16,000 km s^{-1}, a velocity regime where recent quasar wind models (e.g., Proga et al. 2000) predict variable overdensities as a result of plasma instabilities. Another characteristic of the observed monthly BAL variations is that they mainly affect the depth of the absorbing troughs while changes in velocity are more rare. These depth variations seem not to be correlated with changes in the source continuum, which probably

means that they are due to changes in the covering factor, i.e. as a result of transverse clouds crossing the outflow in a more or less perpendicular trajectory with respect to the line of sight.

A recent work addresses the variability of BALs on timescales of about years (Gibson et al. 2008). These results confirm that stronger variations are more likely to happen in relatively narrow absorption features. Gibson et al. (2008) also found that higher variations are seen when monitoring BAL absorbing troughs during longer periods. Their observations allowed them to set a tentative lower limit for the lifetime of a typical BAL feature, $t_{BAL} \geq$ 18 yr, although the authors note that this time can be longer by several orders of magnitude.

2.1.6 Differences in the UV spectra of BAL and non-BAL QSOs

The first systematic comparison between the UV continuum and emission line properties between BAL and non-BAL QSOs was done by Weymann et al. (1991). They selected a sample of 42 BAL QSOs (25 from the Luminous Bright Quasar Survey, LBQS, and 17 from other samples), and a comparison sample of 25 non-BAL QSOs from LBQS, matching both samples in luminosity to avoid introducing luminosity effects as a consequence of different properties of the broad emission line region. In this comparison they built several subsamples and statistically compared different spectral properties like spectral indices, line ratios, velocity shifts, etc., finding that:

- the continuum and the emission line properties of BAL and non-BAL QSOs are remarkably similar.
- relative velocity shifts between the peaks of C IV, C III] and Mg II are present. There is a small bluewards displacement of the C IV peak relative to the C III] peak, strongly correlated with the much larger bluewards shift of C IV relative to Mg II. But there are no noteworthy differences on these shifts between BAL and non-BAL QSOs.
- there is a strong correlation between the strength of the Fe II emission (2070, 2400 Å) and the BI, but no correlation between the detachment index (DI) and the strength of Fe II.
- LoBAL QSOs showing strong Mg II and Al III absorptions are much redder in the interval [1550−2200 Å] than non-BAL and HiBAL QSOs. LoBAL QSOs also show strong Fe II emission and much stronger evidence for Fe III than C III].

The main conclusion they obtained from these similarities is that these samples of BAL and non-BAL QSOs are likely drawn from the same parent population, and the small differences seen between both groups can be attributed to a mixture of orientation effects. They also suggested that LoBAL QSOs are probably a population of highly obscured QSOs with high column densities along the line of sight to them.

A more recent study with the same scope has been done with a much larger sample by Reichard et al. (2003). They used the catalogue of BAL QSOs from the SDSS Early Data Release (Reichard et al. 2003) and got to similar conclusions. A direct comparison of the observational properties of the different classes of BAL QSOs and the group of non-BAL QSOs can be seen in Figure 2.6, extracted from Reichard et al. (2003). There, the composite spectra of the different BAL QSO sub-classes in their sample are shown. The composites were built taking the geometric average of the spectra of all objects in each class, after bringing them to the rest-frame and normalising. The details can be found in Reichard et al. (2003).

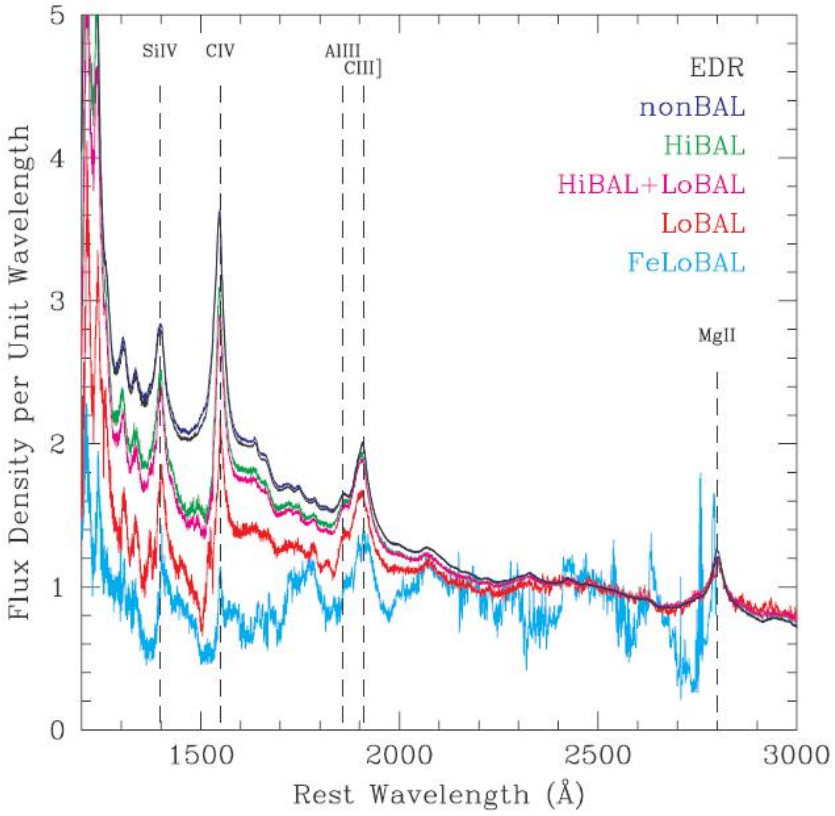

Figure 2.6: Composite spectra of different types of QSOs. In this plot the different spectral slopes of the various classes of BAL QSOs and the non-BAL QSOs can be seen. EDR means all QSOs from the Early Data Release from SDSS. Extracted from Reichard et al. (2003).

The most evident information in this plot is that there seems to be a sequence of increasing reddening going from non-BAL QSOs, followed by HiBAL, LoBAL and finally FeLoBAL QSOs. The main conclusions extracted from the composites of these different groups of objects were:

- LoBAL QSOs are significantly more reddened than HiBAL QSOs and these more

reddened than non-BAL QSOs.

- The C IV emission peak is, on average, more shifted respect to Mg II in BALs QSOs than in noBAL QSOs, but this difference is not very high, and shift values found in BAL QSOs are within the limits of observed shifts found in normal QSOs without the BAL phenomenon.
- BAL QSOs are best described by a bluer quasar composite compared to normal QSOs, once the reddening contribution has been subtracted. However, they are not intrinsically bluer than typical blue normal QSOs.

Again, the authors suggested that these small differences between BAL and non-BAL QSOs make them occupy a slightly different position in the parameters space, but there is no obvious need for a different parent population to explain these differences.

2.2 Optical Polarisation of BAL QSOs

At the beginning of the eighties, polarisation surveys in the optical of bright normal QSOs (e.g., Stockman et al. 1984) showed that most (i.e., 99 per cent) QSOs are weakly polarised in the optical, with fractional polarisation < 3 per cent, and the majority of them with fractional polarisations smaller than 1 per cent. A subset of quasars constitute an exception to this rule, the so-called highly polarised QSOs (HPQs). These are mostly radio-loud quasars which emit optical synchrotron light boosted by relativistic motion in a jet pointing in a direction close to the line of sight, and they show fractional polarisation higher than 3 per cent.

However, optical QSO samples are strongly biased against reddened or obscured quasars. Subsequent infrared observations of highly obscured quasars showed that these are more polarised because the thermal unpolarised emission is more highly attenuated than the scattered emission.

It was soon discovered that apart from these HPQs, a second class of objects, the BAL QSOs, presented an anomalously high polarised emission when compared to normal radio-quiet quasars, but not as high as in HPQs. Differently from the latter group, BAL QSOs show little or no variability in their polarisation, which indicates a different origin or physical configuration/geometry of the emission mechanism.

Figure 2.7 shows an illustrative example, which represents the typical situation of BAL QSOs as far as the polarised emission is concerned. The polarised radiation comes mainly from the absorbed troughs and is less pronounced in the broad emission lines than in the continuum. In addition, the polarisation of the continuum seems to decrease slightly towards the blue.

An important step forward towards the characterisation of the polarised emission in BAL QSOs was done almost simultaneously by three different groups who made polarimetric observations at the end of the nineties. Schmidt & Hines (1999) compiled a list of 53 BAL QSOs from different surveys using mostly the 2-m class telescopes at the Steward

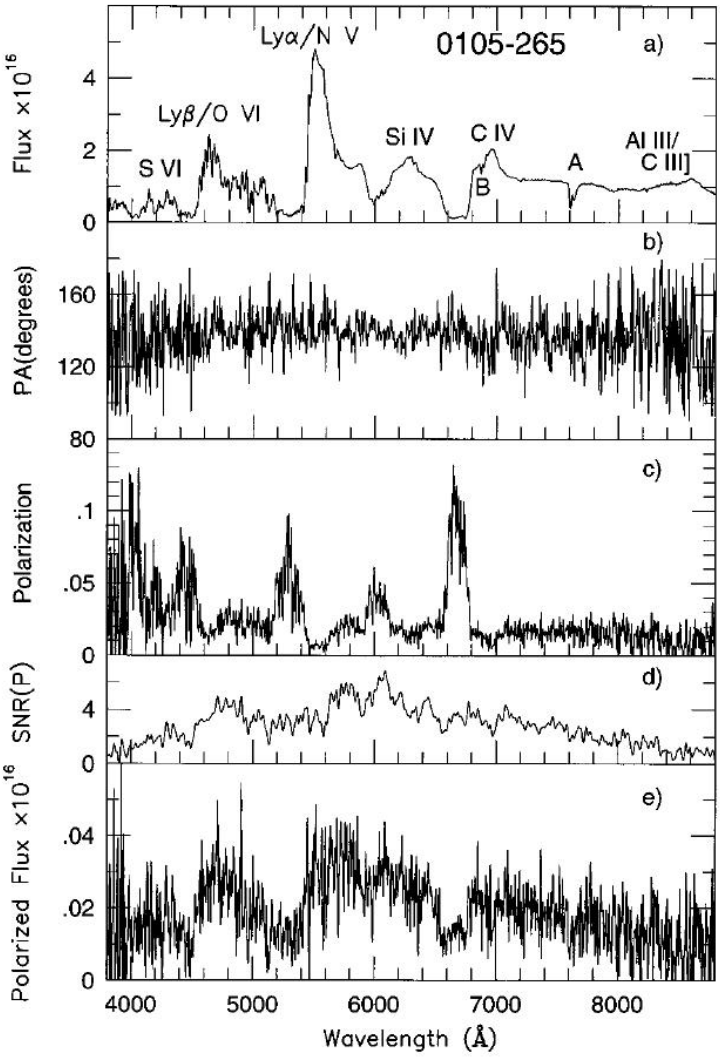

Figure 2.7: Keck spectropolarimetry of 0105−265. (a) Total flux (b) Polarisation position angle (c) Fractional linear polarisation (d) Signal-to-noise ratio in fractional polarisation and (e) Polarised flux. Extracted from Cohen et al. (1995).

and McDonald observatories. Almost simultaneously, Hutsemekers et al. (1998) published polarimetric observations of a sample of 29 BAL QSOs with the 3.6-m telescope at La Silla Observatory. A bit later, Ogle et al. (1999) presented polarimetric observations of a sample of 36 BAL QSOs with the Keck and Palomar telescopes. All three works firmly stated that BAL QSOs are on average more highly polarised than normal QSOs.

Typical polarisation degrees found in BAL QSOs are of the order of 1 per cent but several authors have found polarisation in LoBAL QSOs of the order of 1.5 per cent, on average slightly higher than in HiBAL QSOs. This trend might be consistent with the higher

obscuration of LoBAL QSOs that was mentioned in the previous section. However, polarisation in BAL QSOs is not as high as in the most obscured IRAS QSOs/Hyperluminous IR galaxies (Hines & Wills 1990)

Another important result is the anticorrelation found by Lamy & Hutsemekers (2004) between the optical polarisation degree and DI, being on average BAL QSOs with P-Cygni profiles (small DI) more highly polarised than BAL QSOs with more detached troughs. This anticorrelation can be interpreted as a dependence on the geometry and orientation of the scattering region causing the polarisation, suggesting a different orientation for BAL and non-BAL QSOs.

The main mechanism responsible for the observed optical polarisation in the continuum of BAL QSOs seems to be electron scattering in the thick X-ray absorber. However, there is uncertainty in the exact geometry and location of this absorber (e.g. Punsly 1999; Wang et al. 2005), which is related to the assumed model for the dynamics of the BAL phenomenon (see later Section 2.7).

2.3 X-ray characteristics of BAL QSOs

The first observations of BAL QSOs in the X-ray domain were first done in the early nineties thanks to the ROSAT Observatory and its Position Sensitive Proportional Counter (PSPC). This instrument was used to perform the ROSAT All Sky Survey (RASS).

The column densities deduced at that time from the UV-optical spectra of BAL QSOs were about $N_H \sim 10^{20}-10^{21}$ cm^{-2}. With these not very high column densities it was expected that BAL QSOs would be relatively bright in the X-ray domain. However, Green et al. (1995) stated and later Green & Mathur (1996) confirmed that BAL QSOs are mainly weak objects in the soft X-rays. Since the UV-properties of BAL and non-BAL QSOs had been found to be so similar, this lack of X-ray emission was interpreted as due to absorbing material and not as an intrinsic deficit of X-ray emission in BAL QSOs. In fact, Green & Mathur (1996) found that column densities higher than 10^{22} cm^{-2} should be expected to explain the absorbed X-ray spectra. Similarly, Gallagher et al. (1999) obtained ASCA observations of the optically brightest known BAL QSOs and deduced that the column density needed to explain the low rate of detections was even higher, i.e. $> 10^{23}$ cm^{-2}.

Higher sensitivities were possible with the new generation of X-ray observatories, and Green et al. (2001) observed a sample of 10 optically-selected BAL QSOs with Chandra detecting 8 of them, in contrast with previous X-ray observations where the detection rates were much smaller. These detections allowed them to fit the underlying X-ray spectra and the conclusion was that HIBAL QSOs definitely have an intrinsic X-ray emission similar to that of non-BAL QSOs, confirming the absorbing hypothesis as responsible for the X-ray flux deficit. They also found that the rare class of LoBAL QSOs are particularly X-ray weak as compared to HiBAL QSOs, and that the two examples of FeLoBAL QSOs in their sample could be Compton-thick (i.e. $N_H > 10^{24}$ cm^{-2}). A subsequent study with a larger and more homogeneous sample of optically-selected BAL QSOs (Gallagher et al. 2006) con-

firmed all these results. They also found evidence that the intrinsic absorption responsible for the X-ray flux deficit is not well explained assuming a simple neutral absorber. Better fits to the data are obtained considering complex or partially ionized absorbers, or maybe partially covered sources.

Nevertheless, not all BAL QSOs might show the presence of such a relatively dense absorber. A recent study by Giustini et al. (2008) has shown that when analysing *X-ray-selected* samples instead of *optically-selected* samples of BAL QSOs, the obtained column densities are somewhat lower (sometimes up to three orders of magnitude smaller). They also note that the lowest column densities correspond to those QSOs at the limit of the definition of BAL QSOs, i.e., those with BI = 0 but AI > 0. In addition, Wang et al. (2008) have found that the X-ray spectra of 3 out of 4 *polar* BAL QSOs (for which the axis is likely aligned to the line of sight) are consistent with normal X-ray behaviour and no absorption. The fourth object in their sample belongs to the class of FeLoBAL QSOs and shows strong intrinsic absorption.

The conclusion is that there are some X-ray properties of BAL QSOs that have been determined but there are still several aspects to be understood. Since many of these objects are obscured, the current facilities require relatively high integration times to observe large samples with high signal-to-noise spectra, in order to make accurate statistics. The advent of new observatories in the future, like the International X-ray Observatory (IXO) will lead to significant advance in this discussion.

2.4 Studies of BAL QSOS in the IR and sub-mm

As we have seen in previous sections there is considerable evidence from studies at several wavelengths for the presence of obscuring dust and/or gas in at least a sub-group of BAL QSOs: e.g., flatter UV continuum emission, weaker (non-intrinsic) soft X-ray flux density and high optical polarisation (but not as high as in most IRAS QSOs). Since most of the radiation emitted by dust is released in the IR, this is a very interesting spectral range to probe this possible dust.

Near-IR properties

The flatter optical spectral index in BAL QSOs could, in principle, be also manifested as an enhanced emission in the near-IR. In order to study the combined optical+infrared colours in a large sample of BAL QSOs, Dai et al. (2008) cross-correlated the SDSS-DR3 QSO catalogue against the 2MASS (Skrutskie et al. 2006) official Point Source Catalogue, which is 99 per cent complete[2]. They realised that BAL QSOs show a different $i-K_S$ colour distribution than normal QSOs, being the former redder than the latter. For this reason many BAL QSOs might be lost in optically-selected samples. A similar conclusion was obtained by Maddox et al. (2008) who used deeper IR data from the UKIRT (UK Infrared

[2]See `http://www.ipac.caltech.edu/2mass/releases/allsky/doc/sec6_5a1.html`

Telescope) Infrared Sky Survey (UKIDSS)[3], in combination with the SDSS-DR3 catalogue. They suggested that the excess in i−K colour they found in BAL QSOs can be explained by an additional average value of E(B−V)=0.02−0.03. They also proposed an algorithm for selecting high-redshift BAL QSOs using optical and near-IR colours (see Figure 2.8).

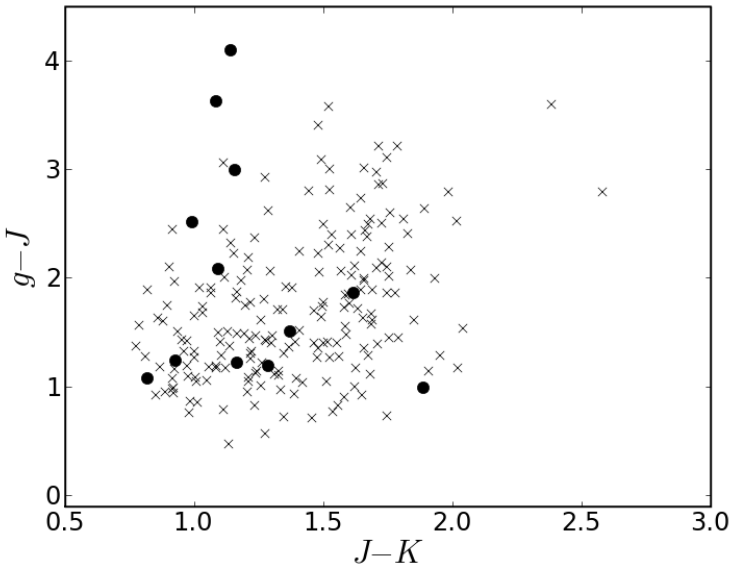

Figure 2.8: This g−J vs. J−K diagramme shows the location of the BAL QSOs (circles) compared to the normal QSOs (crosses). The sample contains all QSOs detected by Maddox et al. (2008) in a cross-correlation between SDSS-DR3 and UKIDSS data. The authors propose that high-z BAL QSOs can be selected with a high efficiency using the constraints: J−K $\sim$ 1 and g−J $>$ 2.5. In this region the fraction of extreme BAL QSOs is high as compared to the number of non-BAL QSOs.

As far as the spectroscopic analysis in the near-IR is concerned, a subsample of IR-bright BAL QSOs was studied by Egami (1999) who found several remarkable properties of some of these objects:

- They present a significantly large Balmer decrement, H_α/H_β, which indicates higher absorption by dust than in normal QSOs.
- Some show very weak or sometimes complete absence of the [O III] λ 5007 Å emission line, suggesting obscuration of ionizing radiation (see also Boroson & Meyers 1992 or Yuan & Wills 2003).
- They usually show strong Fe II emission, which tends to be weak or nonexistent in most normal QSOs.

[3]See `http://www.ukidss.org`

These characteristics again suggest the presence of large amounts of obscuring dust around the AGN. In fact, since these are properties also shown by another class of objects, the so-called warm ULIRGs, Egami (1999) proposed that LoBAL QSOs could be the high-z counterparts of warm ULIRGs. These objects are defined as bright IR galaxies with L_{IR} luminosities typically $> 10^{12}$ $L_{\odot}$, and with IRAS colours in the range $0.2 < f_{\nu}(25\ \mu m)/f_{\nu}(60\ \mu m) < 2.0$. According to the theory proposed by Sanders et al. (1988) warm ULIRGs could be transition objects between cooler ULIRGs and QSOs. We will get back to this topic later.

Mid- and Far-IR properties

Already in samples of IRAS-selected QSOs it became clear that BAL QSOs were present in a significant proportion. Low et al. (1989) found 2 BAL QSOs with Mg II absorptions (LoBALs) in a sample of 11 Palomar Green (PG) QSOs detected by IRAS. However, only 6 of them were at the appropriate redshift to be able to see these absorptions in their optical spectra, so the rate of LoBAL QSOs (2 out of 6) could be really high. This is consistent, in principle, with the higher amount of reddening inferred from the flatter UV continua, especially in the classes of LoBAL and FeLoBAL QSOs (Weymann et al. 1991; Sprayberry & Foltz 1992; Reichard et al. 2003).

More recently, Gallagher et al. (2007) presented Spitzer MIPS observations of 38 BAL QSOs at 24, 70 and 160 µm, and complemented them with literature data at other frequencies to study the overall SED of these objects from the radio to the X-rays. They compared the SEDs of BAL QSOs with those of a suitable comparison sample of normal QSOs and the conclusion was that no significant differences were found between the mid-IR emission in both classes of objects. However, it is worthwhile to mention two facts: (i) only 6 out of 38 BAL QSOs were actually classified as LoBAL QSOs in their sample, while most of the results previously mentioned apply mainly to LoBAL QSOs; (ii) about two thirds of the objects in their sample were non-detections at 70 µm, and more than 90 per cent of them were not detected at 160 µm. This makes the statistical comparison depend on other sources of uncertainty, for instance the selection of suitable MIR/FIR SED templates to describe both population of quasars.

Similar observations with Spitzer by Farrah et al. (2007) were focused on a small sample of nine objects belonging to the the rare FeLoBAL QSO class. While the majority of the objects analysed by Gallagher et al. (2007) were not detected at 160 µm (suggesting little contribution from starburst) in this sample roughly half of the objects are detected in this band, and all but two are detected at 70 µm. This is evidence of strong starburst, and they deduced star formation rates of about hundreds of solar masses per year in many of these objects, which are typical values found in local ULIRGs and in high-z sub-mm bright sources.

Emission in sub-mm

Several works have addressed the determination of the mm and sub-mm properties of BAL QSOs, mainly through SCUBA observations, but all with similar conclusions. Lewis

et al. (2003) and Willott et al. (2003) studied the sub-mm flux density distribution of BAL QSOs and tested them against similar samples of non-BAL QSOs finding no significant differences in both groups. However, the observations presented in these works are relatively shallow with typical 1-σ sensitivities of about 2.5 mJy, and many of the BAL (and non-BAL) QSOs are non-detections. The subsequent work by Priddey et al. (2007) reached slightly deeper limits (about 1.5 mJy, 1-σ, at 850 µm) and their similar comparison was consistent with no differences between the sub-mm emission of BAL and non-BAL QSOs. They found however, a tentative correlation between sub-mm flux density and the equivalent width of the characteristic C IV BAL.

2.5 Radio emission in BAL QSOs

For a long time BAL QSOs were believed to be extremely rare among the population of luminous radio quasars. As an example, Stocke et al. (1992) found a strong anticorrelation between radio emission and the presence of BALs in a sample of 68 BAL QSOs they observed with the VLA. They argued that if BAL and non-BAL QSOs are extracted from the same parent population (in which the radio-loud/radio-quiet dichotomy is present) the probability of finding powerful radio sources among BAL QSOs is about 1 per cent. In light of these results, they hypothesised that quasars can develop either a low-power sub-relativistic BAL wind or a highly collimated jet giving rise to strong radio emission, but not both at the same time.

Despite this lack of BAL QSOs among strong radio sources, there was evidence that some of these BAL QSOs emit in the radio at low radio-powers, below the canonical definition of radio-loud QSOs. Francis et al. (1993) discovered an overdensity of about 10 times more BAL QSOs among radio-moderate radio quasars, with $0.2 < R < 1.0$, compared to radio-quiet objects. In this work R is defined as the ratio of the rest-frame Johnson B-band flux density to the rest-frame 8.4-GHz flux density, applying the appropriate K-correction. Radio-loud objects are those with $R > 1.0$ and radio-quiet those with $R < 0.2$. It is not clear though, whether this overdensity has any physical origin, because it can just be the effect of a higher obscuration of the optical continuum emission from BAL QSOs, which makes the R value increase with respect to radio-quiet, less obscured, normal QSOs.

However, it was the advent of the large comprehensive radio surveys, like FIRST, which manifested the existence of a substantial population of radio-loud BAL QSOs. For the first time Becker et al. (1997) reported the existence of a radio-loud BAL QSO (1556+3517) with FeLoBAL features in its UV spectrum. Again the heavy reddening affecting this object could be the cause of such a high radio-loudness. To avoid this selection bias, Brotherton et al. 1998 matched the FIRST catalogue of radio sources against 111 QSOs selected by their UV excess, and thus, relatively free of obscuration effects, finding five radio-loud BAL QSOs (two HiBAL and three LoBAL QSOs). This discovery preceded the compilation of the first relatively big samples of radio-loud BAL QSOs, by cross-correlating the FIRST catalogue with the FBQS (Becker et al. 2000, 2001).

The analysis of these samples allowed these authors to obtain some radio properties of

BAL QSOs:

- They display compact morphologies, in contrast to the majority of quasars in the FBQS which show both compact and extended structures.
- The radio spectral indices (calculated between observed 1.4 and 8.4 GHz) in the sample were found to be both flat and steep, having stated the boundary between both categories in $\alpha_{1.4}^{8.4}$=−0.5.
- BAL QSOs seem to be less common among radio-powerful objects (see Figure 2.9). The relative fraction of HiBAL to normal QSOs was found to be 4 times smaller in QSOs with log(R*) > 2. The authors defined R* as the ratio of the 5 GHz radio flux density to the 2500 Å optical flux density in the QSO rest frame. A similar conclusion would be valid for LoBAL QSOs but their statistics are low to obtain a sensible estimate. Later on, in the same line, Hewett & Foltz (2003) estimated that the probability for a BAL QSO to be detected at the FIRST flux density limit ($\sim$ 1 mJy) is about half that for a non-BAL QSO.

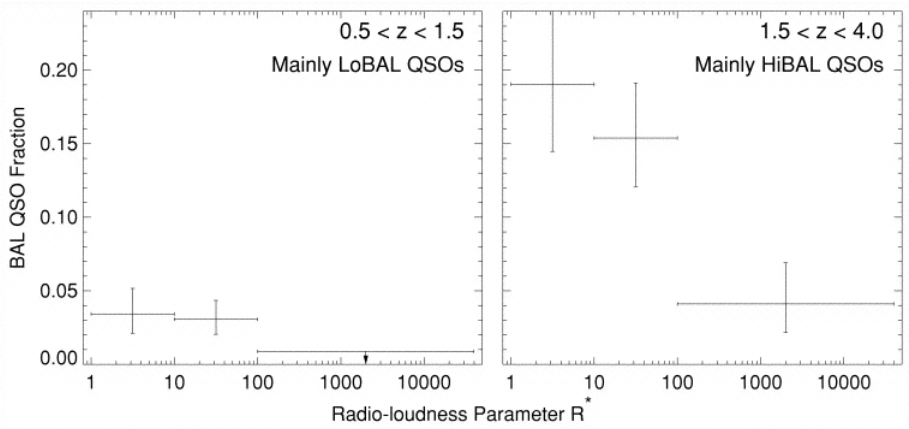

Figure 2.9: The dependence of the BAL QSO fraction as a function of radio-loudness for the QSOs in the FBQS can be seen. Extracted from Becker et al. (2001).

These studies were mainly based on two-frequency radio observations, i.e. 1.4 and 8.4 GHz, the minimum to obtain a radio spectral index. But questions like the overall shape of the radio spectra, or the effect that the redshift distribution might have in the analysis of the spectral indices remained opened. Another interesting question suggested by these results is whether the compact sizes of radio sources associated with BAL QSOs are real or only due to projection effects. Many of these questions are addressed in this thesis and will be developed in Chapters 5 and 7.

Some of the mentioned observations with the VLA were done in the B and A configurations with typical resolutions of about 5 and 1.5 arcsec at 1.4 GHz, respectively. The first attempts to observe these objects at the sub-arcsec scale were done by Jiang & Wang

(2003) who presented EVN observations at 1.6 GHz of only three BAL QSOs in Becker's list, confirming their compactness. They all presented projected linear sizes (i.e., measured on the plane of the sky) of less than 1 kpc and only the radio BAL QSO 1312+23 showed a two-sided symmetric structure similar to that displayed by Compact Symmetric Objects (CSOs), but with the difference of being the core and not the lobes the brightest component in 1312+23.

Another interesting VLBI observation of the BAL QSO 1045+352 was later published by Kunert-Bajraszewska & Marecki (2007). They reported EVN and MERLIN multi-frequency observations of this CSS source which presents a two-sided asymmetric morphology extending up to several hundred parsecs in two different directions. It was suggested that this behaviour might be explained by intermittent radio activity in this object. More recently, Liu et al. (2008) presented EVN+MERLIN 1.6-GHz observations of 8 additional radio BAL QSOs, which mainly showed unresolved or marginally resolved cores, except one source showing a two-sided structure at scales of about 2 kpc.

Variability studies in the radio have also culminated in important discoveries about radio BAL QSOs. Analysing the variability between the two epochs of FIRST and NVSS radio surveys, first Zhou et al. (2006) and later Ghosh & Punsly (2007) identified a small subset of BAL QSOs highly variable in the radio. They interpreted these variations as the result of strong beaming, and concluded that these BAL QSOs have their radio axes closely aligned to the line of sight, representing the subpopulation of "polar" BAL QSOs.

In opposition, Gregg et al. (2006) identified a small subgroup of BAL QSOs with indications of an extended morphology and the presence of two lobes at kpc distance from the nucleus. They called this an FR-II morphology because it reminds of the disposition of radio galaxies of type Fanaroff-Riley II (Fanaroff & Riley 1974). They found these FR-II type BAL QSOs while analysing the radio morphology of the 45,000 QSOs in the SDSS catalogued at that time. They discovered a similar correlation between radio-loudness and BAL strength, which seems to be even stronger in these FR-II radio-loud BAL QSOs.

2.6 The number of BAL QSOs

Quasars showing BAL features were taken for many years as simple curiosities because only few were known. But when the first catalogues of quasars were compiled, thanks to more sensitive instruments and new techniques of optical-colour selection, it was seen that a considerable fraction of luminous quasars showed these absorptions. Later, the advent of the Hubble Space Telescope (HST) with sensitive instrumentation in the UV range facilitated the observation of similar phenomena in low-luminosity AGN (see e.g. Weymann et al. 1997; Crenshaw et al. 1999).

The fraction of QSOs showing BAL winds is a very important number to understand the origin and nature of these objects. For this reason many authors have tried to constrain this number from several different samples. In the following a brief review will be given

on the different attempts to quantify how many BAL QSOs are there compared to the number of normal non-BAL QSOs. A small summary will be given on the results found from samples selected at different wavelengths and the main difficulties to get an accurate estimate will be stressed.

Estimates in optical and near-IR samples

Up to now, the largest volume of spectroscopic data comes from the wide-area optical surveys, and only a limited amount of near-IR spectra have been collected. For this reason, the estimates on the fraction of BAL QSOs are mainly based on QSOs showing absorptions detected in the optical window. In practice, this means that at redshifts higher than 1.5, the analysis has mainly reduced to HiBAL QSOs only, for which the C IV absorbing trough can be seen in the optical. Above this redshift Mg II absorptions move towards near-IR wavelengths as redshift increases. That is why most of the following works determine the fraction of HiBAL QSOs only, instead of the global fraction of BAL QSOs.

The first estimates of the (observed) fraction of BAL QSOs were obtained at the beginning of the nineties studying the sample of LBQS quasars. This sample includes all quasars in the survey with magnitudes brighter that $B_J \sim 18.7$. The result was that about 9 per cent of these objects presents the BAL phenomenon. Foltz et al. (1990) considered the bias consisting of a small fraction of objects not being included in the sample because the flux density decrease in their absorbing troughs makes their B_J magnitude to increase above the limit that defines the sample. After correcting for this bias they calculated that 12 per cent of quasars might show the BAL phenomenon.

More recently, Hewett & Foltz (2003) analysed a sample of 67 BAL QSOs from the LBQS, and created composite spectra of the different classes of BAL QSOs in order to take into account the K-correction in the counting process. They deduced an observed fraction of (15 ± 3) per cent, slightly higher than previous estimates, and an intrinsic fraction of (22 ± 4) per cent of BAL QSOs in the redshift range between 1.5 and 3.0.

But the advent of the SDSS and the large amount of good quality spectra obtained allowed Reichard et al. 2003 to determine this fraction using a significantly larger sample of 224 QSOs with $i \leq 20$. After considering the K-correction and some biases inherent to the SDSS quasar selection algorithm, they concluded that (13.4 ± 1.2) per cent of QSOs would present the BAL phenomenon, without any redshift dependence in the range $1.7 \leq z \leq 3.45$.

All the works mentioned above have used the BI in their estimates to separate BAL QSOs from non-BAL QSOs, and usually the reference absorbing trough is the one found in C IV. As shown in Section 2.1.4, BI is considered to be a quite reliable but not complete index, because there are QSOs with BI=0 that should clearly be considered BAL QSOs. Trump et al. (2006) compiled a much larger sample of 4784 BAL QSOs from the SDSS third data release and they used the less conservative AI to select them. With these criteria they conclude that 26 per cent of QSOs have BALs in C IV, about 1.3 per cent show Mg II absorptions and only 0.3 percent show FeLoBALs. This estimate almost doubles the ones

previously obtained using the traditional BI, and this proves how sensitive this fraction is on the algorithm used to measure the absorbing troughs.

However, there is another important bias which affects these estimates. As said above, one of the main characteristics of BAL QSOs (especially from the LoBAL type) is that they are significantly reddened. This means that many of them will not be detected in optical surveys, which might suggest that the intrinsic fraction of BAL QSOs will be higher that the inferred values. For instance, the near-IR-selected sample by Dai et al. (2008) contains an observed fraction of BAL QSOs of about 40 per cent, much higher than in optical surveys. However, this high fraction should be compared with the "optical" estimate by Trump et al. (2006) because the authors use the same parent sample and the same criterion (AI) to select BAL QSOs. In a subsequent work by Maddox & Hewett (2008), the authors selected a sample with deeper photometric limits. They cross-correlated the QSOs from the SDSS-DR5 in the Stripe 82 (22h 24m $<$ RA $<$ 04h 08m, -1.27 deg $<$ Dec $<$ $+1.27$ deg, ~ 290 deg^2), more sensitive than the overall SDSS database, with the UKIDSS Large Area Survey DR3. Using the traditional BI index, they found an observed BAL QSO fraction of about 25 per cent, still higher than the fraction found in optical surveys.

Estimates in radio-selected samples

The obscuration effects can be avoided analysing radio-selected samples. However, it should be taken into account that the fraction of BAL QSOs could, in principle, be different in radio-quiet and radio-loud objects.

The first statistically significant estimate of the fraction of radio-loud BAL QSOs was made by Becker et al. (2000) who collected a large enough sample of these objects from the FBQS. They deduced a fraction of (18 ± 3.8) per cent of BAL QSOs, taking into consideration those with BI > 0 and including also some objects with BI=0 but subjectively classified as BAL QSOs by their spectra. Adding to the sample some more objects discovered in the Southern region of the FBQS (Becker et al. 2001) they obtained a fraction of BAL QSOs close to the previous value when considering only objects with $R^* < 100$. The fraction decreases down to $\sim$4 per cent for the most radio powerful, i.e. with $R^* > 100$. However, Carballo et al. (2006) pointed out that the FBQS is not a pure-radio survey because the colour cut B$-$R < 2 was imposed for selecting the spectroscopic targets (or the similar colour cut O$-$E > 2, based on the APM photometry of the digitised POSS-I plates in the northern hemisphere). This colour constraint would be missing the reddest objects with B$-$R > 2 among which many are probably BAL QSOs.

Carballo et al. (2006) performed the complementary survey to the FBQS, that is, they selected candidates for spectroscopy with both radio-emission at 1.4 GHz and an optical counterpart with B$-$R > 2. This survey was specifically designed to efficiently select high-z QSOs with $3.7 < z < 4.4$. They obtained a fraction of BAL QSOs of (27 ± 10) per cent and noted that this should be considered as an upper limit of the true BAL QSO fraction because a smaller value had been reported with only the bluer objects in the FBQS. In any case, the conservative BI criterion adopted in their work might translate into a somewhat

higher fraction.

It is the recent work by Shankar et al. (2008) which fully focuses on the determination of an accurate fraction of BAL QSOs showing radio emission. The cross-correlation of the SDSS-DR3 catalogue against the FIRST database allowed these authors to find a fraction of classical (i.e., BI-selected) BAL QSOs of $20.5^{+7.3}_{-5.9}$ per cent at the faintest radio-power detected ($L_{1.4\mathrm{GHz}} \sim 10^{25}$ W Hz^{-1}), while this fraction drops to < 8 per cent at $L_{1.4\mathrm{GHz}} \sim 3 \times 10^{26}$ W Hz^{-1}. These two values translate into $44^{+8.1}_{-7.8}$ and $23.1^{+7.3}_{-6.1}$ per cent, respectively, if the selection is based on the less restrictive AI.

The results of some of these works confirm that the BAL phenomenon happens less frequently among powerful radio-loud objects, and that BAL QSOs are more common when the radio power decreases. Although the flux density limit of the FIRST survey is about 1 mJy it is worth questioning whether this trend will continue at fainter radio regimes. The interesting work by White et al. (2007) addressed this question by analysing the population of μJy radio sources using the stacking technique and combining the wide coverage of both the SDSS and the FIRST surveys. Surprisingly, they found that, *on average*, BAL QSOs show stronger radio emission than normal non-BAL QSOs at this very faint radio flux densities. They reached similar conclusions when considering both the radio power and the radio-loudness parameter as a measure of radio strength, which suggests that the results are not dependent on the UV energy distribution of both groups of objects, and therefore on the presence of dust.

The true fraction of QSOs with outflows

As just mentioned there are different works trying to constrain the fraction of QSOs presenting the BAL phenomenon, using different techniques and with samples selected at different wavelengths. Table 2.1 summarises all these results. The main issues in the determination of a close-to-real value are: (i) the use of a good algorithm to classify BAL QSOs in a reliable and complete way and (ii) the determination and correction of the biases that affect the samples under study.

Regarding the first problem, the best method found so far to build reliable and complete samples of BAL QSOs seems to be the Balnicity Index as a first stage (in order to identify those objects with more obvious absorptions) in combination with a second refined classification of the limiting cases with BI ~ 0. This second revision can be based on a visual inspection or on more sophisticated classification methods. For instance, Ganguly et al. (2007) made use of a visual inspection to classify the BAL QSOs in the SDSS-DR2 catalogue. They compared their own analysis on the fraction of BAL QSOs with the results of Trump et al. (2006) using the AI, and they found on the same parent sample a difference of about 15 per cent of objects that according to Ganguly et al. (2007) can be considered as false positives (most of them narrower absorptions that could be due to associated systems but not linked to the BAL phenomenon). A different approach was taken by Knigge et al. (2008) who classified the limiting cases making use of neural networks and in their analysis they concluded that the AI distribution of BAL QSOs seem to be bi-modal, with genuine

Table 2.1: Estimates of the BAL QSO fraction.

Reference	Selection	N	z range	Observed (per cent)	Intrinsic (per cent)
Foltz et al. (1990)	opt,Vis	?	1.6≤z<2.1	∼ 8	11±3
Foltz et al. (1990)	opt,Vis	?	2.1≤z<3.0		15±5
Becker et al. (2000)	rad,Vis	18	1.4≤z	18±3.8	–
Becker et al. (2001)	rad,Vis	31	1.4≤z	∼17 (R^* <100)	–
Becker et al. (2001)	rad,Vis	31	1.4≤z	∼5 (R^* >100)	–
Ganguly et al. (2007)	opt,Vis	562	1.7≤z≤2	11.0	–
Hewett & Foltz (2003)	opt,BI	67	1.5≤z≤3.0	15±3	22±4
Reichard et al. (2003)	opt,BI	224	1.7≤z≤3.45	13.4±1.2	–
Trump et al. (2006)	opt,BI	4784	1.7≤z≤4.38	10.4±0.2	–
Dai et al. (2008)	NIR,BI	∼56	1.7≤z≤4.38	23±3	–
Maddox et al. (2008)	NIR,BI	9	1.7≤z≤3.8	∼25	–
Maddox & Hewett (2008)	NIR,BI	25	1.7≤z≤3.8	∼27	–
Becker et al. (2000)	rad,BI	18	1.4≤z	∼24	–
Carballo et al. (2006)	rad,BI	7	2.0≤z≤4.4	27±10	–
Shankar et al. (2008)	rad,BI	?	1.7≤z≤4.38	$20.5^{+7.3}_{-5.9}$ (low L_{rad})	–
Shankar et al. (2008)	rad,BI	?	1.7≤z≤4.38	<8 (high L_{rad})	–
Trump et al. (2006)	opt,AI	4784	1.7≤z≤4.38	∼26.0	–
Knigge et al. (2008)	opt,AI		1.9≤z≤4.36	13.5	17 ± 3
Dai et al. (2008)	NIR,AI	99	1.7≤z≤4.38	$40.4^{+3.4}_{-3.3}$	43±2
Shankar et al. (2008)	rad,AI	?	1.7≤z≤4.38	$44^{+8.1}_{-7.8}$ (low L_{rad})	–
Shankar et al. (2008)	rad,AI	?	1.7≤z≤4.38	$23.1^{+7.3}_{-6.1}$ (high L_{rad})	–

BAL QSOs only corresponding to one of the modes.

The second problem is much more difficult to solve completely. As far as the reddening and intrinsic obscuration is concerned, the samples selected in the near-IR should be considered more complete, but a deeper understanding on the dust properties of BAL QSOs is still necessary to fully decontaminate for these effects.

We finally note that most of the estimates on the fraction of BAL QSOs are based on the presence of wide absorptions traditionally defined as BALs. There is other evidence of quasar outflows which can be manifested in the form of mini-BALs, NALs, high-velocity outflows (e.g., Rodriguez Hidalgo et al. 2007) or even outflows taking place in the BLR, detected in the analysis of the broad emission lines (e.g., Holt et al. 2008). Putting all these signatures of outflows together, Ganguly & Brotherton (2008) estimated that about 60 per cent of quasars could host some kind of outflows. This result demonstrates the importance of understanding the outflow phenomenon in order to have a clear and complete picture of AGNs.

2.7 Explanations to the BAL phenomenon

A model that aims at explaining the BAL phenomenon and its relationship with the current AGN paradigm must take into account in a consistent way all the previously presented phenomenology.

Historically, the first interpretations of the absorbing troughs seen in PHL 5200 (see Section 2.1) were given by Lynds (1967) in his work entitled "A Quasi-Stellar Source with a Rapidly Expanding Envelope". Lynds pointed out that "the emitting region is surrounded by an expanding envelope in which the absorption lines originate". This first model (see sketch in Figure 2.7) assumed a simple spherical symmetry, but it already proposed the idea of an outflowing material coming from the central source towards the observer, with the absorption taking place somewhere close to the region where the emission lines are formed. This simple model, however, explained why an absorption is present, why this appears blueshifted with respect to the emission line, and why it spans a relatively wide range of velocities, coincident with the velocity gradient in the outflowing material.

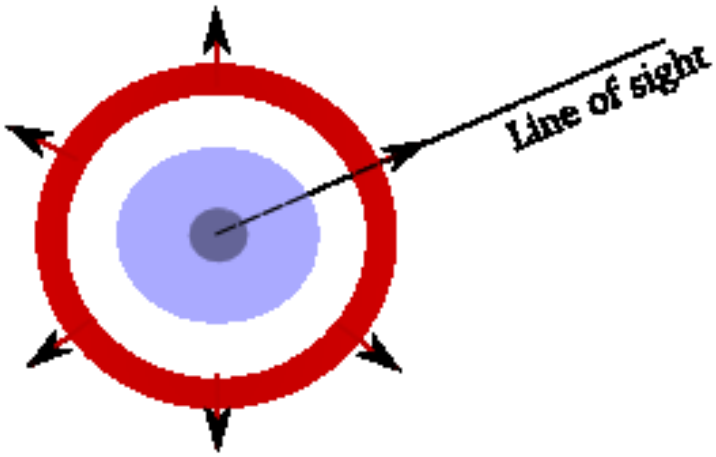

Figure 2.10: Sketch of the model proposed by Lynds (1967) to explain the absorbing features in PHL 5200.

The model proposed by Lynds (1967) turned out to be a good approximation to the idea that today is mostly accepted to explain the BAL phenomenon. However, there are still many unknowns that make a comprehensive model still not existent. One of the reasons is probably the lack of a sufficient number of quality observations from which good constraints on the physical parameters of these outflows can be obtained. For instance, there is no clear idea of the exact distance from the nucleus where these absorptions take place, and the kinetic luminosity of the outflows has only been obtained in a few individual cases. The consequence is that the proposed models that aim to explain quasar outflows

and their effects on the AGN environment use the physical properties of the wind as free parameters.

Nowadays, the more accepted idea is that outflows in QSOs are the consequence of the accretion processes around the central black hole (Murray et al. 1995). According to these models, the expelled matter would have a non-spherical symmetry, since the accretion takes place in a disk-like structure. The formation of quasar winds is an almost indispensable requirement in accretion models, because it helps to remove from the system the necessary angular momentum in order to allow a continuous accretion (Blandford & Payne, 1982). In addition, a nuclear origin of these winds is also suggested by the presence of BAL troughs seen in many low-luminosity Seyfert I galaxies, but with much smaller terminal velocities than those seen in QSOs (e.g. Weymann et al. 1997).

However, there are several alternatives in order to explain the acceleration mechanism that drives these outflows up to velocities that can be as high as $0.2c$:

- **Gas pressure**. Some relativistic particles (like neutrons) can escape from the surroundings of the central core up to distances of 1-10 pc and their energy and momentum can heat and create a bulk acceleration in the surrounding gas, generating in this way a wind (e.g. Begelman et al. 1991).

- **Magneto-centrifugal forces**. Some gas in the outer regions of the accretion disk is being removed away by magnetic stress. In these models, the magnetic field lines are frozen into the outer regions of the accretion disk, and they collimate the outflow into a pair of anti-parallel jets (bipolar outflows) moving perpendicular to the disk (e.g., Blandford & Payne 1982; Emmering et al. 1992).

- **Radiation pressure**. The UV photons created by recombination of ionised species in the BLR are later absorbed or scattered by the plasma in the wind. In this scattering the outward component of the momentum is supplied by the photons to the gas, and the Coulomb interactions between (absorbing) ions and electrons transfer the momentum to the whole plasma (e.g., Murray et al. 1995; Proga et al. 2000). This is the same mechanism that is supposed to take place in the winds of massive stars.

  The excess of IR emission seen in some BAL QSOs, especially in LoBAL QSOs, can be due to a high amount of dust in the nuclear region of the AGN. This dust can also be accelerated by radiation pressure making these objects "buried" AGNs at the stage of expelling outwards their cocoon of dust and gas. (e.g. Voit et al. 1993; Scoville & Norman 1995).

To date no one of these mechanisms can explain the whole phenomenological picture in a satisfactory way. However, there is evidence that radiation pressure might play an

important role in the acceleration process. In any case, a strong radiation field is present in the surroundings of the active nucleus, and the presence in some objects of line-locking or the "Ghost of Ly-α" are possible only as an effect of radiative acceleration.

Line-locking can happen when light of the wavelength required for a given transition in one cloud is absorbed by ions in a cloud closer to the quasar, with different velocity and undergoing a different transition. This reduces the line radiation pressure on the shadowed cloud, and the cloud may lock at a velocity difference from the shadowing cloud corresponding to the wavelength difference of the two transitions.

The fraction of BAL QSOs which show evidence of line-locking is not well known. To know this, a big library of spectra with both relatively high resolution and high signal-to-noise ratio is necessary. However, there are a few convincing cases of line-locking in the literature (Foltz et al. 1987; Vilkoviskij & Irwin 2001; Srianand et al. 2002) which demonstrate that radiation pressure plays a role in the acceleration of BAL winds. Despite this, it is not clear whether this is the main mechanism.

However, there is a second feature that can be interpreted as a sign of radiative acceleration of the outflows. Weymann et al. (1991) already observed a double structure within the C IV absorbing troughs with two minima having relative velocities equal to the separation between N V and Lyman-alpha. They found indications of this *double trough phenomenon* in several BAL QSOs in their sample but they did not discuss the statistical significance of the result.

It was however Arav et al. (1995) who introduced the term *Ghost of Lyman alpha* to refer to a similar feature related to the double trough phenomenon. The presence of the Ghost of Lyman alpha would be also consequence of the dominance of radiative acceleration via resonant line scattering in BAL QSOs, although the presence of magnetic fields is contemplated as a possible ingredient in the process.

The mechanism is sketched in Figure 2.11, extracted from Arav (1996). The presence of a small peak at a velocity of $-5{,}900$ km/s from the N V emission line (panel b) is not surprising, since it corresponds to the photons from the Lyman-alpha emission. The latter, with a higher flux density than the continuum level reduces the optical depth of the outflowing wind (panel a). However, the same feature is not expected within the BAL of C IV at $-5{,}900$ km/s of the emission line, since there is no emission feature at this velocity distance, i.e., at 1520 Å in the quasar's rest-frame. The key is that the ions of the different species are coupled through Coulomb collisions or by the presence of magnetic fields, and this causes the optical depth modulation to be transferred to other species.

Only a few objects have been studied showing clear indications of the Ghost of Lyman alpha in their spectra. A small sample of 4 objects was analysed by Arav (1996). Later, in an attempt of expanding this small sample, North et al. (2006) examined 198 sources from the catalogue of Reichard et al. (2003) with 224 SDSS BAL QSOs from the Early Data Release. Among these, they found 58 BAL QSOs with multiple structure in C IV absorption.

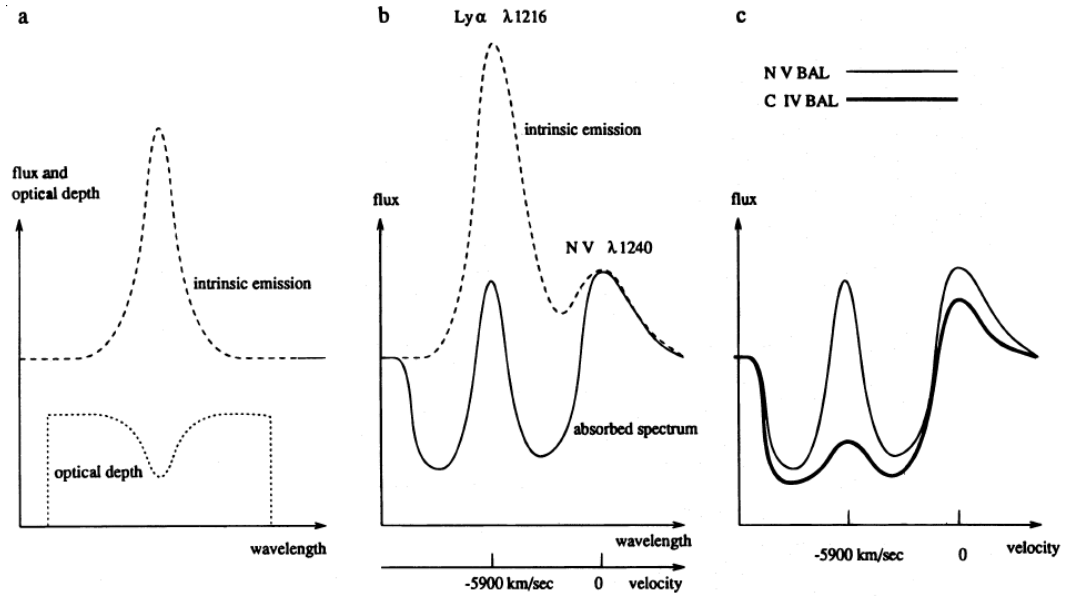

Figure 2.11: Simple model explaining the presence of the Ghost of Lyman alpha in the BAL troughs of the C IV lines. Extracted from Arav (1996).

They applied different quality criteria to classify these objects and ended up with 7 very good candidates which might show a real Ghost of Lyman-alpha feature, although 5 more candidates have high probability of showing this as well. The follow-up of this sample will be very important in the understanding of the acceleration mechanism in BAL QSOs and the importance of radiative acceleration.

Another difficulty that all these proposed models have to solve is the overionisation problem: the energetic X-ray and UV photons created in the continuum source are, in principle, supposed to completely ionise the wind, and the existence of partially ionised species like C IV, N V or Mg II is difficult to explain unless there is some matter that shields in some way these energetic photons. In addition, an overionised wind is not able to accelerate up to the required velocities observed in BAL QSOs. For these reasons almost all models consider the plasma to be in the form of small clouds so that the clouds closer to the nucleus partially shield the remaining clouds from the energetic ionising photons. This, however, introduces the problem of the confinement of these clouds.

Apart from the dynamics of these winds, there is controversy on the reason why these winds are formed and whether they are present or not in the majority of QSOs. There are two main scenarios that have been proposed to explain the presence of BALs in a high fraction of AGNs: those based on orientation, and those based on evolutionary effects.

2.7.1 Orientation models

As it was previously seen there are many similar characteristics in BAL and non-BAL QSOs. They have similar emission line, similar UV continuum and similar intrinsic X-ray emission (independently of the observed reddening), similar mid-IR and sub-mm properties. All these similarities might suggest the idea that BAL and non-BAL QSOs are actually the same objects.

The main premise under the orientation scenario is that all QSOs might host these winds, but whether we see or not signatures of them depends on the orientation of the AGN with respect to the line of sight (see Figure 2.12). In such a scenario the covering factor of the wind should be adjusted to match the rate of observed QSOs showing BAL winds. This means that about 20 per cent of QSOs are oriented in a way that our line of sight to them intersects these outflows.

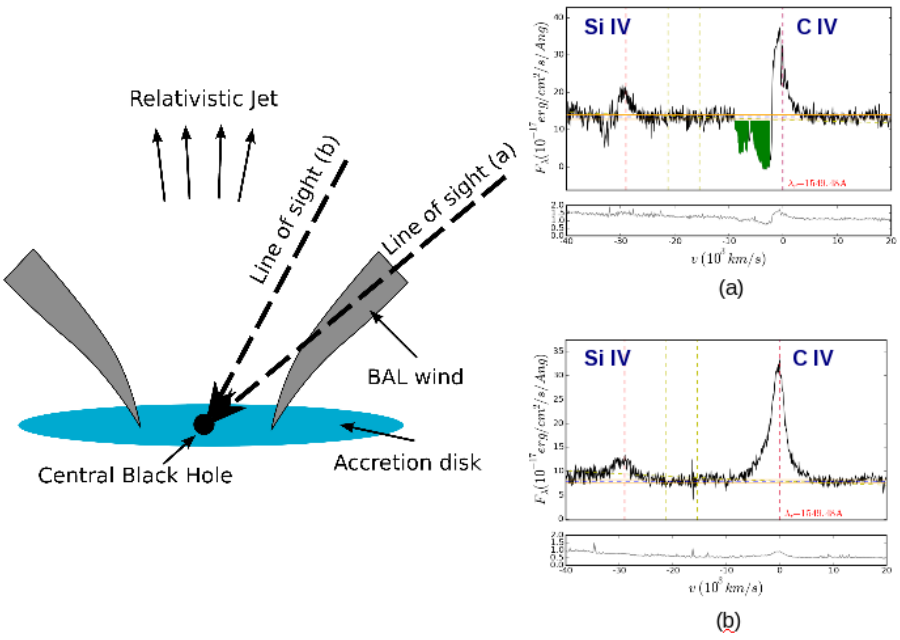

Figure 2.12: Sketch of the orientation scenario. The BALs are seen only when our line of sight to the QSO intersects the BAL wind.

The first geometry suggested for these winds was an *equatorial* one, i.e., with the outflow being initially perpendicular to the accretion disk, but at longer distances from the centre being curved until subtending a relative small angle with respect to the plane of the accretion. These equatorial winds explain the higher reddening seen in BAL QSOs since with these edge-on orientation both the AGN torus and the gas and dust in the disk of the host galaxy might contribute more to cause a higher reddening. A higher optical polarisation in the continuum and the absorbing troughs in BAL QSOs is also better explained

by an equatorial wind: an edge-on orientation attenuates the *direct* light coming from the continuum source, which then diminishes its importance with respect to the *scattered* light responsible for the polarisation (Goodrich, 1997).

An unifying explanation of the structure of QSOs, including the presence of BAL winds was presented by Elvis (2000). His picture is based on a disk-driven wind with a funnel-shaped geometry, composed of a warm highly ionised medium (WHIM). This medium contains the emitting/absorbing clouds and is warmer than these. The assumed pressure equilibrium make these clouds survive as they are not being destroyed trough shear forces. He also suggests that the opening angle of the wind can be luminosity-dependent, with the most luminous QSOs having more "equatorial" winds, while the fainter QSOs would have less curved winds but spanning a larger angle. This would explain the higher fraction of absorbing features observed in Seyfert galaxies compared to luminous QSOs. According to this model, NALs are also observed when QSOs subtend a slightly different angle with respect to the line of sight.

There are several concerns about the equatorial wind model, most of them coming from radio and X-ray observations. Punsly (2006) compared the column densities derived in the literature from deep X-ray observations of BAL QSOs with those derived for obscured type-II QSOs. He found that the latter are not less obscured on average than BAL QSOs. This cannot be explained with a purely equatorial wind because in this model BAL QSOs should show more absorbing material along the line of sight than those obscured (type-II) non-BAL QSOs.

Another problem is that X-ray-selected BAL QSOs have lower column densities of absorbing material than optically-selected BAL QSOs (Giustini et al. 2008), and this might suggest a slightly different orientation of these two populations of objects with respect to the line of sight. Other observations suggesting completely different orientations in BAL QSOs come from the radio, with the discovery of the small population of strongly beamed polar QSOS (Zhou et al. 2006) and some other showing the opposite FR-II morphology (Gregg et al. 2006).

The previous results though, fit quite well in a picture that considers different orientations for different sets of BAL QSOs, as follows:

- optical selection would favour BAL QSOs seen at a closer angle respect to the equatorial disk. This would be consistent with higher column densities of absorbing material found in these objects.

- X-ray selection would favour those objects seen along a line of sight subtending a larger angle with respect to the accretion disk plane. Among these, those with less absorbed spectra (those with AI > 0 and BI $= 0$) would subtend the boundary angle for a BAL QSO, and the column densities would be the smallest, in agreement with the result of Giustini et al. (2008).

- Polar BAL QSOs which subtend the largest angles from the accretion disk should then have almost no absorption as found by Wang et al. (2008).

2.7.2 Evolutionary scenario

In contrast to a purely geometrical interpretation it has been suggested that the BAL phenomenon might occur at a certain stage in the evolution of some/all AGNs. The extreme IR properties found in some BAL QSOs, especially in LoBAL and FeLoBAL QSOs suggest that these objects can be associated with denser environments and higher amounts of dust. These properties inspired the idea that BAL QSOs could be a transition phase that fits in the model of AGN evolution proposed by Sanders et al. (1988). These authors state that there is an evolutionary sequence between "warm" ULIRGs and QSOs. These ULIRGs referred in this work are IRAS-selected galaxies which show evidence of strong merger events (distorted geometries), bright compact cores and have "warm" IR colours, i.e. $f_\nu(25\ \mu m)/f_\nu(60\ \mu m) > 0.2$, as is the case if the AGN component dominates the IR spectral energy distribution. In this scenario, these warm ULIRGs are expelling their cocoon of dust and gas revealing the presence of the active nucleus and evolving into normal QSOs.

With this picture in mind, Lípari & Terlevich (2006) introduced an evolutionary sequence based on the detailed analysis of several nearby ULIRGs showing strong Fe II emission, signatures of violent nuclear starburst, and the presence of BAL troughs in Na ID (e.g., Lípari et al. 2005). The authors point out that the infrared colours of these objects are intermediate between normal QSOs and warm ULIRGs, suggesting an evolutionary sequence between these objects. In these nearby objects also circumnuclear arcs and shells have been found at distances of several hundred parsecs from the nucleus, which are interpreted by the authors as the remainder of strong bubbles triggered by powerful hypernovae associated with a strong nuclear starburst. The typical timescale on which these evolutionary steps take place is, according to the authors, about 10^8 years. This evolutionary track is also supported by the decreasing polarisation found in the following sets of objects: Hyperluminous QSOs/ULIRGs, LoBAL QSOs, HiBAL QSOs, and normal unobscured QSOs.

Further support to an evolutionary picture comes from the anticorrelation between radio-loudness and BI found by Gregg et al. (2006) in their sample of radio BAL QSOs with FR II morphology. This relationship suggests that there is a physical mechanism responsible of suppressing the radio emission when the BAL phenomenon is present and vice versa. According to this, only when the cocoon of matter has been cleaned by the BAL wind, the radio emission starts to develop. Since the number of BAL QSOs with FR II morphology is extremely small, the coexistence of the BAL and radio phase can be as small as $\sim 10^5$ years. This picture is also supported by the fact that most radio BAL QSOs are compact radio sources (Becker et al. 2000) that did not have time to evolve into larger radio structures.

It should be noted however, that all these results from radio observations are not only compatible with a scenario in which BAL QSOs are objects at the first stages of their evolution. Another plausible explanation could be that the BAL phenomenon could happen

various times during the lifetime of QSOs, as seem to be also true for the radio emission, at least in some QSOs. It has been found that some particular radio sources with complex radio morphologies show the presence of various radio axes at different physical scales (e.g., X-shaped geometries). These sources have been interpreted as signatures of restarted radio activity after a period where the radio emission has been absent (Marecki et al. 2006).

Assuming the scheme in which BAL QSOs are young sources that are developing into normal QSOs, a higher rate of BAL QSOs could be expected at very high redshift. The optical studies of large data sets (e.g SDSS) do not find any dependence on the fraction of BAL QSOs with redshift (at least up to z $\sim$ 4.5), but as shown before, these surveys can be significantly biased against BAL QSOs, especially at the highest redshifts. In fact, there are some intriguing hints on a higher fraction of BAL QSOs at very high z. For instance, in a survey of QSOs at z $\sim$ 5 Zheng et al. (2000) found that 3 out of the 5 observed QSOs presented BAL features. Similarly, Maiolino et al. (2004) found 50 percent of BAL QSOs in a sample of 8 QSOs with z $\sim$ 6, for which they took near-IR spectroscopy. Also suggestive is the result found by Chartas (2000) who observed an abnormally high percentage (35 per cent) of BAL QSOs among gravitationally lensed QSOs which suggest that a large fraction of BAL QSOs are missed in current flux-limited optical surveys.

These results are still based on poor statistics, and accurate predictions cannot be done on these basis only. Another suggestive "coincidence" is the fact that the highest-redshift radio-loud QSO observed to date also shows the BAL phenomenon. This BAL QSO at z=6.12 has been recently observed by two independent groups with both the VLA and VLBA reaching relatively high integration times (Frey et al. 2008; Momjian et al. 2008). The radio morphology of this BAL QSO is that of a CSO and these sources are known to be young radio sources in a phase of expansion through the interstellar medium within the host galaxy. In this particular source the separation between the most prominent radio components allows us to infer a kinematic age for the radio source of only 10^3 years.

3

Compact radio sources

SINCE the first detection of extraterrestrial radio emission, which turned out to come from the Milky Way (Jansky, 1932), and after an obligated stop due to World War II, radioastronomy has opened a new window to successfully probe the extragalactic universe. Radio observations have been of particular relevance in the study of AGNs and QSOs, since the first detections of very compact radio sources in the decade of the 1950's.

Millions of radio sources have been classified in the currently available catalogues, covering the whole classical radio window of centimetre wavelengths. The development of radio interferometry has allowed us to map radio galaxies and quasars with unprecedented high resolution as compared to observations at other wavelengths of the spectrum. Generally speaking, radio emission from active galaxies or QSOs can be observed in the vicinity of the core, in jets, or in lobes and hotspots that can be located at kpc or even Mpc distances from the nucleus. As an example, Figure 3.1 shows a radio map of Cygnus A, which illustrates the presence of all these regions.

It is not clearly defined what a compact source is in terms of its size, because any definition is necessarily arbitrary. Another problem with such a definition is that a radio source can have different dimensions depending on the observing frequency. A resolved source can easily be various kiloparsecs long at 1.4 GHz, and be at the same time much smaller or even unresolved when observed at higher frequencies (and therefore higher resolutions). This last problem can be avoided just assigning to the radio source its largest dimension at any observed radio frequency, because this means that at this largest scale there is some plasma responsible for that emission. On the contrary, a radio source might not be resolved at a given wavelength but it can happen to be resolved at higher frequency. In this case, the size of the radio source will be taken as the maximum extension of the resolved structure.

In any case, an operational definition will be adopted, and a compact radio source will be considered here to have dimensions smaller than 20 kpc (O'Dea, 1998). Such radio sources are thus supposed to be partially or completely embedded in the NLR of its host galaxy. Other authors, like Kunert-Bajraszewska et al. (2005) propose a slightly different

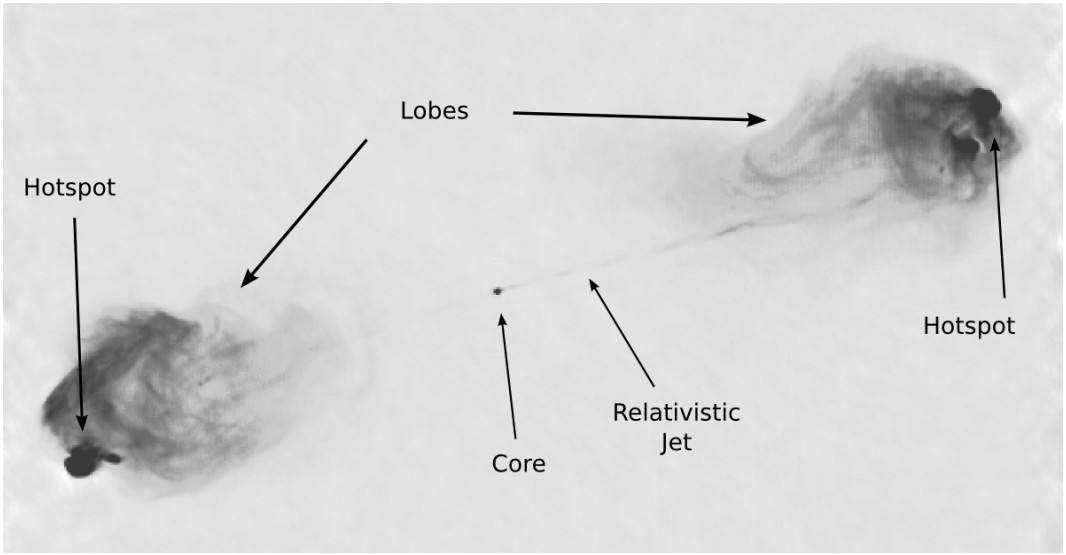

Figure 3.1: Illustrative example of the different regions of radio emission in a radio source, in this particular case, Cygnus A. From the central compact core, two relativistic jets are accelerated in opposite directions. The particles in these jets interact with the intergalactic medium creating the compact and luminous hotspots. Finally the lobes are extended regions that serve as reservoirs where the particles in a lower energy level accumulate during the evolution of the source.

classification applied to the particular class of radio symmetric objects. They consider as compact objects those with dimensions of about 1 kpc or less, while those objects with dimensions between 1 and 20 kpc are called medium-sized objects. In our definition, these two classes will be considered compact, in opposition lo large radio sources, defined to have sizes larger than 20 kpc.

According to this definition, classical radio galaxies, like those classified as FR galaxies (Fanaroff & Riley, 1974) of both types (FR I and FR II) are considered large radio objects. These usually span dimensions of hundreds of kpc, or sometimes even larger than 1 Mpc, like in the case of the giant radio galaxies (e.g. Klein et al. 1996).

The spectrum of a radio source can give information about the physical processes involved in the emission of the observed light, as well as on its evolutionary stage. The polarisation radiation can also probe the ionised matter in the AGN environment, and can be used to extract information about particle densities or the strength of the magnetic fields present in these regions.

In this chapter some basic ideas will be introduced about the mechanism responsible for the radio emission in compact radio sources. The different classes of compact radio sources will be presented and the main proposed models to explain their nature will be outlined. Finally, some techniques that make possible the determination of physical parameters in these sources will be explained. All these diagnostic tools will be used in this thesis.

3.1 Emission from compact radio sources

The main emission mechanism in extragalactic radio sources is the *synchrotron* emission. According to this mechanism, particles moving at relativistic velocities are accelerated by strong magnetic fields present within the source and in the surrounding interstellar medium (see e.g. Chapter 6 of Rybicki & Lightman (1986) for a detailed insight on the physics of synchrotron radiation). This interaction results in the emission of photons with frequencies in the radio domain. Typically, the classical radio bands are considered those covering the range between $\sim$ 100 MHz and $\sim$ 10 GHz.

It is usually assumed that the energy distribution of the particles responsible for the synchrotron emission follows a power law E^p. This translates into an emitted synchrotron spectrum, $S(\nu)$, that also follows a power law on frequency:

$$n(E)dE = CE^p dE \;\Rightarrow\; S(\nu) = \int_{E_1}^{E_2} S(E,\nu)n(E)dE \;\propto\; \nu^{\alpha} \tag{3.1}$$

where $n(E)$ is the number density of particles with energies between E and $E + dE$, E_1 and E_2 are, respectively, the minimum and maximum energy considered for the population of moving particles, and α is the spectral index of the synchrotron emission, which relates to p in the following way:

$$\alpha = \frac{p-1}{2} \tag{3.2}$$

A consequence of the synchrotron radio emission is that the so-called synchrotron self-absorption (SSA) will occur in those dense and relatively compact regions. This happens when the same electrons responsible for the emission of the synchrotron photons start to absorb their own emission. The effect of this mechanism is that the source's radio spectrum shows a peak at a certain frequency $\nu_{\rm peak}$. This is the boundary frequency separating the two regimes in which the medium becomes optically-thin ($\tau < 1$) or optically thick ($\tau > 1$) to the synchrotron radiation. Below this *turnover frequency* $\nu_{\rm peak}$, the radio spectrum will drop because the absorbed photons do not contribute to the observed flux density (see Figure 3.2).

Let us consider a source of angular size θ, at redshift z, with a magnetic field **B**. Assuming a power-law energy distribution of the emitting particles (as in Formula 3.1), there is a relationship between the *turnover frequency* $\nu_{\rm peak}$, the angular extension θ, the magnetic field strength B and the peak flux density $\rm S_{peak}$:

$$\nu_{peak} \sim f(p) B^{1/5} S_{\rm peak}^{2/5} \theta^{-4/5} (1+z)^{1/5} \tag{3.3}$$

with θ being measured in milliarcseconds, B in Gauss, S_{peak} in Jy and ν_{peak} in GHz. The function $f(p)$ is weakly dependent on p, the slope of the energy distribution of emitting electrons. According to this relationship, the asymptotic behaviour at very low frequencies will be a spectrum following a power law of spectral index $\alpha = +5/2$.

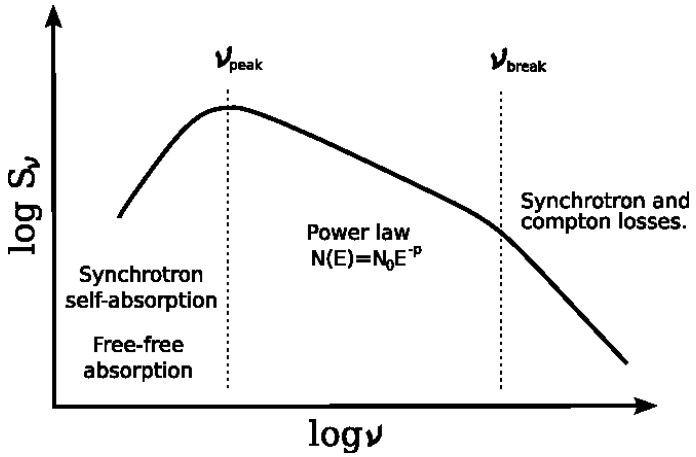

Figure 3.2: Schematic picture showing the different regions in the spectra of a radio source. The peak of the spectrum corresponds to the transition between the optically thin and optically thick regimes. The central region extends through several decades in frequency and corresponds to the power-law regime (a straight line in this log-log representation). At higher frequencies, if losses due to synchrotron or inverse Compton radiation are important (see Section 3.4) a broken slope can be seen, with the break frequency being related to the age of the emitting particles.

There is little doubt that the main process of emission in radio sources is the synchrotron mechanism. However, free-free absorption (FFA), also called bremsstrahlung self-absorption, can take place in the presence of an ionised medium. According to the theory of bremsstrahlung radiation, the spectrum is expected to decrease at low frequencies, but following a power law of slope $\alpha = +2$ (which corresponds to the Rayleigh-Jeans regime dominating the optically thick part of the spectrum), slightly smaller than the slope predicted by the SSA theory. Formula 3.4 gives the frequency at which the optical depth due to free-free absorption becomes about unity:

$$\nu_{\rm peak}^{ff} = 23.4 \left(\frac{n_e}{1\,{\rm cm}^{-3}}\right) \left(\frac{T^{-3/2}}{10^4\,{\rm K}}\right) \left(\frac{\ell^{1/2}}{1\,{\rm kpc}}\right) {\rm MHz} \tag{3.4}$$

In principle, in order to determine which of the two mechanisms (SSA or FFA) dominates in a radio source, the best way is to constrain the spectral slope at low frequencies. However, this simple approach has a series of problems. First of all, a combination of SSA and FFA can take place in the same source. Then, the combined spectrum at low frequency

can have a different spectral slope than the previously predicted values. In addition, in a complex source observed at insufficient resolution there might be several emitting components with different dimensions (i.e., with different turnover frequencies) contributing to a combined radio spectrum with less clear characteristics. In any case, even if SSA seem to fit well the majority of cases, at least in several sources, FFA has been found to be important (e.g., Marr et al. 2001; Kameno et al. 2003; Mutoh et al. 2002; Shen et al. 2005).

Apart from these difficulties there is also a practical problem when trying to explore this issue. The spectral regions wherein these low-frequency slopes can be constrained (i.e. $1-100$ MHz) are almost unexplored up to now. The reason is that observing at these low frequencies becomes a real challenge from a technical point of view, especially due to the effect of the Earth's ionosphere that strongly distorts the radio waves coming from the radio sources under study. In this sense, the new generation of instruments that will be available in the near future will greatly improve the situation. These are, for instance, the Low-Frequency Array (LOFAR)[1] (see Snellen et al. 2009), whose core is currently being built in The Netherlands, or the Long-Wavelength Array (LWA)[2] that will operate in the United States.

Another effect caused by synchrotron radiation is the loss of energy of the emitting particles. These energy losses are more important at higher frequencies and are responsible for the broken power law seen in Figure 3.2. This topic will be covered later because it allows us to estimate the radiative age of the radio source.

3.2 Classification of compact radio sources

According to Equation 3.3 the compactness of a radio source is related to the turnover frequency where the radio spectrum peaks. In this way the most compact radio sources will have a higher turnover frequency. This is the motivation for the adopted classification of radio sources in different groups attending to the spectral region where their radio spectrum peaks:

- **Compact Steep Spectrum (CSS) sources**: These are powerful radio sources with typical monochromatic power of $P_{1.4\,\mathrm{GHz}} \sim 10^{25}$ W Hz^{-1}. The spectra of these sources peak at frequencies below 500 MHz and their typical dimensions are between 1 and 20 kpc.

- **GigaHertz-Peaked Spectrum (GPS) sources**: These sources are as powerful as CSS sources but are smaller than those, with typical dimensions $\lesssim 1$ kpc, and a turnover frequency between 500 MHz and about 5 GHz.

- **High-Frequency Peakers (HFP)**: This term proposed by Dallacasa et al. (2000) describes those sources which are even more compact than GPS sources, with typical

[1] LOFAR Website: `http://www.lofar.org`
[2] LWA Website: `http://lwa.unm.edu`

dimensions of ~ 0.1 kpc. The spectra of these sources peak at frequencies higher than 5 GHz.

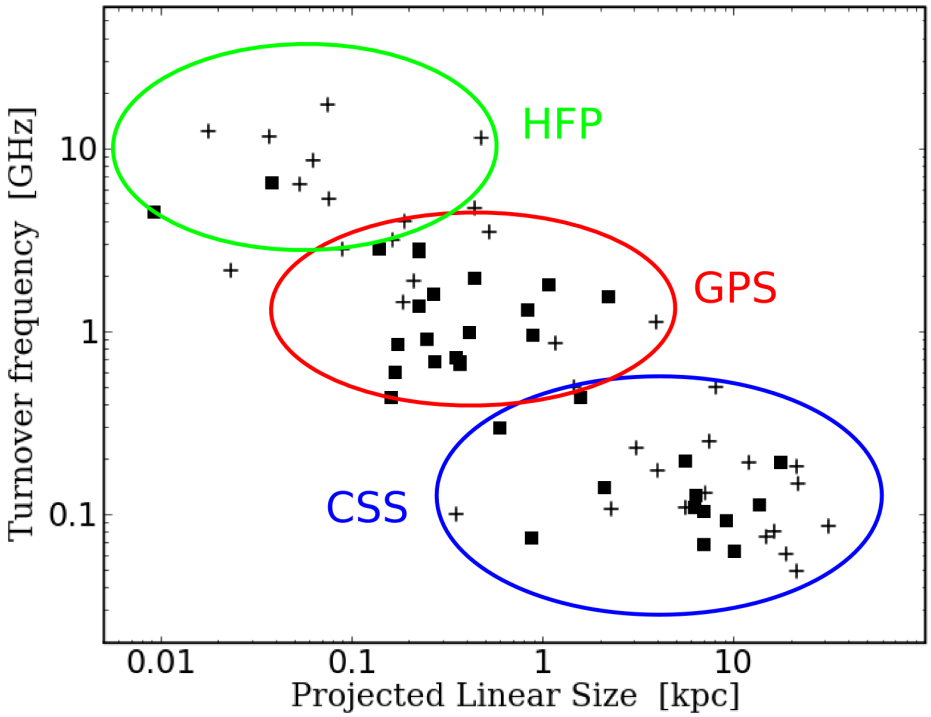

Figure 3.3: According to their projected linear dimensions and the frequency at which their radio spectrum peaks, compact radio sources have been classified into CSS, GPS sources and HFPs. The symbols in the plot correspond to compact radio galaxies (pluses) and quasars (squares) studied by O'Dea (1998). The samples plotted are the CSS sample of Fanti et al. (1990) and the GPS sample of Stanghellini (1992). The term HFP was later introduced by Dallacasa et al. (2000) and some of the GPS sources in Stanghellini's sample were included in this group.

In Figure 3.3 the approximated regions occupied by these three groups in a θ vs $\nu_{\rm peak}$ diagramme are shown. Actually, the angular dimensions have been converted into projected linear sizes (in kpc). This plot nicely illustrates the relationship between these two quantities in the samples of compact radio quasars and galaxies studied by O'Dea & Baum (1997).

The separation in three different groups of compact radio sources may seem a bit artificial because of the continuity in the distribution of both the linear sizes and the peak frequencies (see Figure 3.3). However, historically it was done in this way because the various radio surveys operating at a given radio frequency favoured the detection of the particular sources preferentially peaking at that frequency. For instance, the Third Cambridge (3C) catalogue (Edge et al. 1959) or the Third Bologna (B3) catalogue (Ficarra et al., 1985), contain sources selected at 178 and 408 MHz, respectively. These surveys

are more efficient selecting CSS sources peaking at MHz frequencies or less, while surveys at higher frequencies are more efficient at selecting GPS sources, like in the catalogue of (Bicknell et al. 1997) that contains sources observed at 2.7 GHz.

Compact radio sources constitute a considerable fraction of the bright radio source population. The percentage of CSS sources is about 30 per cent (O'Dea, 1998). The number of GPS sources and HFPs is more difficult to estimate, since many of them are lost in surveys selected at the classical radio wavelengths, e.g. 5 GHz. At these frequencies their flux density decreases considerably and many are below the survey limiting flux density. For instance, GPS radio sources are found in the classical catalogues (at cm wavelengths) in a number of about 10 per cent, but on the other hand they constitute about 24 per cent of the Molonglo quasar catalogue (Baker et al. 1995). Regarding HFPs, it seems clear that these sources are very rare, and could constitute even less than 1 per cent of the population of radio sources (Dallacasa, 2003).

Particular attention among the population of compact radio sources deserve the so-called Compact Symmetric Objects (CSOs; Wilkinson et al. 1994). These sources have been identified by their symmetric morphology at the milliarcsecond scale, showing small dimensions of about hundreds of parsecs. They usually display a central core and two small lobes (sometimes also hotspots) extending in opposite directions from the core. This core is usually fainter than the lobes and is sometimes even undetected. The remarkable symmetry between both lobes (not only in dimensions but also in brightness) is in contrast with the majority of radio galaxies that usually show more asymmetric structures. A high percentage of GPS radio sources have been observed with VLBI at the milliarcsecond scale, showing a morphology typical of CSOs, which suggest a link between these two types of sources.

3.3 The nature of compact radio sources

Compact radio sources are reduced in size, as powerful as the more extended radio galaxies and constitute a significant fraction of the population of radio sources. In order to explain these three characteristics, two main models have been proposed. The first one suggests that these objects could be compact because the interstellar medium within the radio source is dense enough to trap or *frustrate* the expansion of the radio jets. The second solution would be that these compact radio sources are just *young* radio sources that are evolving into larger radio sources. These two scenarios will be discussed below.

3.3.1 Frustration scenario

The so-called frustration scenario has been discussed by various authors, e.g., van Breugel et al. (1984). The explanation for the relatively high fraction of CSS and GPS sources in radio surveys, which is similar to the fraction of powerful FR-I or FR-II radio galaxies,would be that both kind of sources have similar ages, of the order of 10^7 years. The classical double galaxies would have expanded during this time through the interstellar medium and evolved into larger structures, while compact sources would have been trapped for a sub-

stantial fraction of their lives, not being able to expand and to become larger.

The reason of this confinement could be that the jets are propagating through a dense and inhomogeneous interstellar medium. The jets would then collide with clouds, heating and accelerating the ambient gas through shocks. These would account for the high radio brightness of the source. Figure 3.4, proposed by Bicknell et al. (1997), illustrates the interaction of the jet with the interstellar medium.

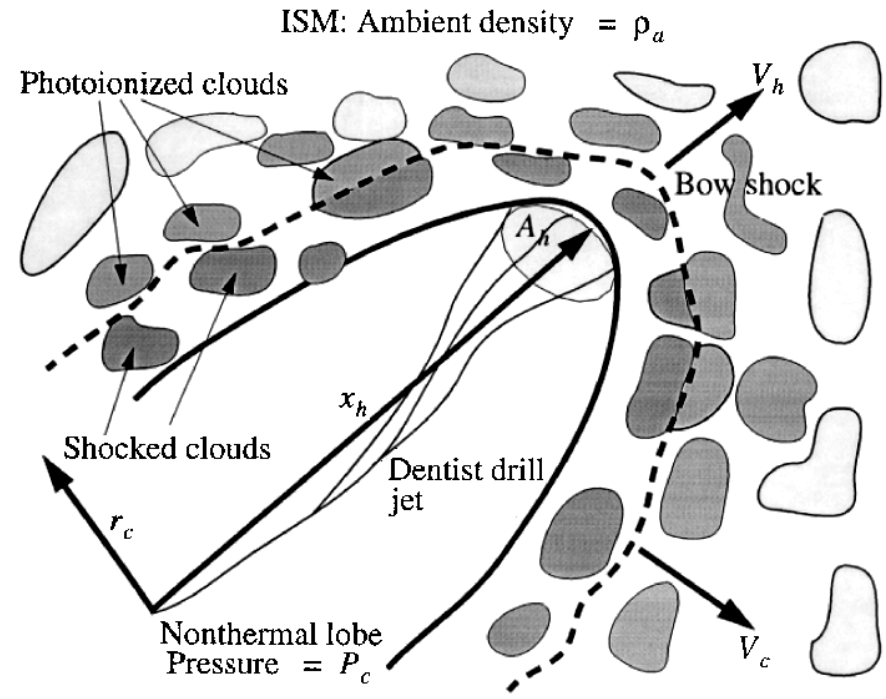

Figure 3.4: Picture showing the proposed model for the interaction between the radio jet and a dense and inhomogeneous interstellar medium. Extracted from Bicknell et al. (1997).

Various arguments have been given in order to support this frustration scenario, based on observations that suggest the presence of an anomalously dense environment. For instance, Gelderman (1994) found evidence of distorted geometries analysing the optical images of a sample of CSS sources. Similarly, O'Dea et al. (1996) analysed the geometries in the optical of a sample of 30 GPS sources finding a high fraction showing signals of interaction or mergers. Evidence for distorted geometries have also been found in the radio maps of several CSS and GPS radio sources (see e.g. O'Dea 1998 and references therein).

The so-called *alignment effect* has also been claimed to be an evidence in favour of the frustration scenario. Bicknell et al. (1997) proposed that the emission-line gas shocked by the radio source will strongly emit in the optical, creating a sort of structure aligned with the radio jet. Various observations with the Hubble Space Telescope have shown the

presence of such structures in at least some CSS sources (Gelderman 1994; de Vries et al. 1997).

There is other evidence demonstrating that the host galaxies of CSS and GPS sources contain significant amounts of dense gas. One is the fact that many of these sources are strongly depolarised (e.g. Cotton et al. 2003), some showing strong rotation measures due to the presence of a Faraday screen of ionised material. In the model presented by Bicknell et al. (1997) this ionisation could come from the radiation emitted in the shock produced by the jet in the interstellar medium.

The frustration scenario seems to be less preferred than the youth scenario (see below) to explain the phenomenology of compact radio sources. The reason for this might be that although there seem to be several indications of dense, ionised matter interacting with the radio jet, the derived column densities are not as high as needed for the radio source confinement (e.g., Gupta et al. 2006). So, the presence of this matter does not necessarily mean that the jet will remain trapped. In fact, a dense environment can also be expected if the source is at the first stages of its evolution (Morganti, 2008).

3.3.2 Youth scenario

The youth scenario is based on the assumption that an evolutionary sequence exists that accounts for the different classes of compact radio sources. According to this evolutionary track, CSS sources will be the more evolved versions of GPS sources, and these in turn will probably be evolved HFPs. The size distribution in these sources would then be a consequence of their different evolutionary stages and their relative fraction among radio sources would match the fraction of time that these sources remain in each stage of their evolution.

The first and most obvious argument in favour of the youth scenario is that compact radio sources have similar structure of the larger radio galaxies, with the presence of cores, jets and lobes. In this sense, most of CSS/GPS sources would be "entire" radio sources and not just a part of a larger radio source. Stanghellini et al. (1998) found only 10 percent of the GPS sources in their sample which shows faint, extended radio emission around the bright compact components, which indicates that most of them actually have small dimensions.

In principle, it is not straightforward to assume that the observed compactness is a consequence of a real reduced dimension. Another possibility is that their apparent sizes might be small due to projection effects and their true physical dimensions would thus be much larger. Fanti et al. (1990) explored this possibility analysing the distribution of linear sizes in a sample of CSS sources. Even when considering the effect of Doppler boosting in their simulations they concluded that most CSS/GPS sources are not likely compact as a consequence of projection effects, but are probably intrinsically compact. This is consistent with a relatively small dispersion in Figure 3.3 because that relationship is based on a

physical link between the *real* source dimension and the spectral peak due to SSA.

Two main approaches have been followed to estimate the age of compact radio sources:

- The most direct one is based on kinematic measurements. The expansion velocities of CSOs have been determined in a series of cases thanks to accurate multi-epoch measurements of the separation between hotspots. The deduced kinematic ages found by Polatidis & Conway (2003) in a sample of 10 CSOs are of the order of 10^3 years, which confirms their youth. More recently, Gugliucci et al. (2005) found similar results in a larger sample, with the distribution of derived ages peaking below 500 years.
- Murgia et al. (1999) found that the radiative ages of CSS sources obtained through the analysis of their radio spectra are $\lesssim 10^5$ years (see Section 3.4 for a basic overview of the method). These results seem to be definitely valid in CSS sources associated with optical galaxies. However, the derived spectral ages of CSS/GPS QSOs, for which the beaming effects might be more important, should be treated with care.

Several models have been proposed to explain the evolution of these compact objects while they expand within the interstellar medium (e.g., Fanti et al. 1995; Snellen et al. 2000). As explained by Labiano (2006), current models assume that GPS sources increase their luminosity while crossing the core of their host galaxy. When they reach typical sizes of CSS sources, their luminosity will decrease as the source continues its expansion, because the density of the interstellar medium decreases (Snellen et al. 2003). However there is to date no clear model that explains whether CSS radio sources evolve in all cases into larger radio sources (like classical double radio galaxies) or, on the contrary, wether they fade out, dying before expanding further into the intergalactic medium.

The youth scenario presents a coherent explanation for the evolution of radio sources, although many details of the theory are still not clearly stated. However, the phenomenology that favours this paradigm (i.e. the derived kinematic and radiative ages) is also consistent with a slightly different interpretation: compact radio sources might not necessarily be young, but could be going through an episode of radio activity maybe preceded by additional foregoing episodes. This assumption is based on two ideas:

- Evidence has been found in some radio sources for recurrent or restarted radio activity, especially in two groups of objects: X-shaped radio galaxies (see e.g. Rottmann 2001 and references therein) and double-double radio galaxies (e.g., Lara et al. 1999; Schoenmakers et al. 2000). Although this recurrent activity has been mainly found in large, evolved radio galaxies, there are also signatures of multiple activity episodes in compact radio sources (Marecki et al. 2006). Multiple radio activity could be a common phenomenon, since it can only be detected in those sources for which the remainders of the old activity can be seen after a new episode has started. Therefore, many CSOs might not necessarily be going through their *first* episode of activity.
- The spectral ages derived from a synchrotron analysis are those of the relativistic particles emitting this radiation. Only in those sources for which the main contribution

to the total flux density comes from the radio lobes, the derived spectral age is likely similar to the source's age (Fanti et al. 1995). But if, for instance, the main contribution came from a bright hotspot, the derived spectral age would not correspond to the age of the radio source, but to the age of the electrons fueling the hotspot.

On the other hand, even if recurrent radio sources constitute a fraction of the population of compact sources, only a few cases of this kind were found (Marecki et al. 2006). If the reason for this lack of sources is that recurrent activity is not a common phenomenon, then it would not constitute a major problem for the youth interpretation of compact radio sources.

3.4 Radiative age of radio sources

According to the theory of synchrotron radiation it is possible to estimate the age of the particles that are fuelling a certain component in a radio source. In this section, the *spectral ageing analysis* used in this thesis will be presented, showing the different models commonly used to explain the evolution of the emitting particles within the radio source.

The magnetic field interacting with these particles plays an important role in this process. Since the derived spectral ages are strongly dependent on the magnetic field strengths, a good estimate of the latter is necessary to obtain sensible ages. Therefore, let us start outlining how the magnetic field can be estimated from energetic considerations, and what the assumptions are on which this estimate is based.

3.4.1 Estimate of the magnetic field

Magnetic fields are present in many astrophysical contexts and they are for instance responsible of the synchrotron emission coming from radio sources. They play an important role also from a dynamical and energetic point of view because they strongly interact with the ionized medium and their presence is probably relevant in the formation and evolution of galaxies and galaxy clusters. However their origin is not yet clear and in fact is one of the most challenging problems in modern astrophysics. A recent review that addresses the different proposed explanations to understand the origin of the galactic and extragalactic magnetic field was presented by Widrow (2002).

The classical formula to estimate the magnetic field strength B from the synchrotron spectrum was explained in detail by Pacholczyk (1970) and assumes that the cosmic rays (electrons, positrons and heavy nuclei) and the magnetic field are strongly coupled and exchange energy until equilibrium holds. This is known as the *minimum energy* assumption. Another approach which yields similar results is to assume energy *equipartition* between the cosmic rays and the magnetic field. The procedure consists of calculating the total energy of the system including magnetic field and particles. Heavy particles like protons are assumed to have an energy proportional to that of electrons and positrons: $U_P = \mathcal{K}U_e$. The total energy is then a function of the magnetic field:

$$U_{tot} = G(1+\mathcal{K})L_{syn}B^{-3/2} + \frac{B^2}{8\pi}\eta V \tag{3.5}$$

The synchrotron luminosity L_{syn} can be calculated integrating the observed radio spectrum over the appropriate range of frequencies [ν_1, ν_2]. The observed spectrum typically follows a power law (i.e., $S_\nu \propto \nu^\alpha$) and the range of integration has traditionally been [10 MHz, 10 GHz] for observational reasons. G is a function only dependent on α, ν_1, ν_2; η is the fraction of the source occupied by the magnetic field (filling factor) and V the source's volume. The conditions of minimum energy holds when $\partial U_{tot}/\partial \mathrm{B} = 0$, which gives the classical minimum-energy formula:

$$B_{min}^{(c)} = \left[\frac{6\pi G(\mathcal{K}+1)L_{syn}}{\eta V}\right]^{2/7} \tag{3.6}$$

where the superscript (c) accounts for *classical*. The resulting magnetic energy is 3/4 of the cosmic rays energy, so the equipartition value is just slightly different:

$$\frac{B_{min}^{(c)}}{B_{eq}^{(c)}} = (3/4)^{2/7} \sim 0.92 \tag{3.7}$$

Miley (1980) proposed a more practical version of the same formula in which B_{class} depends on quantities that can be directly measured or inferred from observations:

$$B_{min}^{(c)} = 7.9\left[\frac{(\mathcal{K}+1)S_0(\nu_2^{\alpha+1/2} - \nu_1^{\alpha+1/2})}{\eta\nu_0^\alpha(\alpha+1/2)\theta_x\theta_y\ell sin^{3/2}i}(1+z)^{3-\alpha}\right]^{2/7} \quad \mu G \tag{3.8}$$

where S_0 is the flux density (in mJy) measured at frequency ν_0 (in GHz), θ_x and θ_y are the angular dimensions of the radio source (in arcseconds) or in case of a non-resolved source the equivalent beam widths and ℓ is the assumed path length along the line of sight (in kpc). Finally, i is the angle between the uniform magnetic field and the line of sight. The last term accounts for the redshift of the source.

However, a series of problems in the classical formula have been raised in the literature. One of them is the fact that the formula is to some extent formally incorrect. A fixed integration interval ν_1 to ν_2 introduces in the classical minimum-energy formula (Equation 3.5) an additional term dependent on the magnetic field strength B. The total energy depends on a constant power of B (see Longair 1994, p. 292) and the wrong derivative $\partial U_{tot}/\partial \mathrm{B}$ leads to the constant exponent 2/7 in Equation 3.6.

A possible approach to solve this difficulty is to establish a low energy cut-off ($\epsilon_1 = \mathrm{mc}^2\gamma_{min}$) in the particle energy distribution instead of a frequency cut-off, ν_1 in the emitted

synchrotron spectrum. This is the approach followed by Brunetti et al. (1997), and the first consequence is that the energy density of the electromagnetic particles is exactly equal to that of the magnetic field (instead of 4/3, as it happens in the classical calculation). This revised equipartition formula gives:

$$B_{eq} = \left[C(\alpha) \frac{P(\nu)}{V} \nu^{-\alpha} (1 + \mathcal{K}) \right]^{\frac{1}{3-\alpha}} \gamma_{min}^{\frac{1+2\alpha}{3-\alpha}} \tag{3.9}$$

where $P(\nu)$ is the source synchrotron power at a frequency ν, and C(α) is a constant dependent on the exponent, δ, of the energy distribution of particles, N(γ)=$K_e\gamma^{-\delta}$, and thus on the synchrotron spectral index α=(1-δ)/2.

Brunetti et al. (1997) give, for practical purposes, a way to calculate B_{eq} as a function of the classical formula, which was expressed in terms of observable quantities. Using Equations 3.8 and 3.7, they obtain:

$$B_{eq} = D(\alpha) \gamma_{min}^{\frac{1+2\alpha}{3-\alpha}} (B_{eq}^{(c)})^{\frac{7}{6-2\alpha}} \tag{3.10}$$

where D(α) $\sim$ 1 for typical values of the spectral index α (see Brunetti et al. 1997 for exact numeric values of these constants).

Finally, Beck & Krause (2005) proposed an alternative approach in which the number density ratio $\mathbf{K_0}$ of protons to electrons (instead of the energy ratio $\mathcal{K}$) is assumed to be constant. This is true only in a certain range of particle energies $E_p < E < E_{syn}$ where the energy losses can be neglected or they affect protons and electrons in the same way. The lower limit in the energy above which this formula applies is determined by the proton energy E_p, while at E > E_{syn} the synchrotron or inverse Compton losses are important making $\mathbf{K_0}$ an increasing function of E. Within these limits, the revised formula is thus:

$$B_{min} = 10^6 \left[\frac{4\pi(2\alpha - 1)(\mathbf{K_0} + 1) S_0 E_p^{1+2\alpha} (2c_1/\nu_0)^{\alpha}}{(2\alpha + 1) c_2(\alpha) l c_4(i)} (1 + z)^{3-\alpha} \right]^{1/(3-\alpha)} \quad \mu\mathrm{G} \tag{3.11}$$

where $c_1 = 6.26428 \cdot 10^{18}$ erg^{-2} s^{-1} G^{-1}, c_2 is a function of the spectral index:

$$c_2 = 4.66395 \cdot 10^{-24} \, \frac{5 + 3\alpha}{3 + 3\alpha} \, \Gamma\left(\frac{5 + 3\alpha}{6}\right) \Gamma\left(\frac{1 + 3\alpha}{6}\right) \quad \mathrm{erg\,G^{-1}\,sterad^{-1}} \tag{3.12}$$

and $c_4 = [\cos(i)]^{1-\alpha}$ makes sense only when the magnetic field is constant and oriented at a fixed angle. In case it is supposed to be completely turbulent it is reasonable to assume no preferred orientation in the angle distribution and this term can be replaced by

$c_4 = (2/3)^{(1-\alpha)/2}$, its average over all possible directions.

Now the ratio of minimum-energy and equipartition field strengths depends on the spectral index, and is not a constant as it was in the classical case (Formula 3.7):

$$\frac{B_{min}}{B_{eq}} = \left[\frac{1-\alpha}{2}\right]^{1/(3-\alpha)} \tag{3.13}$$

Summarising, the two new proposed equations to determine the equipartition magnetic field (Formulae 3.9 and 3.13) should be used, respectively, in those systems where the light and the heavy particles are supposed to dominate the energetic balance of the system.

3.4.2 Spectral ageing

The shape of the synchrotron spectra of a radio source can be used to estimate the radiative age of the brightest component contributing to the integrated flux density of the source (Murgia et al. 1999). Synchrotron emission constitutes an energy output of the emitting particles and these energy losses increase with the energy of the particles. Therefore, during the lifetime of the radio source the number of highly energetic particles will strongly decrease due to these synchrotron losses, while this decrease will be smaller in those less energetic particles. The consequence of this phenomenon is a drop of the high-energy part of the radio spectrum, visible as a double or broken power-law. The so-called break frequency ($\nu_{\rm break}$) at which a change of slope is observed in the synchrotron spectrum is related to the age of the source ($\tau_{\rm syn}$, see Figure 3.2), according to the following equation:

$$\tau_{\rm syn} = 1610 \frac{B^{1/2}}{B^2 + B^2_{\rm CMB}} \frac{1}{[\nu_{\rm break}(1+z)]^{1/2}} \tag{3.14}$$

where $\nu_{\rm break}$ is in MHz, $\tau_{\rm syn}$ in Myr, the magnetic field B and the magnetic field equivalent to the cosmic microwave background, $B_{\rm CMB}$=3.25 $\cdot$ (1+z)^2 in µG. If the observed emission mainly comes from the more relaxed particles emitting in the lobes, τ_{syn} is representative of the age of the source because these particles have been accumulating in the lobes during the source's lifetime (Fanti et al. 1995).

Three models considering different evolutions of the supply of energetic particles will be considered in this work. These models predict a different spectral shape at high frequency:

- The model by Kardashev-Pacholczyk (KP, Kardashev 1962; Pacholczyk 1970) assumes that a single particle injection occurred in the past and ceased at some point. This model assumes a constant pitch angle for the accelerating particles. This, in practise, is equivalent to assume a time-scale for the isotropisation of the electrons much longer than the radiative timescale. The spectrum follows a steeper power law at $\nu > \nu_{\rm break}$ than at low frequencies, which spectral index depends on the balance between the synchrotron (and eventually inverse Compton) losses and the rate of previously injected particles.

- The model by Jaffe-Perola (JP, Jaffe & Perola 1973) is physically similar to the KP model, but with the difference that JP considers scattering of the pitch angle. As a result of the energy losses via the scattered particles there is an exponential drop which can model arbitrarily steep spectra at high frequencies, in opposition to the KP model.

- The Continuous-injection model (CI; Kardashev 1962), as its name indicates, assumes a continuous injection of fresh relativistic particles with energy distribution following a power law. Due to this particle replenishment, there is a maximum allowed spectral index at high frequency, $\alpha = \alpha_{\rm inj} - 0.5$. Here, $\alpha_{\rm inj}$ is the spectral index of the synchrotron radiation emitted by the injected particles, which can be assumed to be similar to the spectral index of the radio source at frequencies below the break frequency.

These three models do not include the effects of possible energy losses due to expansion of the radio source that makes the magnetic field to decrease accordingly. Even if these expansion effects are in principle important in young radio sources it has been shown by Murgia et al. (1999) that worst fits are in general achieved when considering a decreasing magnetic field.

JP versus KP model

As shown before, the CI model is best suited to explain an active radio source, while there are two different models describing the evolution of a radio source for which the activity ceased in the past, i.e. JP and KP models.

The main differences between the KP and JP emission spectra come from differences in the assumed microphysics. It has been argued that the KP model relies on a less physical basis than the JP model because the electrons' pitch angle are expected to change while they move among regions with different field strengths. Despite this, many spectra of compact radio sources seem to be quite well fitted by the KP model. The reason might be that while all these models simplistically assume a constant magnetic field strength, it might be more reasonable to consider a magnetic field with a random Gaussian distribution. In this case the angles are isotropically distributed and the field strenght is drawn from a Maxwellian distribution. This modification of the JP model produces an aged spectrum which is flatter than the one produced by the classical JP model and therefore more similar to the KP model (Tribble 1993). The reason of this flattening is easy to explain, since in an environment with different field strengths there will be different $\nu_{\rm break}$ values that will superimpose in the combined spectrum, which will become flatter. As will be shown later, this scenario with a distribution of magnetic field strengths nicely explains the relatively small observed polarisation in many radio sources.

The conclusion is that the lack of an exponential drop in an observed spectra (as predicted by the classical JP model) does not necessarilly imply lack of isotropy in the pitch angle distribution, but can be due to a distribution of field strengths (e.g. a random Gaus-

sian distribution). This also means that a good fit to a KP model might not guarantee that the determined radiative age is entirely correct.

3.5 Polarisation and Faraday Rotation

Synchrotron emission from a single electron is elliptically polarised, but when the emission from a population of electrons is considered, the elliptical components cancel with each other resulting in a net linearly polarised component (see e.g. Rybicki & Lightman 1986). Assuming a constant and homogeneous magnetic field, the polarisation degree of the emitted radiation can be as high as 75 per cent, because it is only dependent on the spectral index of the radiation:

$$m = \frac{2\alpha + 3}{2\alpha + 10/3} \tag{3.15}$$

but in real situations the assumption of a constant and homogeneous magnetic field is unrealistic. Magnetic field tends to be in real situations either tangled or turbulent, i.e. its components at different depths along the line of sight are aligned in different directions. These linearly polarised components cancel with each other, on average, reducing the net polarisation degree, m, to a smaller value (e.g., a few percent).

A linearly polarised light beam can be decomposed in two different circularly polarised components, one of them right-handed and the other left-handed. When this beam moves trough a magneto-ionic medium each component sees a slightly different refraction index, which makes them advance with different phase velocities. In this way, the relative phase between both components changes and the net effect is a progressive rotation of the plane of polarisation. This phenomenon is called *Faraday Rotation* and the rotating angle of the plane of polarisation (containing the electric vector) is proportional to the wavelength squared (see e.g., Longair 1981):

$$\Delta\chi = 812 \times \lambda^2 \int_L \left(\frac{n_e}{1\,\mathrm{cm}^{-3}}\right)\left(\frac{B_\parallel}{1\,\mu\mathrm{G}}\right)\left(\frac{ds}{1\,\mathrm{kpc}}\right) \qquad \mathrm{rad} \tag{3.16}$$

The term inside the integral is called *Faraday depth* and it is measured in rad/m^2, n_e is the electron density and $B_\parallel$ is the component of the magnetic field parallel to the line of sight. The integral extends over the line of sight and the so-called *Rotation Measure* is just the amount of Faraday depth integrated along the line of sight, that is, the term multiplying λ^2 in Formula 3.16. That is:

$$\Delta\chi = \chi - \chi_0 = RM \times \left(\frac{\lambda}{1\mathrm{m}}\right)^2 \qquad \mathrm{rad} \tag{3.17}$$

where RM is the Rotation Measure (in rad/m^2). This value can be estimated from multi-wavelength observations, fitting a slope to the polarisation angle as a function of λ^2. Since the polarisation angle is formally a pseudovector, there is an ambiguity of nπ in its value. For this reason a minimum of three (but better four) observations at different frequencies are needed to break this indeterminacy. The sign of RM can also give information about the weighted mean direction of the magnetic field parallel to the line of sight. If RM is positive the mean $\mathbf{B}_{\parallel}$ points towards the source, while if RM is negative it points towards the observer.

When the medium is not homogeneous, the amount of Faraday rotation is different for each different Faraday depth, and the degree of polarisation diminishes in a phenomenon called *depolarisation*. This depolarisation is called intrinsic if it happens in the same region of emission, or external if it happens in a region between the emission and the observer. A similar depolarising effect can happen when the medium is not homogeneous within the plane of the sky, but this *beam depolarisation* is easily identified because it depends on the angular resolution of the observing telescope. Finally, the *bandwidth depolarisation* can happen if the observing bandwidth is wide enough to have significant RM within the bandwidth. As a consequence part of the linearly polarised emission can be substantially cancelled out.

3.6 Beamed radio sources

As shown above, synchrotron radiation is supposed to be emitted by relativistic particles accelerated by the central nucleus. This relativistic nature of the emitting particles introduces some effects that should be considered when extracting information about the synchrotron emission. These effects are for instance the flux density amplification, or the relativistic corrections to be applied to lengths or time lags. If these corrections are not correctly taken into account, unphysical conclusions can be inferred from the observations as in the case of superluminal motions.

The main difficulty when accounting for these effects is the determination of the Doppler factor, D, which is dependent on the geometric disposition of the source, through the angle ϕ between the direction of the particle's velocity v and the line of sight:

$$D = \frac{1}{\gamma(1 - \beta cos\phi)} \tag{3.18}$$

where $\beta = v/c$ and $\gamma = (1-\beta)^{-1/2}$. In many cases the orientation of the radio source, and therefore θ are not known. However, there are several ways to estimate the Doppler factor from radio observations. Some of the more important are listed in Chapter 2 of Giroletti (2004).

Here emphasis will be given to the jet/counter-jet ratio because it will be used to constrain the orientation of a radio source in Chapter 7. Let us consider two identical jets moving in opposite directions from the central core, with relative velocities with respect to the observer v and $-v$, respectively. The relativistic Doppler factors will be $D = 1/\gamma(1\pm\beta)$ with the plus sign corresponding to the approaching jet and the minus sign to the receding jet.

As previously mentioned, the spectrum of a synchrotron jet is described by a power law $S_\nu \propto \nu^\alpha$, and the observed brightness is D^p times the brightness in the source's rest-frame. Depending on the nature of the jet, p can be $2+\alpha$ (continuous jet) or $3+\alpha$ if the jet is formed by several moving spheres or blobs. The brightness ratio between the jet and the counter-jet is given by the formula:

$$R = \left(\frac{1+\beta\cos\phi}{1-\beta\cos\phi}\right)^p \tag{3.19}$$

If the jet is closely aligned to the line of sight, the brightness of the approaching jet can be strongly enhanced, while the receding jet can be easily below the detection limit of the observation. The opposite will happen if the radio source is contained in the plane of the sky (e.g., $\phi \sim 0$) because then jet and counter-jet will show similar brightnesses. In this case, Formula 3.19 can only be used to set a valid range on the Doppler factor as well as on ϕ.

Additionally, this method can only give an approximation of the Doppler factor, since it assumes *identical* jets moving in opposite directions, which is not always the case, for instance in the presence of an inhomogeneous interstellar medium.

4

Definition of BAL QSO samples

As explained in Chapter 2, the absorbing features in the spectra of BAL QSOs are only associated with certain resonant emission lines like C IV, Si IV, N V, Al III or Mg II. However, the most common lines showing prominent troughs are C IV, Mg II and Si IV. Also N V troughs might be prominent but their presence can be confused by an, usually strong and broad, Ly-α emission in the same spectral region. Therefore, the wavelengths bluewards the C IV and Mg II emission lines have been traditionally used to define BAL QSO samples.

The so-called optical window to which most optical CCDs are sensitive, can be considered to cover an approximate range between 4000 and 9200 Å. Away from these limits, either the quantum efficiency of the CCD substantially decreases or the atmospheric absorption degrades the quality of the data in that particular spectral region. Figure 4.1 shows a schematic representation of the wavelength versus redshift space. The Mg II line "crosses" the 4000 Å limit at about z = 0.4. However, only LoBALs with low detachment from the emission can be observed at this redshift. Progressively increasing z, Mg II BAL QSOs with more detached troughs can also be identified. This emission line "crosses" the 9000 Å limit at about z = 2.2. A similar window exists for C IV covering the redshift range between 1.6 and 4.8.

Very few QSOs have also been found showing BAL troughs in the Balmer hydrogen lines. These hydrogen troughs allows one, in principle, to identify BAL QSOs at lower redshifts than traditional HiBAL or LoBAL QSOs. For instance, Hall (2007) reported the discovery of SDSS J125942.80+121312.6, a z = 0.75 QSO with prominent absorptions in at least six transitions of the Balmer series of hydrogen (Hβ to H9). These extremely rare objects are characterised by having, apart from hydrogen absorptions, many narrow troughs due to Fe absorptions. In fact, two more examples, SDSS 0839+3805 (Aoki et al. 2006) with redshift 2.31 and SDSS 1723+5553 (Aoki et al. 2007) with redshift 2.11 are also classified as FeLoBAL QSOs, being the Balmer absorptions detected in the near-IR with Subaru observations. The three just mentioned cases are the only QSOs of this class identified to date, and NGC 4151 the only known Seyfert galaxy with this kind of absorption. Since

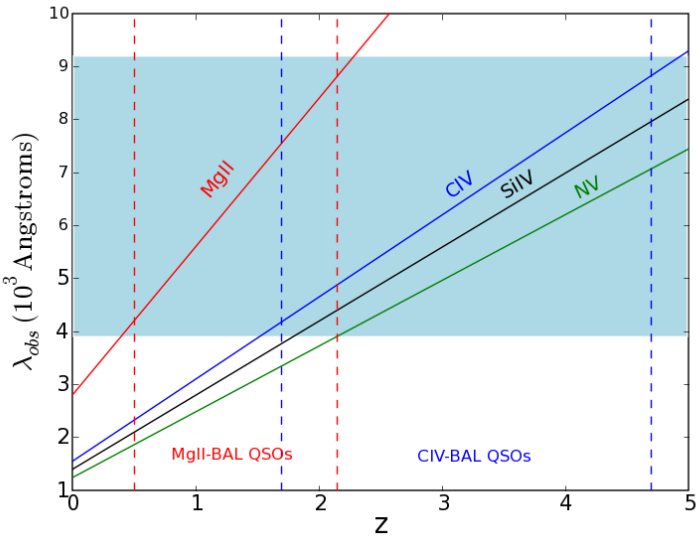

Figure 4.1: Position of the relevant lines in HiBAL and LoBAL QSOs in the wavelength versus redshift space. The shaded region delimits an approximate optical spectroscopic window, between 3900 and 9200 Å.

they are so rare, no statistically significant samples of these objects have been yet defined.

The aim of this chapter is mainly to introduce the sample of BAL QSOs to be studied in the following chapters. This sample has been defined on the basis of other existing samples of BAL QSOs appeared in recent years in the literature. Most BAL QSO samples defined so far are based on purely optical selection criteria and not many efforts have been made in obtaining large or complete samples of radio-selected BAL QSOs. The first part of the chapter will thus summarise and briefly describe the main samples of BAL QSOs on which our sample of radio-loud BAL QSOs is based. Some of the properties of these samples are important to identify possible biases in the definition of our sample, that could affect the statistical conclusions extracted from its analysis.

The recently available large databases of QSOs released by SDSS make it possible now to select larger and more homogeneous samples of radio-loud BAL QSOs than that studied in this thesis. For this reason, at the end of the chapter, a bigger and more homogeneous sample will be defined based on the last available SDSS QSO catalogue complemented with radio data from the FIRST survey. This new sample will be perfectly adapted to be used in the near future to test some of the conclusions obtained in this thesis.

4.1 BAL QSOs in the Luminous Bright QSO Survey

The Large Bright QSO Survey (LBQS), formerly known as the APM QSO survey (Foltz et al. 1987) aimed at identifying a homogeneous sample of about 1000 bright QSOs de-

tected in the Palomar Sky Survey plates, with optical magnitudes B_J between 16.0 and 18.5. Several papers presented the quasars discovered in the late eighties during the completion of the project, but the main catalogue summarising the entire sample of 1055 QSOs was published by Hewett et al. (1995).

All the sub-fields surveyed have at least a limiting magnitude of $B_J = 16.4$ mag, which is then the limiting magnitude of the entire catalogue although it also includes fainter objects. The LBQS sample is a very well studied sample of QSOs and before the SDSS it was the biggest and most homogeneous sample of QSOs with optical spectra of high quality.

A sample of 67 BAL QSOs from the LBQS was presented by Hewett & Foltz (2003) as a result of a visual classification and a measurement of the BI for those with absorptions associated with C IV. Hewett & Foltz (2003) assigned a flag to every source to account for the probability of being a true BAL QSO. Sources that were classified as *definite* BAL QSOs were marked with P(BAL) = 1.0, those *probable* BAL QSOs with P(BAL) = 0.7, and *possible* BAL QSOs with P(BAL) = 0.3. There are 57 objects with either P(BAL) = 0.7 or P(BAL) = 1.0, and they are listed in Table 4.1.

Table 4.1: List of BAL QSOs from the LBQS sample with P(BAL) > 0.5. Columns are: (1) LBQS ID; (2-3) coordinates in J2000; (4) redshift; (5) optical magnitude B_J; (6) Balnicity Index; (7) Observations available at other wavelengths. The codes in last column are 'X' (X-ray observations with Chandra by Gallagher et al. 2006), 'O' (optical photometry from SDSS-DR5), '2' (near-IR photometry from the 2MASS catalogue), 'I' (Mid- and Far-IR observations with Spitzer/MIPS by Gallagher et al. 2007), 'S' (Sub-mm observations with SCUBA presented by Priddey et al. 2007) and 'R' (radio data either at 1.4 GHz in the FIRST or NVSS databases or at 5 GHz observed by Stocke et al. 1992). All flux densities referred to in the last column at the various wavelengths are summarised in Gallagher et al. (2007).

Name	RA (J2000)	DEC (J2000)	z	B_J	P_{BAL}	BI	Other observations					
	hms	° ′ ″		mag		*km/s*						
B0004+0147	00:07:22.50	+02:04:12.5	1.710	18.13	1.0	255	X	O	2	I	–	R
B0009+0219	00:12:19.67	+02:36:35.7	2.642	17.99	1.0	1738	–	O	2	I	–	R
B0018+0047	00:21:27.91	+01:04:19.9	1.835	17.82	1.0	329	–	–	–	–	–	–
B0019+0107	00:22:27.48	+01:24:12.7	2.130	18.09	1.0	2305	X	O	2	I	S	R
B0020−0154	00:23:02.34	−01:38:16.2	1.460	18.27	1.0	1502	–	–	–	–	–	–
B0021−0213	00:24:10.90	−01:56:47.1	2.348	18.68	1.0	5179	X	O	2	I	S	R
B0022+0150	00:24:35.35	+02:06:48.3	2.826	18.35	1.0	224	–	–	–	–	–	–
B0025−0151	00:27:33.80	−01:34:52.3	2.076	18.06	1.0	2878	X	O	2	I	S	R
B0029+0017	00:31:35.58	+00:34:21.1	2.253	18.64	1.0	5263	X	O	2	I	S	R
B0045−2606	00:48:12.56	−25:50:04.2	1.242	18.05	0.7	292	–	–	–	–	–	–
B0049−0123	00:51:35.29	−01:07:09.4	1.560	17.84	0.7	28	–	–	–	–	–	–
B0051−0019	00:53:55.14	−00:03:09.4	1.713	18.67	1.0	3244	X	O	2	I	–	R
B0054+0200	00:56:44.65	+02:16:30.1	1.872	18.65	1.0	498	X	O	2	I	–	R
B0059−0206	01:02:05.60	−01:50:38.5	1.321	18.76	1.0		–	–	–	–	–	–
B0059−2735	01:02:17.04	−27:19:50.0	1.593	18.13	1.0	11053	X	O	2	I	–	R
B0103−2753	01:05:34.75	−27:36:58.2	0.848	18.07	1.0		–	–	–	–	–	–
B0106−0113	01:08:55.03	−00:57:47.1	1.668	18.07	1.0	377	–			I	–	R
B0109−0128	01:12:27.59	−01:12:21.8	1.758	18.32	1.0	399	X	O	2	I	–	R

Continues on next page...

Table 4.1 – Continued from previous page

Name	RA (J2000)	DEC (J2000)	z	B_J	P_{BAL}	BI	Other observations					
	hms	° ′ ″		mag		*km/s*						
B1009+0222	10:11:49.00	+02:07:31.8	1.349	18.62	1.0	1565	–	–	–	–	–	–
B1029−0125	10:31:49.51	−01:41:11.1	2.029	18.68	1.0	1848	X	O	2	I	S	R
B1133+0214	11:36:31.88	+01:58:00.6	1.468	18.38	1.0	1950	X	O	2	I	–	R
B1138−0126	11:41:11.62	−01:43:06.6	1.266	18.52	1.0	3523	X	–	–	–	–	–
B1203+1530	12:06:26.14	+15:13:35.4	1.628	18.70	1.0	1517	X	O	2	I	–	R
B1203+1703	12:06:20.17	+16:46:39.1	1.401	18.71	0.7	1052	–	–	–	–	–	–
B1205+1436	12:08:25.34	+14:19:20.9	1.643	18.38	1.0	788	X	O	2	I	–	R
B1208+1535	12:11:25.46	+15:18:51.5	1.961	17.93	1.0	4545	X	O	2	I	S	R
B1212+1445	12:14:40.28	+14:28:59.5	1.627	17.87	1.0	3618	X	O	2	I	–	R
B1214+1753	12:16:56.88	+17:37:13.3	0.679	17.65	0.7		–	–	–	–	–	–
B1216+1103	12:19:30.93	+10:47:00.9	1.620	18.28	1.0	4791	X	O	2	I	–	R
B1219+1244	12:22:21.75	+12:28:20.0	1.309	18.66	1.0	3138	–	–	–	–	–	–
B1224+1349	12:26:35.58	+13:32:51.6	1.838	18.18	1.0	420	–	O	2	I	–	R
B1228+1216	12:31:16.43	+12:00:24.1	1.408	17.54	1.0	496	–	–	–	–	–	–
B1230+1705	12:33:10.69	+16:49:05.8	1.420	18.44	1.0	2945	X	–	–	–	–	–
B1231+1320	12:33:55.62	+13:04:08.9	2.380	16.86	1.0	3473	X	O	2	I	S	R
B1234+0122	12:37:24.55	+01:06:15.2	2.025	18.00	1.0	4	–	–	–	–	–	–
B1235+0216	12:38:13.01	+02:00:19.6	0.672	17.65	0.7		–	–	–	–	–	–
B1235+0857	12:37:54.82	+08:41:06.4	2.898	18.17	1.0	815	X	O	2	I	S	R
B1235+1453	12:37:36.40	+14:36:40.5	2.699	18.56	1.0	2657	X	O	2	I	S	R
B1235+1807B	12:38:20.22	+17:50:38.0	0.449	16.86	1.0		–	–	–	–	–	–
B1239+0028	12:42:02.65	+00:12:28.8	1.214	17.46	1.0	1733	–	–	–	–	–	–
B1239+0955	12:41:35.89	+09:39:31.5	2.013	18.38	1.0	708	X	O	2	I	S	R
B1240+1607	12:43:03.62	+15:50:47.6	2.360	18.84	1.0	2867	X	O	2	I	–	R
B1243+0121	12:45:51.45	+01:05:05.0	2.796	18.50	1.0	5953	X	O	2	I	S	R
B1314+0116	13:17:14.23	+01:00:13.0	2.686	18.65	1.0	2626	X	O	2	I	–	R
B1331−0108	13:34:28.05	−01:23:48.8	1.881	17.87	1.0	7911	X	O	2	I	–	R
B1429−0036	14:31:43.77	−00:50:11.9	1.180	17.76	1.0	1500	–	–	–	–	–	–
B1442−0011	14:45:14.84	−00:23:58.4	2.226	18.24	1.0	5142	X	O	2	I	–	R
B1443+0141	14:45:45.29	+01:29:12.4	2.451	18.20	1.0	7967	X	O	2	I	S	R
B2111−4335	21:15:06.97	−43:23:09.5	1.708	16.68	1.0	7249	X	O	2	I	–	–
B2116−4439	21:20:11.66	−44:26:53.8	1.480	17.68	1.0	2594	X	O	2	I	–	–
B2140−4552	21:43:28.91	−45:38:50.7	1.688	18.30	1.0	1410	X	O	2	I	–	–
B2154−2005	21:57:05.92	−19:51:13.6	2.035	18.12	1.0	962	X	O	2	I	S	R
B2201−1834	22:04:01.61	−18:19:42.0	1.814	17.81	1.0	1612	X	O	2	I	S	R
B2208−1720	22:11:15.47	−17:05:25.4	1.210	17.65	1.0	4271	–	–	–	–	–	–
B2211−1915	22:14:37.90	−19:00:57.3	1.952	18.02	1.0	27	X	O	2	I	S	R
B2212−1759	22:15:31.68	−17:44:08.7	2.217	17.94	1.0	2221	–	O	2	I	–	R
B2241+0016	22:44:31.49	+00:32:25.8	1.394	18.30	1.0	396	–	–	–	–	–	–
B2350−0045A	23:52:53.50	−00:28:50.7	1.617	18.63	1.0	6964	X	O	2	I	–	R
B2358+0216	00:01:21.70	+02:33:04.9	1.872	18.61	1.0	6283	X	O	2	I	–	R

Figure 4.2 shows, in the left, the distribution of B_J as a function of redshift for the complete LBQS QSO sample and for the subsample of BAL QSOs. This plot reflects one of the main characteristics of BAL QSO samples. The majority of them are clustered in the redshift range between 1.4 and 2.2, but this is just a selection effect. As seen in Figure 4.1

this redshift range is particularly sensitive to include BAL QSOs because both HiBAL and LoBAL QSOs can be found in it. Below redshift 1.5 only a few LoBAL QSOs are found because these are rare and their absorptions difficult to quantify. At redshift higher than 2.5 only HiBAL QSOs, which are the majority of BAL QSOs, can be identified.

The right panel in Figure 4.2 displays the histogram of BI in the FBQS sample. It shows that typical BI values are below 5000 km s^{-1}, with the median BI of the sample being $\sim$ 1900 km s^{-1}. The most extreme case is LBQS 0059−2735, a FeLoBAL QSO with two wide troughs in C IV and therefore BI $>$ 11000 km s^{-1} (its optical spectrum can be seen in Weymann et al. 1991).

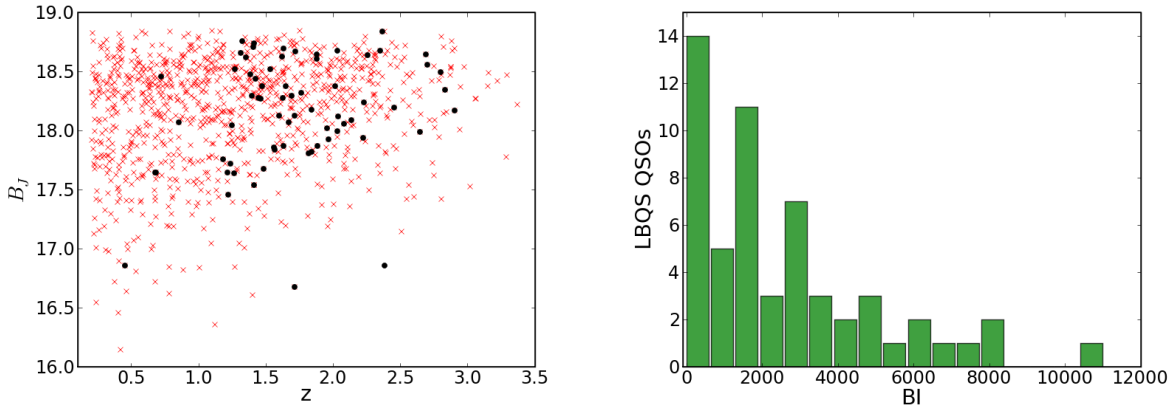

Figure 4.2: Left: B_J versus redshift diagramme for the LBQS QSO sample. Crosses represent the whole sample, while circles are the 57 objects with high probability of being BAL QSOs, i.e. those with P(BAL) > 0.5, catalogued by Hewett & Foltz (2003). Right: Histogram of Balnicity Index (BI) for the LBQS BAL QSOs with P(BAL) > 0.5.

An extensive multiwavelength follow-up has been done of the LBQS BAL QSO sample listed in Table 4.1, especially of those objects with P(BAL) $>$ 0.5. In the last column of this table observations recently made at various wavelengths (from X-rays up to radio) and published in several papers are noted. The flux densities corresponding to these multi-wavelength observations were summarised by Gallagher et al. (2007) who discussed the overall spectral energy distribution of this sample.

As mentioned in Chapter 2, the radio observations of this sample by Stocke et al. (1992) revealed no strong detections at 5 GHz of these LBQS BAL QSOs. The interpretation of this was that BAL QSOs were exclusively radio-quiet, maybe because the BAL phenomenon would suppress in some way the mechanism responsible for the radio emission.

4.2 The FIRST Bright QSO Survey sample of BAL QSOs

The FIRST Bright QSO Survey (FBQS, Gregg et al. 1996) benefited from the accurate positions with uncertainties within the arcsec and the from the high sensitivity obtained in the VLA maps of the FIRST radio survey. All of this allowed them to obtain a large list of radio-selected quasars in a relatively efficient way.

The FBQS was built matching the FIRST catalogue with the APM catalogue of the Palomar Observatory Sky Survey (POSS-I). The match radius was established in 1.2 arcsec and only point-like objects in either of the two POSS-I emulsions (O and E, similar to Johnson B and Cousins R) were considered. A brightness cut was also set in the recalibrated and extinction-corrected POSS-I E magnitude, considering only objects with $E < 17.8$. As a final step, a cut in colour of $O-E < 2$ was also applied (White et al. 2000) in order to increase the efficiency avoiding very red objects (like late-type stars).

The FBQS survey was later extended towards the southern galactic cap (Becker et al. 2001) covering a smaller area but with an increased limiting magnitude of the survey. The selection procedure was similar to that applied to the northern sample, matching the FIRST meridional extension with the UK Schmidt survey on the southern sky (McMahon & Irwin 1992). The new flux density cut was based on the recalibrated, extinction-corrected optical SERC R magnitude (5600-5900 Å) on the UK Schmidt red plate, imposed to be $R < 18.9$. A similar colour cut $B-R < 2$ was also considered in this meridional sample.

A total of 43 BAL QSOs were found in both the northern and southern extensions of the FBQS, 29 of them in the north, presented by Becker et al. (2000) and 14 in the south presented by Becker et al. (2001). These objects are listed in Table 4.2. This was the first relatively large sample of radio-loud BAL QSOs, which according to previous findings, were supposed to be extremely rare objects among luminous QSOs (Stocke et al., 1992). The FBQS BAL QSO sample thus demonstrated for the first time the existence of a substantial population of radio-emitting BAL QSOs.

Table 4.2: List of BAL QSOs from the FBQS sample. The first block, with 29 objects, corresponds to the northern sample and the second block, with 14 objects, to the southern sample. Columns are: (1) Source ID; (2-3) FIRST radio positions in J2000; (4) redshift; (5) Extinction-corrected POSS-I E magnitude (north) or extinction-corrected R magnitude (south); (6) Optical colour O−E (north) or B−R (south); (7) Peak flux density at 1.4 GHz from the FIRST catalogue in mJy; (8) Balnicity Index calculated in C IV for HiBAL QSOs and in Mg II for LoBAL QSOs (except LoBAL QSOs 1054+25, 1324+24, 2347−10 and 0014−01 for which BI was calculated in C IV); (9) Classification as a BAL QSO.

Name	RA (J2000)	DEC(J2000)	z	E	B−R	$S^{peak}_{1.4\ GHz}$	BI	Type
	hms	° ′ ″		mag	mag	(mJy)	km/s	
0724+41	07:24:18.492	+41:59:14.40	1.552	17.65	1.05	7.89	1300	Lo
0728+40	07:28:31.661	+40:26:15.85	0.656	15.13	0.14	16.96	200	Lo
0809+27	08:09:01.332	+27:53:41.67	1.511	17.17	0.40	1.17	7000	Hi
0840+36	08:40:44.457	+36:33:28.41	1.230	16.20	1.34	1.63	0	FeLo
0910+26	09:10:44.902	+26:12:53.71	2.920	17.78	1.48	7.84	320	Hi

Continues on next page...

Table 4.2 – Continued from previous page

Name	RA (J2000)	DEC(J2000)	z	E	B−R	$S^{peak}_{1.4\ GHz}$	BI	Type
	hms	°′″		mag	mag	(mJy)	km/s	
0913+39	09:13:28.260	+39:44:44.17	1.580	17.16	0.83	2.06	10700	Hi
0934+31	09:34:03.978	+31:53:31.47	2.419	17.43	0.39	4.68	1200	Hi
0946+27	09:46:02.299	+27:44:07.04	1.748	16.89	0.76	3.54	260	Hi
0957+23	09:57:07.367	+23:56:25.32	1.995	17.63	0.84	136.10	0	Hi
1031+39	10:31:10.647	+39:53:22.81	1.082	17.73	0.92	2.45	20	Lo
1044+36	10:44:59.591	+36:56:05.39	0.701	16.51	0.72	14.61	400	FeLo
1054+25	10:54:27.150	+25:36:00.33	2.400	16.93	1.45	2.99	1200	Lo
1122+31	11:22:20.462	+31:24:41.19	1.448	17.08	1.11	12.64	0	Lo
1150+28	11:50:23.570	+28:19:07.50	3.124	16.46	1.54	13.96	0	Hi
1200+35	12:00:51.501	+35:08:31.41	1.700	15.21	1.24	2.03	4600	Hi
1214+28	12:14:42.303	+28:03:29.01	0.698	15.87	1.16	2.61	0	FeLo
1304+42	13:04:25.543	+42:10:09.66	1.916	16.33	0.75	1.52	2900	Hi
1312+23	13:12:13.560	+23:19:58.51	1.508	16.95	0.89	43.27	1400	Hi
1324+24	13:24:22.536	+24:52:22.25	2.357	17.40	1.47	4.89	1300	Lo
1408+34	14:08:00.454	+34:51:25.11	1.215	17.03	1.41	2.91	260	Lo
1408+30	14:08:06.207	+30:54:48.67	0.842	17.30	1.69	3.34	4800	Lo
1413+42	14:13:34.404	+42:12:01.76	2.810	17.60	0.80	17.79	0	Hi
1420+25	14:20:13.072	+25:34:03.71	2.200	16.78	1.47	1.27	4500	Hi
1427+27	14:27:03.637	+27:09:40.29	1.170	17.68	1.37	2.58	30	FeLo
1523+37	15:23:14.434	+37:59:28.71	1.344	17.37	1.04	1.67	3700	Hi
1523+39	15:23:50.435	+39:14:04.83	0.657	15.93	1.00	3.75	3700	Lo
1603+30	16:03:54.159	+30:02:08.88	2.026	17.36	0.65	53.69	0	Hi
1641+30	16:41:52.295	+30:58:51.79	2.000	17.57	1.14	2.14	10600	Lo
1655+39	16:55:43.235	+39:45:19.91	1.747	17.74	0.37	10.15	4500	Hi
2124−07	21:24:10.271	−07:22:19.95	1.760	17.10	0.78	13.96	800	Hi
2300−10	23:00:11.749	−10:21:44.02	2.300	17.99	0.52	166.18	0	Hi
2336−09	23:36:11.627	−09:54:27.05	1.760	18.73	−0.19	1.83	100	Hi
2347−10	23:47:11.497	−10:37:42.18	1.780	17.45	0.20	1.08	9000	Lo
0014−01	00:14:38.279	−01:07:50.31	1.800	18.28	1.66	1.41	0	Lo
0046+01	00:46:13.548	+01:04:25.78	2.150	17.74	0.31	3.04	2100	Hi
0128−00	01:28:41.876	−00:33:16.79	1.650	18.34	0.91	3.03	2700	Hi
0135−02	01:35:15.239	−02:13:49.26	1.820	17.12	0.60	22.42	1900	Hi
0140−01	01:40:18.199	−01:38:05.94	2.240	17.64	0.34	1.51	1400	Hi
0148−00	01:48:12.829	−00:51:09.01	1.820	18.41	0.77	3.19	6800	Hi
0153−10	01:53:45.346	−10:08:40.06	1.900	18.86	0.46	3.95	600	Hi
0200−08	02:00:22.031	−08:45:11.76	1.930	18.58	1.04	7.75	2300	Hi
0221−01	02:21:00.743	−01:22:12.16	1.210	18.26	0.92	1.80	50	Lo
0256−01	02:56:25.641	−01:19:11.51	2.490	18.41	0.29	25.78	250	Hi

As seen in Table 4.2, most FBQS BAL QSOs are radio faint, mostly with 1.4-GHz flux densities below 10 mJy and none above 200 mJy. This is in contrast with the flux density distribution of the whole population of FBQS QSOs. This effect can be better seen in Figure 4.3, where the flux density $S_{1.4\ GHz}$ is plotted against redshift. The lack of BAL QSOs at the highest radio flux densities is evident, a space region where a substantial fraction of normal QSOs are located.

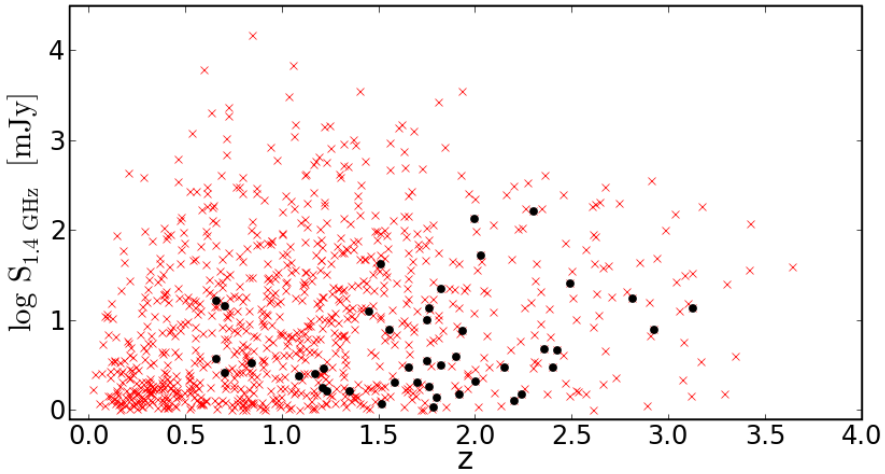

Figure 4.3: Flux density at 1.4 GHz, in logarithmic scale, against redshift for the QSOs in the FBQS catalogue, comprising both the northern and southern surveys. The whole sample is represented as crosses, while BAL QSOs are plotted as black circles.

This apparent lack of radio bright BAL QSOs is still not completely understood, but it is probably a real physical effect, and not a bias inherent to the BAL QSO identification and selection processes. As will be shown below, the red BAL QSOs missed in the FBQS (those with O−E $>$ 2) are not particularly radio powerful to significantly balance both fractions of radio-loud BAL and non-BAL QSOs. In order to further investigate this issue, the properties of the most radio powerful BAL QSOs deserve particular interest. For this reason the radio brightest BAL QSOs in the FBQS are ideal candidates to be included in our sample to be studied later.

4.3 FIRST-APM-SDSS radio BAL QSOs with red optical colour

Even if the FBQS BAL QSO sample can be considered a relatively homogeneous sample of radio-emitting BAL QSOs, its definition is based on a colour constraint that results in an important bias when selecting these objects. This colour constraint, O−E $<$ 2, causes that many BAL QSOs are probably not selected in this sample because BAL QSOs are, on average, redder than normal QSOs (Reichard et al. 2003). In order to make an estimate of the number of BAL QSOs lost in the FBQS a complementary survey was recently done by Carballo et al. (2006) using similar selection criteria but with the opposite colour constraint, i.e., O−E $>$ 2. They also profited from the better resolution of the SDSS imaging survey compared to the Palomar plates, in order to better identify and reject extended objects, probably associated with galaxies instead of QSOs. The selection criteria used in this survey were:

- Observed APM magnitude E $\leq$ 19.1.

- Star-like objects in the Palomar plates.
- Radio flux density above the FIRST catalogue limits, i.e. $S_{1.4\ \mathrm{GHz}} > 1$ mJy.
- Radio-optical separation below 1.5 arcsec.
- Colour O−E > 2 (including O non-detections).
- Star-like objects in the SDSS images.

The area covered by this survey was 1378.5 deg^2 from which 94 candidates satisfying the previous criteria were selected. From these, 78 were spectroscopically classified (84 per cent of the sample) with dedicated Telescopio Nazionale Galileo (TNG) observations and other data from the literature and the SDSS databases. Out of 26 QSOs in the redshift range [2.0 − 4.4], where the C IV and Si IV emission lines are observed in the TNG optical spectra, seven were found to have BALs satisfying the criterion BI > 0. These red radio BAL QSOs are presented in Table 4.3. The resulting observed fraction of BAL QSOs in this survey is relatively high (27 ± 10) per cent, which suggests that many red BAL QSOs are not present in the FBQS survey.

Table 4.3: List of red BAL QSOs in the APM-SDSS-FIRST survey of Carballo et al. (2006). Columns are: (1) Source ID; (2-3) SDSS coordinates in J2000; (4) redshift; (5-6) APM E magnitude and O−E optical colours, recalibrated with respect to APS and corrected by Galactic extinction; (7) Integrated flux density at 1.4 GHz from the FIRST catalogue except those with $S_{1.4\ \mathrm{GHz}} < 10$ mJy, for which FIRST peak flux density at 1.4 GHz is given; (8) Balnicity Index; (9) Classification. BAL QSO 1134+43 shows the presence of a weak absorption bluewards Al III, suggesting that it could be a LoBAL QSO.

Name	RA (J2000)	DEC(J2000)	z	E	B−R	$S_{1.4\ \mathrm{GHz}}$	BI	Type
	hms	° ′ ″		mag	mag	mJy	km/s	
0837+36	08:37:49.60	+36:41:45.5	3.416	18.65	2.75	27.10	5600	Lo
1134+43	11:34:45.83	+43:18:58.0	2.184	18.69	2.14	28.00	9800	Lo?
1219+48	12:19:57.18	+48:49:27.0	3.201	19.69	>2.86	6.92	4800	Lo
1408+55	14:08:15.25	+55:53:46.5	2.446	19.29	>3.08	3.41	4500	Hi
1459+49	14:59:26.33	+49:31:36.9	2.370	18.71	1.69	5.22	12850	Lo
1516+43	15:16:01.52	+43:09:31.5	2.590	18.50	<3.11	1.34	6000	Lo
1624+37	16:24:53.48	+37:58:06.6	3.377	18.47	2.03	56.44	2990	Hi

The relatively high fraction of LoBAL QSOs in this sample, 4 to 5 out of 7, is consistent with previous findings suggesting that these objects are more abundant among redder objects (see various evidence summarised in Chapter 2). The conclusion is that in order to end up with samples of radio BAL QSOs as complete as possible, these relatively red objects should be taken into account. In fact, these objects might constitute a high fraction of the radio powerful BAL QSO population. It should be noted that 3 out of 7 ($\sim$ 43 per cent) BAL QSOs in Table 4.3 have 1.4-GHz flux densities higher than 20 mJy, while only 6 out of 43 (14 per cent) FBQS BAL QSOs are above this threshold.

4.4 Sloan Digital Sky Survey BAL QSO samples

The Sloan Digital Sky Survey (SDSS; York et al. 2000) data base contains the biggest and most homogeneous sample of QSOs selected to date. It includes more than 10^5 identified QSOs up to redshift ~ 6. These QSOs were first imaged in various optical bands, u*, g*, r*, i*, z* (Fukugita et al. 1996), and then selected for spectroscopy using a complex selection algorithm involving multi-colour restrictions and matches with other radio or X-ray source catalogues (Richards et al. 2002). These complex selection algorithms have been found to be relatively efficient in selecting QSOs at different redshifts, but there are particular regions in the parameter space where the SDSS QSO catalogues are substantially incomplete (see e.g. Carballo et al. 2008).

The SDSS spectroscopic observations were done with a dedicated 2.5-m telescope on Apache Point (NM, USA), equipped with a pair of spectrographs fed by optical fibers. As soon as the observations are done and the data reduced, they are offered to the community in successive data releases. Each data release complements the previous one with bigger data volumes and a more accurate check of the quality and classification of previous data. In Table 4.4 the area surveyed in the different data releases is presented.

Table 4.4: Releases of SDSS and SDSS QSO catalogues

Release	Date	Imaging	Spectroscopy	Version	N. QSOs	Ref.
		deg^2	deg^2			
EDR	5-Jun-2001	462	386	I	3810	Schneider et al. (2002)
DR1	4-Apr-2003	2099	1360	II	16713	Schneider et al. (2003)
DR2	15-Mar-2004	3324	2627			
DR3	27-Sep-2004	5282	3732	III	46420	Schneider et al. (2005)
DR4	29-Jun-2005	6670	4783			
DR5	28-Jun-2006	8000	5740	IV	77429	Schneider et al. (2007)
DR6	29-Jun-2007	9583	7425			
DR7	31-Oct-2008	11663	9380			

After detailed inspection and analysis of the data in major releases, different versions of the SDSS QSO catalogue have been presented, each one containing well-defined samples of QSOs (see Table 4.4). The fourth version of the SDSS QSO catalogue (Schneider et al. 2007) contains 77,429 QSOs from the fifth data release (DR5). They are fainter than i* $\sim$ 15 mag and have luminosities larger than $M_{i^*} = -22$ mag, and present at least one emission line with FWHM larger than 1,000 km s^{-1} or interesting/complex absorption line features.

Given that about 15 per cent of optically-selected QSOs show BAL troughs, large samples with several thousands of these objects are supposed to be available in the SDSS databases. Already before the Early Data Release (EDR), efforts were done in cataloguing those BAL QSOs present in the preliminary SDSS spectroscopic databases. One of the first attempts, particularly interesting for our purposes, was done by Menou et al. (2001) who obtained a small sample of 13 SDSS radio-emitting BAL QSOs selected from the initial

$\sim$ 290 deg^2 surveyed by SDSS, a region also covered by the FIRST radio survey. In this relatively small area with fainter objects in the optical than the FBQS, Menou et al. (2001) measured a surface density of radio BAL QSOs 4 times as high as in the FBQS. This once more confirmed the presence of a considerable fraction of radio-moderate BAL QSOs among optically-selected sources.

Table 4.5: List of BAL QSOs collected by Menou et al. (2001) within the first 290 deg^2 surveyed by SDSS, with a radio counterpart at 1.4 GHz in FIRST. Columns are: (1) Source ID; (2-3) SDSS coordinates in J2000; (4) redshift; (5) reddening-corrected r*-band magnitude; (6) r*-band absolute magnitude; (7) FIRST peak flux density at 1.4 GHz from the FIRST catalogue; (8) Balnicity Index; (9) Classification as a BAL QSO.

Name	RA (J2000)	DEC(J2000)	z	r*	M$_{r^*}$	S$^{\rm peak}_{1.4\ \rm GHz}$	BI	Type
	hms	$^\circ\ ' \ ''$		mag	mag	mJy	km/s	
0039−00	00:39:23.20	−00:14:52.7	2.233	20.07	−25.15	21.2	0	Hi
0305−01	03:05:43.45	−01:06:22.1	2.850	19.89	−25.99	5.2	400	Hi
1154+00	11:54:04.14	+00:14:19.5	1.604	17.90	−26.68	1.5	4100	Lo
1159+01	11:59:44.81	+01:12:07.1	1.989	17.23	−27.82	266.5	0	Hi
1302−00	13:02:08.27	−00:37:31.6	1.672	17.93	−26.48	11.2	1200	Lo
1321−00	13:21:39.86	−00:41:52.0	3.080	19.25	−25.83	4.1	3500	FeLo
1323−00	13:23:04.58	−00:38:56.7	1.821	18.24	−26.58	8.9	300	Hi
1331+00	13:31:50.52	+00:45:18.8	1.892	19.14	−25.94	2.9	1300	Hi
1339−00	13:39:03.41	−00:42:41.2	1.518	21.02	−23.11	2.0	0	Lo
1401+01	14:01:12.01	+01:11:12.3	1.771	19.59	−25.17	3.1	1500	Lo
1516+00	15:16:36.78	+00:29:40.5	2.248	17.65	−27.05	2.2	6700	FeLo?
1604−00	16:04:12.39	−00:08:07.9	2.832	19.42	−26.42	1.4	600	Hi
2357−00	23:57:02.55	−00.48:24.0	3.005	19.03	−26.77	4.0	0	Lo

At a later stage, still preliminary descriptions of the SDSS BAL QSO population were made by Tolea et al. (2002) who collected 116 BAL QSOs identified in the EDR database, with only 5 BAL QSOs found to be detected in FIRST. Tolea et al. (2002) did not publish their list of SDSS-EDR BAL QSOs because a more complete catalogue of EDR BAL QSOs would be later published. At the same time Hall et al. (2002) published an interesting list of 23 BAL QSOs with unusual characteristics, most of them LoBAL or FeLoBAL QSOs from the SDSS-EDR. These objects are unusual in being extremely reddened, or having many narrow absorbing troughs or possessing very intense Fe absorptions. In this heterogeneous list of 23 objects (see Table 4.6) there are 18 unusual BAL QSOs from the EDR, another two are rare objects which could also be unusual BAL QSOs, and three additional QSOs have SDSS photometry but were spectroscopically identified as BAL QSOs with other telescopes. None of these objects are particularly radio bright and many of them are undetected at the $\sim$ 1-mJy limit.

But it was finally Reichard et al. (2003) who presented the final catalogue of 224 SDSS BAL QSOs in the EDR, from a parent sample of 3814 QSOs. In opposition to the previous analysis by Tolea et al. (2002), who selected the BAL QSOs using traditional techniques (i.e., determining BI with power-law fits to the non-absorbed continuum), Reichard et al. (2003) presented a new method based on fits to QSO templates in order to precisely de-

Table 4.6: List of unusual BAL QSOs from SDSS collected by Hall et al. (2002). Columns are: (1) Source ID; (2-3) SDSS coordinates in J2000; (4) redshift; (5) reddening-corrected r^*-band magnitude;(6) r^*-band absolute magnitude; (7) FIRST peak flux density at 1.4 GHz from the FIRST catalogue; (8) Balnicity Index; (9) Classification. "Fe III?" or "Fe III" mean it is a candidate or confirmed Fe III > Fe II FeLoBAL, respectively. "He I" means it shows neutral helium absorption. "mnt" means a FeLoBAL with many narrow troughs. "ot" means an overlapping trough FeLoBAL. "?" means curious object that might be a FeLoBAL QSO. "Red" or "Red Fe" mean a reddened LoBAL or FeLoBAL, respectively.

Name	RA (J2000)	DEC(J2000)	z	r^*	M_{i^*}	$S^{peak}_{1.4\ GHz}$	BI	Type
	hms	° ′ ″		mag	mag	mJy	km/s	
0105−00	01:05:40.75	−00:33:14.0	1.179	18.01	−26.59	4.59	0	?
0127+01	01:27:02.52	+01:14:12.5	1.157	17.87	−26.84	1.06	0	Red, He I
0149−01	01:49:05.28	−01:14:04.9	2.100	20.13	−25.76	<1.05	56	Fe III?
0300+00	03:00:00.57	+00:48:28.0	0.892	16.79	−27.23	<0.93	>11520	ot
0318−06	03:18:56.62	−06:00:37.7	1.967	17.60	−28.15		4017	Red, Fe
0338+00	03:38:10.85	+00:56:17.6	1.627	18.68	−26.74		360	Red, Fe
0342+00	03:42:58.00	+00:45:39.1	2.418	22.18	−24.63		0	Red, Fe
0437−00	04:37:42.81	−00:45:17.6	2.818	21.45	−26.40		16330	ot
0810+48	08:10:24.75	+48:06:15.5	2.240	19.51	−26.93	<1.45	5670	Fe III?
0819+42	08:19:48.91	+42:09:30.0	1.926	22.86	−23.53	<0.95	>13050	ot
0834+51	08:34:13.91	+51:12:14.6	2.391	19.80	−27.01	2.23	760	Red
0947+62	09:47:36.70	+62:05:04.6	2.125	19.77	−26.70		0	Red
1125+00	11:25:26.13	+00:29:01.3	0.865	18.35	−25.54	<0.99	0	mnt,He I
1128+01	11:28:28.31	+01:13:37.9	0.893	18.61	−25.30	<0.98	0	mnt
1154+03	11:54:36.60	+03:00:06.4	1.458	20.28	−26.97	<0.99	>13840	ot
1214−00	12:14:41.43	−00:01:37.9	1.045	18.83	−25.19	1.79	2880	Fe III
1324−02	13:24:44.11	−02:17:46.6	2.264	20.59	−26.02	<1.01	0	Red
1453+00	14:53:33.01	+00:29:43.7	1.297	19.82	−24.95		0	Red,He I
1456+01	14:56:03.08	+01:14:45.5	2.363	20.55	−26.21	8.56	1350	Red
1723+55	17:23:41.10	+55:53:40.5	2.113	18.36	−26.96	<0.93	4350	mnt
1730+58	17:30:49.11	+58:50:59.5	2.035	21.39	−24.54		>10900	ot, He I
2204+00	22:04:45.26	+00:31:42.0	1.353	17.39	−27.83	2.94	0	?
2215−00	22:15:11.94	−00:45:49.9	1.476	16.53	−28.42	<0.94	1160	Fe III

termine the QSO continuum. After choosing the best fit to any of the available templates, they used the BI criterion in C IV and Mg II in order to classify HiBAL and LoBAL QSOs. The authors concluded that both the traditional and the template-fitting methods, when applied to the same set of QSOs, end up with a very similar classification.

The list of 224 SDSS BAL QSOs catalogued by Reichard et al. (2003) includes a "complete" sample with 185 objects in the redshift range $1.7 \leq z \leq 4.2$ (156 HiBAL, 24 LoBAL and 8 FeLoBAL QSOs). They also compiled a supplementary list of BAL QSOs outside the mentioned redshift range, comprising 39 BAL QSOs (27 HiBAL, 10 LoBAL and 2 FeLoBAL QSOs). In order to compare the average properties of the different classes of BAL QSOs, they created geometrically-averaged templates of HiBAL, LoBAL and FeLoBAL QSOs using the objects catalogued in each subtype (see Figure 2.6).

After the EDR several releases have been made public, increasing by more than a factor

10 the number of QSOs catalogued. Trump et al. (2006) used as a parent sample the 46,420 QSOs in the SDSS-DR3 (Schneider et al. 2005) to obtain a sample with several thousands of SDSS BAL QSOs. They employed a similar fitting algorithm to that used by Reichard et al. (2003) in order to measure the continuum and calculated both the BI and the AI to characterise the C IV and Mg II troughs. The final catalogue comprises 4,843 BAL QSOs satisfying the AI criterion.

As mentioned in Chapter 2 this catalogue should be treated with care when studying the population of BAL QSOs because the use of the AI criterion might select other types of objects not related to the BAL phenomenon. According to the more subjective classification by Ganguly et al. (2007), the absorption present in about 15 per cent of the quasars classified as BAL QSOs in Trump's list might actually be due to intervening systems instead of having an intrinsic origin. Some examples of these false positives are shown in Figure 2 of Ganguly et al. (2007).

4.5 Definition of RBQ and SDSS-DR5 radio samples

A detailed study of the radio properties of BAL QSOs requires a relatively large sample of BAL QSOs which are bright enough in the radio to perform multi-frequency observations and also polarimetric measurements. As we have seen, the large-area FIRST survey is ideal to define samples of radio sources, which implies the necessity of selecting sources at 1.4 GHz. But in order to obtain the radio spectra of these sources up to relatively high frequency (e.g. up to 43 GHz) a minimum 1.4-GHz flux density cut has to be imposed, since the radio spectra are expected to decrease as the frequency increases. A similar cut in flux density is mandatory to be able to measure the polarised emission that usually constitutes only a few per cent of the total power emitted by the source.

Current radiotelescopes like the Effelsberg 100-m single dish or the VLA can detect sources up to $\sim$ 1 mJy in reasonable observing times. For instance, obtaining a 5-σ detection of a 1-mJy source using the Q-band receiver (centred at 43 GHz) with the VLA requires about 35 minutes of integration time. However, this time increases in practise by a factor of three due to overheads because these high-frequency observations of faint sources require to regularly switch the telescope between the target and a nearby phase calibrator.

One of the aims of this thesis is to define suitable samples for detailed radio studies. At a first stage a sample will be defined, called the RBQ (Radio BAL QSO) sample. This is a pilot sample with BAL QSOs satisfying some requirements of radio brightness, that have been extracted from several works in the literature at the time when we begun this work. The following chapters will focus on the radio follow-up of the BAL QSOs in this preliminary sample.

However, as shown before, several releases of SDSS have been made recently public, which made possible the classification of more than 10^5 QSOs. A fraction of them can be associated with FIRST radio sources allowing us to obtain homogeneous and large samples of radio bright QSOs with very good-quality optical spectra at reasonable resolution. Prof-

iting from this excellent database, a SDSS-based sample of radio-loud BAL QSOs will be also defined here. A complete analysis on the radio properties of this sample will be left for the near future. This will serve as an additional test for some of the results obtained in this thesis, which are based on the analysis of the RBQ sample.

4.5.1 Radio-loud BAL QSOs: RBQ sample

The sample of 29 radio BAL QSOs presented by Becker et al. (2000) was observed by these authors at only two frequencies, 1.4 and 4.8 GHz, which allowed them to determine the radio spectral index of these sources. However, the overall spectra of radio sources are usually complex and valuable information can be obtained from their analysis, as explained in Chapter 4. For this reason, we aim at establishing a representative sample of radio-loud BAL QSOs with radio spectra covering a wide range in frequency (i.e. between 74 MHz and 43 GHz).

The selection was based on the available samples of radio-loud BAL QSOs in the literature when the project was started. The main selection criterion was a cut in flux density of $S_{1.4\ \mathrm{GHz}} > 15$ mJy in order to facilitate total power detections at high frequencies and also the detection of polarised emission from those sources with a higher degree of linear polarisation. Assuming a typical steep spectrum with $\alpha = -0.7$, a source with $\mathrm{S}_{1.4\,\mathrm{GHz}} = 15$ mJy is expected to have a flux density of 1.4 mJy at 43 GHz, which is within our expected limits.

Therefore, we have defined a sample of radio-loud BAL QSOs (RBQ sample) composed of 15 objects. Seven of them were present in the list of Becker et al. (2000) or its extension in the southern Galactic cap (Becker et al. 2001). The remaining eight objects are SDSS quasars classified as BAL QSOs by visual inspection and associated with FIRST sources within a 2 arcsec radius. Two of these were presented by Menou et al. (2001), three more by Reichard et al. (2003) and the unusual BAL QSO 1624+37 in the sample was discovered in a survey for z $\sim$ 4 quasars (Holt et al. 2004). These 13 objects are *the only* BAL QSOs present in the mentioned samples with $S_{1.4\ \mathrm{GHz}} > 15$ mJy. Finally, the other two BAL QSOs satisfying this flux density criterion were identified by us from the SDSS-DR3. These sources were found during the definition of the FIRST-APM-SDSS sample mentioned in Section 4.3. Actually, the BAL QSO 0837+36 is one of these "red" BAL QSOs in the sample of Carballo et al. (2006).

Table 4.7 shows the main properties of the RBQ sample and in Figure 4.4 their optical spectra are presented. The spectra of BAL QSOs 0135−02, 0256−01, 0728+40, 0957+23 and 1312+23 were kindly provided by Robert Becker, while the rest were obtained from the SDSS archive. Figure 4.5 shows the flux density at 1.4 GHz versus redshift for all BAL QSOs belonging to the previously mentioned samples. Sources above the horizontal line of 15 mJy define the RBQ sample.

At a later stage, Trump et al. (2006) presented their catalogue with 4,784 SDSS BAL QSOs selected from the SDSS-DR3, using homogeneous selection criteria. In fact, all SDSS quasars in the RBQ sample belong to the list of Trump et al. (2006), except 0039−00 which

Table 4.7: Pilot sample of 15 radio-loud BAL QSOs studied in this thesis. Columns are: (1) source ID; (2,3) Optical coordinates in J2000.0; (4) angular distance between the optical and FIRST radio positions; (5) optical spectroscopic redshift; (6) FIRST 1.4-GHz flux density; (7) APS E magnitude corrected from Galactic extinction; (8) 5-GHz rest-frame luminosity, computed using the radio spectra presented in this paper; (9) reference where the BAL QSO appears in the literature and (10) BAL classification as given in that reference.

ID	RA(J2000)	DEC(J2000)	r_{ro}	z	$S^{\rm peak}_{1.4\ \rm GHz}$	E	$\log(L_{5\ \rm GHz})$	Ref	Type
	hms	$^\circ\ '\ ''$	$''$		mJy		W/Hz		
0039−00	00:39:23.18	−00:14:52.6	0.22	2.233	21.2	19.50	26.33	1	HiBAL
0135−02	01:35:15.22	−02:13:49.0	0.31	1.820	22.4	16.79	26.22	3	LoBAL
0256−01	02:56:25.56	−01:19:12.1	0.66	2.491	27.6	18.57	26.54	3	HiBAL
0728+40	07:28:31.64	+40:26:16.0	0.33	0.656	17.0	15.27	24.97	2	LoBAL
0837+36	08:37:49.59	+36:41:45.4	0.20	3.416	25.5	19.16	26.66	6	LoBAL
0957+23	09:57:07.37	+23:56:25.2	0.12	1.995	136.1	17.64	27.05	2	HiBAL
1053−00	10:53:52.86	−00:58:52.7	0.14	1.550	24.7	18.03	26.02	4	LoBAL
1159+01	11:59:44.82	+01:12:06.9	0.07	1.989	268.4	17.30	27.31	1	HiBAL
1213+01	12:13:23.94	+01:04:14.7	0.13	2.836	21.5	19.69	26.65	4	HiBAL
1228−01	12:28:48.21	−01:04:14.5	0.27	2.653	29.4	17.74	26.62	4	HiBAL
1312+23	13:12:13.57	+23:19:58.6	0.10	1.508	43.3	17.13	26.32	2	HiBAL
1413+42	14:13:34.38	+42:12:01.7	0.10	2.810	17.8	17.63	26.42	2	HiBAL
1603+30	16:03:54.15	+30:02:08.6	0.28	2.028	53.7	17.61	26.61	2	HiBAL
1624+37	16:24:53.47	+37:58:06.6	0.05	3.377	56.1	17.62	27.06	5	HiBAL
1625+48	16:25:59.90	+48:58:17.5	0.02	2.724	25.3	17.41	26.59	6	HiBAL

References key: 1- Menou et al. (2001); 2- Becker et al. (2000); 3- Becker et al. (2001); 4- Reichard et al. (2003); 5- Holt et al. (2004); 6- Identified directly from SDSS-DR3 database.

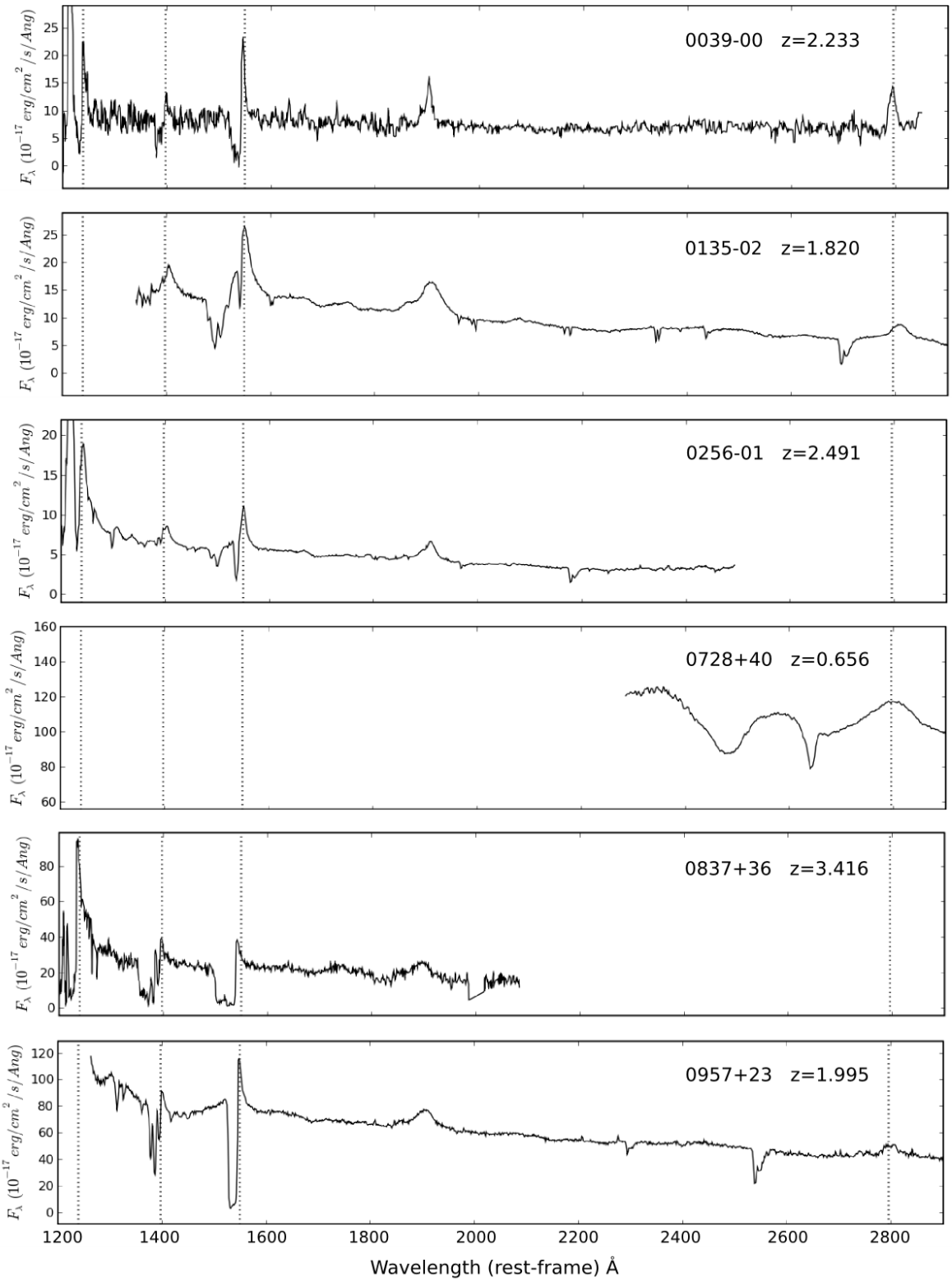

Figure 4.4: Rest-frame UV spectra of the BAL QSOs in the RBQ sample studied in this thesis. Vertical dotted lines mark the positions of the most typical emission lines where BALs can be found: Mg II λ 2799 Å, C IV λ 1549 Å, Si IV λ 1400 Å and N V λ 1240 Å.

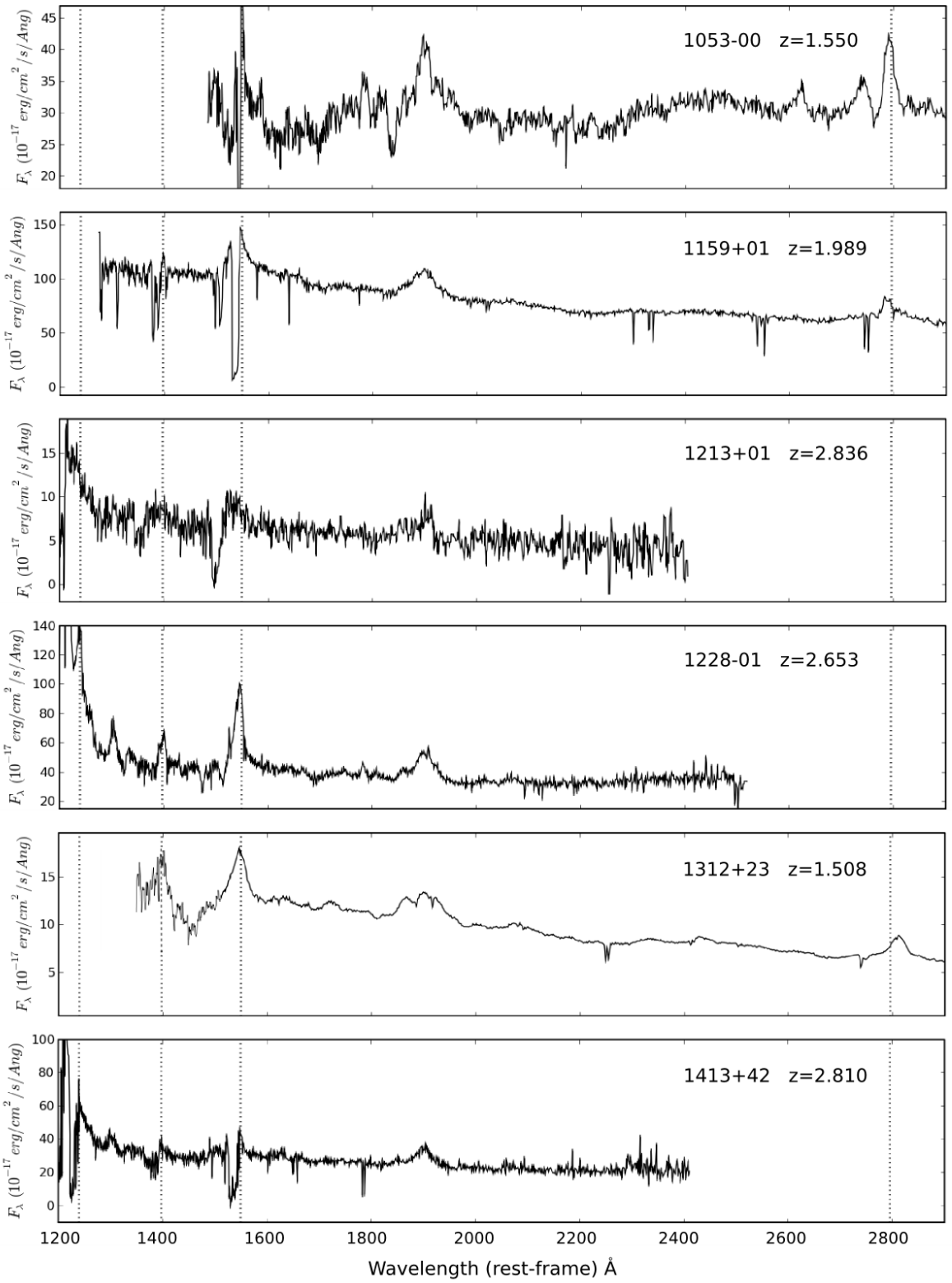

Figure 4.4. Continued.

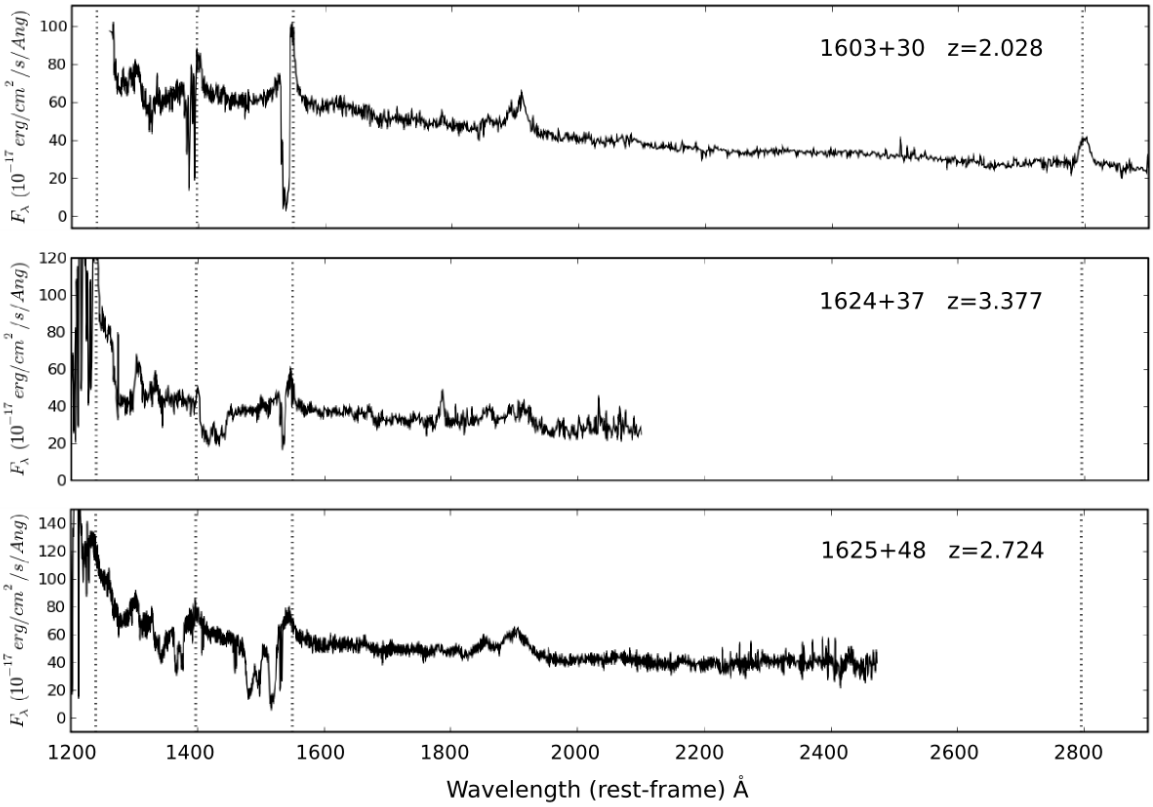

Figure 4.4. Continued.

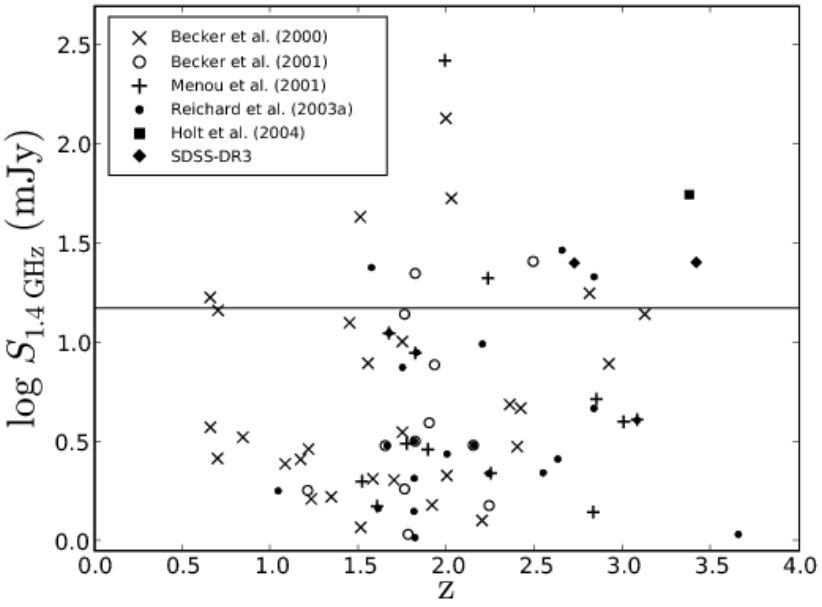

Figure 4.5: *Distribution of known radio-loud BAL QSOs in log S and z before going on-sky. The sample to be studied in this thesis was selected by taking all those with* $S_{1.4\mathrm{GHz}} > 15$ *mJy.*

is not included in the SDSS-DR3 quasar catalogue, but appears in the more recent SDSS-DR5 quasar catalogue (Schneider et al. 2007).

The RBQ sample, with only 15 objects might seem small to be statistically significant but it contains a number of bright radio BAL QSOs comparable to the number found in the entire SDSS-DR3 catalogue. This can be easily checked if we select all BAL QSOs with BI > 0 among the 4,786 BAL QSOs in the catalogue of Trump et al. (2006). The number of these *bona fide* BAL QSOs is 1,948 objects within all the SDSS-DR3 area. From these, only 170 have a radio counterpart in the FIRST survey within 2 arcsec from the optical position. Finally, establishing a radio flux density cut at 15 mJy, we end up with a sample of 19 BAL QSOs. This SDSS-DR3 BAL QSO radio bright sample thus contains a similar number of these objects than the RBQ sample.

4.5.2 SDSS-based radio-loud BAL QSOs

The fourth version of the SDSS QSO catalogue (Schneider et al. 2007) contains 77,429 QSOs from SDSS-DR5. This master catalogue contains the FIRST radio counterparts of the SDSS QSOs when there is a positional coincidence between the optical and the radio sources within 2 arcsec. This is, to date, the best parent catalogue to extract a homogeneous sample of radio-loud SDSS BAL QSOs.

In the whole catalogue there are 6,626 objects with a radio counterpart at 1.4 GHz

detected in the FIRST radio survey. However, not all of these can be inspected for the presence of BAL troughs because of their redshifts. As previously seen in Figure 4.1, the Mg II line can start to be detected in the optical spectra at z $\sim$ 0.4. However, in order to be able to see the region that extends $\sim$ 30,000 km s^{-1} bluewards the Mg II peak, we will consider the minimum redshift for suitable inspection to be z = 0.5. For the same reason, z = 2.2 will be considered the maximum redshift to look for Mg II absorptions. A similar "redshift window" was selected for C IV to be $1.7 < z < 4.7$. Therefore, we will inspect for the presence of BALs in all QSOs with $0.5 < z < 4.7$.

Applying this last redshift restrictions to the radio sample of 6,626 QSOs, we end up with a subsample of 5,538 QSOs. Finally, we have established a similar flux density cut as that applied to define the RBQ sample, i.e. $S_{1.4\ \mathrm{GHz}} > 15$ mJy, which reduces the number of objects to 1,875. In the subsequent visual inspection of the spectra we have discovered 6 objects that have probably been incorrectly classified as QSOs in the catalogue of Schneider et al. (2007). They are SDSS J013435.66-093102.9, SDSS J091156.06+033758.1, SDSS J092853.50+570735.3, SDSS J105115.88+464417.3, SDSS J153007.41+373532.2 and SDSS J155633.77+351757.3. These six objects will not be further considered, and after subtracting them we end up with a parent sample of 1869 QSOs.

We have visually inspected the optical spectra of the QSOs in this sample to look for the presence of BAL troughs in C IV and/or Mg II. It is much easier to identify BAL troughs associated with C IV because the continuum in non-absorbed spectra is relatively smooth and free of other features in the spectral range between the C IV and Si IV peaks. However, the main problem with the identification of Mg II BAL troughs is the presence in some QSOs of the so-called *small blue bump* at about 3000 Å. The contribution of numerous blends of high order Balmer lines and many Fe II emission lines create superposed bumps and depressions around the Mg II broad emission line that sometimes remind of the shape of BAL profiles. The effect of these features in this spectral region is nicely illustrated in Figure 3 of Wills et al. (1985).

The visual inspection was independently done in each of the C IV and Mg II lines for those objects belonging to the adequate redshift window. The classification was done including each object in only one of the following categories: (a) exhibits clear BAL features; (b) presents narrower absorptions than BALs, like mini-BALs or NALs; (c) it is faint or with noisy spectra and it is not possible to decide whether BALs are present or not; (d) the remaining QSOs, most of them non-BAL QSOs. The final goal is to establish a well-defined sample of radio-loud BAL QSOs, so we are mainly interested in the first category. A total of 60 QSOs with clear HiBALs in C IV and 15 with clear LoBALs in Mg II have been identified. This master list with 66 SDSS-DR5 radio bright BAL QSOs is shown in Table 4.8, and the plots showing their optical spectra can be seen in Appendix D.

Table 4.8: List of BAL QSOs in the SDSS-DR5 with $0.5 < z < 4.7$ and a radio counterpart in the FIRST catalogue with $S_{1.4\,GHz} > 15$ mJy. Columns are: (1) SDSS ID; (2) redshift; (3) reddening-corrected i*-band magnitude; (4) absolute i*-band magnitude; (5) peak flux density at 1.4 GHz (in mJy) from the FIRST catalogue; (6) BI measured in C IV; (7) BI measured in Mg II; (8) classification; (9) Notes: [1]Belongs to the catalogue of BAL QSOs (with BI > 0) from SDSS-DR3 by Trump et al. (2006); [2]Belongs to the RBQ sample.

SDSSJ	z	i*	M_{i^*}	$S_{1.4\,GHz}$	BI (km/s)		Type	Notes
		mag	mag	mJy	C IV	Mg II		
002440.99+004557.7	2.243	20.10	−25.56	48.8	0		Hi	
003923.18−001452.6	2.231	19.83	−25.81	21.2	608		Hi	2
004444.06+001303.5	2.286	19.75	−25.94	51.4	0		Hi	
074610.50+230710.8	2.092	18.37	−27.19	22.9	0		Hi	
075310.42+210244.3	2.291	18.85	−26.93	16.8	4588		Hi	1
080601.16+262400.0	3.072	20.19	−26.21	29.8	0		Hi	
081102.91+500724.5	1.837	18.84	−26.44	23.1	133	0	Hi	1
081618.99+482328.4	3.572	18.90	−27.86	72.3	0		Hi	
082231.53+231152.0	0.653	17.54	−25.23	28.0		0	Lo	
082813.47+065326.3	3.001	19.01	−27.34	19.0	183		Hi	
082817.25+371853.7	1.353	19.69	−24.84	21.2		0	Lo	
083749.59+364145.4	3.416	18.63	−28.01	25.5	4347		Hi	1,2
084218.39+362504.1	2.244	19.09	−26.61	52.6	0		Hi	
084224.38+063116.7	2.455	19.92	−25.97	48.0	1747		Hi	1
084914.27+275729.7	1.728	18.50	−26.61	52.8	0	0	Hi	
085417.61+532735.3	2.418	16.88	−28.95	21.3	0		Hi	
085641.58+424254.1	3.061	18.46	−27.90	20.1	308	0	Hi	1
090552.40+025931.4	1.818	16.56	−28.64	43.5	393	0	Hi	
092556.56+063015.8	2.474	19.17	−26.78	15.6	0		Hi	1
092913.96+375742.9	1.915	17.53	−27.75	43.2	1	0	Hi	
093348.37+313335.2	2.598	18.84	−27.15	18.3	1053		Hi	
094732.09+325220.5	2.339	19.05	−26.70	22.9	1205		Hi	
100515.98+480533.2	2.371	17.48	−28.29	206.1	0		Hi	
104059.79+055524.4	2.442	19.31	−26.55	40.2	2404		Hi	1
104452.41+104005.9	1.882	17.40	−27.88	16.4	1902	0	Hi	
104514.12+054031.6	0.986	19.30	−24.44	33.7		0	Lo	
104713.16+353115.6	2.437	19.62	−26.22	28.3	0		Hi	
105001.04+591111.9	2.169	19.07	−26.49	21.4	0		Hi	
105352.86−005852.7	1.570	17.56	−27.32	24.0		0	Lo	2
105416.51+512326.0	2.341	18.50	−27.24	32.0	0		Hi	
105527.55+150040.2	1.561	17.67	−27.16	19.2		0	Lo	
110206.66+112104.9	2.351	18.02	−27.74	82.3	0		Hi	
110440.82−000441.6	1.344	18.93	−25.58	31.6		0	Lo	
112938.47+440325.0	2.212	17.86	−27.78	41.1	0	0	Hi	
113445.83+431858.0	2.183	18.70	−26.91	27.4	0	0	Lo	
114516.74+493259.3	1.158	18.41	−25.70	29.8		0	Lo	
115852.86−004302.0	0.983	19.10	−24.63	51.6		0	Lo	
115901.75+065619.0	2.190	18.98	−26.61	116.5	1622		Hi	
115944.82+011206.9	1.999	17.00	−28.40	266.5	661	0	Hi	2

Continues on next page...

Table 4.8 – Continued from previous page

SDSSJ	z	i*	M_{i^*}	$S_{1.4\,GHz}$	BI (km/s)		Type	Notes
		mag	mag	mJy	C IV	Mg II		
120839.00+054829.1	1.854	20.26	−24.96	15.5	0	0	Hi	
121323.94+010414.7	2.829	20.18	−26.02	21.5	502		Hi	1,2
122848.21−010414.5	2.655	17.91	−28.13	29.3	0		Hi	1,2
122909.64+093810.1	2.649	19.35	−26.69	66.3	0		Hi	
123411.73+615832.6	1.946	18.42	−26.90	22.1	3248		Hi	1
123717.44+470807.0	2.270	18.40	−27.28	78.5	238	0	Hi	
130448.06+130416.5	2.568	18.72	−27.26	49.6	0		Hi	
132703.21+031311.2	2.826	18.57	−27.62	60.7	0		Hi	
133325.06+472935.3	2.620	18.31	−27.72	44.0	0		Hi	1
133701.39−024630.3	3.063	18.52	−27.90	43.3	0		Hi	
135910.45+563617.4	2.247	17.79	−27.86	17.2	0	0	Hi	
140126.15+520834.6	2.972	18.23	−28.04	36.2	0		Hi	1
140653.84+343337.3	2.567	18.50	−27.45	164.4	0		Hi	
141334.38+421201.7	2.817	18.26	−27.89	17.8	840		Hi	2
143010.83+114954.9	0.971	18.85	−24.86	143.4		0	Lo	
145239.17+542808.6	2.837	18.13	−28.04	28.8	0		Hi	
151630.30−005625.5	1.921	18.46	−26.95	24.6	0	0	Hi	
153013.94+580802.4	2.275	17.96	−27.71	16.7	0		Hi	
155429.40+300118.9	2.692	17.71	−28.38	40.0	0		Hi	
160354.15+300208.6	2.029	17.81	−27.66	53.7	214	0	Hi	2
162419.96+353845.2	1.772	17.79	−27.33	28.5	0	0	Lo	
162453.47+375806.6	3.380	18.17	−28.38	56.1	1841		Hi	1,2
162559.90+485817.5	2.723	17.72	−28.36	25.3	1674		Hi	1,2
162917.15+445650.1	1.541	18.81	−25.97	32.1		0	Lo	
210757.67−062010.6	0.645	16.85	−25.95	19.2		216	Lo	1
212916.60+003756.6	2.958	17.75	−28.59	49.1	0		Hi	
224800.69−090744.8	2.110	19.02	−26.55	32.4	0		Hi	1

This new sample includes all the SDSS QSOs in the RBQ sample (10 out of 15). It also includes 16 of the 19 bona-fide SDSS-DR3 BAL QSOs (BI > 0) in the catalogue of Trump et al. (2006) satisfying the 15-mJy flux density criterion. The other three SDSS-DR3 BAL QSOs not recuperated here are SDSS J145756.27+574446.9, SDSS J152516.62+351613.0 and SDSS J223843.56+001647.9, all three with BI < 20 km s^{-1} as measured by Trump et al. (2006). In this group, SDSS J152516.62+351613.0 was included by us in the (b) category (narrow absorber) and the other two in the (d) category (non-BAL QSOs).

The radio follow-up of this sample has already been started with multi-frequency observations with the 100-m Effelsberg radio telescope and the VLA. The results coming from the detailed analysis of this sample and a discussion comparing those with the conclusions of this thesis will be left for the near future.

5

Radio-loud BAL QSOs: radio spectra and polarisation properties

As seen in Chapter 2 various authors have found that BAL QSOs seem to be less frequent among the population of radio-powerful QSOs but the reason for this is not completely understood. We saw in Chapter 3 that observations in the radio can constitute an important diagnostic tool to improve our understanding of the BAL phenomenon. In particular, radio emission can be used in various ways as an orientation indicator because of the asymmetric disposition of the radio jets in AGNs. This characteristic is particularly useful to determine whether BAL QSOs are objects subtending a particular orientation with respect to the line of sight or objects at a particular stage of their evolution.

Even if only two decades ago radio-powerful BAL QSOs were supposed to be extremely rare, now it has become clear that a substantial population of these objects exist. As seen in Chapter 4 modern surveys like SDSS or FIRST have allowed us to define large and statistically significant samples of radio BAL QSOs, in order to study them as a population and not just in individual cases. Until now, very few observations of BAL QSOs in the radio domain have been done and the general radio properties of these objects as a population are not known.

This chapter reports the first results of a study in which a systematic approach is taken to characterise the radio-loud BAL QSO population. The final goal is to locate these objects in the framework of an adequate orientation and/or evolutionary scenario. In order to do this, the radio spectra and polarisation properties of a small sample of radio-loud BAL QSOs will be presented. The results of this chapter have already been published in Montenegro-Montes et al. (2008).

In Section 5.1 the samples of BAL and non-BAL QSOs used in this chapter are introduced. In Section 5.2 the observations, data reduction and the treatment of the errors are described. In Section 5.3 the results of the observations are presented. The radio morphologies of BAL QSOs, their polarisation properties and the variability of some of these

objects with 2-epoch observations are analysed. In addition, the shape of the radio spectra is described and the radio spectral index distributions of radio quasars with and without associated BALs are compared. All these results are reviewed together in Section 5.4 and compared with other findings trying to put emphasis on those aspects related to the orientation vs. evolutionary dilemma. Some of the limitations of the analysis are noted and solutions to some of these caveats are proposed.

5.1 Samples of BAL and non-BAL QSOs used

The sample under study here is the RBQ sample composed of 15 radio-loud BAL QSOs, that was defined in Section 4.5.1. In this chapter the radio spectra of these BAL QSOs are described, and in particular, the spectral index distribution as compared with that of a non-BAL QSO sample. This is an interesting exercise because the spectral index is known to be a statistical indicator of the orientation of quasars, and this comparison can give some information about the orientation of BAL QSOs. This comparison sample of non-BAL QSOs has been extracted from the complete B3-VLA quasar catalogue (Vigotti et al. 1997). The B3-VLA survey (Vigotti et al. 1989) consists of 1049 sources selected from the B3 survey (Ficarra et al. 1985) in five flux density bins between declination +37 and +47 deg. It was designed to be complete down to flux densities of 100 mJy at 408 MHz. In addition to the original flux densities at 408 MHz the entire classical radio frequency range has been covered for most of the sources in the sample, both from already existent surveys (6C at 151 MHz, WENSS at 325 MHz, NVSS at 1400 MHz, GB6 at 4850 MHz) and from dedicated observations, mainly at higher frequencies (74 MHz, Mack et al. 2005; 2.7 GHz, Klein et al. 2003; 4.85 GHz, Vigotti et al. 1999 and 10.5 GHz, Gregorini et al. 1998). Based on this radio survey, Vigotti et al. (1997) presented a complete sample of 125[1] quasars and this will be used as a comparison sample of radio-loud non-BAL quasars.

In Figure 5.1 the flux density is plotted against the redshift but now the sample of Vigotti et al. (1997) is presented together with that of Becker et al. (2000) and the one studied in this chapter. The redshift range covered by the BAL QSOs goes from 0.656 to 3.124 (Becker's list) and to 3.416 (RBQ sample). The sources in the list of Vigotti et al. (1997) are on average at smaller redshift ($z_{mean} = 1.25$), but they cover the redshift range between 0.096 and 2.757. Figure 5.1 also illustrates how the RBQ sample represents intermediate flux densities between the flux density coverage spanned by the relatively faint sample of Becker et al. (2000) and that covered by the list of brighter quasars from Vigotti et al. (1997).

5.2 Observations and data reduction

Radio-continuum flux densities with full polarisation information were collected for the RBQ sample at different frequencies in several runs with the Effelsberg 100-m radiotelescope and the Very Large Array (VLA). A summary of the different observing runs can be

[1] In practise 124 because the redshift of quasar B3 2329+398 is not known.

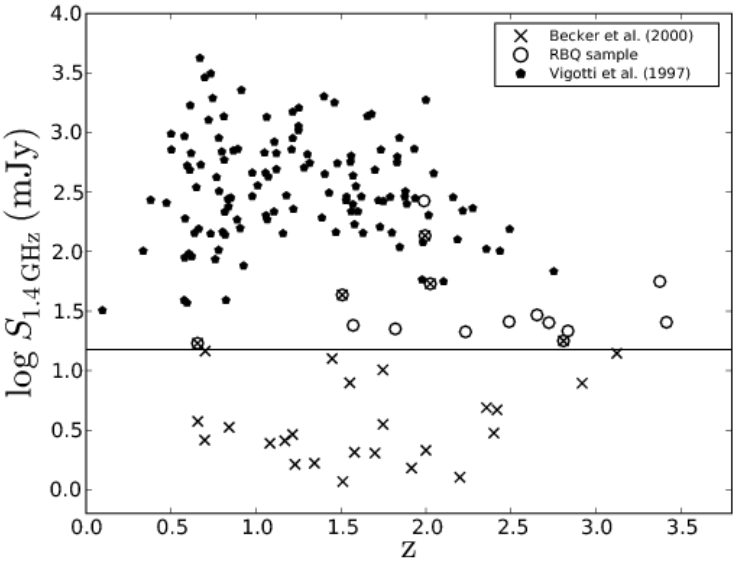

Figure 5.1: Same plot as Figure 4.5 in which the sample of normal radio-loud quasars from Vigotti et al. (1997) is shown, together with the samples of radio-fainter BAL QSOs.

Table 5.1: Summary of the observations

Run	Date	Telescope	Frequencies (GHz)
1	26−30 Jan 05	Effelsberg	4.85, 8.35, 10.5
2	15−16 Jul 05	Effelsberg	4.85, 8.35, 10.5
3	27 Oct 05	Effelsberg	4.85, 8.35, 10.5
4	23−26 Jun 06	Effelsberg	2.65
5	13 Feb 06	VLA(A)	8.45, 14.5, 22.5, 43.5
6	7 Mar 06	VLA(A)	8.45, 14.5, 22.5, 43.5

found in Table 5.1, and the list of frequencies used with their characteristics (e.g., angular resolutions) are displayed in Table 5.2.

5.2.1 Effelsberg 100-m telescope

The single-dish observations at 4.8, 8.4 and 10.5 GHz took place in January 2005. Some sources were re-observed in July and October 2005 in order to confirm doubtful values or improve the signal-to-noise ratio. Observations at 2.65 GHz were carried out in June 2006. All receivers used in these observations are mounted on the secondary focus of the 100-m antenna. The recently installed 2.7-GHz hybrid feed can observe simultaneously in 9 channels, 8 of them 10-MHz wide and the ninth covering the full 80-MHz range. Since the sources in our sample are too faint to have a high signal-to-noise ratio per channel, only the wide-band channel centred at 2.65 GHz has been used. The receivers at 4.8 and 10.5 GHz have multi-feed capabilities with 2 and 4 horns, respectively, allowing real-time sky

subtraction in every subscan measurement.

The observational strategy consisted of cross-scanning the source position in azimuth and elevation. These perpendicular scans were added to gain a factor $\sqrt{2}$ in sensitivity since the higher resolution FIRST maps ($\sim$ 5 arcsec) showed that none of these sources has structure more extended than 1 arcmin, the highest resolution in our observations (see Table 5.2). The cross-scan length was chosen to be about four times the beam size at each frequency for a correct subtraction of linear baselines. The scanning speed ranged from $8''$ to $32''$/s depending on the frequency, stacking typically 8 subscans at 2.65 GHz, and some 16 subscans in the rest of the frequencies (32 for the faintest sources at 10.5 GHz). This translates into on-source integration times between 15 and 75 sec per source and per frequency. Before combining, individual subscans were checked to remove those affected by radio frequency interference, bad weather, or detector instabilities.

The calibration sources 3C 286 and 3C 295 were regularly observed to correct for both time-dependent gain instabilities and elevation-dependent sensitivity of the antenna and to bring our measurements to an absolute flux density scale (Baars et al. 1977). The quasar 3C 286 was also used as a polarisation calibrator obtaining the polarisation degree m and the polarisation angle χ in agreement with the values in the literature (Tabara & Inoue 1980) within errors < 1 per cent and < 5 deg, respectively. The unpolarised planetary nebula NGC 7027 was also observed to have an estimation of the instrumental polarisation at each frequency.

The measurement of flux densities from the single-dish cross-scans was done by fitting Gaussians to the signal from all the polarimeter outputs (Stokes I, Q and U) and identifying the Gaussian amplitudes with the flux densities S_I, S_Q and S_U. For all sources with significant S_Q and S_U contributions, the polarised flux density S_P, the degree of linear polarisation m and the polarisation angle χ were computed, using the expressions given in Klein et al. (2003).

5.2.2 Very Large Array

VLA data were taken during February/March 2006 in the most extended A configuration using the receivers corresponding to the X, U, K and Q bands, i.e., centred at 8.4, 15, 22 and 43 GHz, respectively. Integration times were chosen on the basis of the predicted flux densities at these frequencies, after extrapolating from the Effelsberg frequencies with the adequate spectral indices. Those sources with indications of measurable polarised emission were observed more deeply and those expected to be too faint for this purpose were observed to have at least a good signal to noise ratio in S_I. Integration times range from $\sim$1 minute at 8.4 GHz up to $\sim$1 hour at 22 or 43 GHz for some sources.

At the two highest frequencies the fast-switch method was used, quickly switching between target and calibrator in order to have phase stability, taking care of the rapid atmospheric fluctuations. The duration of the cycles target-calibrator was of $\sim$ 150 to 200 seconds at the two highest frequencies.

Table 5.2: Observing frequencies and beam sizes

Telescope	Frequency (GHz)	Bandwidth (MHz)	$\theta_{\rm HPBW}$ (arcsec)
Effelsberg	2.65	350	265
Effelsberg	4.85	500	145
Effelsberg	8.35	1200	80
Effelsberg	10.5	300	65
VLA(A)	8.45	700	0.24
VLA(A)	14.5	700	0.14
VLA(A)	22.5	2000	0.08
VLA(A)	43.5	10000	0.05

3C 286 was the primary flux density calibrator and 3C 48 was used to test the goodness of the flux scale solution. Several phase calibrators chosen from the VLA calibrator manual[2] were observed during the run. Most were selected at about 2 to 5 deg from their target sources, and in all cases within 10 deg. This is especially important to avoid the loss of coherence at the highest frequencies. Again the flux density scale is the one of Baars et al. (1977) except at 22 and 43 GHz where the Baars expressions are not valid. At these frequencies the adopted scale is based on emission models and observations of planet Mars, and is supposed to be accurate at a level of 5 to 10 per cent.

The 31DEC06 version of the AIPS package was used to flag, calibrate, clean and image the VLA data. The standard recipe was followed in all frequencies. However, at 22 and 43 GHz opacity and gain curve corrections were applied as a previous step to the standard calibration, and the calibration table was gridded in intervals of 3 seconds to get rid of rapid atmospheric fluctuations. The appropriate clean component models were used for 3C 286 and 3C 48 at these two frequencies. The peak flux densities were measured by fitting 2-D Gaussians to the source profiles. The integrated flux densities were computed using the BLSUM task, adding the signal in small boxes containing each source. The same boxes were used to measure the Stokes parameters S_Q and S_U. The local noise of the maps was estimated from a circular region around each individual source. Peak and integrated flux densities have essentially the same values because most sources are unresolved, as will be discussed below.

The polarisation calibration of the VLA data was determined using the AIPS tasks PCAL and RLDIF. The first solves for the feed parameters in each antenna, using repeated observations of a strong unresolved source (in our case several snapshots of 3C 286 were taken) covering a range of different parallactic angles. RLDIF determines and subtracts any phase difference between the right and left polarisation systems. The residual instrumental polarisation at the VLA frequencies was estimated measuring the linear polarisation of 3C 84 after having applied the polarisation calibration. Aller et al. (2003) report that this

[2]Available at `http://www.vla.nrao.edu/astro/calib/manual`

Table 5.3: Values used to calculate the errors of the Stokes parameters and obtained instrumental polarisations.

Telescope	Frequency	ΔS_{conf}		ΔS_{cal}	P_{instr}
	(GHz)	(I)	(Q,U)	(per cent)	
Effelsberg	2.65	1.5	0.5	0.8	0.7
Effelsberg	4.85	0.45	0.15	0.9	0.7
Effelsberg	8.35	0.23	–	1.0	0.6
Effelsberg	10.5	0.08	–	1.9	0.8
VLA	8.45	–	–	1.9	<0.1
VLA	15.0	–	–	2.9	0.6
VLA	22.5	–	–	1.8	0.7
VLA	43.5	–	–	5.3	2.1

source shows a percentage of linear polarisation of (0.12 ± 0.01) per cent at 14.5 GHz, and for our purposes it can be considered unpolarised.

5.2.3 Error determination

We consider three main contributions to the flux density error as in Klein et al. (2003). These are (i) the calibration error ΔS_{cal} (in percentage) which is estimated by the dispersion of the different observations of the flux density calibrators; (ii) the error introduced by noise, $\Delta S_{n,i}$, which is estimated from the local noise around the source; and (iii) the confusion error $\Delta S_{conf,i}$ due to background sources within the beam area. This last term can be neglected in interferometric data where the synthesised beam has small dimensions.

Thus the expressions for the total uncertainty of Stokes parameters are Equations 5.1 and 5.2 for Effelsberg and the VLA, respectively:

$$\Delta S_i = \sqrt{(S_i \cdot \Delta S_{cal})^2 + \Delta S_{n,i}^2 + \Delta S_{conf,i}^2} \quad i = \mathrm{I, Q, U} \tag{5.1}$$

$$\Delta S_i = \sqrt{(S_i \cdot \Delta S_{cal})^2 + S_{n,i}^2 \cdot \frac{A_{src}}{A_{beam}}} \quad i = \mathrm{I, Q, U} \tag{5.2}$$

where A_{src} is the area of the box used to measure the source flux density, and A_{beam} is the beam area. The expressions for the uncertainties of S_P, m and χ can be taken from Klein et al. (2003).

Table 5.3 shows the coefficients used for the calculation of errors ΔS_i. The confusion limits at 2.7, 4.8 and 10.5 GHz have been extracted from Klein et al. (2003) and that at 8.35 GHz (not determined by Klein et al. 2003) was obtained from our own observations inspecting the behaviour of the signal rms at long integration times. This value is consistent with the interpolation over frequency from the two adjacent bands (at 4.85 and 10.5 GHz). The last column in Table 5.3 lists the instrumental polarisation for the different frequencies and telescopes.

Table 5.4: RBQ sample of 15 radio-loud BAL QSOs: Flux densities (in mJy), errors or 3-σ upper limits from 74 MHz to 1.4 GHz obtained from the literature. The symbol † indicate data from WENSS at 325 MHz, the rest are from the Texas Survey at 365 MHz.

ID	$S^{\rm VLSS}_{0.074}$	$S^{\dagger}_{0.365}$	$S^{\rm FIRST}_{1.4}$	$S^{\rm NVSS}_{1.4}$
	mJy	mJy	mJy	mJy
0039−00	<475	<80	21.2	19.5 ± 0.7
0135−02	<350	<80	22.4	22.8 ± 1.1
0256−01	<385	<80	27.6	22.3 ± 0.8
0728+40	<300	15 ± 3.3†	17.0	17.2 ± 0.6
0837+36	<290	184 ± 3.4†	25.5	–
0957+23	<260	<80	136.1	136.9 ± 4.1
1053−00	<500	<80	24.7	22.7 ± 1.1
1159+01	<320	887 ± 30	268.5	275.6 ± 8.3
1213+01	<340	<80	21.5	27.5 ± 7.9
1228−01	<340	<80	29.4	29.1 ± 1.0
1312+23	<300	<80	43.3	46.5 ± 1.4
1413+42	<330	16 ± 3.2†	17.8	16.8 ± 0.6
1603+30	<225	33 ± 4.4†	53.7	54.1 ± 1.7
1624+37	<355	59 ± 4.0†	56.1	55.6 ± 1.7
1625+48	<290	26 ± 3.7†	25.3	26.0 ± 0.9

5.3 Results

5.3.1 Radio flux densities

Tables 5.4 and 5.5 show the measured flux densities and errors (in mJy) between 74 MHz and 43 GHz for the RBQ sample. At frequencies below 2.6 GHz there are available flux densities from the literature and these are listed in Table 5.4. The flux densities at 325 MHz were obtained from the Westerbork Northern Sky Survey (WENSS; Rengelink et al. 1997). In addition, 3-σ upper limits and a detection from the Texas survey (Douglas et al. 1996) at 365 MHz are given for those sources not covered by the WENSS survey. At 74 MHz none of the sources is detected in the VLA Low-Frequency Sky Survey (VLSS; Cohen et al. 2007), but 3-σ upper limits have been computed measuring the local noise around the source position in the available images. Flux densities at 1.4 GHz from FIRST and NVSS (Condon et al. 1998) can be also found in Table 5.4.

The BAL QSO 1624+37 was observed in this campaign at 2.65 GHz with Effelsberg and at 15 and 43 GHz with the VLA. All the flux densities in the remaining frequencies were presented by Benn et al. (2005).

Table 5.5: RBQ sample of 15 radio-loud BAL QSOs: Flux densities (in mJy) from 2.6 to 43 GHz obtained in this work. Superscripts on the errors indicate the run number of that observation, according to the key in Table 5.1. The exception is 1624+37 (with superscript 0), for which several flux densities were presented in Benn et al. (2005).

ID	$S_{2.6}$	$S_{4.8}$	$S_{8.3}$	$S_{8.4}$	$S_{10.5}$	S_{15}	S_{22}	S_{43}
0039−00	–	19.3 ± 0.6^{1}	12.0 ± 0.4^{1}	12.3 ± 0.1^{5}	9.7 ± 0.4^{1}	6.2 ± 1.1^{5}	2.2 ± 1.2^{5}	1.1 ± 0.1^{5}
0135−02	–	27.2 ± 0.6^{1}	31.9 ± 0.8^{1}	30.8 ± 0.4^{5}	29.5 ± 0.7^{3}	22.7 ± 0.8^{5}	14.7 ± 0.2^{5}	2.3 ± 0.2^{5}
0256−01	–	12.0 ± 0.5^{1}	7.2 ± 0.3^{1}	7.2 ± 0.4^{5}	5.9 ± 0.4^{1}	4.3 ± 1.5^{5}	2.2 ± 0.3^{5}	1.4 ± 0.1^{5}
0728+40	6.7 ± 1.5^{4}	6.4 ± 0.7^{1}	3.1 ± 0.2^{1}	2.5 ± 0.3^{5}	1.6 ± 0.3^{1}	1.9 ± 0.3^{5}	0.83 ± 0.06^{5}	–
0837+36	50.4 ± 1.6^{4}	30.2 ± 2.3^{2}	12.1 ± 0.8^{1}	12.5 ± 0.1^{6}	13.0 ± 0.4^{2}	3.3 ± 1.3^{6}	2.2 ± 0.5^{6}	1.3 ± 0.2^{6}
0957+23	93.7 ± 2.4^{4}	78.7 ± 1.1^{1}	48.5 ± 1.2^{1}	53.2 ± 0.5^{5}	39.8 ± 1.2^{1}	31.4 ± 0.7^{5}	22.4 ± 0.3^{5}	9.8 ± 0.9^{5}
1053−00	13.6 ± 1.6^{4}	15.7 ± 0.6^{1}	11.8 ± 0.4^{1}	13.1 ± 0.1^{5}	12.3 ± 0.6^{1}	8.2 ± 1.6^{5}	5.9 ± 0.7^{5}	2.3 ± 0.7^{5}
1159+01	133.9 ± 2.0^{4}	137.8 ± 1.7^{1}	158.0 ± 2.0^{2}	160.8 ± 1.2^{5}	150.6 ± 3.7^{2}	123.8 ± 1.6^{5}	105.5 ± 1.1^{5}	74.6 ± 2.1^{5}
1213+01	23.0 ± 1.7^{4}	15.2 ± 0.5^{1}	9.7 ± 0.3^{1}	11.6 ± 0.1^{5}	8.2 ± 0.5^{1}	5.6 ± 1.4^{5}	3.6 ± 0.5^{5}	1.4 ± 0.2^{5}
1228−01	19.4 ± 1.6^{4}	18.6 ± 0.5^{1}	15.5 ± 0.4^{1}	16.9 ± 0.2^{5}	13.5 ± 0.7^{1}	11.5 ± 1.6^{5}	8.1 ± 0.2^{5}	2.5 ± 0.7^{5}
1312+23	28.9 ± 1.6^{4}	25.7 ± 0.6^{1}	19.8 ± 0.5^{1}	19.4 ± 0.2^{5}	16.1 ± 0.6^{1}	10.5 ± 0.3^{5}	7.7 ± 0.1^{6}	5.4 ± 0.4^{6}
1413+42	7.6 ± 2.9^{4}	8.8 ± 0.7^{2}	13.4 ± 0.3^{2}	13.4 ± 0.1^{6}	12.7 ± 0.4^{2}	9.5 ± 1.5^{6}	7.0 ± 0.2^{6}	2.2 ± 0.4^{6}
1603+30	22.8 ± 1.7^{4}	26.1 ± 0.7^{1}	19.1 ± 0.5^{1}	22.1 ± 0.3^{5}	16.8 ± 0.6^{1}	12.5 ± 1.7^{5}	8.3 ± 0.1^{5}	1.9 ± 0.5^{5}
1624+37	33.5 ± 1.6^{4}	23.3 ± 1.1^{0}	–	15.0 ± 0.1^{0}	10.5 ± 0.8^{0}	9.6 ± 0.6^{5}	5.41 ± 0.02^{0}	2.1 ± 0.3^{5}
1625+48	17.6 ± 1.5^{4}	9.4 ± 0.7^{2}	8.0 ± 0.2^{2}	7.0 ± 0.2^{5}	6.3 ± 0.2^{2}	5.8 ± 1.3^{5}	1.9 ± 0.3^{5}	1.7 ± 0.2^{5}

5.3.2 Morphologies

The FIRST maps at 1.4 GHz show a compact morphology for all 15 BAL QSOs in the RBQ sample, at a resolution of ~ 5 arcsec. To quantify this we have computed the morphological parameter Θ, based on the FIRST integrated and peak flux densities, $\Theta = \log(S_{int}/S_{peak})$, and for all 15 sources $\Theta < 0.03$. All sources, with the exception of 1053−00, appear essentially point-like at this resolution. The FIRST map of 1053−00 is shown in Figure 5.2 where a point-like core and two faint components (5- and 8-σ detections) can be seen. The faint components seem to be real and this source has been included in the catalogue of double-lobed radio quasars from SDSS (de Vries et al. 2006). This is thus an additional example of the rare class of BAL QSOs showing double-lobed morphology, and it is not included in the list of 8 SDSS BAL QSOs of this type compiled by Gregg et al. (2006).

Our VLA maps at higher frequencies confirm the compactness of the 15 BAL QSOs, having all of them point-like structure at 8.4 and 15.0 GHz. The faint components of 1053−00 cannot be seen at these frequencies, probably due to a steep spectral index in these two regions.

The combination of the 43-GHz band with the A configuration provides the highest resolution available with the VLA ($\theta_{HPBW} \sim 50$ mas). However, as can be seen in Table 5.5 most sources are very faint at 43 GHz, i.e., close to the 1 mJy level. For those the self-calibration process is not appropriate and the way to recover the flux densities was to assume an initial point-source model before the first mapping. This procedure is to some extent well justified since at lower frequencies the morphology is still point-like, although the precise astrometric and morphological information about the sources at 43 GHz is lost.

Self-calibration at high frequency was only possible for the brightest sources: 0957+23, 1159+01 and 1312+23. The first two sources appear point-like in the 43-GHz maps. Figure 5.3 shows the naturally weighted maps of 1312+23 at 43 and 22 GHz, revealing an extension towards the north coming from the central unresolved component. Although the feature, possibly a jet, is detected at both frequencies, its significance is higher at 43 GHz.

The small feature in the 43-GHz map at ∼120 mas south from the central source is probably not real because it is located in a region affected by a stripe due to a sidelobe that could not be completely removed. It must be noticed that at this high frequency this flux density level is probably close to the limit where signal coherence allows accurate mapping. For the remaining 12 sources the mapping at 43 GHz was not possible and an upper limit on their sizes was obtained using the observations at 22 GHz ($\theta_{HPBW} \sim 80$ mas), where they are bright enough for mapping. For those, the task IMFIT was used to fit an elliptical Gaussian component and a zero level within a small box containing the radio source, yielding the major and minor axes of the fitted Gaussian, position angle and the formal beam-deconvolved dimensions. The uncertainty in the dimensions was estimated following Equation 1 of White et al. (1997). Eight of the twelve sources are clearly more extended than the beam size and their fitted parameters are given in Table 5.6. Also in this table the dimensions of 1312+23 and 1624+37 are shown, as measured from the map in Figure 5.3

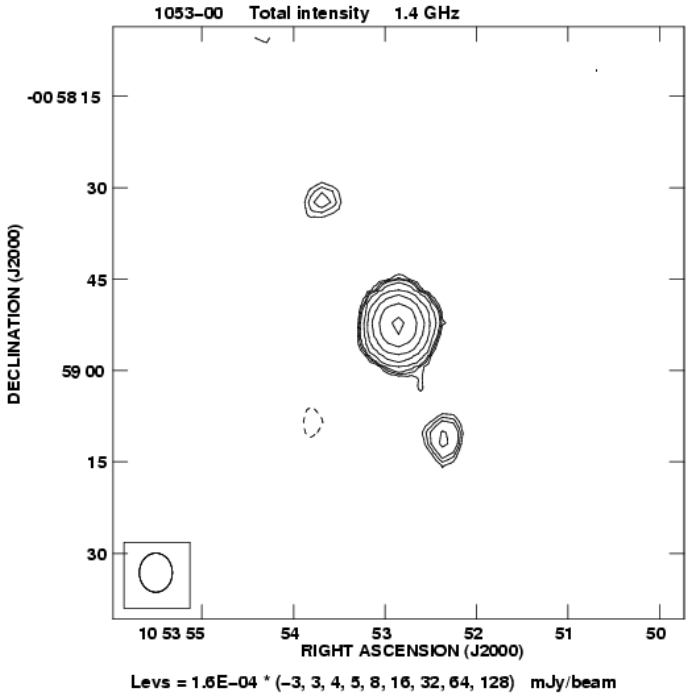

Figure 5.2: Map of BAL QSO 1053−00 from FIRST at 1.4 GHz. The synthesised beam-size is shown in the lower-left corner.

and from VLBA observations to be presented in Chapter 7, respectively. The remaining three sources (0039−00, 0256−01, 1053−00) plus 0957+23 and 1159+01 can be considered strictly unresolved at high frequencies.

VLBI observations of 0957+23 and 1312+23 have been presented by Jiang & Wang (2003) using the European VLBI Network at 1.6 GHz. With a restoring beam of only 18.5 × 6.86 mas, 0957+23 appears as a single point-like component, while 1312+23 is resolved. This last source shows a symmetric morphology with a central core and two components in the northern and southern directions with a total extension of ∼150 mas (i.e., about 1 kpc). Although an extended morphology is also present in our 22-GHz and 43-GHz maps (Fig. 5.3), only the northern part is detected.

Summarising, our VLA maps show very compact morphologies for all 15 sources at all frequencies, at a maximum resolution of 80 mas. The exceptions are 1053−00 (Figure 5.2), which is extended at 1.4 GHz showing two faint lobes not detected at higher frequencies and 1312+23 (Figure 5.3) which shows some elongation at 22 and 43 GHz.

5.3.3 Variability

We have checked for variability at 1.4 GHz comparing the flux densities from FIRST and NVSS epochs in those 14 sources with NVSS measurement. The same has been done at 8.4

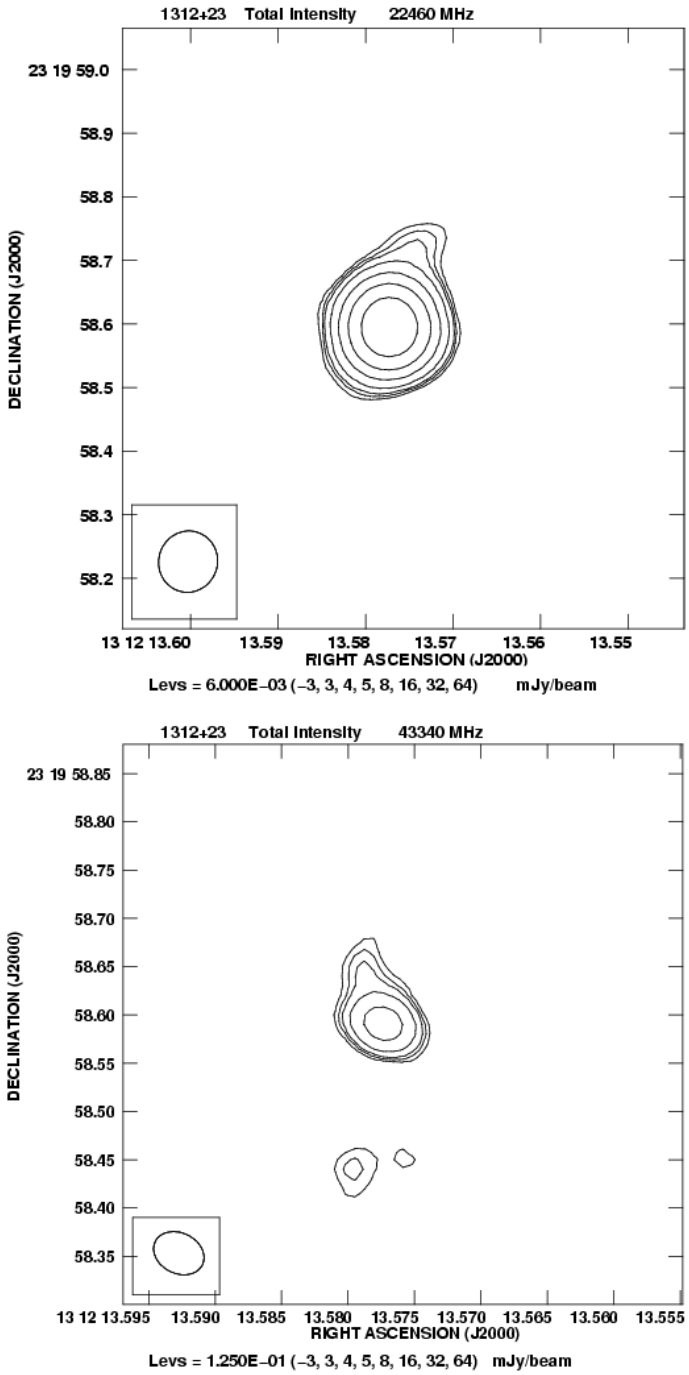

Figure 5.3: VLA map of BAL QSO 1312+23 at 22 GHz (top) and at 43 GHz (bottom). The synthesised beam-size is shown in the lower-left corner of each map.

Table 5.6: Angular dimensions for the extended sources. † Not deconvolved size, but measured from the extended structure in Figure 5.3. †† Measured from VLBA map at 4.8 GHz to be presented in Chapter 7.

Source	Freq. (GHz)	θ_{maj} (mas)	θ_{min} (mas)	PA (deg)	$\theta_{maj}^{(dec)}$ (mas)
0135−02	22	112.4	78.7	−12	11 ± 4
0728+40	22	85.5	73.0	26	26 ± 6
0837+36	22	94.0	85.9	34	19 ± 10
1213+01	22	111.7	75.5	−19	27 ± 11
1228−01	22	95.3	76.3	−30	19 ± 4
1312+23	43	54.5	41.8	64	69 ± 12†
1413+42	22	92.0	69.5	−60	9 ± 3
1603+30	22	95.8	71.0	−71	15 ± 3
1624+37	4.8	–	–	–	36 ± 5††
1625+48	22	157.0	71.8	76	63 ± 20

GHz for those 5 sources in common with the list of Becker et al. (2000). They observed these sources with the VLA in A and D configuration (resolutions of 0.8 and 9 arcsec respectively) and all 5 sources presented point-like structure at both resolutions. As mentioned before this is again confirmed by our observations at 8.4 GHz in A configuration. This means that flux densities of both measurements can be directly compared. The same is true at 1.4 GHz because all sources except 1053−00 are point-like at the resolution of FIRST (B configuration) and the resolution of NVSS is poorer (VLA D and CnB configurations). Although 1053−00 is resolved, it has a compact nucleus and the two extensions are not expected to contribute much to the total flux density (Section 5.3.2).

We measure the flux density variations with the parameter $Var_{\Delta S}$, as defined e.g. by Torniainen et al. (2005):

$$Var_{\Delta S} = \frac{S_{max} - S_{min}}{S_{min}} \tag{5.3}$$

As an estimate of the significance of the source variability the σ_{var} parameter defined by Zhou et al. (2006) is used, adopting the *integrated* flux densities S_1 and S_2 at the two epochs:

$$\sigma_{Var} = \frac{|S_2 - S_1|}{\sqrt{\sigma_2^2 + \sigma_1^2}} \tag{5.4}$$

where σ_2 and σ_1 are the uncertainties in the integrated flux densities. Table 5.7 shows flux densities, $Var_{\Delta S}$ and σ_{Var} at 1.4 and 8.4 GHz, for those sources exhibiting $\sigma_{Var} > 3$. For the flux densities of Becker et al. (2000), whose errors are not given in their work, a 5 per cent error is assumed.

Table 5.7: Sources showing significant flux density variability. At 1.4 GHz, S_1 comes from NVSS and S_2 from FIRST. At 8.4 GHz, S_1 comes from Becker et al. (2000), S_2 from this work (Table 5.5).

Source	Freq	S_1	S_2	$Var_{\Delta S}$	σ_{Var}
	GHz	mJy	mJy		
0256−01	1.4	22.3±0.8 D	27.5 B	0.23	3.2
1213+01	1.4	27.5±0.9 D	22.9 B	−0.20	3.2
1312+23	8.4	12.6 A	19.4±0.2 A	0.54	10.3
1413+42	8.4	11.3 D	13.4±0.1 A	0.19	3.7
1603+30	8.4	18.1 A	22.1±0.3 A	0.22	4.2

A low percentage of the sample (only 2 out of 14 sources) show variability at 1.4 GHz, both sources varying about 20 per cent with a significance just above 3 standard deviations. At 8.4 GHz, 3 out of 5 sources are variable at this level and 1312+23 constitutes the most extreme case, showing variations of about 50 per cent with significance above 10.

Flux density variations have recently been used to constrain the orientation of several BAL QSOs. Zhou et al. (2006) and later Ghosh & Punsly (2007) found a few examples of BAL QSOs with variability as high as 40 per cent at 1.4 GHz between the NVSS and FIRST, i.e., in periods of about 1-5 years. These variations were high enough to make the brightness temperature T_B exceed the 10^{12} K limit associated to the Compton catastrophe. This was interpreted as a sign of beaming and the jet was supposed to be oriented at a few degrees from the line of sight.

The same procedure can be applied to 0256−01 and 1213+01, accepting the 3-σ significance as real. Following the formalism in Ghosh & Punsly (2007) and knowing that the time differences between the NVSS and FIRST observations are 2.1 and 3.4 years, respectively, the observed variations imply brightness temperatures of T_b=3.1·10^{13} K for 0256−01 and 1.3·10^{13} K for 1213+01. These translate into upper limits for the jet orientation angle with respect to the line of sight of ∼20 and 25 deg, respectively.

One concern about this approach is that it is based on variability at a single frequency and from only two measurements. Moreover, the flux densities we obtained for 0256-01 at 8.4 GHz, with Effelsberg and almost one year later with the VLA, show a good match, i.e., (7.2 ± 0.3) and (7.2 ± 0.4) mJy respectively, in contradiction to the expected stronger variability at high frequencies.

5.3.4 Shape of the radio spectra

Sample of radio BAL QSOs

Figure 5.4 show the spectra of the 15 objects. Many of them have a relatively steep spectrum at high frequency. About 75 per cent of the sample show flattening or inversion of the spectrum at low frequencies (typically below 1-5 GHz) which could indicate synchrotron self-absorption. However, in some cases some variability cannot be excluded, since the 1.4-GHz measurements were taken some years before the others. About 1/3 of the sample

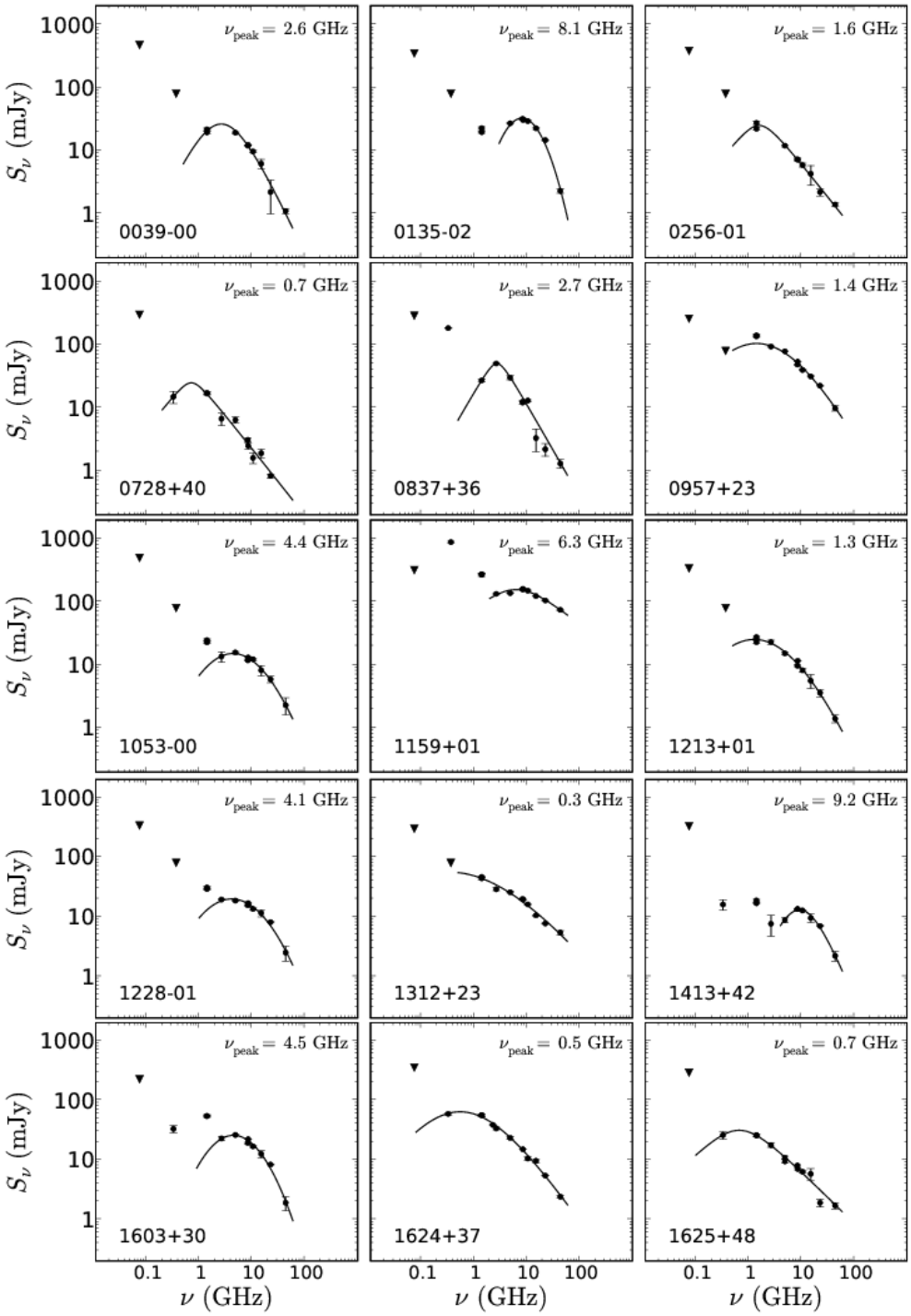

Figure 5.4: Radio spectra of the 15 BAL QSOs in the RBQ sample. Errors are shown if larger than the symbol size. Triangles mean 3-σ upper limits. Solid lines are fits to the analytical function give in Section 5.3.4. The peak frequencies given at the top-right of each panel were obtained from the fit. Some sources like 1159+01, 1413+42 and 1603+30 seem to have a second component at low frequencies.

show, in addition, enhanced emission at MHz frequencies which could be indications of a second component emitting mostly in this range. Again, variability cannot be ruled out, but any possible time variability is expected to be less pronounced at lower frequencies. The source 1159+01 is the one which best fits in this category with both, a depression of the spectrum towards low frequency and a contribution from a second component in its spectrum.

Following the approach by Dallacasa et al. (2000), we have fitted each spectrum with the analytical function:

$$logS_\nu = a - \sqrt{b^2 + (c\ log(\nu) - d)^2} \tag{5.5}$$

where a,b,c,d are numerical constants. This function, presented in Dallacasa et al. (2000) was used by these authors to obtain the frequency turnover, $\nu_{\rm peak}$, of sources with convex spectra peaking above a few GHz, referred to in that paper as High Frequency Peakers. The value of $\nu_{\rm peak}$ approximately marks the frequency region where the source starts to be optically thick to synchrotron radiation.

These fits have been done excluding some points in order to obtain a reduced χ^2 below 0.05. This was possible for most of the sources which present a smooth radio spectrum, especially at high frequency, but not for 0728+40 ($\chi^2 = 0.08$) which presents a large scatter. At low frequencies, as we noted before, there are sources for which a possible second component arises. Again in these cases we decided whether to include or not in the fit these (low frequency) points trying to maintain the reduced χ^2 within the mentioned limit. An exception was done with 0957+23 because even if an acceptable χ^2 was obtained when including the 1.4-GHz flux densities, the resulting fit was not compatible with the 365 MHz upper limit.

In our sample we find 9 sources for which the spectrum peaks at a frequency higher than 1 GHz in the observer's frame and there are 4 displaying a peak in the range 300-700 MHz. For the remaining three objects (0256−01, 0957+23 and 1312+23) the spectrum is slightly convex but not does not show an obvious peak. However, a certain amount of flux density decrease is expected because the extrapolation to low frequencies of the power-law behaviour would not be compatible with the Texas upper limits. In these cases extrapolated peaks compatible with both the spectrum curvature and these upper limits have been determined. The peak frequencies have to be multiplied by (1+z) to obtain intrinsic peak frequencies.

In order to understand the global trends on the spectral shape of BAL QSOs, we compare in Figure 5.5 all the spectra bringing them first to the rest-frame in order to avoid the effect of the redshift. The rest-frame normalisation frequency was chosen to be 25 GHz. This is a compromise to choose a region representative of pure synchrotron emission, where neither synchrotron self-absorption nor synchrotron losses might be present in the majority of sources. This frequency also makes the dispersion of the normalised spectra relatively

small compared to other normalisation frequencies.

We see in Figure 5.5 a variety of spectral slopes around 25 GHz. There is one object in the sample which differs more strongly from the main trend, This is 1413+42 which has a spectrum with two components separated at 4 GHz (see Figure 5.4), and for this reason it shows in Figure 5.5 an inverted spectrum around the normalisation frequency. Apart from this object, and assuming that variability effects are not very important, Figure 5.5 reflects the rest-frame spectrum of a typical BAL QSO in the RBQ sample. It is in general convex, quite flat below 10 GHz, and becoming steeper around 25 GHz. About half of the objects become even steeper at frequencies higher than 50 GHz.

The spectral shape can be quantified by means of the spectral indices. Table 5.8 provides the turnover frequencies and representative spectral indices at different frequencies, both in the observer's and in the rest-frame. The spectral indices $\alpha_{0.365}^{1.4}$, $\alpha_{4.8}^{15}$ and $\alpha_{8.4}^{43}$ describe the low-, medium- and high-frequency regions. Moreover, the index $\alpha_{1.4}^{8.4}$ is shown for comparison with Becker et al. (2000). It is worth noting that the spectral indices $\alpha_{1.4}^{8.4}$ shown in Table 5.8 are *not* based on simultaneous observations, but as we previously have shown, variability might not be very important at this frequency, and in any case it only affects a small number of sources. In the rest-frame the indices $\alpha_{6.0}^{25}$, α_{12}^{25}, α_{25}^{50} and α_{50}^{100} are also given in Table 5.8.

Looking at the rest-frame spectral indices of BAL QSOs and Figure 5.5, we see on average a flattening below 10 GHz, which is probably due to synchrotron self-absorption, and an overall convex shape. The low-frequency flattening is reflected in the median α_6^{25}=−0.32, while the median α_{12}^{25} decreases to −0.57. The steepening at high frequency can be seen from the median α_{25}^{50} dropping to −0.92 and finally becoming steeper at higher frequencies with a median α_{50}^{100}=−1.24.

The radio spectral index is known to be a statistical indicator of the orientation of radio sources (Orr & Browne, 1982). Becker et al. (2000) found respectively two thirds and one third of the radio-loud BAL QSOs in their list with steep and flat spectral index. However, it is worth to note that they define the limit between flat and steep to be α=−0.5, and about one third of the sample has spectal index close to this value $-0.6 \leq \alpha \leq -0.4$. They suggest that this result is not consistent with BAL QSOs being oriented along a particular direction with respect to the line of sight to them. We find in our sample, which overlaps with that of Becker et al. (2000) in 5 objects, 60 per cent (9/15) of flat and 40 per cent of steep (6/15) spectrum sources, with 27 per cent of objects (4/15) being in the range $-0.6 \leq \alpha \leq -0.4$. These percentages are roughly consistent within the errors, which are large because the samples are relatively small.

Comparison with non-BAL QSOs

To further investigate the question of the orientation of BAL QSOs we want to compare in this paper the spectral index distribution of quasars in a pure BAL QSO sample with

Table 5.8: Turnover frequencies (in GHz) and spectral indices for the RBQ sample in the observer's frame (columns 2-6) and the rest frame (columns 7-11). The spectral indices in the observer's frame have been computed from each pair of observed flux densities while the rest-frame spectral indices are based on interpolation over the whole spectrum. Median values of the spectral indices are given in the last row.

	Observer's frame					Rest frame				
ID	S_{peak}	$\alpha_{0.365}^{1.4}$	$\alpha_{1.4}^{8.4}$	$\alpha_{4.8}^{15}$	$\alpha_{8.4}^{43}$	S_{peak}	$\alpha_{6.0}^{25}$	α_{12}^{25}	α_{25}^{50}	α_{50}^{100}
(1)	(2)	(3)	(4)	(5)	(6)	(7)	(8)	(9)	(10)	(11)
0039−00	2.60	–	−0.30	−1.01	−1.48	8.45	−0.32	−0.54	−1.21	−1.88
0135−02	8.15	–	0.18	−0.16	−1.59	22.90	+0.17	+0.18	−0.70	−2.26
0256−01	1.60	–	−0.75	−0.91	−1.01	5.50	−0.74	−0.80	−0.90	−1.28
0728+40	0.70	+0.08	−1.07	−1.08	–	1.15	−0.88	−0.75	–	–
0837+36	2.70	−1.35	−0.40	−1.96	−1.39	12.00	−0.09	−1.00	−1.30	−2.16
0957+23	1.40	–	−0.52	−0.81	−1.04	4.25	−0.51	−0.60	−0.91	−1.09
1053−00	4.40	–	−0.35	−0.58	−1.07	11.15	−0.14	−0.30	−0.94	−1.31
1159+01	6.30	−0.81	−0.29	−0.09	−0.47	18.90	−0.09	+0.22	−0.44	−0.48
1213+01	1.30	–	−0.35	−0.88	−1.30	4.90	−0.35	−0.61	−1.02	−1.20
1228−01	4.15	–	−0.31	−0.43	−1.17	15.10	−0.29	−0.12	−0.55	−1.12
1312+23	0.35	–	−0.45	−0.79	−0.79	0.85	−0.43	−0.58	−1.01	−0.57
1413+42	9.20	+0.07	−0.16	+0.07	−1.11	35.05	−0.23	+0.45	−0.06	−1.04
1603+30	4.50	+0.33	−0.50	−0.65	−1.51	13.50	−0.29	−0.16	−0.98	−1.73
1624+37	0.55	−0.03	−0.74	−0.79	−1.21	2.40	−0.71	−0.64	−0.99	−1.00
1625+48	0.65	−0.02	−0.72	−0.43	−0.87	2.45	−0.76	−0.81	−0.41	−1.69
Median:		−0.02	−0.40	−0.79	−1.14		−0.32	−0.57	−0.92	−1.24

that of a sample of non-BAL QSOs with the idea of interpreting possible differences with different orientations of both samples. In this comparison we will use the spectral range 1.4-8.4 GHz in the observer's frame and 6.0-25 GHz in the rest frame.

The list of non-BAL QSOs is that of Vigotti et al. (1997) presented in Section 5.1, but in all the following discussion we will restrict it to objects with z > 0.5. This restriction only reduces the total number of objects from 124 to 119. We have computed the spectral indices in the same way as in our sample, considering pairs of observed flux densities in the observer's frame and interpolating over the whole spectra in the rest frame. The spectral range covered by the non-BAL QSO sample goes from 74 MHz up to 10.5 GHz, and only those sources with z > 1.5 will reach 25 GHz in the rest frame.

As a BAL QSO sample we will add to our RBQ sample the list of Becker et al. (2000). They only provide flux densities in two frequencies, i.e., 1.4 and 8.4 GHz. Thus, combining these we end up with a combined sample of 38 BAL QSOs. These spectral indices can be found in Table 5.8 for objects in the RBQ sample, and in Table 2 of Becker et al. (2000) for the remaining objects.

The Vigotti et al. sample could in principle contain both BAL QSOs and non-BAL QSOs. However, a low contamination of BAL QSOs is expected. Becker et al. (2001) showed that in the radio-powerful regime the fraction of BAL QSOs is small. They used the definition of radio-loudness parameter R^* given by Stocke et al. (1992), i.e., the ratio of radio power at 5 GHz to optical luminosity at 2500 Å in the rest frame. In the regime of QSOs with $log(R^*) > 2$ they estimated a fraction of 4 per cent (< 1.5 per cent) of HiBAL (LoBAL) QSOs from the FBQS, in the interval of redshift [1.5,4.0] ([0.5,1.5]) where the C IV (Mg II) absorbing features would be covered in optical spectra.

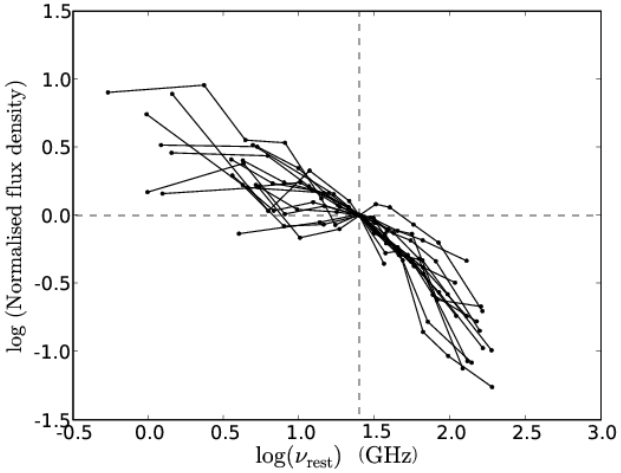

Figure 5.5: Rest-frame spectra of 15 BAL QSOs in the RBQ sample. They have been normalised to ν_{rest}=25.0 GHz (log(ν_{rest})=1.398)

We have calculated $log(R^*)$ for all quasars in Vigotti's list. For this purpose, the radio luminosity at 5 GHz has been computed on the basis of the observed radio spectra, applying the appropriate K-correction interpolating between each pair of observed frequencies with the adequate spectral index. The optical luminosities at 2500 Å were computed using the POSS-I APM E magnitudes published in Vigotti et al. (1997), but corrected from Galactic extinction following the maps of Schlegel et al. (1998) and assuming an optical spectral index of $\alpha_{opt} = -1$ ($S_\nu \propto \nu^\alpha$), which is the value adopted by Becker et al. (2001).

In Figure 5.6 the histogram shows how $log(R^*)$ ranges from 1.9 to 4.6. To estimate the fraction of BAL QSOs following the mentioned proportions, we split this sample in two groups, one with $0.5 < z \leq 1.5$ and the other with $z > 1.5$, comprising 80 and 44 quasars respectively. About 1-2 HiBAL QSOs are expected in the high-z subsample and about 1 BAL QSO in the low-z subsample.

We made use of the NASA Extragalactic Database (NED) and the SDSS-DR6 database to look for the optical spectra of QSOs from Vigotti et al. (1997) and check whether they are BAL QSOs. From 119 objects with $z < 0.5$, 55 were found in the SDSS-DR6 database. These were visually inspected to look for the presence of BAL features. All of them are non-BAL QSOs and only one of them (SDSS J080016.09+402955.6, associated with the radio source B3 0756+406) shows some broad absorption component bluewards of the C IV emission line, also present in Si IV. This absorption has a width of $\sim$ 1,000 km s^{-1} and it is located within 3,000 km s^{-1} from the line emission. It is therefore better classified as a mini-BAL or a Narrow Absorption Line (NAL) system (see Figure 5.7).

We searched for the remaining 64 spectra in the NED and found 14 of them in different publications, most of them in Vigotti et al. (1997) and Lahulla et al. (1991). From these

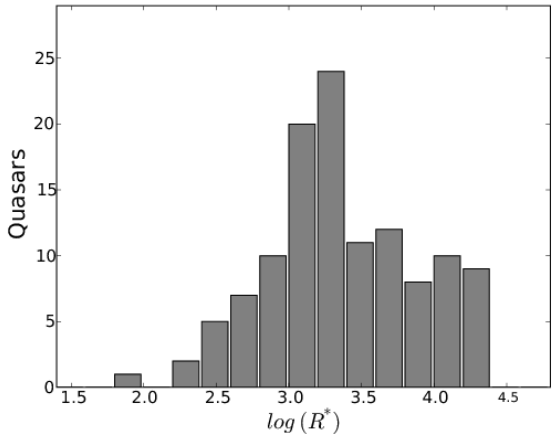

Figure 5.6: Histogram of radio-loudness parameter R^* as defined by Stocke et al. (1992) for the sample of Vigotti et al. (1997).

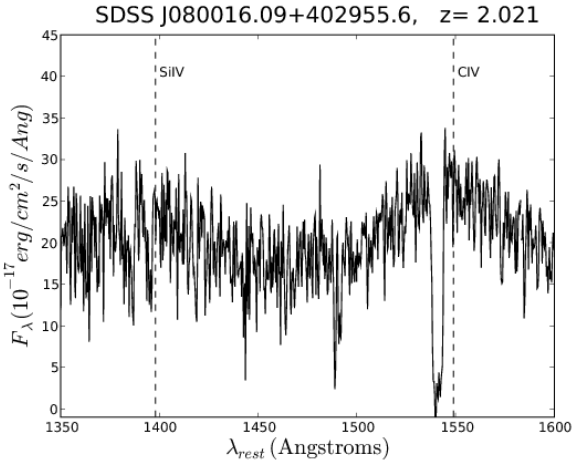

Figure 5.7: Spectrum of SDSS J080016.09+402955.6, showing a relatively narrow absorption in C IV and Si IV.

14, only 4 could be identified as normal QSOs without BALs: B3 0034+393 with z= 1.94 (Osmer et al. 1994); B3 0219+443 with z=0.85 (Djorgovski et al. 1990); B3 0249+383 with z=1.12 (Henstock et al. 1997) and B3 2351+456 with z=2.00 (Stickel & Kühr 1993). The other 10 are difficult to classify because they are either faint, with low signal-to-noise ratio in the continuum (just good enough for a correct redshift identification), or the wavelength coverage does not include the region where the absorbing troughs could be present. Summing up, 59 out of 119 QSOs (roughly half of the sample) were inspected, with no one clearly showing the BAL phenomenon. These results justify the assumption that the list of Vigotti et al. (1997) can be used as a representative sample of non-BAL quasars.

Table 5.9 summarises the number of elements and the basic statistics on the spectral index for the samples under comparison. Since BAL QSOs are compact objects as Becker et al. (2000) discovered and is confirmed by us, we will also consider in our comparison a subsample of non-BAL QSOs extracted from Vigotti et al. (1997) which includes only those compact sources with angular sizes < 0.5 arcsec at 1.4 GHz. The angular sizes at 1.4 GHz in Vigotti's sample were measured from maps taken with the VLA in C and D configurations (Vigotti et al. 1989) and for the most compact sources from observations in A configuration (priv. communication).

The first four rows in Table 5.9 show that non-BAL QSOs have a median $\alpha_{1.4}^{8.4}$ lower than BAL QSOs (-0.92 and -0.53, respectively). The conclusion could be that BAL QSOs tend to have flatter spectra and are, on average, oriented at a lower angle with respect to the line of sight than normal QSOs. On the other hand, when the non-BAL QSOs sample is restricted to compact objects only, the median spectral index becomes -0.49, very similar to that of BAL QSOs. When the full sample of non-BAL QSOs is considered, those extended objects have a higher contribution of emission produced in the lobes, which translates into steeper spectral indices for non-BAL QSOs. A similar behaviour can be found when analysing the rest-frame spectral indices α_{12}^{25} and also α_{6}^{25} although in this last case the median values for BAL QSOs and compact non-BAL QSOs are more distant, i.e. -0.32 and -0.47 respectively.

A Kolmogorov-Smirnov (K-S) test has been done in order to compare the $\alpha_{1.4}^{8.4}$ spectral index distributions of these samples. The test yields a probability $P < 0.001$ that both distributions are statistically equal, confirming that they are indeed different populations. A similar K-S test restricted to only compact sources from Vigotti et al. (1997) yields $P = 0.204$ which is consistent with both samples having a similar distribution. The percentile plot in the upper panel of Figure 5.8 illustrates the shape of the spectral index distribution of these three samples. It can be seen that the important contribution of extended sources from Vigotti et al. (1997) makes the percentile curve rise more rapidly than in the other samples. This result essentially means that the differences in spectral indices between BAL and non-BAL QSOs arise only because BAL QSOs are compact sources, while normal QSOs include both compact and extended.

We will also compare the rest-frame spectral indices to look for possible intrinsic variations between BAL and non-BAL QSOs, once the redshift effect has been corrected for.

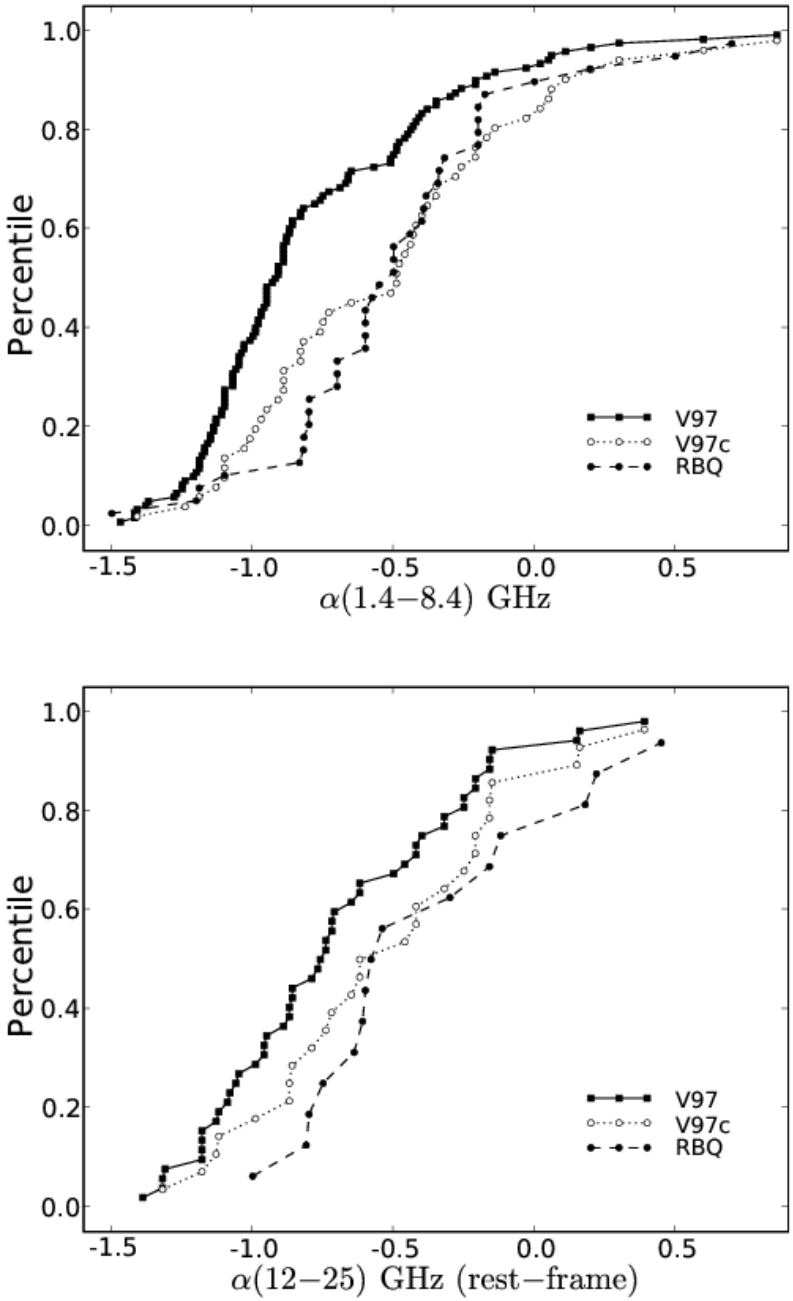

Figure 5.8: Percentile plot of the samples involved in the K-S tests, illustrating the shape of the spectral index distributions.

Table 5.9: Statistics on spectral indices. B00: Becker et al. (2000); V97: Vigotti et al. (1997); V97c: sources from Vigotti et al. (1997) with sizes <5 arcsec at 1.4 GHz.

Sample	N	Min	Max	Mean	Median	Std
Observer's frame: α [1.4 − 8.4] GHz						
RBQ+B00	38	−1.50	0.70	−0.50	−0.53	0.43
RBQ	15	−1.19	0.20	−0.52	−0.44	0.34
V97	119	−1.47	0.86	−0.80	−0.92	0.43
V97c	50	−1.41	0.86	−0.53	−0.49	0.49
Rest frame: α [6.0 − 25] GHz						
RBQ	15	−0.87	0.17	−0.38	−0.32	0.30
V97	51	−1.27	0.17	−0.71	−0.82	0.38
V97c	27	−1.21	0.17	−0.53	−0.47	0.40
Rest frame: α [12 − 25] GHz						
RBQ	15	−1.00	0.45	−0.40	−0.58	0.43
V97	51	−1.39	0.39	−0.71	−0.76	0.42
V97c	27	−1.31	0.39	−0.54	−0.62	0.44

The most reasonable comparison is using α_{12}^{25} where the effect of synchrotron self-absorption seems less pronounced. Two K-S tests have been done comparing these samples. The first compares Vigotti's sources and RBQ yielding P = 0.048, while the second compares only the compact sources in Vigotti et al. (1997) and RBQ, yielding P = 0.629. Again we can talk about statistically different populations when all QSOs are included in the comparison, but not when only spectral indices of compact sources are compared. The percentile plot is shown in the lower panel of Figure 5.8.

Even if the previous statistical tests are consistent with similar spectral index distributions for BAL QSOs and non-BAL compact sources, it is interesting to note in Figure 5.8 that there might be a small deficit of steep sources among BAL QSOs with spectral index ~ -0.7, compared to the compact sources in Vigotti et al. (1997). This effect is more marked in the upper panel, but also insinuated in the lower panel where, nevertheless, the number of objects is significantly smaller.

5.3.5 Polarisation

The RBQ sample was searched in the NVSS database looking for polarised emission and only one BAL QSO, 1159+01, shows a high amount of linear polarisation at 1.4 GHz. For the rest of the sources only upper limits could be established typically below 1.5 per cent at this frequency.

At higher frequencies and up to 43 GHz we have measured the S_Q and S_U parameters as explained in Section 3, in order to obtain the degree of linear polarisation, m, and the polarisation angle χ. Table 5.10 shows the fractional polarised intensity, mostly upper limits, for the BAL QSOs in the RBQ sample. The only sources which are clearly polarised showing significant m at various frequencies are 1159+01 and 1624+37. These sources are presented

Table 5.10: Degree of polarisation, m_ν (in percentage), at several frequencies, ν (in GHz), for the RBQ sample. Most of the values are 3-σ upper limits and those showing a measured value can have a relatively large error but come from an at least 3-sigma detection in Stokes Q or Stokes U. The BAL QSOs 1159+01 and 1624+37 presented separately (see Table 5.11 in this paper and Table 2 from Benn et al. 2005) are the only two sources with significantly detected polarisation.

ID	$m^a_{1.4}$	$m_{2.6}$	$m_{4.8}$	$m_{8.3}$	$m_{8.4}$	$m_{10.5}$	m_{15}	m_{22}	m_{43}
(1)	(2)	(3)	(4)	(5)	(6)	(7)	(8)	(9)	(10)
0039−00	< 1.59	–	< 3.8	< 14.5	< 0.67	<24.8	<10.5	<14.7	< 8.3
0135−02	< 1.26	–	< 3.1	< 5.0	< 0.87	< 8.6	3.9±4.0	< 1.7	< 7.4
0256−01	< 1.41	–	< 4.5	< 26.4	< 3.9	<16.4	< 1.7	<22.7	< 7.2
0728+40	< 1.17	–	<17.5	< 30.7	< 10.1	–	<10.9	< 5.1	–
0837+36	–	< 27.9	< 2.2	< 6.9	< 0.6	<16.4	<27.8	<15.2	<10.1
0957+23	< 1.23	–	< 0.7	< 1.8	< 0.5	< 3.4	< 0.9	2.0±1.4	< 5.6
1053−00	< 1.29	–	< 4.2	< 18.1	1.3±1.0	<20.8	<12.8	< 7.3	<22.1
1213+01	< 1.29	–	< 5.4	< 13.7	< 0.5	<37.1	<19.0	< 9.9	< 7.3
1228−01	< 1.35	–	< 4.3	< 10.7	< 0.5	<24.6	<10.9	< 1.0	<23.7
1312+23	< 1.17	–	< 2.5	< 8.2	2.7±0.7	<16.2	< 1.5	3.6±2.3	< 6.5
1413+42	< 1.26	–	< 6.7	< 8.9	< 0.5	<15.5	<10.2	< 1.1	< 9.5
1603+30	< 1.32	< 19.3	< 2.4	< 5.8	1.0±1.0	<14.0	<11.2	< 0.8	<19.3
1625+48	< 1.08	< 24.0	< 6.4	< 7.4	< 4.9	<16.6	<19.9	<19.8	17.6±14.0

[a] Degree of linear polarisation at 1.4 GHz extracted from the NRAO VLA Sky Survey, NVSS (Condon et al., 1998).

in different tables (Table 5.11 in this paper and Table 2 from Benn et al. 2005). These two are the only bright sources displaying relatively high (i.e., > 10 per cent) polarised intensity at some frequency. In fact, 1159+01 shows $m_{1.4}$ = 15 per cent and 1624+37 shows with $m_{10.5}$ = 11 per cent. Apart from these, also the weak source 1625+48 with only 1.7 mJy at 43 GHz shows m_{43} ∼18 per cent but this measurement is based on a $\gtrsim$ 3-σ detection in S_U and the uncertainty in this measurement is high. From the remaining sources in Table 5.10, 1312+23 shows significant polarisation at 8.4 and 22 GHz, and there are 5 more sources with significant detections at only one frequency, in all cases below 4 per cent.

It should be noted from Table 5.10 that the most stringent upper limits are given by the VLA observations at 8.4 GHz. At this frequency the sources are bright enough to have reliable detections and the relatively low noise achieved facilitates the determination of reasonable upper limits for the non-detections. At higher frequencies this is more difficult because the total power spectra drops down to fainter levels.

At 8.4 GHz, one third of the sample (i.e, 5 out of 15) show at least a 3-σ detection in S_Q, S_U or both. From these 5 BAL QSOs only 1624+37 is strongly polarised showing 6.5 per cent of linearly polarised flux density (Benn et al. 2005). The fractional polarised intensity in the other four objects (1053−00, 1159+01, 1312+23 and 1603+30) is below 3 per cent. The upper limits for most of the 10 undetected sources are below 1 per cent indicating strong depolarisation.

For 1159+01 and 1624+37 the determination of the Rotation Measure, RM, ($\chi = \chi_0 + RM \cdot \lambda^2$) is possible fitting a slope to the polarisation angles χ_i as a function of the square of the observed wavelengths. Benn et al. (2005) already reported for 1624+37 a RM of

Table 5.11: Polarisation properties of BAL QSO 1159+01. The second measurement at 2.65 GHz comes from Simard-Normandin et al. (1981).

Frequency (GHz)	Telescope	m (per cent)	χ (deg)
1.40	NVSS	15.03 ± 0.44	−31.1 ± 0.6
2.65	Effelsberg	<16	–
2.65	–	3.1 ± 1.9	111 ± 17
4.85	Effelsberg	2.1 ± 0.2	−42 ± 6
8.35	Effelsberg	0.95 ± 0.05	−29 ± 5
8.45	VLA	0.9 ± 0.4	−29 ± 7
10.5	Effelsberg	<1.2	–
15.0	VLA	<1.2	–
22.5	VLA	<0.4	–
43.5	VLA	<1.2	–

(−990 ± 30) rad m^{-2}, which in the rest-frame translates into the extremely high intrinsic Rotation Measure, RM = (−18350 ± 570) rad m^{-2}. For 1159+01 we have fitted the angles χ_i in Table 5.11. Our observations give a poor upper-limit at 2.65 GHz, but an additional measurement at this frequency was obtained by Simard-Normandin et al. (1981). We get a best fit with a RM = (−72.1 ± 1.4) rad m^{-2} and an intrinsic polarisation angle χ_0 = (−24 ± 3) deg. This observed value should be corrected by the RM introduced by our own Galaxy, which is quite difficult to estimate. To have a rough estimate we have inspected the all-sky map presented by Wielebinski & Krause (1993) where the RMs of 976 extragalactic sources are plotted. The neighbouring sources around the position of 1159+01 have small RMs (i.e., |RM| < 30 rad m^{-2}), which suggests that the Galactic contribution might be smaller than the determined value. Assuming no Galactic correction, the fitted RM brought to the rest-frame would be higher by a factor (1+z)^2 becoming RM = (644 ± 12) rad m^{-2}.

5.4 Discussion

The morphologies and dimensions of the radio sources in BAL QSOs seem to be the keys to understand the orientation and evolutionary status of these sources. There is evidence that BAL QSOs are associated with compact radio sources, which are supposed to constitute a high fraction of the young population of radio sources, like e.g., CSS or GPS sources. Becker et al. (2000) noted that 90 per cent of their sample of radio-loud BAL QSOs (extracted from the FBQS survey) present point-like structure at the resolution of 5 arcsec in contrast to the diversity of both point-like and extended sources they found within the whole population of FBQS quasars. In fact, only a few BAL QSOs are known to have an extended FR II radio structure (Gregg et al. 2006). Our 22-GHz observations of the RBQ sample confirm this tendency, because most sources appear unresolved at all frequencies constraining their apparent dimensions up to $\lesssim$ 0.1 arcsec. This translates into projected linear sizes (LS) $\lesssim$ 1 kpc which are typical of GPS/CSS sources. It could be argued that an extended component with a steep spectrum might be present, observable only at lower frequencies, and thus being the source sizes larger than those found at high

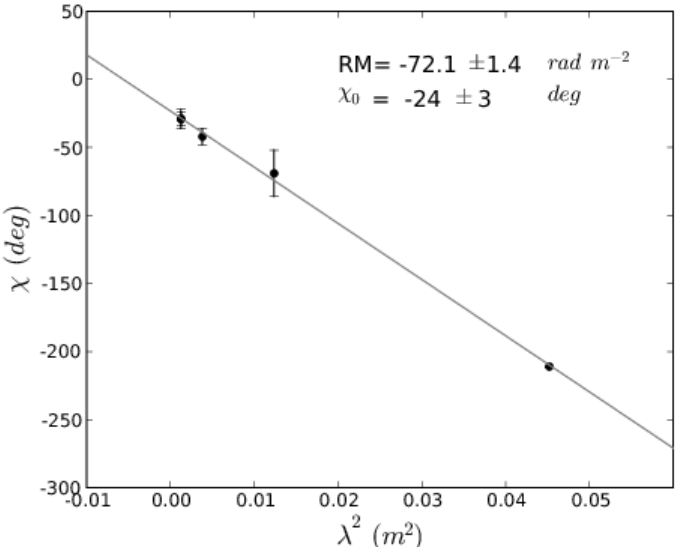

Figure 5.9: Determination of the RM for 1159+01.

frequencies. This hypothesis is *a priori* not supported by the fact that most sources are still point-like at 1.4 GHz as can be seen in the FIRST maps, with the exception of 1053−00.

The radio spectra in Figure 5.4 also display the typical convex shape of GPS-like sources, in most cases with a peak at $\sim 0.5-10$ GHz suggested by at least one or two points, or by upper limits at MHz frequencies. One concern about this result is that FIRST or WENSS flux densities were observed at different epochs and variability might be an issue, although noticeable flux density variations are likely to be stronger in the optically thin region of the spectrum. However, relatively deep integrations at MHz frequencies would be desirable to better constrain the shape of the spectra at low frequency. In addition, a project with VLBI multi-frequency observations and the analysis on the pc-scale properties of several BAL QSOs of the RBQ sample has been started by us, and results will be presented in Chapter 7.

If radio sources associated with BAL QSOs are actually CSS/GPS sources, they should follow the anticorrelation between intrinsic turnover frequency and projected linear size found by Fanti et al. (1990) for CSS sources. This was, for instance, quantified by O'Dea & Baum (1997) in a combined sample of CSS and GPS sources compiled by Fanti et al. (1990) and Stanghellini (1992), respectively. This relationship was found to be valid for both galaxies and quasars. The anticorrelation suggests that the mechanism producing the turnover simply depends on the source size. Figure 5.10 shows the relationship between intrinsic ν_{peak} and projected LS for the samples of CSS and CPS sources mentioned before, and we have also plotted for comparison our sample of radio-loud BAL QSOs. The turnover frequencies for the BAL QSOs appear in Table 5.8 while projected linear sizes have been extracted from the deconvolved sizes in Table 5.6.

A group of 5 BAL QSOs match quite well the distribution of CSS/GPS sources, and they all show simple convex spectra, i.e., 0728+40, 1213+01, 1312+23, 1624+37 and 1625+48. The three additional BAL QSOs displaying simple convex spectrum, 0039−00, 0256−01 and 0957+23 are unresolved in our observations and their position can only be constrained by upper limits. Nevertheless these 8 sources with simple complex spectrum are consistent with the correlation.

From the remaining 7 objects, 5 are resolved in our observations (0135−02, 0837+36, 1228−01, 1413+42 and 1603+30) and are located above the cloud of CSS/GPS sources. All of them have in common a complex spectrum with indications of a double component. In these sources the turnover has been determined using the high frequency component but in the spectra of 1413+42 and 1603+30 a fit to a second peak at lower frequencies (at 0.7 and 0.8 GHz respectively) can be fitted. A second peak at low frequency could also be fitted to 1159+01 but we will not do that because this source is unresolved and we cannot give anyway the exact location in the diagramme. When considering the low frequency peaks of 1413+42 and 1603+30 in the diagramme, these two sources also agree very well with the anticorrelation as shown in Figure 5.10. This better agreement could mean that the high-frequency part of these spectra could be dominated by the emission coming from a compact and active (possibly beamed) region smaller than the entire source, like a hot-spot. Unfortunately we do not have enough data to check whether this could be the case also for 0135−02, 0837+36 and 1228−01. Low-frequency data will be important to sample this part of the spectra to search for a possible second peak. Again, VLBI observations are crucial to further investigate this interpretation.

In fact, it has been shown that some GPS sources associated with optical QSOs can be just normal flat-spectrum quasars for which a jet/knot/hot-spot dominates the spectrum, which then adopts the characteristic convex shape of a GPS source, as discussed e.g. by Snellen et al. (1999). Recently Stanghellini et al. (2005) and Orienti et al. (2006) have studied VLBI samples of GPS sources and High Frequency Peakers (HFP, 5 GHz $< \nu_{\rm peak} <$ 10 GHz) confirming this scenario. In fact, these "contaminant" quasars seem to be present, even in high percentages, in many well-defined samples of GPS sources (Torniainen et al. 2005). Two characteristics of "genuine" young GPS radio sources are low polarisation and low variability (O'Dea, 1998), while flat-spectrum quasars show higher polarisation and variability.

Torniainen et al. (2005), who have used an extensive database of sources with multifrequency data from several long-term variability programs, define as "bona fide" GPS sources those with a maximum variability $Var_{\Delta S} < 3$. From our comparison in Section 5.3 which is, of course, based on only two epochs we see that many sources do not show significant variations at 1.4 GHz, and 3 out of 5 inspected at 8.4 GHz show significant but not very strong variations. Thus we cannot exclude these sources from the candidates to young sources. As also shown in Torniainen et al. (2005) the maximum variations are found at high frequencies, so multi-frequency multi-epoch observations of the RBQ sample will be very interesting for a more precise variability study.

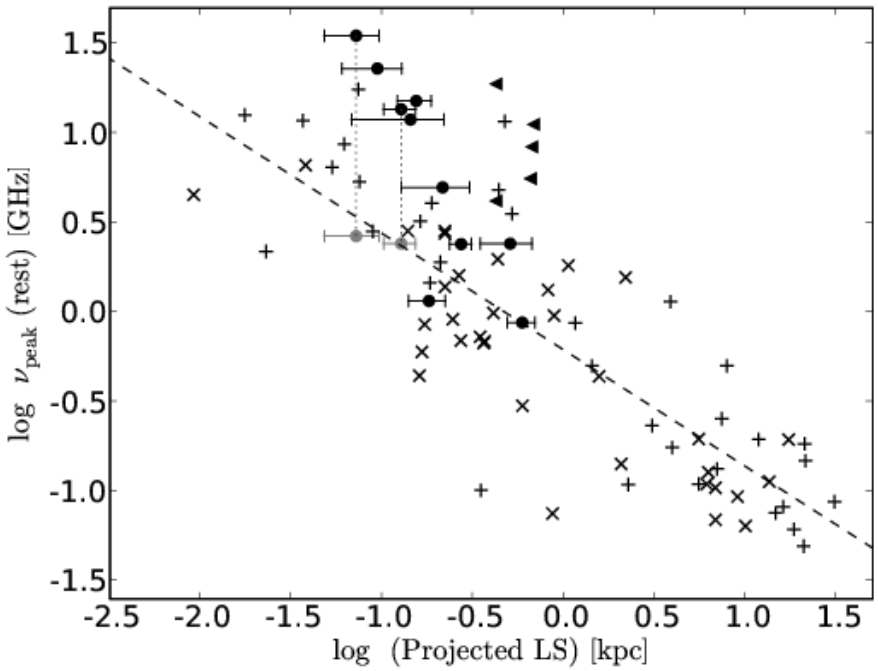

Figure 5.10: Rest-frame turnover frequency versus projected linear size relation for samples of CSS and GPS sources (adapted from O'Dea & Baum 1997). Galaxies are represented by the symbol '×', quasars by the symbol '+' and the RBQ sample is plotted as solid circles. Upper limits for those BAL QSOs unresolved at 22 or 43 GHz are marked by triangles. The dashed line represent the anticorrelation found by O'Dea & Baum (1997): $\log \nu_{peak} = -0.21 - 0.65 \log$ LS. In those two resolved sources with two peaks in the spectrum (1413+43 and 1603+30) the grey points indicate the new location in the plot when the lower frequency peak is considered.

Compact GPS sources are supposed to be completely embedded in their narrow line region. On this basis, Cotton et al. (2003) proposed the existence of a typical frequency-dependent scale, below which the GPS source becomes completely depolarised, the so-called "Cotton effect". Fanti et al. (2004) and later Rossetti et al. (2008) have confirmed this behaviour analysing the polarisation properties of the B3-VLA CSS sample (Fanti et al. 2001), and they propose models to describe the depolarising screen. The BAL QSOs in the RBQ sample have probably physical sizes of $\lesssim 1$ kpc and if Faraday effects are important they should be completely depolarised even up to relatively high frequencies. This is the case for all sources except 1159+01 at 1.4 GHz, and also for about 70 per cent of the sample at 8.4 GHz. At these two frequencies the upper limits obtained for the degree of linear polarisation are reasonably small. From Table 5.10 only 1312+23 seems to be weakly polarised at 8.4 and 22 GHz, but no polarisation was found at 15 GHz.

The two exceptions are 1159+01 and 1624+37. The first source is weakly polarised at 8.4 GHz but it is worth to note that the degree of linear polarisation increases as frequency decreases, becoming strongly polarised at 1.4 GHz. The opposite is expected when a depolarising plasma curtain is present. The reason for this anomalous behaviour might be that the emission at low frequencies arises from a different component, as suggested by the complex radio spectrum (see Figure 5.4). A hypothetical extended structure with a relatively ordered magnetic field would contribute with substantial linear polarisation, and this may only be detected at low frequencies if a steep spectral index is assumed for the emission of this extended component.

The moderate observed RM of (-72.1 ± 1.4) rad m^{-2} in 1159+01 is consistent with the fact that it is strongly polarised in the NVSS. Should the RM be much higher, the large bandwidth used for the NVSS observations would produce a strong bandwidth depolarisation effect, probably hiding any measurable polarised intensity. The extreme RM of J1624+37, RM $= -18350$ rad m^{-2} (Benn et al. 2005) which is the second highest value known among QSOs and the highest among BAL QSOs, seems to be an exception and not representative of the BAL QSOs family.

The median $m_{8.4}$ of the 5 polarised BAL QSOs in the RBQ sample is ~ 1.3 per cent, but the remaining 10 BAL QSOs show $m_{8.4} \lesssim 1$ per cent. As a comparison Saikia et al. (1987) found a median polarisation degree at 6 GHz of about 2 per cent in a subsample of quasars extracted from the sample of ∼400 compact sources of Perley (1982). Saikia et al. (1987) found no significant differences between the median value of flat-spectrum cores and CSS quasars whereas radio sources associated with galaxies or with empty fields (no optical identifications) were found to be less polarised at 6 GHz, with a median value of ~ 0.5 per cent. More recently, Stanghellini (2003) found a mean fractional polarisation of 1.2 and 1.8 per cent for GPS and flat-spectrum quasars, respectively, and $m < 0.3$ per cent for galaxies.

The sources showing some polarisation in the RBQ sample have probably polarised intensities consistent with flat-spectrum quasars. It is also likely that some of them (e.g., 1159+01 or 1603+30) can show polarised emission due to Doppler boosted knots in jets,

which is again compatible with their multi-component radio spectra peaking at high frequencies. However, our whole sample seems to be in better agreement with the GPS class than with the class of flat-spectrum quasars, because of the high percentage of unpolarised or weakly polarised sources. Of course, to firmly test this hypothesis it is particularly interesting to do polarimetric multi-frequency observations of a radio brighter sample, which is now available after the recent releases of SDSS. To this respect, we are currently collecting observations of the BAL QSOs in the SDSS-DR5 BAL QSO sample presented in Chapter 4, and results will be published in the near future.

As far as the spectral index distribution is concerned, the different statistical tests suggest that the spectral index distributions of BAL and non-BAL QSOs are different. This difference is however due to the fact that all BAL QSOs in the sample have compact structures, while non-BAL QSOs have both extended and compact morphologies. When comparing the samples of BAL QSOs and compact non-BAL QSOs, no significant differences are found in the spectral index distributions. Thus, from our comparison no preferred orientation can be attributed to BAL QSOs. When larger samples become available, the comparison of spectral indices of BAL and non-BAL QSOs as a function of radio power and UV luminosity will be possible, allowing us to look for particular orientations in different bins of luminosity, as has been suggested by Elvis (2000).

The majority of evidence collected in this chapter seems to favour an evolutionary scenario to explain the nature of radio BAL QSOs. In the following chapter it will be shown how all this evidence can be complemented by a synchrotron ageing analysis, from which we will derive approximate radiative ages for these sources.

6

Spectral ages of BAL QSOs

One of the main conclusions of the previous chapter is that radio sources associated with BAL QSOs share several characteristics with CSS and GPS radio sources. These are most likely, as explained in Chapter 3, young radio sources in the first stages of their evolution. This association fits well with the idea of an evolutionary scenario in order to explain the nature of BAL QSOs.

Synchrotron ageing analyses have been successfully used in the literature to estimate the radiative ages of radio sources. In particular, these analyses have been applied to CSS/GPS sources, revealing that these have been radiating for 10^3 to 10^5 years. These ages are consistent with estimates based on the separation of hotspots with time.

One can think on applying this same technique to our sample of BAL QSOs, since we have all the ingredients to perform this analysis. The high-frequency coverage of the radio spectra, up to 43 GHz, presented in Chapter 5 is essential to estimate the break frequency, which is directly related to the synchrotron age. In addition, the high-resolution VLA maps allow us to constrain the angular extension of these objects which is the minimum requirement in order to estimate their magnetic field, assuming equipartition conditions. Therefore, the main scope of this chapter is to estimate the radiative ages of the BAL QSOs in the RBQ sample, to check whether similar values as those obtained for young CSS/GPS radio sources can be derived.

6.1 Spectral ageing analysis

The theoretical framework on which the spectral ageing analysis is based was presented in Chapter 3. The idea is to fit the observed spectra of the BAL QSOs to different models describing in different ways the source evolution. These would be the KP model (Kardashev 1962; Pacholczyk 1970) and the JP model (Jaffe & Perola 1973), both based on a single particle injection that ceased in the past, and the CI model (Kardashev 1962) for which a continuum injection of the relativistic particles responsible for the radio emission is assumed. Following the discussion in 3.4.2, we will exclude the KP model in the following

analysis, since it has a less physical basis than the JP model.

Independently of the model, there are three free parameters in the fit, i.e. the spectral index of the injected particles, $\alpha_{\rm inj}$, the break frequency, $\nu_{\rm br}$ and the normalisation factor. The SYNAGE software developed by M. Murgia (e.g. Murgia et al. 1999) was used to fit the mentioned two models (CI and JP) to the BAL QSO spectra. The programme assumes an initial spectral index for the injected particles describing the pure-synchrotron region of the spectrum. At the same time, SYNAGE considers a second slope in order to fit the high frequency region of the spectrum, which depends on the model under consideration. In consecutive iterations, these slopes are progressively modified in order to minimize the χ^2 of the global fit, and $\nu_{\rm br}$ is obtained as the frequency where the two asymptotic slopes intersect.

The drop of the model emission at low frequency can be explained by synchrotron self-absorption and is the result of a consecutive fitting procedure driven in most cases by one or two measurements, or by an upper limit at MHz frequencies.

Since some kind of activity is expected to take place in these compact sources, we first tried to reproduce the spectra with a CI model. A few sources for which this model does not fit the spectra were best described by a JP model.

In all 15 sources from our RBQ sample, the break frequency was derived from the best-fitted model. In Figure 6.1 the spectra of the BAL QSOs and the models that best fit their shapes are presented. The curves describing the models at high frequency are not sharp as would be expected by a broken power law, but have been smoothed by SYNAGE in order to obtain a more realistic curve.

As seen in the previous chapter, some sources present complex spectra which suggest the presence of different components. In these cases, the component at higher frequency was fitted, and it has been plotted as a solid line in Figure 6.1. The possible component at lower frequency is described by a second tentative fit represented by a dotted line. A summary of the parameters obtained from the fits to each source is shown in Table 6.1.

According to Equation 3.14, the strength of the magnetic field has to be known in order to determine the synchrotron age. An estimate can be done assuming that the energy is equally distributed between the cosmic rays (protons and electrons) and the magnetic field. Under these equipartition conditions we can follow the revised formula of Beck & Krause (2005) (see Equations 3.11 and 3.13) to calculate the equipartition magnetic field from several observed quantities, i.e. the flux density S_0 at a certain frequency ν_0, the synchrotron spectral index, α, the angular dimensions of the radio source, θ_x and θ_y, an estimate of the source's extension along the line of sight, ℓ, and the redshift, z.

The first two quantities, ν_0 and S_0, should be selected from the region of the spectrum where neither synchrotron self-absorption (at low frequencies) nor synchrotron/inverse-Compton losses (at high frequencies) could be important, i.e., in a region between the spectral peak where the turnover takes place and $\nu_{\rm br}$ where radiative losses start to be-

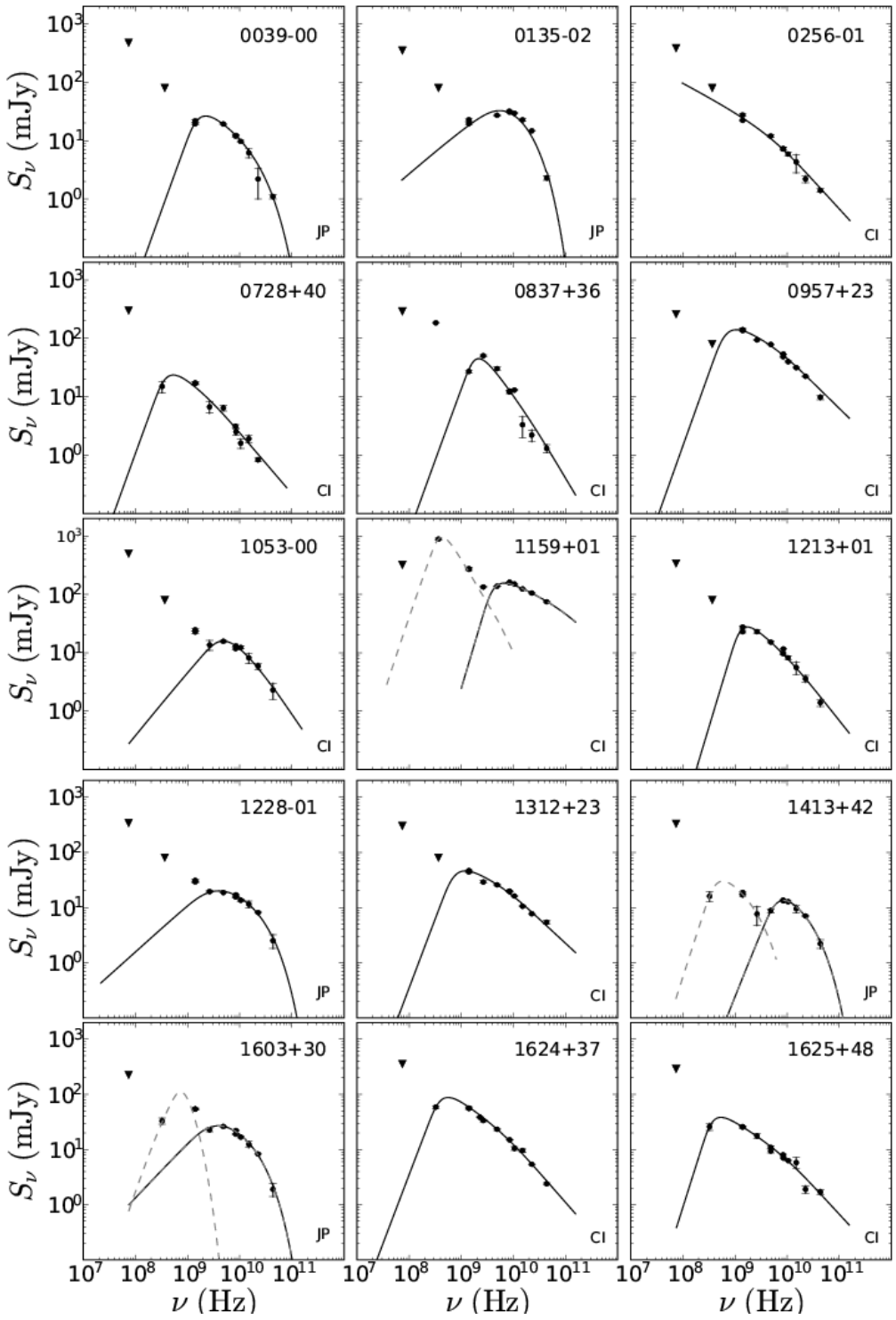

Figure 6.1: Radio spectra of the RBQ sample composed of 15 BAL QSOs. Points are flux densities and triangles mean 3-σ upper limits. The solid lines are fits to the synchrotron emission model specified in the lower right corner of each panel. In case of a second component this is suggested as a dashed line.

Table 6.1: Parameters from the SYNAGE fits.

ID (comp)	Best Fit Model	α_{inj}	ν_{br} [GHz]	ν_{br}(1+z) [GHz]	ℓ_k [kpc]	$B_{\rm eq}$ [μG]	τ_{syn} [kyr]	$v_{\rm exp}$/c
0039−00	JP	0.467	25.5	82.6	0.715	715	9.2	0.15
0135−02	JP	0.375	18.0	50.7	0.816	735	11.3	0.14
0256−01	CI	0.475	6.2	21.9	0.794	510	29.8	0.05
0728+40	CI	0.542	2.4	4.0	0.551	625	51.0	0.02
0837+36	CI	1.000	22.5	99.5	0.676	640	9.9	0.12
0957+23	CI	0.375	6.0	18.1	0.672	1260	8.4	0.14
1053−00	CI	0.809	26.6	67.9	0.856	570	14.4	0.11
1159+01	CI	0.375	94.1	281.3	0.892	1950	1.1	1.55
1213+01	CI	0.622	11.2	43.0	0.744	545	19.2	0.08
1228−01	JP	0.375	30.1	110.0	0.694	720	7.9	0.16
1312+23	CI	0.375	6.1	15.4	0.817	680	23.2	0.06
1413+42	JP	0.375	28.9	109.9	0.644	745	7.5	0.16
1603+30	JP	0.375	22.3	67.4	0.706	765	9.3	0.14
1624+37	CI	0.577	7.8	34.1	0.368	1055	8.0	0.09
1625+48	CI	0.521	9.3	34.3	0.921	480	26.1	0.08

come important. The synchrotron spectral index was chosen to be the local inclination (i.e., the slope in the log-log representation) of the model which better fits the spectrum at the suitable frequency ν_0. The beam size at 22 GHz from the VLA maps was used as an estimate of the sources' angular dimensions, to be considered as an upper limit. Since they are unresolved sources, a spherical symmetry is assumed and the beam size translated into linear dimensions is considered to be an estimate of the source's path length.

It can be seen in Table 6.1 that the derived magnetic field strengths are of the order of the milligauss, i.e. they range between 0.5 and 2 mG. In order to obtain the radiative age, the following step is to insert these values in Equation 3.14 together with $\nu_{\rm br}$, obtained from the fitting procedure. After the determination of the radiative ages, one can define a sort of typical expansion velocity (in units of the speed of light) dividing half the estimated size of the radio source by its synchrotron age $v_{\rm exp} \sim c\ell/2\tau_{\rm syn}^{-1}$. This expansion velocity only makes sense when the radiative age is indicative of the age of the source.

In five sources the model that best fit the spectrum is the JP model which has an exponential cut-off at high frequencies, while the rest are best described by a CI model. In the first group 1413+42 and 1603+30 are included, both sources displaying a possible second component at lower frequencies. The derived synchrotron ages range from 1 kyr to about 50 kyr which remind of the ages of young GPS sources.

According to the considered upper limits for the size of these objects, the expansion velocities have sensible values except in the case of 1159+01, for which a superluminal expansion velocity has been obtained. Apart from this source, an outlier in the distribution, the median expansion velocity of the sample is 0.12c.

6.2 Main uncertainties

The synchrotron ageing analysis is affected by many sources of uncertainty, which translate into a high error of the derived radiative ages. Some of these uncertainties can be somehow quantified, but some other are more difficult to estimate since they come from our ignorance on the physics involved (e.g. the strength and configuration of the magnetic field, the assumption of equipartition conditions, etc). This is one of the main criticisms usually made against this kind of analysis. Some of the main sources of uncertainty that affects the derived ages will be discussed in this Section.

As explained in Chapter 3 the revised formula by Beck & Krause (2005) that we used to derive $\tau_{\rm syn}$ can only be applied when the heavy particles (protons and nuclei) dominate the energy of the system. The dominance in terms of energy of the protons or the electrons depends on the acceleration mechanism taking place in the system (e.g., Fermi shock acceleration, secondary electrons, etc) and also on the different energy losses affecting the system. Since these are difficult to know from the observations, we will discuss how the derived ages would change in case the electrons were energetically more important.

Let us assume a scenario where the electrons dominate the system, and the formula by Brunetti et al. (1997) (Equation 3.9) applies. Figure 6.2 illustrates the ratio of the derived equipartition magnetic field strengths, $\mathrm{B}_{\rm eq}^{B97}$ (Brunetti et al. 1997) and $\mathrm{B}_{\rm eq}^{BK05}$ (Beck & Krause 2005), as a function of the spectral index. The calculations are done for the particular case of BAL QSO 0039−00, a source with a flux density of 18.9 mJy at $\nu_0 = 8$ GHz, located at z = 2.23, unresolved at 22 GHz, which implies an estimated angular dimensions of 0.098×0.073 arcsec, and with an extension along the line of sight estimated to be about 0.71 kpc. In can be seen in Figure 6.2 (solid line) how $\mathrm{B}_{\rm eq}^{B97}$ becomes between 3 and 10 times higher than $\mathrm{B}_{\rm eq}^{BK05}$ within the expected range of variation of the pure synchrotron spectral index ($\sim$ between -0.6 and -1.5). This suggests that the derived synchrotron age is expected to decrease as compared to the values presented in Table 6.1. In fact, in Figure 6.2 the (dashed) curve describing the ratio of derived synchrotron ages when considering both equipartition formulae has also been plotted. This ratio is expected to behave as $(\mathrm{B}_{\rm eq}^{B97}/B_{\rm eq}^{BK05})^{-1/2}$, if we assume $\mathrm{B}_{\rm CMB} \ll \mathrm{B}_{\rm eq}$. Then, when electrons dominate, the spectral age is expected to become smaller by 30 to 70 per cent compared with the values in Table 6.1.

Another source of uncertainty in $\tau_{\rm syn}$ may be the error in the determination of $\nu_{\rm br}$ from the fitting procedure, which is quite difficult to estimate. Instead of considering the purely mathematical error inherent to the fit, we take the following approach: if the derived $\nu_{\rm br}$ represents a break in the spectrum, the accuracy to determine this break will increase with the number of points describing this particular region of the spectrum, e.g. with the resolution in frequency. For instance, if the spectral break is located between the two measurements at 22 and 43 GHz, then the derived $\nu_{\rm br}$ will be more accurate if we have an additional measurement at, say, 30 GHz. A pessimistic estimate of the error of $\nu_{\rm br}$ could then be the spectral resolution, i.e. in the previous example $43 - 22 = 21$ GHz. Dividing this difference by the average of both limiting bands, $0.5 \times (43 + 22)$ GHz, we obtain a rel-

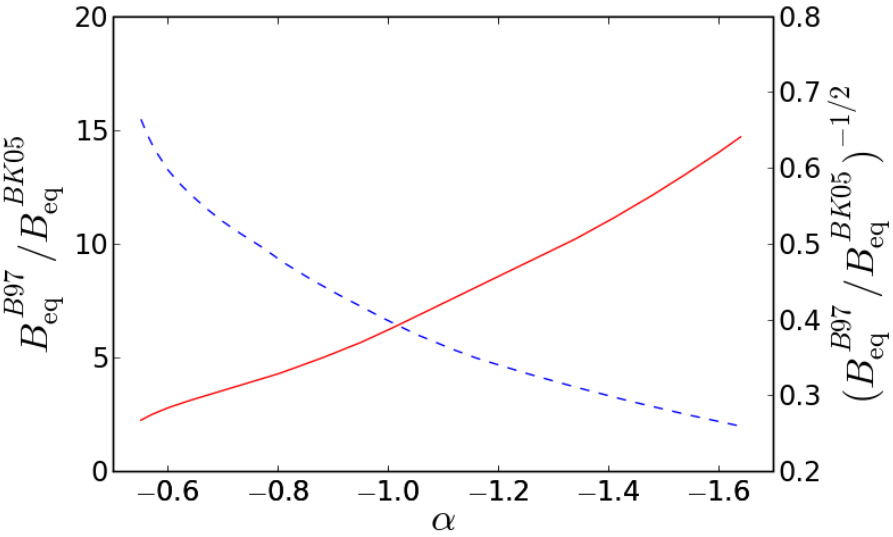

Figure 6.2: The solid curve indicates the ratio of the magnetic field strengths determined with the formulae by Brunetti et al. (1997), $B_{\rm eq}^{B97}$, and Beck & Krause (2005), $B_{\rm eq}^{BK05}$, as a function of spectral index. The dashed line represents the quantity specified on the right vertical axis, which corresponds to the ratio of the derived synchrotron ages using both expressions, when $B_{\rm CMB} \ll B_{eq}$. The calculations were done for the particular case of the radio BAL QSO 0039−00, at redshift 2.23.

ative error of about 60 per cent in $\nu_{\rm br}$. This implies relative errors in $\tau_{\rm syn}$ above 30 per cent.

In order to better visualise the effects of some different sources of error, the estimated linear sizes as a function of the derived synchrotron ages are plotted in Figure 6.3. The solid lines represent two constant values of the expansion velocity, $0.2c$ and c, respectively, and those points above the c limit should in principle have no physical meaning. An expansion velocity of $0.2c$ can be considered as a typical expansion velocity of young Compact Symmetric Objects (CSOs), consistent with multi-epoch global VLBI kinematic measurements (Owsianik et al. 1999). The exact location of the points in this plot can be affected by several uncertainties of which we consider three as the most important that we can quantify: (1) the uncertainty in the source dimensions is probably very large. First of all, as mentioned before, rough upper limits are being considered for these unresolved sources. Moreover the spherical symmetry assumption might not take into account important projection effects. On the other hand, the possible extended emission that could be indicative of the real source dimensions might not be detected at 22 GHz, because this emission usually drops with a steep spectral index. (2) The magnetic field might be different from $B_{\rm eq}$ if equipartition conditions do not hold; (3) The flux density S_0 might be amplified due to relativistic beaming.

The three panels (a), (b) and (c) in Figure 6.3 show how these uncertainties can affect the position of each source in the graph. In all three panels the filled circles represent the same situation, being the path length ℓ that inferred from the beam size in the 22-GHz map, assuming $B \sim B_{\rm eq}$ and no flux density amplification by beaming. We will call this the

"reference" situation. The median expansion velocity of these sources, $0.12c$, is represented by a dashed line.

In panel (a) the positions change when assuming different dimensions of the source along the line of sight. Triangles and empty circles imply 10ℓ and $\ell/2$, respectively. When comparing these with the reference situation, apart from the obvious shift along the ordinate axis there is a smaller shift towards lower ages when dimensions decrease. This is due to the dependence $B_{eq}(\ell)$ which is intrinsic to the equipartition assumption. An increase of a factor 10 in size (triangles) could be an example of a source larger than its projected size, for instance in which the line of sight is closely aligned to the radio jet. In this last case the median $v_{\rm exp}$ represented by a dash-dotted line increases because the sources must become

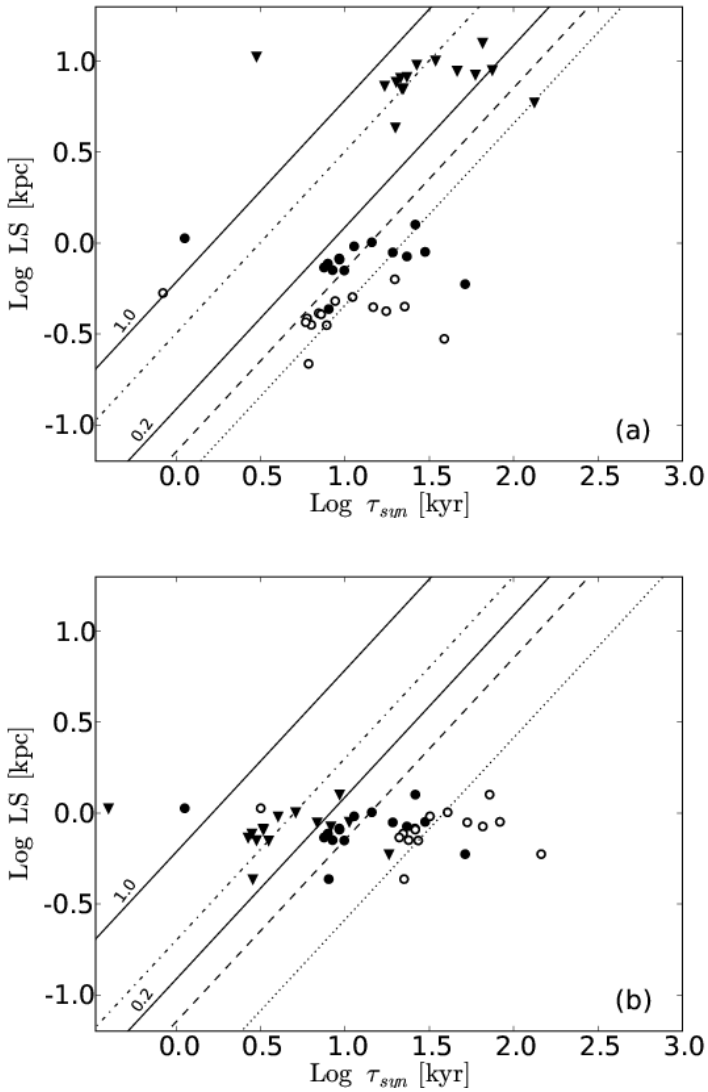

Figure 6.3: Continues on next page...

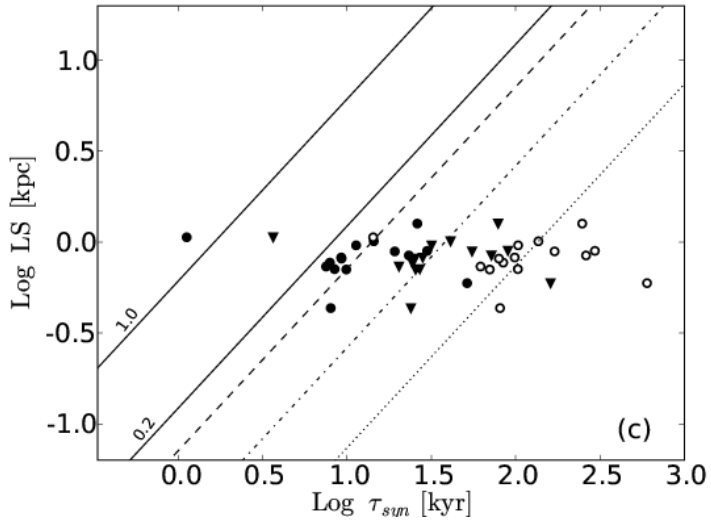

Figure 6.3: Linear sizes as a function of derived synchrotron ages. Black circles have the same position in all three plots and indicate the reference situation in which upper limits for LS given by the K-band beam size, equipartition conditions and no beaming were considered. Triangles and filled circles have different meanings in each panel (see text): (a) variations in path length are considered; (b) the assumed magnetic field changes; (c) different degrees of beaming are shown. The slopes correspond to expansion velocities to be compared with those marked with solid lines (0.2c and 1.0c). The dashed line indicates the median $v_{\rm exp}$ of the reference situation; the dotted slope represents the median $v_{\rm exp}$ of the filled circles and the dashed-dotted slope the same for the triangles.

larger while the synchrotron ages do not increase so much. For the same reason a decrease in size translates into a smaller median expansion velocity, as shown by the corresponding dotted line.

In panel (b) different magnetic field strengths are represented by different symbols. Triangles and empty circles represent $2B_{\rm eq}$ and $B_{\rm eq}/2$, respectively. Only a change by a factor 2 in the magnetic field strength can significantly change the radiative ages (actually, by a factor $\sim 2^{-3/2}$ according to Equation 3.14). The corresponding expansion velocities change accordingly.

Finally panel (c) shows how an artificial increase in flux density in beamed sources can make them appear younger. Now, in addition to the reference situation with $S_{\nu_0}^{obs}$, we consider $S_{\nu_0}^{obs}/16$ (triangles) which is about the maximum possible amplification when considering a relativistic $\beta = 0.6$ and $\phi = 0$ in the classical Doppler formula (Equation 6.1). Empty circles mean $S_{\nu_0}^{obs}/400$ (the same as before but with $\beta = 0.9$). As in the previous cases the dotted and dashed-dotted lines represent median $v_{\rm exp}$ values of the empty circles and triangles, respectively.

$$\frac{S_\nu^{obs}}{S_\nu} = \frac{(1-\beta^2)^2}{(1-\beta\cdot\cos\phi)^4} \tag{6.1}$$

The real situation might be more complex, and various of the effects represented in panels (a), (b) and (c) of Figure 6.3 could take place at the same time. This could happen, for instance, in a source with its jet closely aligned to the line of sight. This hypothetical source would probably suffer from relativistic beaming, and at the same time, the jet, if relatively extended, might appear shortened due to projection effects.

6.3 Discussion

The synchrotron ageing analysis shows that the radiative ages in our sample range form 1 to 50 kyr, which are similar to the ages of young GPS sources. Assuming that those correspond to the source ages, the inferred expansion velocities are not far from those expected in typical CSO sources. However, as discussed before, several important uncertainties affect the determination of the radiative ages. This means that the derived ages should only be taken as an indication, and they should be complemented by additional information in order to conclude that the ages are actually those of young sources.

A similar synchrotron ageing analysis as the one presented here was previously done by Murgia et al. (1999) with a sample of radio-powerful CSS sources. They split their sample of 38 CSS sources in 2 groups according to their morphological characteristics. In sources of class "*a*" the spectrum is dominated by lobes, while in sources of class "*b*" the spectrum is dominated by a bright jet or hotspots. Their ageing analysis indicates a correlation between $\tau_{\rm syn}$ and LS for type-"*a*" sources but no correlation was found for the type-"*b*" sources. The authors concluded that at least the first group is actually composed of young sources for which the break frequency constitutes a clock indicating their evolutionary stage. In group "*a*" they found sensible expansion velocities with a median value of $0.22c$, close to typical expansion velocities in CSO sources from multi-epoch VLBA measurements. They also concluded that type-"*a*" sources present magnetic field strengths within a factor 2 from the equipartition value.

In our analysis the lack of morphological information is probably the main source of uncertainty in the determination of $B_{\rm eq}$. Assuming that BAL QSOs have the same range of orientations as normal quasars, a special configuration in which the jet is closely aligned to the line of sight is not likely to occur to *the majority* of the sources in the sample, but perhaps to some individual cases. For those, a better constraint of the path length will be necessary to estimate the magnetic field and thus the synchrotron ages.

On the other hand, if BAL QSOs are oriented in a particular way as claimed by orientation scenarios, the high amount of unresolved radio sources might imply that most of them have their jets closely aligned to the line of sight and therefore projection effects will be important in most cases. This would mean that our current estimates on the radiative ages of these sources will be systematically underestimated.

Actually, VLBI observations will improve to clarify this situation in several ways, possibly constraining the orientation of these sources and giving a better estimate on the source size and thus providing some clues about the presence of beaming. In addition, the morphology will hopefully help us to identify those sources with the presence of lobes for which the synchrotron age can be identified with the source age, and those with strong jets or hot-spots for which the radiative age indicates the age of these dominant structures. A project with VLBI multi-frequency observations and the analysis on the pc-scale properties of several BAL QSOs of the RBQ sample has been started by us, and results will be presented in the following chapter.

7

Radio morphology of BAL QSOs in the milliarcsecond scale

THE previous chapters have shown that radio-loud BAL QSOs posses a very compact morphology in the radio. We have seen how most of the sources in the RBQ sample show unresolved or barely resolved morphology at high frequencies with the VLA in A configuration up to relatively high frequency. These results are compatible with previous findings by Becker et al. (2000) who found that FBQS BAL QSOs are more compact than the normal population of FBQS QSOs.

The apparent compactness of these objects can be explained either by projection effects or by the fact that these sources are intrinsically compact. In the first case, a high amount of compact sources could mean a relatively high fraction of beamed sources pointing towards us. This would state a relationship between the orientation of BAL QSOs and their observed characteristics. In the second case, the compactness of BAL QSOs could mean either a certain evolutionary stage or maybe a more dense environment that could frustrate the radio source to expand further.

VLBI observations of BAL QSOs are therefore crucial to reveal the geometry and orientation of these objects. The presence of extended emission in the surroundings of the compact core can give indications of past activity (Stanghellini et al. 2005), maybe suggesting a possible recurrent scenario for the radio emission. The pc-scale morphology can also show a core-jet structure associated with some beaming and possibly with flux density variability, or can reveal a very compact symmetric object, which would be indicative of a very young or a frustrated radio source. As an example, the recent VLBA analysis of BAL QSO 1045+352 has allowed Kunert-Bajraszewska & Marecki (2007) to propose a scenario of a merger event accompanied by a jet reorientation and intermittent activity.

Complementing the multi-frequency observations and polarisation measurements presented in Chapter 5, we present in this chapter two-frequency VLBA observations of some radio BAL QSOs in order to learn about their pc-scale characteristics. These will be dis-

Table 7.1: List of 5 BAL QSOs observed with VLBA. Flux densities come from previous Effelsberg radio continuum observations.

ID	RA (J2000)	DEC (J2000)	z	$S_{4.8\,GHz}$ (mJy)	$S_{8.3\,GHz}$ (mJy)
0135−02	01 35 15.243	−02 13 49.37	1.820	27.2 ± 0.6	31.9 ± 0.8
0837+36	08 37 45.589	+36 41 45.60	3.416	30.2 ± 2.3	12.1 ± 0.8
1159+01	11 59 44.827	+01 12 06.98	1.989	137.8 ± 1.7	158.0 ± 2.0
1537+58	15 37 29.549	+58 32 24.80	3.059	26.5 ± 0.4	40.6 ± 0.8
1624+37	16 24 53.481	+37 58 06.66	3.377	23.3 ± 1.1	15.0 ± 0.1

cussed in the framework of the models proposed to explain the nature of BAL QSOs.

7.1 The sample

We have selected a sample of relatively radio bright BAL QSOs in order to be able to observe them with high enough signal-to-noise ratio with the VLBA. All BAL QSOs except 1537+58 which is presented here belong to the RBQ sample previously selected for observations with VLA and Effelsberg. This means that multi-frequency data are available for them as well as morphological information with the most compact configuration of the VLA. In addition, the phased-reference high-resolution observations with the VLA in A configuration provided us with precise coordinates to observe these objects at a resolution of ~ 1 mas with a field of view of the order of 0.1 arcsec.

The list of observed objects can be found in Table 7.1, with columns being radio coordinates in J2000, redshift and flux densities at 4.8 and 8.3 GHz from previous continuum Effelsberg observations. Details on the radio spectra and polarisation properties of these objects can be found in Chapter 5.

7.2 VLBA Observations and data reduction

In order to study the pc-scale structure of the BAL QSOs in our sample an image resolution around the milliarcsecond scale and a sensitivity around or below the milliJansky level would be desirable with the aim of detecting possible extended low-brightness components. For these reasons the VLBA was chosen for these observations because it is composed of a homogeneous set of antennas with adequate capabilities for our purposes in terms of sensitivity and resolution.

Observations took place with the VLBA at different dates, profiting from the dynamic scheduling mode. Most of the observations were done within the last quarter of 2007, except the observations of 1624+37 which were allocated in January 2005 as an initial pilot programme. Observations were done in snapshot mode using a minimum of 8 out of the 10

Table 7.2: Observational setup for the VLBA observations and observing times. Key code for the VLBA antennas: SC (St. Croix), MK (Mauna Kea)

ID	Obs. Date (yyyy/mm/dd)	Antennas not scheduled	Bands	Rec. rate (Mbps)	t_C (min)	t_X (min)
0135−02	2007/10/21	SC	C,X	128	126.9	122.6
0837+36	2007/11/06		C,X	128	98.3	136.4
1159+01	2007/12/23		C,X	128	105.1	108.8
1537+58	2007/11/25	SC, MK	C,X	128	100.0	100.0
1624+37	2005/01/23		C,X	128	106.8	126.8

antennas in the array. Two receivers were used, C and X bands (centred at approximately 5.0 and 8.4 GHz, respectively). A minimum of two frequencies allows us to have different resolutions to look for individual components. In addition, the usage of two or more bands enables us in principle to study the spectral indices and the polarisation properties of sub-components. Table 7.2 summarises the observational setup in the different observations.

Exposure times range between 100 and 120 min per source and frequency. Since most sources were expected to have flux densities below 100 mJy, phase-referencing was used (Beasley & Conway 1995). This technique involves regular observations of a bright nearby calibrator to determine phase corrections to be applied to the target visibility data. To this aim relatively bright phase calibrators were selected among the list of VLBA calibration sources[1] within 10 degrees of each target position. The quasars DA193 and 3C279 were used as primary calibration sources. The first quasar is almost unresolved at the resolution of the observed bands and show little polarisation, while 3C279 contains two components corresponding to core and jet. This last source was also used together with J2136+0041 and J1357+7643 as polarisation calibrators.

Calibration was done using the 31DEC08 version of the AIPS software (Greisen 2003) and a semi-automatic reduction pipeline written in ParselTongue[2]. The visibility data was initially cleaned from a few scans affected by interference or bad antenna behaviour and the "a priori" calibration was performed. Then, the parallactic angle contribution was subtracted with the VLBAPANG task. The bandpass calibration was done using previously generated maps of the flux density calibrators. The accuracy of the total power calibration was estimated comparing the flux densities of the calibration sources in our maps with those found in the VLBA calibrator monitoring database[3], where measurements of these objects a few days before of after our target observations could be found. The recovered flux densities in our maps agree with the ones in the database within ~ 10 per cent, on average, with discrepancies for individual sources between 5 and 17 per cent.

Even if the main goal of these observations was not to obtain polarimetric data, we

[1] `http://www.vlba.nrao.edu/astro/calib/`
[2] `http://www.radionet-eu.org/rnwiki/ParselTongue`
[3] `http://www.vla.nrao.edu/astro/calib/polar/`

decided to perform also the polarisation calibration as a final step. The only source in our sample for which polarisation observations could be useful is 1159+01 because it is very bright and polarised enough in the observed bands to expect sensible results with VLBA. The polarisation calibration was done with the task PCAL using previously obtained maps of the polarisation calibrators.

The mapping procedure was done using the version 2.4k of the Caltech difference mapping program (DIFMAP; Shepherd 1997). A modification of the script created by G.B. Taylor for semi-automatic mapping in the VLBA Imaing and Polarimetry Survey (VIPS; Helmboldt et al. 2007) was used for mapping the Stokes I, Q and U parameters. The first iterations of the "clean" algorithm were performed using natural weighting, while the final loops were done using uniform weighting to recover fainter structures and improve the final map noise. The pixel size was selected to be 0.3 and 0.2 mas at 5.0 and 8.4 GHz, respectively, in order to optimally sample each synthesised beam with at least three pixels.

7.3 Results

In this section the main characteristics of each individual source will be summarised and the VLBA maps at the two observed frequencies will be described. In the light of these maps, a brief discussion will be done for each object, taken into consideration all the multi-wavelength information collected so far.

BAL QSO 0135-02

The BAL QSO 0135−02 was discovered in the FBQS (Becker et al. 2001) and catalogued as a HiBAL QSO. It is quite luminous in the optical with an APM POSS-I E magnitude of 17.5 at redshift 1.82. It is also very bright at NIR wavelengths, being detected in the 2MASS survey (Skrutskie et al. 2006) and included in the 2MASS Point Source Catalogue with J=16.3, H=16.0 and K_s=15.0. The FBQS optical spectrum (see Figure 4.4) shows a BAL trough associated with C IV, about 10,000 km s^{-1} wide and including several sub-troughs.

The radio source is quite compact at cm wavelengths, with the VLA map at 22 GHz revealing a single component of (11± 4) mas (deconvolved size). The radio spectrum has a convex shape and becomes very steep at high frequency with a spectral index $\alpha_{8.4}^{43} = -1.59$. The spectrum peaks at very high frequency, 8.2 GHz in the observer's frame, or about 20 GHz in the rest-frame, which means that this source can be classified as a HFP (Dallacasa et al. 2002).

The source might be variable at 1.4 GHz, with the flux density being 16 per cent higher in the FIRST epoch compared to the previous NVSS epoch. Such a change is not significant taking into account the errors in the measurements, and the parameter σ_{Var} defined in Equation 5.4 yields 2.4 (slightly below the level of significance). The flux densities obtained from the VLBA maps at 5 and 8 GHz are also, respectively, 16 and 26 per cent higher than

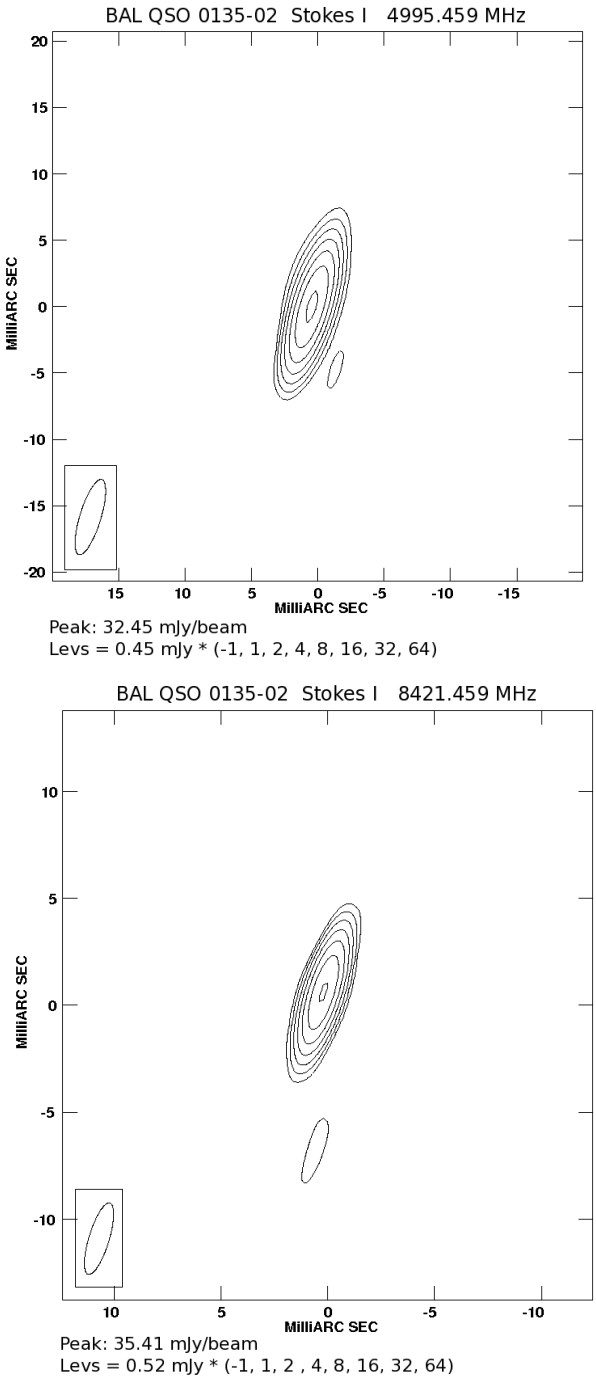

Figure 7.1: VLBA maps at 5 GHz (top) and 8 GHz (bottom) showing the pc-scale structure of BAL QSO 0135−02. The synthesised beam is shown in the lower left corner of the map. Contours are in logarithmic scale according to the legend.

the ones previously measured with the VLA and Effelsberg using similar passbands. Again, these variations are not significant at the 3-σ_{Var} level. However, these two comparisons considered as a whole might suggest the possibility of an increasing flux density with time.

The maps in Figure 7.1 show an unresolved source also at mas-scale. The beam size is quite elliptical due to the low declination of the source. A 2-dimensional Gaussian fit to the source profile at 8.4 GHz gives an angular extension of 3.5 × 0.9 mas, which translates into ∼ 30 × 8 pc.

According to our previous VLA data, the polarisation of 0135−02 in the radio is very small at 8.4 GHz, with an upper limit of < 0.9 per cent. In fact, no significant polarisation can be seen in the Stokes Q and Stokes U VLBA maps, both of them with a noise level of ∼ 0.1 mJy.

The extreme compactness of this source and the absence of any visible extended structure, together with some indications of variability might suggest that this could be a beamed source with its jet closely aligned to the line of sight, like a *blazar*. However, these kind of objects are expected to show relatively strong linear polarisation (e.g. ∼ 2 per cent) in the radio (Saikia & Salter 1988) and this is not seen in our two different observing epochs with the VLA and the VLBA, at 8.4 GHz. To explain this, there is still the possibility that this presumed blazar might be in a quiescent state of low polarisation.

Another possibility would be that this source is extremely compact because it is extremely young, i.e. showing the typical age of a HFP source. This would be, in principle, consistent with the spectral peak found at high frequency, the low level of polarisation and the moderate variability detected to date. However, as pointed out by Torniainen et al. (2007), there is a high fraction of GPS and HFP sources associated with quasars that can incorrectly be classified as young sources, being actually flat-spectrum sources temporarily showing a curved spectrum while they present an outburst.

The best approach to test both hypotheses is doing subsequent follow-up of these sources. Performing multi-epoch polarimetric observations with temporal differences of several years has proved to be a successful tool to identify changes in the overall spectrum of GPS and HFP sources (Orienti et al. 2007, Torniainen et al. 2007) in order to reveal their nature.

BAL QSO 0837+36

This BAL QSO is the one at highest redshift in the RBQ sample, with z = 3.42. It is quite luminous in the optical, having $M_i = -28$ as shown in the fourth version of the SDSS QSO catalogue (Schneider et al. 2007). It is also detected in 2MASS with NIR magnitudes J, H and K_s, 17.0, 16.8 and 15.3 respectively.

The SDSS optical spectrum (Figure 4.4) shows wide troughs associated with Si IV, C IV, N V, O VI but also with Al III. This is thus classified as a LoBAL QSO, although the Mg II

line is not seen in the optical window. The BI as measured in C IV yields (4350 ± 10) km s^{-1}.

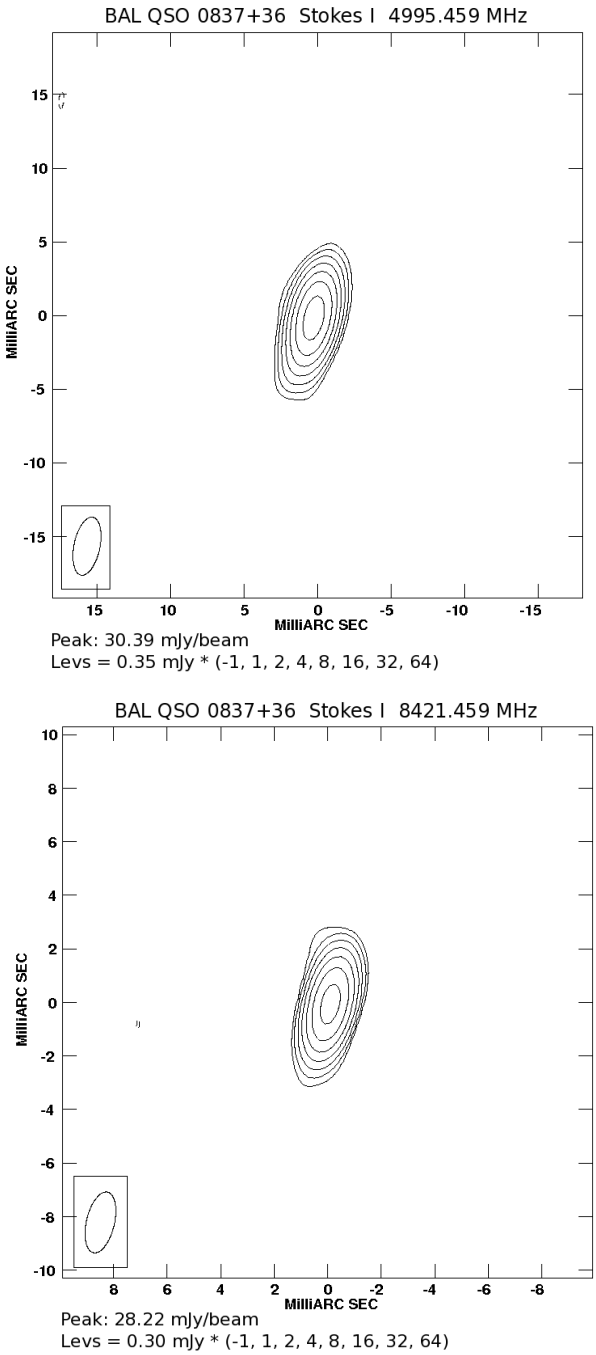

Figure 7.2: VLBA maps at 5 GHz (top) and 8 GHz (bottom) showing the pc-scale structure of BAL QSO 0837+36. The synthesised beam is shown in the lower left corner of the map. Contours are in logarithmic scale according to the legend.

The radio spectra is steep at high frequency, with $\alpha_{8.4}^{43} = -1.39$, and there is a peak in the spectrum at 2.7 GHz (observer's frame). It was stated in Montenegro-Montes et al. (2008) that this source could have a bright counterpart at 325 MHz from the WENSS catalogue. However, a more detailed examination reveals that this WENSS source can be better associated with another nearby radio source: FIRST J083751.2+364232, which is located at 48 arcsec towards the NNE from the BAL QSO position. Again the spectral shape and the radio compactness at 22 GHz (with a deconvolved size of 19 ± 10 mas), together with its low polarisation at 8.4 GHz (< 0.6 per cent) are consistent with an extreme GPS source.

The maps in Figure 7.2 show once more an unresolved component at both observed frequencies. Fits to elliptical Gaussians give dimensions of 4.1 × 1.8 mas at 5 GHz and 2.3 × 1.0 mas at 8.4 GHz.

Although the VLBA 5-GHz flux density perfectly matches the previous Effelsberg measurement (both give ∼ 30 mJy), at 8.4 GHz the source may have increased its flux density from 12.1 mJy (VLA) up to 30.1 mJy (VLBA). This increase in flux density of about 150 per cent means a variability significance of σ_{Var}=5.8. If this variability is real and not due to a calibration problem, the radio spectra of this source might have changed considerably, because the VLBA maps suggest a nearly flat spectrum for this source between 5.0 and 8.4 GHz, while the VLA measurements in Chapter 5 give $\alpha_{4.8}^{8.4} = -1.58$. In fact, a variability scenario due to the presence of a burst could explain the complex shape of the radio spectrum shown in Figure 6.1. Unfortunately, no map is available for this source in the NVSS, so variability at 1.4 GHz between the FIRST and NVSS epochs cannot be studied. However, variability usually tends to be higher (and therefore more easily detected) at high frequencies.

As in the case of 0135−02, subsequent follow-up of this source can be definitive to establish its possible variability character.

BAL QSO 1159+01

The BAL QSO 1159+01 is the radio source with the highest radio luminosity in the RBQ sample, with a flux density of 268.5 mJy at 1.4 GHz (log $P_{1.4\,GHz}$= 27.6 W m^{-2}) and also detected at 365 MHz with 884 mJy. For this reason it has been detected in several radio surveys, like the GB6 survey (Green Bank 6-cm Survey; Bennett et al. 1986) or the Texas survey (Douglas et al. 1996). The optical counterpart is only 0.07 arcsec apart from the radio position, and also quite bright, with SDSS r ∼ 17.2 (psf magnitude).

This z = 1.99 QSO shows a relatively narrow BAL trough very close to the C IV emission line. It has BI = 0 km s^{-1} but the AI gives 2887 km s^{-1} as given by Trump et al. (2006). The classification of this object as a BAL QSO was extensively discussed by Briggs et al. (1984) who concluded that even if it does not rigorously satisfy the classical definition of a BAL QSO, it shares the main characteristics of this class of objects. In addition, the presence of a high column density, low velocity dispersion absorption system at z = 1.943 causes the Ly-α emission to be partially suppressed. The presence of this absorber was

confirmed by H I absorption detected in the radio by Wolfe & Briggs (1981).

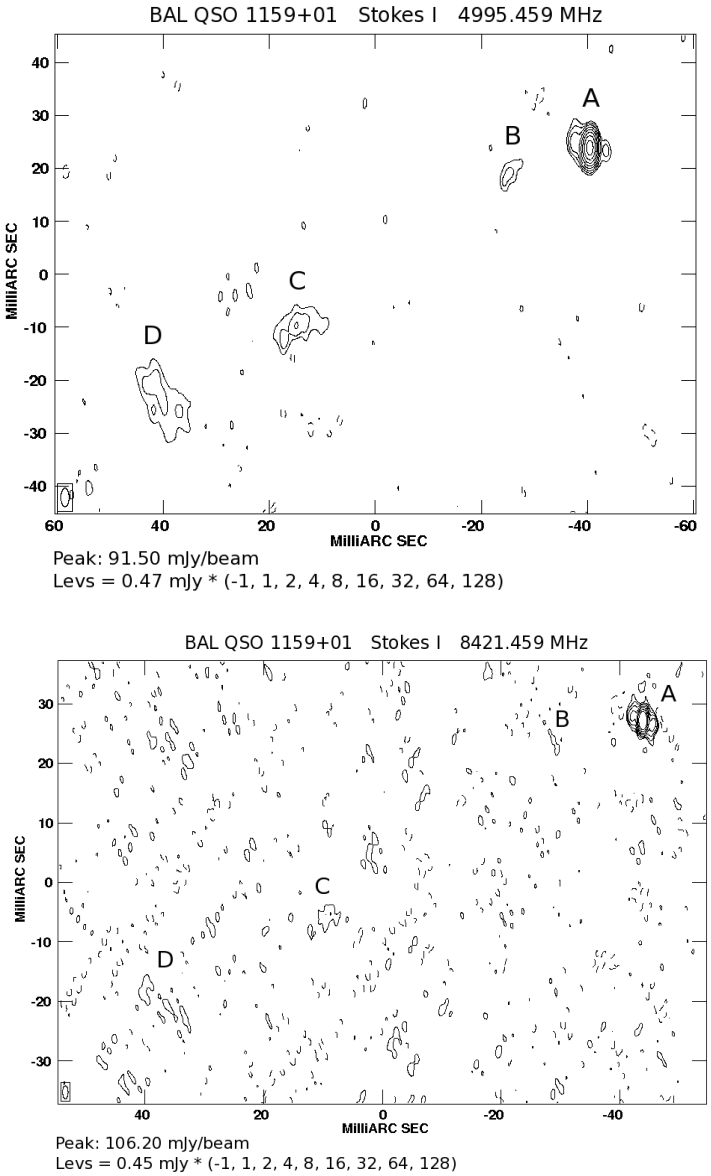

Figure 7.3: VLBA maps at 5 GHz (top) and 8 GHz (bottom) showing the pc-scale structure of BAL QSO 1159+01. The synthesised beam is shown in the lower left corner of the map. Contours are in logarithmic scale according to the legend.

BAL QSO 1159+01 is quite radio bright and this is the clearest case in the RBQ sample showing a double-component radio spectrum. The low-frequency component is steep, with $\alpha^{1.4}_{0.365} = -0.8$, while the high-frequency component is quite flat, with $\alpha^{15}_{4.8} = -0.09$. This suggest the presence of different emitting regions. This can actually be seen at mas

resolution in the 5-GHz VLBA map (see Figure 7.3).

A compact and bright component (A) associated with the radio core can be seen, and also some faint extended emission which extends about (at least) 100 mas towards the SE from the central core. The faintness of this emission and the absence of an active hot-spot suggest that this can be the remainder of a jet that was active and ceased its activity. An estimate of the extension of the diffuse emission can be done by measuring the distance between the components A and D (100 mas correspond to a projected linear size of 0.85 kpc). If no variability is assumed, not much more additional flux density is expected beyond component D because the flux densities of all 4 components shown in the map (A, B, C, and D) added together equal the continuum flux density from the Effelsberg measurement.

As expected from the relic emission of relative relaxed particles, the radio spectra of components B, C and D should be steep, which is the reason why this diffuse emission is very faint at 8.4 GHz. In fact, a marginal detection of components C and D can be perceived on the 8.4-GHz map, although definitely at the limit of the sensitivity. The emission coming from this jet probably dominates the steep component of the radio spectra shown in Figure 7.3, which means that it is likely brighter and maybe more extended at lower frequencies. As before, at 8.4 GHz the sum of the flux density recovered from all the different components approximately equals the flux density from the previous VLA measurement. The emission from the central core would then be dominant in the flat, high frequency part of the combined radio spectrum.

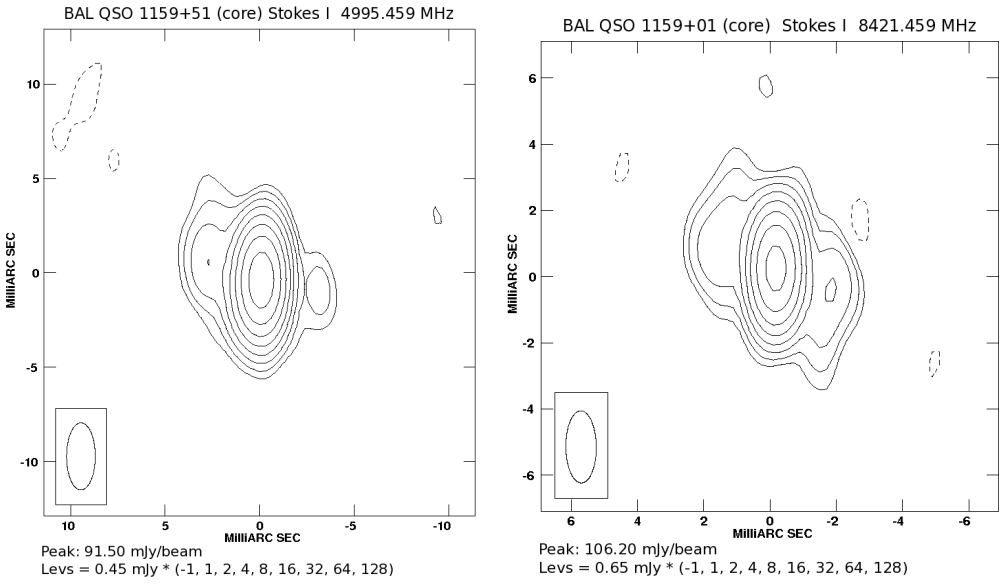

Figure 7.4: VLBA maps at 5 GHz (left) and 8 GHz (right) showing the pc-scale structure of the brightest component of BAL QSO 1159+01. The synthesised beam is shown in the lower left corner of the map. Contours are in logarithmic scale according to the legend.

Another remarkable characteristic of 1159+01 is the presence of two symmetric extensions very close to the central core (component A). This region has been amplified for a better visualization in Figure 7.4. In both the 5 and 8.4 GHz maps a central brighter core and two symmetric components at about 2 mas from the centre can be seen. One of them is located towards NWW and the other in the opposite direction, towards SEE. At 5 GHz, there is a slight asymmetry in the flux densities of both components but at 8.4 GHz they have similar flux densities, as can be seen in the contour map. This feature could likely be the origin of a new jet coming from the central nucleus. The direction of this new jet is not the same as the direction of the large-scale jet, with the first subtending an angle of about 50 degrees with respect to the second.

As shown in Chapter 5, 1159+01 was found to be polarised in several bands, and therefore a RM could be determined combining various VLA, Effelsberg and literature polarisation measurements. The fractional polarisation at 8.4 GHz from the VLA maps was found to be (2.1 ± 0.2) per cent for this source. This value was determined using the total emission of all components that contribute to the global integrated flux density, even if none of them is resolved out at the resolution of the VLA. Now, our VLBA maps allow us

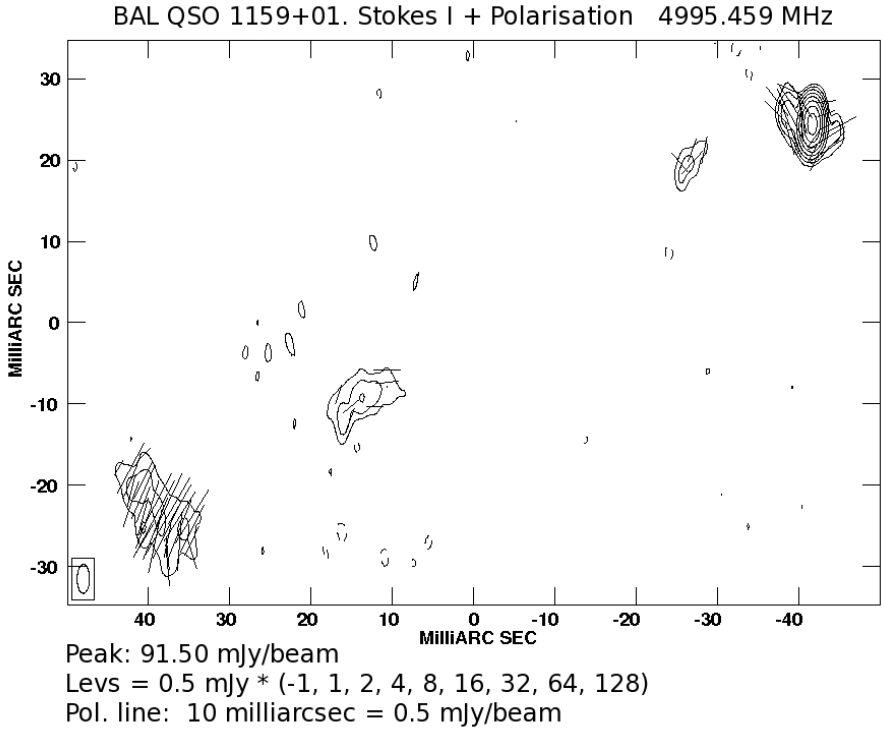

Figure 7.5: VLBA map of 1159+01 at 5 GHz showing contours in total intensity and segments representing the direction and intensity of the magnetic field. The synthesised beam is shown in the lower left corner of the map. Contours are in logarithmic scale according to the legend.

to investigate the distribution of this polarisation.

In Figure 7.5 some segments have been superposed to the total intensity contours. Their lengths are proportional to the measured linear polarisation and their directions perpendicular to the measured electric vectors, and therefore parallel to the magnetic field vectors. The correction due to the Faraday Rotation determined in Chapter 5 has not been applied to the magnetic vector position angles in Figure 7.5 because the RM was computed without separating the different sub-components. In any case, if the correction was applied, the effect would be an overall rotation of the polarisation segments by only +15 degrees, since the RM is not very high.

In opposition to the previous sources, no variability has been detected in 1159+01 between the VLA and VLBA observing epochs, neither at 5 GHz nor at 8.4 GHz, although the ideal would be to perform a second-epoch VLBA experiment to compare the flux densities of individual components. The unfortunate situation could occur that the faint jet component would have decreased its flux density at a similar rate that the core/inner jet emission would have increased, leading to similar global flux densities in both epochs.

In any case, the structure of the jet features indicates that this source is likely not oriented pole on, and beaming effects are probably not very important. In order to constrain its orientation, one possibility could be to use the jet-counterjet flux ratio, and follow Equation 3.19, but in this particular case this is difficult to do. The large-scale jet is very faint, and no counterjet is visible in the map, so the obtained flux density ratio would be very uncertain. In addition, the small-scale jet is too close to the core, and it is difficult to measure the amount of flux density belonging to each sub-component.

The pc-scale structure of 1159+01, showing the remainders of a large-scale jet and a relatively bright and compact small-scale jet suggests a scenario of intermittent activity. The occurrence of different episodes of radio activity has been proposed to explain the morphology and properties of some peculiar groups of objects, like X-shaped radio sources (Leahy & Parma 1992; Dennett-Thorpe et al. 2002), double-double radio galaxies (Schoenmakers et al. 2000; Kaiser et al. 2000), or core-dominated triple sources (Marecki et al. 2006).

However, in order to explain why the large- and small-scale jets are misaligned, a possibility could be that there has been a reorientation of the jet axis between the two jet events. This same hypothesis has been proposed by Kunert-Bajraszewska & Marecki (2007) to explain the X-shaped structure of another BAL QSO: 1045+352. The authors argue that in this source, an ongoin merger event could explain the restarting radio activity as well as the realignment of the jet axis.

A similar realignment-by-merger scenario could be assumed for 1159+01 since a merger event may be supported by the presence of a considerable amount of H I at a distance > 10 kpc from the radio core. This was inferred by the detection of 21 cm absorption by neutral hydrogen in front of the radio source 1159+01 (PKS 1157+014; Wolfe & Briggs 1981) and a H I column density of $(6.3 \pm 1.0) \times 10^{21}$ cm^{-2} was derived from these observations.

According to Wolfe & Briggs (1981) this absorbing system is likely "part of a H I disk of a galaxy gravitationally bound to a cluster containing the QSO".

BAL QSO 1537+58

The BAL QSO 1537+58 is faint in the optical with a SDSS psf magnitude r $\sim$ 20.2 at redshift 3.059. The optical spectra of this QSO can be seen in Figure D.2 of Appendix D. It shows at least two separated absorbing troughs in C IV, and also some broad absorption component (width $>$ 1,000 km s^{-1}) in Al III. The Mg II line is not included in the optical window. The QSO has formally BI = 0 km s^{-1}, but it can be considered a BAL QSO, having AI = 4,496 km s^{-1} as measured by Trump et al. (2006).

Table 7.3: Flux densities at different frequencies for BAL QSO 1537+58.

Frequency (GHz)	S_ν (mJy)	Telescope/ Survey	Frequency (GHz)	S_ν (mJy)	Telescope/ Survey
0.325	$<$15.0	WENSS	8.350	26.5 $\pm$ 0.4	Effelsberg
0.365	$<$60.0	Texas	8.460	27.2 $\pm$ 0.3	VLA(A)
1.400	14.2 $\pm$ 0.7	FIRST	10.450	21.3 $\pm$ 0.6	Effelsberg
1.400	14.5 $\pm$ 0.6	NVSS	14.940	18.2 $\pm$ 1.9	VLA(A)
2.640	52.4 $\pm$ 1.7	Effelsberg	22.460	12.5 $\pm$ 0.7	VLA(A)
4.850	40.6 $\pm$ 0.8	Effelsberg	43.340	3.4 $\pm$ 0.7	VLA(A)

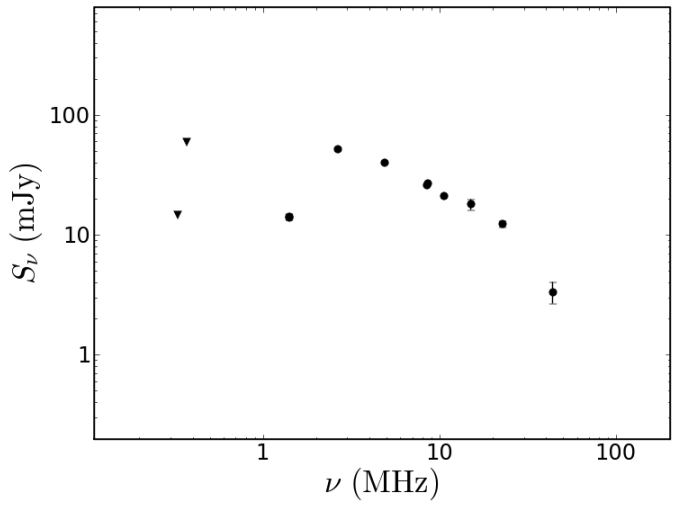

Figure 7.6: Radio spectrum of BAL QSO 1537+58. Observations have been done with the Effelsberg radio telescope and the VLA, in the same way as for the RBQ sample. For details see Chapter 5

The FIRST flux density at 1.4 GHz of 1537+58 is 14.2 mJy, just below the limit of the definition of the RBQ sample, so this source was not included in it. However, as can be seen in Figure 7.6, the flux density at 1.4 GHz probes the self-absorbed region of the

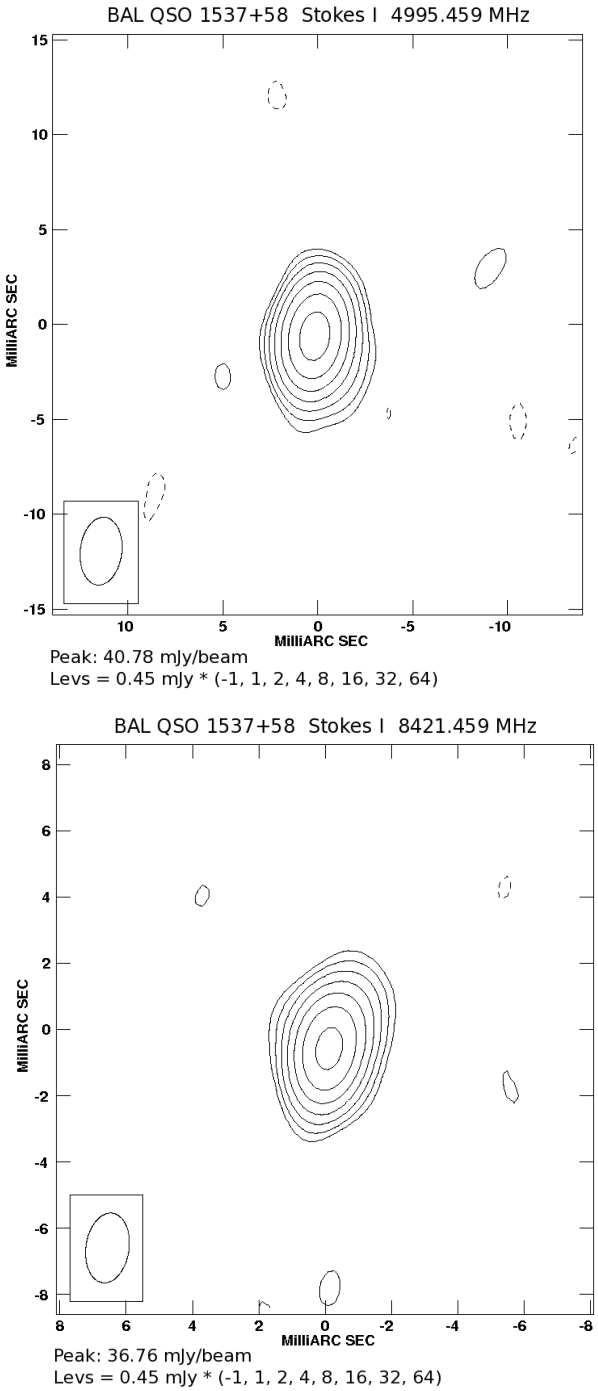

Figure 7.7: VLBA maps at 5 GHz (top) and 8 GHz (bottom) showing the pc-scale structure of BAL QSO 1537+58. The synthesised beam is shown in the lower left corner of the map. Contours are in logarithmic scale according to the legend.

spectrum. This means that the object is of similar characteristics as those in the RBQ sample, but the spectrum is peaking at 2-3 GHz which makes it relatively faint at 1.4 GHz. The high frequency part seems to behave as a broken power-law as expected for example if the synchrotron losses are important. The spectral index in the pure synchrotron region is steep ($\alpha_{4.8}^{15} = -0.7$). Table 7.3 shows the measured flux densities for this object with Effelsberg and the VLA in A configuration.

The VLBA maps in Figure 7.7 show a single compact component at both frequencies. The last contours do not follow exactly the elliptical shape of the beam. This could indicate a faint extended emission around the central core or indications of a polar-like orientation, but it could also be an artefact from the mapping process.

As in the cases of 0135−02 and 0837+36 the variability might reveal signs of beaming. The integrated flux at 5 GHz equals the one measured in Effelsberg, but again it seems that there has been an increase in flux density at 8 GHz, going from 27.2 mJy (VLA) up to 36.7 mJy (VLBA), which gives a significance $\sigma_{Var} \sim 2.6$. As in the previous sources, these indications need to be confirmed with a subsequent follow-up of this source.

BAL QSO 1624+37

The unusual BAL QSO 1624+3758 was discovered during a search of high redshift quasars at the position of FIRST radio sources (Benn et al. 2002; Holt et al. 2004). It is quite luminous both in the radio, having a monochromatic radio power of $P_{1.4GHz} = 4.3 \times 10^{27}$ W Hz^{-1}, and in the optical with $L_{1450\mathring{A}} \sim 5 \times 10^{24}$ W Hz^{-1}.

A detailed study of the optical spectrum taken with WHT/ISIS by Benn et al. (2005) shows the presence of several absorbers. Among them the most prominent one is the wide and highly detached BAL trough which extends from −29300 to −20700 km s^{-1} and yields a BI of 2990 km s^{-1}. This BAL trough is also detected in N V, Si IV and maybe Ly-α. An additional mini-BAL system with a resolved doublet allows the independent determination of the covering factor and the optical depth, and the mean covering factor is about 0.65.

The radio spectrum of this object was also presented in Benn et al. (2005). It shows a steep spectrum at high frequency with $\alpha_{4.8}^{15} = -0.79$. The spectrum turns over at low frequency, at about 0.55 GHz or 2.6 GHz in the rest-frame, which suggests compact dimensions. This is consistent with the VLA observations that show it unresolved at all frequencies up to 43 GHz.

The radio emission is polarised at the four highest observed frequencies: 4.8, 8.4, 10.5 and 22 GHz, showing a degree of polarisation of 11.3 per cent at 22 GHz. This made possible the determination of the rotation measure, giving RM = (−960 ± 30) rad m^{-2} in the observer frame, which translates into the extremely high value of RM = (−18350 ± 570) rad m^{-2}, the highest RM known for a BAL QSO and the second among QSOs, after OQ172 (Kato et al. 1987). This large RM can imply either a relatively dense line of sight or a relatively high magnetic field, or both, provided the source is intrinsically compact.

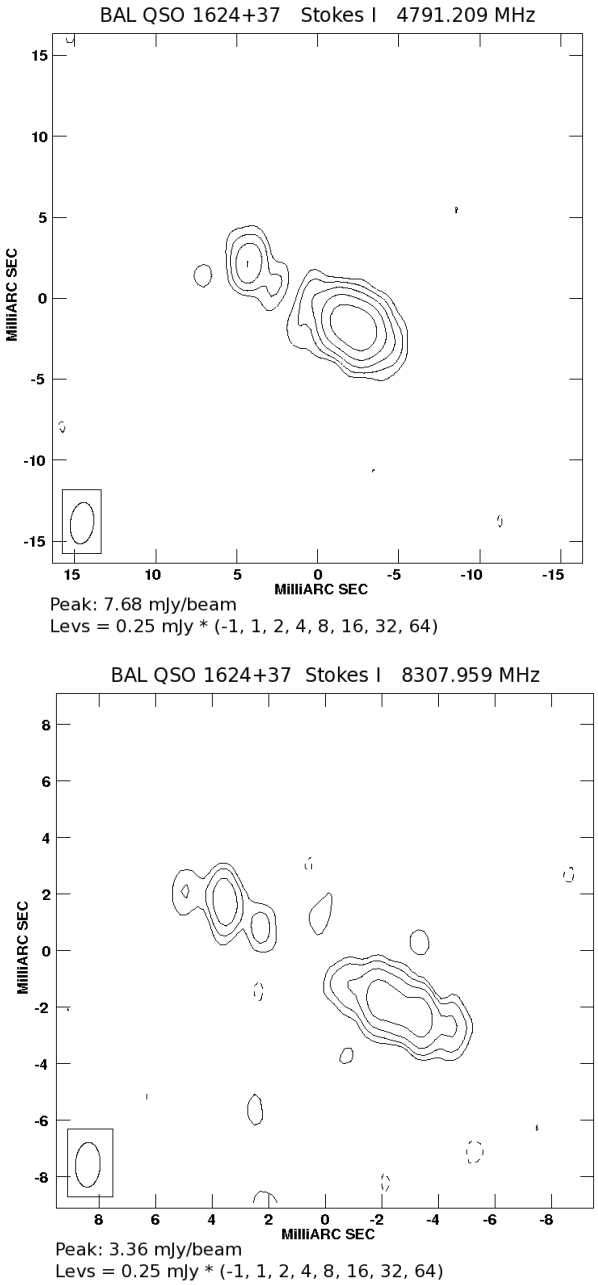

Figure 7.8: VLBA maps at 5 GHz (top) and 8 GHz (bottom) showing the pc-scale structure of BAL QSO 1624+37. The synthesised beam is shown in the lower left corner of the map. Contours are in logarithmic scale according to the legend.

In Figure 7.8 we see a core-jet structure for this object, clearly visible in both maps. There is a more compact component that we think might be the "core" and a more extended

one towards the SE direction, the "jet component". The separation between the peaks of emission from the core and the jet component is 8 mas (or about 60 pc). Close to the core there seems to be a very faint component at 1-2 mas towards the jet direction that could be the emission from the base of the jet. At 8 GHz a symmetric structure suggests the presence of what could be the counter-jet close to the nucleus, but both features are very faint and at the limit of detection. Also at 8 GHz it can be seen that the jet component is almost resolved out in at least two or maybe three or more sub-components. The distance between the core and the more distant sub-component in the jet is 10 mas ($\sim$ 75 pc), that could be an estimate of the angular dimension of the jet.

To confirm the nature of the two main components we have measured separately their flux densities in both bands. The core component yields 3.01 and 2.95 mJy at 5 and 8 GHz respectively. This is consistent with this component being actually the core of the system, because the spectral index is quite close to zero (~ -0.04), which indicates a flat radio spectrum. On the other hand, the jet component, comprising the combined emission from one or more knots and maybe a lobe, yields 17.30 and 10.25 mJy at 5 and 8 GHz, respectively. This gives a spectral index $\alpha_{5.8}^{8.4}$=-0.97, consistent with this emission coming from a less active region.

Unfortunately we did not get conclusive results from the polarisation observations. The source is quite extended and relatively faint, which did not allow us to measure a significant polarised emission in the Stokes Q and Stokes U channels. Given the unusual nature of this object deeper polarimetric observations are highly desirable to investigate the polarisation distribution at the mas-scale, in order to constrain the location of the magneto-ionic screen responsible for the observed high rotation measure.

Given the core-jet structure of the BAL QSO, it is possible to have a constraint on the orientation of the jet, following the procedure explained in Section 3.6. For this purpose we have used the 5-GHz map because the object is brighter and the signal-to-noise ratio is higher than at 8 GHz. In order to measure the jet flux density we have created an aperture that contains the most extended component. Since the counter-jet is not seen on the map, a lower limit on the viewing angle can be obtained assuming that the upper limit of the counter-jet flux density is three times the rms noise on the map. Applying then Equation 3.19 we get sensible values of $\beta < 1$ only when $\phi < 37$ deg.

7.4 Discussion

The five observations presented here show a variety of radio morphologies for BAL QSOs, but the fraction of unresolved sources at mas resolution is higher, 3 out of 5. The two resolved sources are 1624+37 with a compact core-jet morphology and 1159+01 showing a low brightness extended radio jet and a CSO-like morphology at smaller scale, close to the central core. These two sources are probably not "polar sources" because their jet axis seems not to be too closely aligned with the line of sight to the QSO. The orientation of the unresolved sources is *a priori* difficult to establish.

The size of our sample is in principle too small to make any general conclusion about the typical radio morphology of BAL QSOs. However, our observations complement other VLBI data of BAL QSOs in the literature that we can put together to have a more general perspective. Jiang & Wang (2003) observed 3 BAL QSOs with EVN at 1.6 GHz, Kunert-Bajraszewska & Marecki (2007) analysed EVN+MERLIN observations of BAL QSO 1045+352 and, more recently, Liu et al. (2008) performed EVN+MERLIN polarimetric observations of 8 additional BAL QSOs.

Table 7.4 summarises the morphological and polarisation information of these 17 sources. The columns indicate: (1) source name; (2) literature work where the observations come from; (3,4) frequency and instrumentation used for the observations; (5) morphological classification in one of these 4 groups: (U) unresolved or barely resolved, (CJ) core-jet, (CSO) compact and symmetric structure around a central bright core and (CX) complex; (6) polarisation detection. In this last case a hyphen means no information available, a star means that the information comes from our previous VLA polarimetric observations at 8.4 GHz, and no star means polarised data coming from the reference in column 2. A question mark is added when the degree of polarisation provided in that reference is not greater than 3 times the uncertainty given for that polarisation degree.

Table 7.4: Combined list of 17 BAL QSOs observed with VLBI, including the 5 objects observed by us and other sources found in the literature. Code for references: (1) This work; (2) Jiang & Wang (2003); (3) Kunert-Bajraszewska & Marecki (2007); (4) Liu et al. (2008). Morphological classification can be: 'U' unresolved or barely resolved; 'CJ' core-jet; 'CSO' compact with symmetric structure around a central bright core; 'CX' complex morphology

Source	Reference	Frequency	Instrument	Morphology	Polarisation
0135−02	1	5.0, 8.4 GHz	VLBA	U	No*
0724+4159	4	1.6 GHz	EVN+MERLIN	U	Yes?
0728+4026	4	1.6 GHz	EVN+MERLIN	CJ	Yes
0837+36	1	5.0, 8.4 GHz	VLBA	U	No*
0957+2356	2	1.6 GHz	EVN	U	−,No*
1044+3656	4	1.6 GHz	EVN+MERLIN	CJ	Yes?
1045+352	3	1.7,5.0,8.5 GHz	EVN+MERLIN	CX	−
1122+3124	4	1.6 GHz	EVN+MERLIN	CSO	Yes?
1150+2819	4	1.6 GHz	EVN+MERLIN	U	Yes?
1159+01	1	5.0, 8.4 GHz	VLBA	CX	Yes*
1312+2319	2	1.6 GHz	EVN	CSO	−,Yes*
1413+4212	4	1.6 GHz	EVN+MERLIN	CJ	Yes?, No*
1537+58	1	5.0, 8.4 GHz	VLBA	U	No*
1556+3517	2	1.6 GHz	EVN	U	−
1603+3002	4	1.6 GHz	EVN+MERLIN	CJ	Yes, Yes*
1624+37	1	5.0, 8.4 GHz	VLBA	CJ	Yes*
1655+3945	4	1.6 GHz	EVN+MERLIN	CJ	Yes?

The first conclusion that can be extracted from Table 7.4 is that there is a variety of morphologies for these sources. The most common geometries seem to be either unresolved (7 sources out of 17) or "core-jet" (6 out of 17). Only two of them are classified as compact "CSO" objects, although we note that this classification does not correspond to the classical "Compact Symmetric Objects" in which the core component is usually faint or even undetected. On the contrary, these two examples show a core which is brighter than the two external symmetric components. Finally, two objects show a complex morphology, in both cases with indications of restarting radio activity.

Something remarkable is the fact that all the mas-unresolved sources seem to present low polarisation. For five unresolved sources (three in our list and two in the list of Jiang & Wang 2003) the polarisation information comes from our VLA observations at 8.4 GHz presented in Chapter 5. The remaining two unresolved sources, 0724+4159 and 1150+2819, belong to the sample of Liu et al. (2008) who report polarisation degrees for these sources at 1.6 GHz of (11 $\pm$ 3.9) and (3.1 $\pm$ 1.3) per cent, respectively. It is not clear from their work whether these large uncertainties come from a relatively high noise in the Stokes Q and U maps, or if it is because the flux density calibration has a large error. In the former case, one should not consider these sources to be significantly polarised above the 3-σ level.

The sample defined in Table 7.4 is not ideal to make rigorous statistical conclusions because the sources have been selected with different criteria and because the maps are given at different frequencies and resolutions. However, the trend seems to be a high fraction of unresolved sources at the mas-scale, a similarly high fraction of core-jet sources and only a few sources showing CSO-like structure. Depending on the presumed nature of the unresolved sources one can think of two possible scenarios:

1 Assuming that most unresolved sources are actually beamed variable "polar" sources foreshortened by projection effects, then $\sim$ 30-40 per cent of BAL QSOs would have small inclinations between the radio axis and the line of sight, about $\sim$ 50 per cent would have intermediate inclinations (core-jet) and a smaller fraction, $\sim$ 10-20 per cent, would have inclinations high enough to display a symmetric morphology. This simple interpretation assumes that the radio geometry directly reflects the source orientation, neglecting for instance, the interaction of the jet with a possible inhomogeneous medium. According to this, BAL QSOs could basically span all possible inclinations, with an approximate orientation distribution suggested by the above percentages. This would mean that BAL QSOs are actually not restricted to a limited set of orientations.

   The problem with this interpretation is the unpolarised nature of these "polar" sources which is, in principle, not consistent with their presumed blazar-like nature. The polarisation behaviour of blazars is not yet completely understood since it appears to be a very complex phenomenon, but these objects seem to present radio continuum polarisations at a level of a few per cent (see Saikia & Salter 1988 and references therein). This polarisation is usually found to be variable, in some cases with erratic variations including quiescent periods of very low polarisation. However, this explanation is not satisfactory in the case of these "polar" BAL QSOs since *most* (if

not all) of them seem to be unpolarised or weakly polarised. A subsequent follow-up of these sources in order to confirm or not their variability and to understand their polarisation properties are of crucial importance to fully explore this issue.

2 If, however, most of the unresolved sources are actually extremely compact non-evolved sources then little can be said about their orientation. But they are expected to be completely depolarised according to the "Cotton effect". Given that at least some radio BAL QSOs show indications of multiple episodes of radio activity, these unresolved sources could be in a quiescent state between two of these episodes, or maybe at the very early stages of starting one of them. The core-jet and CSO-like sources would reflect subsequent evolutionary steps, where both groups might correspond to different orientations. If so, those sources with their jets spanning higher inclinations with respect to the line of sight would be less abundant.

This second possibility implies a certain evolutionary sequence. From the relative rate of extended to unresolved sources one can establish rough relative durations for these stages. Roughly similar fractions of radio BAL QSOs displaying core-jet/symmetric and unresolved morphologies imply comparable durations for the "jet" and the "quiescent" periods. However, the small fraction of sources with complex morphology, those presumably showing emission from two different radio episodes, suggests that the amount of time over which these two stages overlap is small. This would actually mean that this "jet period" could be somewhat shorter than the period between radio episodes. However, the two sources classified with complex morphology are actually the most radio powerful in the list (both of them with log $P_{1.4\,GHz} \sim 27.6$ W m^{-2}), which would explain why the "jet period" could exceptionally be longer in these particular sources.

Gregg et al. (2006) proposed an evolutionary picture for BAL QSOs in the framework of the merger-driven models previously introduced by Hopkins et al. (2005) to explain the evolution of QSOs. According to Gregg et al. (2006) the BAL phase could account for the transition period of QSOs in which they emerge from shrouded dusty objects, becoming luminous normal QSOs. This transitional period would last for about 10^6 years in this model. During this time, several jet episodes can be developed. If we assume a jet expanding up to ~ 1 kpc from the central core at an expansion rate of 0.01c, it will take $\sim 10^5$ years for the jet to fully develop. The quiescent period could then take, for instance, 1 to $2 \cdot 10^5$ years.

Another interesting indication of such an evolutionary picture is the fact that those BAL QSOs with indications of a double jet could have suffered a reorientation of the jet axis. This behaviour can be thus relatively common in BAL QSOs and might be the result of intense merger activity. In our case, only 2 objects out of 17 might show this phenomenon. However, this realignment could in principle affect more sources since it can only be seen in those powerful enough showing radiation from different burst episodes.

8

Deep H I observations towards the peculiar BAL QSO J1624+3758

OBSERVATIONS of H I in emission at 21 cm represent a challenge for present instrumentation when the target of interest has moderate redshift. This hyperfine transition has a very small probability to occur, and even if huge amounts of hydrogen are present in many astrophysical systems, only a very weak emission can be detected in objects within the local Universe. With present telescopes it is possible to detect the emission from massive H I systems only out to z $\sim$ 0.2 (Catinella 2008). At higher redshift, the study of hydrogen clouds is mainly done through H I absorption against strong radio sources.

However, a few detections have been reported on H I absorption at z $>$ 1 (e.g. Kanekar et al. 2007). These detections have been possible for systems with a relatively high column density of absorbing material located in front of strong radio emitting sources. Such observations are interesting because they probe the, otherwise invisible, hydrogen clouds corresponding to astrophysical objects in the early stages of the evolution of the Universe. They also provide information about the density of galaxy disks of recently formed galaxies, which are responsible of many of these absorptions.

Several factors make this kind of detections unlikely. First, the absorbing cloud must be massive enough to produce a measurable absorption. On the other hand, current radio telescopes do not cover in all cases large bands to make possible the detection of the redshifted H I line. A good spectral resolution is also required because the detected lines can span only some tenths of km s^{-1}.

Ideal candidates for H I absorption observations are the damped Lyman-α (DLA) systems, whose name derives from the broad damping wings of the absorbing optical profile. DLAs are defined to have H I column densities of at least 2×10^{20} cm^{-2}. Their nature is not completely understood but different authors consider these systems as the progenitors of present spiral galaxies (see e.g. Prochaska & Wolfe 1998) while at least a fraction of them are interpreted as low surface brightness galaxies or dwarf galaxies (Boissier et al.

2003; Haehnelt et al. 1998; Schaye 2001). In any case DLAs are an important component of the high-z Universe because they provide the major hydrogen reservoir available for star formation (Lanzetta et al. 1991).

These systems are usually detected because they absorb the continuum UV emission of foreground quasars, and a fit to the absorbing profile allows the determination of the H I column density. Since the H I detection in the radio is much more difficult and time-consuming in terms of telescope integration than the detection of DLAs in optical spectra, some surveys have been carried out looking for absorbing H I in samples of objects for which DLAs had previously been identified in the optical. A typical fingerprint of DLA/H I systems is the presence of low-ionisation metal lines, like Mg II λ 2799 Å systems (Lu & Wolfe 1994). To increase the probability of a successful H I detection, one strategy consists of establishing a minimum rest-frame equivalent width for the optical absorption, to ensure a relatively high H I column density (Lane & Briggs 2002). These techniques have led to detection rates of about 11 per cent.

These double detections in both the optical and the radio are important because they usually constrain the covering factor of the absorbing material, especially if high-resolution maps of the continuum source and the radio source exist. In addition, for those systems in which the H I column density has been determined by fitting the optical absorbing lines, a radio detection allows one to determine the spin temperature, T_s. This quantity is a measure of the relative populations of H I in its two possible spin states (parallel or antiparallel). Typical values of T_s inferred from observations in our galaxy and local spirals are about 100-200 K (Dickey & Lockman, 1990), but all DLAs associated with dwarf galaxies or low-surface brightness galaxies present $T_s > 1000$ K. At high redshifts spin temperatures have been mainly found to be somewhat higher, of a few thousand K, except in the recently discovered high-z absorber (York et al. 2007) for which a lower spin temperature, $T_s \sim 140$ K, was estimated.

Another useful application of these observations is the possibility in some cases to constrain the variations of cosmological constants like the fine structure constant α, the electron-proton mass ratio $\mu = m_e/m_p$, the proton gyromagnetic ratio g_p, etc., along cosmological time (see e.g., Kanekar et al. 2005).

8.1 Unusual BAL QSO J1624+3758

The quasar J1624+3758 was discovered in a spectroscopic survey of APM point-like objects associated with FIRST radio sources (Benn et al. 2002; Holt et al. 2004). The radio source, with $S_{1.4\,GHz} = 56$ mJy, is located 0.″02E and 0.″0N from the POSS-I/APM optical position. A detailed analysis of the high resolution spectrum (R = 10000) of this object was done by Benn et al. (2005). This spectrum was taken with the ISIS spectrograph of the 4.2m-WHT telescope, with a resolution between 0.8 and 2.3 Å (see Figure 8.1). The emission lines allowed the determination of the systemic redshift, z = 3.377. The spectrum showed different absorbers, including some narrow absorption lines which are probably due

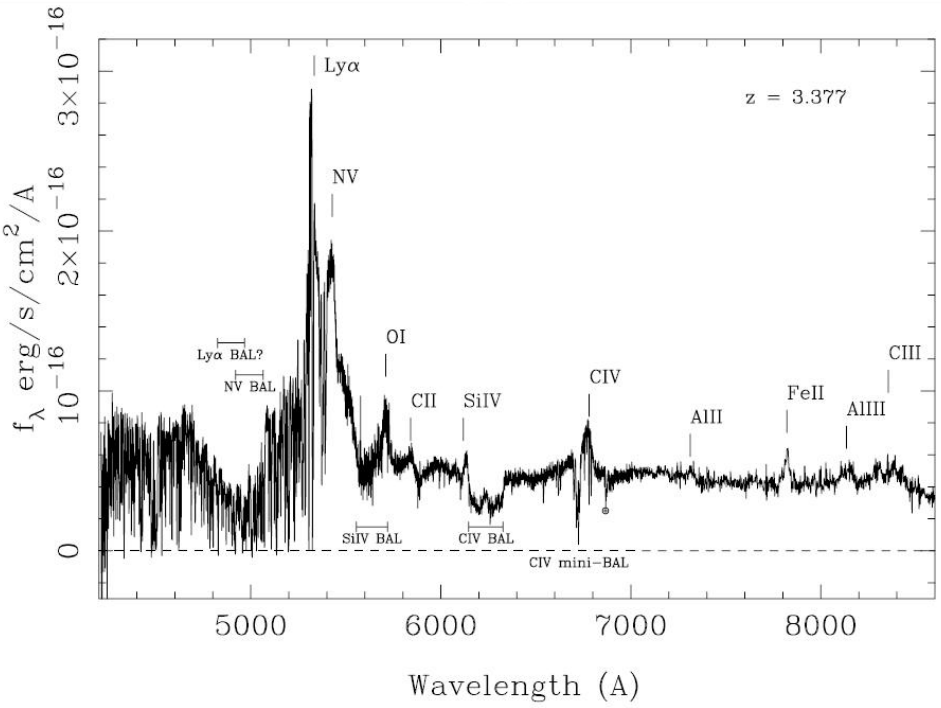

Figure 8.1: Optical spectrum of unusual BAL QSO J1624+3758 taken with ISIS/WHT. Extracted from Benn et al. (2005).

to intervening systems. The main absorbing features which were classified as probably intrinsic are summarised in Table 8.1.

Table 8.1: Intrinsic absorbers identified in the spectrum of BAL QSO J1624+3758. From the identified Lyman Limit System (LLS) the H I column density could be estimated. Extracted from Table 5 of Benn et al. (2005).

Absorber	Velocity	log N (cm^{-2})					C_f
	(km s^{-1})	H I	O VI	N V	Si IV	C IV	
BAL	−21000 to −29000					>16.0	0.3
Mini-BAL	−2300 to −2450	>14	15.1	14.7	≤13.2	14.7	0.6
LLS	**−1870**	**18.6**	**<13.6**	**<13.4**	**<12.5**	**<13.1**	**0.7**
AAL	−824	≲18.0			13.0	13.7	1.0
AAL	206	≲18.0			13.0	13.9	1.0

The BAL absorption is due to high ionisation species, mainly C IV, Si IV, N V and probably Lyα. The Mg II region is not covered by the optical spectrum because of the high redshift, but no absorption was detected associated to Al III. The quasar could then be classified as a HiBAL QSO but the possibility was not excluded that it is an unusual LoBAL QSO with weak Al III absorption.

The mini-BAL spans a velocity range of about 1200 km/s and was detected in C IV, N V and O VI. The two components of C IV were resolved, allowing the authors to determine the covering factor and the optical depth independently, as explained in Section 2.1.2.

A possible Lyman-limit system (LLS) was identified at z = 3.3498 by Benn et al. (2005). The associated absorption did not reach zero intensity, implying partial coverage ($C_f = 0.7$) and a fit to a Voigt profile gave a column density of N(H I) = 4×10^{18} cm^{-2} and a velocity parameter b = 30 km s^{-1}. This is the absorber with the highest H I column density among the ones detected, but it is not dense enough to be classified as a DLA system. However, it belongs to the category of the less H I-massive LLS [17.2 < log N(H I) < 20.3] according to the classification of Lanzetta et al. (1995).

Finally, two narrow absorption lines with small velocities from the quasar redshift were identified, and they are probably associated with the quasar. The residual intensity of these absorbers are consistent with total coverage, and the upper limit for the column density of H I was calculated to be N(H I) < 10^{18} cm^{-2}.

From the radio point of view, J1624+3758 is unusual for being one of the most radio-luminous BAL QSO known ($P_{1.4\,\mathrm{GHz}} = 3 \times 10^{27}$ W/Hz). The flux density ranges from 72 mJy at 327 MHz (WENSS) up to 2 mJy at 43 GHz (VLA). In Chapter 5 it was shown that the radio spectrum turns over at frequencies around 550 MHz in the observer's rest-frame, corresponding to 2.4 GHz in the source frame. Hence, it can be classified as GPS source and is therefore among the most distant known sources of this class. From our VLA high-frequency observations the angular size was derived to be < 0.4 arcsec. The high-resolution VLBA map at 8.4 GHz shown in Chapter 7 reveals a core-jet structure with a projected size of about 60 pc. Polarisation has been detected at high radio frequencies (> 4.8 GHz) showing strong depolarisation towards the lower frequencies. The RM was found to be −18350 rad m^{-2} in the rest frame.

GPS sources (like our target) provide a unique opportunity to study this gas (e.g. Pihlström et al. 2003). Observations show a large incidence of H I in absorption against young radio sources. However, the majority of detections have been observed in radio galaxies which suggests that the H I gas could show a disk-like structure (Pihlström et al. 2003). Rates of H I detection have been reported to be of the order of 50 per cent in galaxies and about 10 per cent in QSOs (Gupta & Saikia 2006; Vermeulen et al. 2003).

8.2 Observations and data reduction

The strategy was to perform a full 12-h synthesis observation in order to be able to detect indications of at least a weak ($\sim$ 2-σ) detection, or establish an upper limit on the contents of H I. In case of a successful tentative detection, additional observations could be done in order to improve the signal-to-noise ratio of the detected line.

Observations in line-mode took place in May 2005 with the 14 antennas of WSRT. The

observing band was centred at 325.6 MHz, covering a bandwidth of 5 MHz per IF. The band was sampled with 512 channels of 5 kHz each and a Hanning frequency taper was used which brings the spectral resolution up to 8 km/s. A 12-h synthesis observation was done in both polarisations (XX and YY) with a sample integration time of 60 seconds. The phase centre was pointed on coordinates $\alpha = 16^\circ\ 24'\ 53.470''$, $\delta = 37^\circ\ 58'\ 06.699''$.

The data reduction was done using the 31DEC06 version of the AIPS package in combination with a flagging routine written in ParselTongue/Python by H.-R. Klöckner from the University of Oxford. This routine determines the barycentre of the real and the imaginary parts of the continuum visibility distribution and computes the distance from each visibility to this barycentre. For each channel the standard deviation σ of those distances is computed and all data further away than $n - \sigma$ is flagged. The selection of n depends on the source structure, and after several tests we chose $n = 5$ as the best solution in order to flag most of the interference without compromising real source structure.

During an initial inspection of the dataset strong ripples were found on the visibility distribution affecting the shorter baselines, probably due to radio-frequency interference. For this reason, it was decided to remove from the dataset all the visibilities from baselines shorter than 0.4 kλ.

The calibration was done in two steps. In the first one the bright sources 3C 48 and 3C 286 were extracted from the multi-source file without any bandpass correction. The flagging routine was run on both sources and after that, phases and amplitudes were calibrated using 3C 48 as flux density calibrator. From the calibrated data the bandpass correction was determined, considering only the central 75% of the available channels. In the second step, this bandpass solution was applied when extracting again 3C 48 and 3C 286, and the calibration procedure was repeated.

Several self-calibration steps were applied making use of the CLEAN algorithm implemented in AIPS. Cleaning boxes were located around the visible sources within the whole region covered by the primary beam, of about 5 degrees wide. The brightest radio source in the field is WN J1628+3932 (corresponding to galaxy NGC 6166) with $S_{peak} = 14.7$ Jy/beam at 330 MHz (de Bruyn et al. 2000), about 1.75 degrees from the phase centre towards NNE. This very strong source is responsible for the presence of some artificial rings due to sidelobes around its position in the final map. The cell size was chosen to be 19 arcsec in order to sample about 1/3 of the synthesised beam size. After several cleaning iterations the final data cube was produced, which we show in Figure 8.2.

In order to correct for the primary beam attenuation, the AIPS task PBCOR was used although some special care needed to be taken in order to build a suitable model for the shape of the primary beam of the WSRT telescope. The ideal model would be determined in the same way as in Popping & Braun (2007), taking a series of holographic measurements in order to sample the full range of angular scales. However to our knowledge these measurements have been done so far only in the frequency range around 1.4 GHz. Thus a beam shape described by a $\cos^6(x)$ function was assumed as an approximation here, where

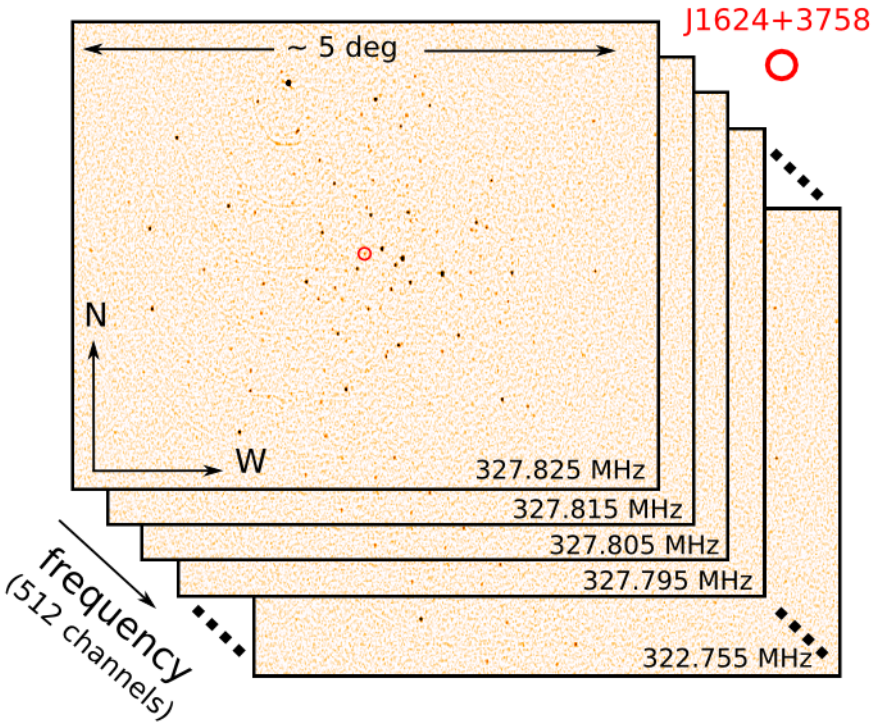

Figure 8.2: Representation of the data cube showing the detected sources within the primary beam. The circle shows the position of BAL QSO 1624+3758, very close to the phase centre.

x is the product of a constant c, the observing frequency ν and the angular distance from the pointing centre[1]. However, a subsequent fitting procedure was done in order to adapt this $\cos^6(x)$ functional shape to a polynomial, as required by the PBCOR task. The required fitting function has the following shape:

$$p(x) = 1.0 + x\frac{a}{10^3} + x^2\frac{b}{10^7} + x^3\frac{c}{10^{10}} + x^4\frac{d}{10^{13}} + x^5\frac{e}{10^{16}} \tag{8.1}$$

where x is the distance from the phase centre in arcminutes times the frequency in GHz. The result of this fit can be seen in Fig 8.3 and the constants determined from the fit are a $= -1.105$, b $= 5.252$, c $= -1.290$, d $= 0.136$.

The continuum emission was subtracted in the image domain instead of the UV frequency domain. A continuum image was obtained with the AIPS task SQASH, summing up 20 channels in a region where no absorption was expected. Then this image is subtracted to each frequency channel to finally get a continuum-subtracted data cube.

[1]WSRT manual: `http://www.astron.nl/wsrt/wsrtGuide/`

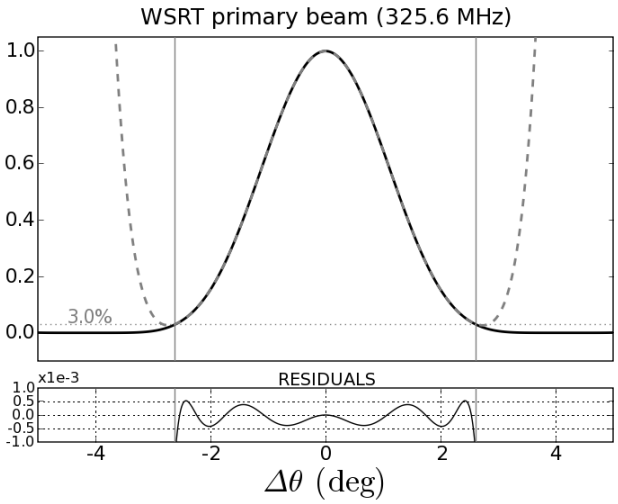

Figure 8.3: Fit to the WSRT primary beam. The thick solid line follows a $\cos^6(\theta)$ law and the dashed line represents the fitted polynomial in the region between the vertical lines.

8.3 Spectrum of J1624+3758

Figure 8.4 shows the continuum-subtracted spectrum of J1624+3758. It was obtained combining for every channel all signal contained within a circle of 2 pixel radius ($\sim$ 38 arcsec) from the source centre. This aperture basically includes the area covered by the synthesised beam. A larger aperture significantly increases the noise of the final spectrum, without adding extra signal.

The H I column density can be estimated from the absorbed radio spectra following Equation 8.2:

$$N(HI) = 1.93 \times 10^{18} \frac{T_{\rm s} \tau_{\rm p} \Delta v}{C_f} \ {\rm cm}^{-2} \tag{8.2}$$

where $T_{\rm s}$ is the spin temperature, $\tau_{\rm p}$ the peak of the absorption line referred to the continuum level, Δv the width of the absorbing feature and C_f the fraction of continuum source covered by the absorber, i.e., the covering factor.

No absorbing feature is present in the observed frequency range, and only an upper limit for the H I column density could be obtained. In order to do that, the local RMS noise σ_{rms} was measured at the expected position of the absorbing feature, and 3-σ_{rms} was inserted in Equation 8.2 instead of τ_p. A value of 30 km s^{-1} was assumed for Δv, and this yields an upper limit of N(H I) $< 9 \times 10^{18}$ T$_s$ cm^{-2}.

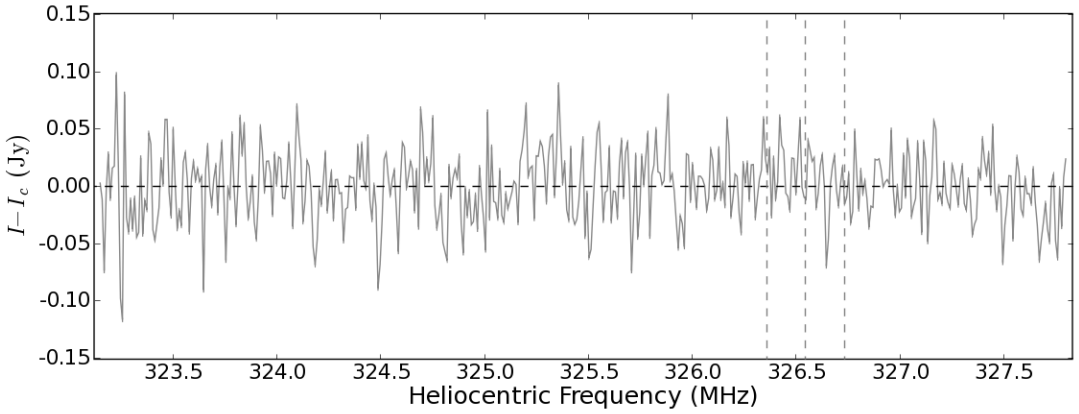

Figure 8.4: Spectrum of the unusual BAL QSO J1624+3758 taken with WSRT. The vertical dotted lines represent the approximated position of the absorption as obtained from the optical spectrum

8.4 Discussion

Despite the difficulty of these observations, several characteristics motivated the search for H I in this unusual high redshift BAL QSO. The outflow signatures seen in the optical spectrum as BAL and mini-BAL systems might possibly extend towards outer, less ionized regions in the form of a neutral hydrogen outflow. In addition, the extremely high RM found in this object could be due to an anomalously high density of H I along the line of sight. From a purely instrumental point of view, the redshift of the source places the expected H I absorption in a frequency range which could be detected by the most sensitive receiver at this band of the WSRT.

Unfortunately the 12-h integration did not allow us to obtain any hint of absorption. The only result that can be extracted from these observations is a not very tight upper limit on the column density of H I against the BAL QSO. If a spin temperature of 140 K is assumed, like that determined by York et al. (2007) in the QSO TXS 0311+430 at z = 2.87, we get an upper limit for the H I column density of about 1.2×10^{21} cm^{-2}.

We can assume that the H I particles are distributed within the volume delimited by the pc-scale structure of the source shown in the VLBA map in Figure 7.8. The angular size of the jet was found to be 75 pc but this is a projected size as measured on the plane of the sky. Assuming a viewing angle of 30 degrees (compatible with the upper limit of 37 degrees determined in Section 7.3) we get a deprojected size of about 150 pc. This gives an upper limit for the H I particle density of 2.7 cm^{-3}.

Given that the RM for this source was determined by Benn et al. (2005), a lower limit for the strength of the magnetic field parallel to the line of sight, $B_{||}$, can be estimated making use of Equations 3.16 and 3.17. Let us consider the previously estimated H I particle density of 2.7 cm^{-3} and assume that the Faraday rotation takes place along the 150 pc corresponding to the deprojected size of the radio jet. This yields $B_{||} \gtrsim 60$ µG. This lower

limit is not very stringent given the obtained limit in the column density, because typical magnetic field strengths are in the range $\sim 0.5-100$ µG in AGN lobes (Hooimeyer et al. 1992), and can be of the order of 1 mG in AGN cores (Taylor 2000).

Apart from obtaining the spectra of J1634+3758, the 5 deg × 5 deg map obtained in these observations contains multi-frequency images for other 50-70 additional sources significantly detected in the surroundings of the target (see e.g. Figure 8.2). The brightest among them are already detected and catalogued in the WENSS survey, but some of them are newly discovered sources. The dataset will thus be useful to study the variability of the brightest sources contained in WENSS, and a catalogue will be created with the new faint sources. In the future, this catalogue might be used to study the local environment of the BAL QSO J1634+3758.

9

Conclusions

THE observations, analysis and discussions presented in the previous chapters have led us to several conclusions, which are summarised here for each chapter, as follows:

These are the conclusions from Chapter 4:

- A sample of 15 BAL QSOs associated with FIRST sources brighter than 15 mJy has been built, which we call the RBQ sample. This was the main working sample for this thesis.

- Additionally, a larger and more homogeneous sample has been defined with a similar FIRST flux density criterion, but based on the QSOs present in the last QSO catalogue from the SDSS-DR5. This sample will be used in the near future to extend the results from this thesis.

These are the conclusions from Chapter 5:

- Radio continuum observations for the RBQ sample have been collected from 2.6 up to 43 GHz in full polarisation. Flux densities covering this radio range have been presented complemented by archive data at lower frequencies from 74 MHz up to 1.4 GHz.

- VLA maps in the most extended configuration of the RBQ sample show very compact morphologies for most sources at all frequencies being unresolved or slightly resolved at 22 GHz with a resolution of 80 mas. These translate into projected linear sizes $\lesssim$ 1 kpc, which are the typical sizes of CSS/GPS sources.

- The spectra of these sources are typically convex, i.e., they seem to become flat or inverted at MHz frequencies probably due to synchrotron self-absorption, while at frequencies higher than 15 GHz they are definitely steeper. The spectra typically peak between 1 and 5 GHz in the observer's frame and about 1/3 of the sample show complex spectra suggesting different components.

- All BAL QSOs in our sample presenting simple convex spectra follow the anticorrelation between projected linear size and turnover frequency found for CSS and GPS sources. Two BAL QSOs with complex radio spectra are also in agreement with this relationship if we consider the lower frequency peak of their spectra. The higher frequency peak might be in this two sources due to emission from a hot-spot or a knot in a jet.

- A high percentage of the sample does not show significant variability when comparing the flux densities in 2 different epochs. Some BAL QSOs show significant variability at 8.4 GHz but not strong enough to exclude them from the candidates to young radio sources.

- Most BAL QSOs in our list are not strongly polarised either at 1.4 GHz or at 8.4 GHz, and sensible upper limits are given at these frequencies. Only two sources show significant polarisation at several frequencies. From these two, only the unusual BAL 1624+37 has a high Rotation Measures suggesting strong depolarisation. The median fractional polarisation of the sample is in better agreement with mean values found in CSS/GPS sources than those found for flat-spectrum quasars.

- A series of statistical tests have been done to compare the spectral index distribution of BAL and non-BAL QSOs finding that these distributions are different. However, no significant differences were found when comparing with compact non-BAL QSOs only. This is consistent with BAL QSOs spanning the same range of orientations as normal quasars with respect to our line of sight to them.

These are the conclusions from Chapter 6

- We have profited from the wide frequency converage in our observations, presented in Chapter 5, in order to model the radio spectra of the BAL QSOs in the RBQ sample. Synchrotron models have been fitted to the high-frequency part of these spectra in order to determine the break frequency, at which synchrotron and inverse-Compton losses start to be important.

- Using the observational parameters collected so far, we have estimated the equipartition magnetic field stength. This was done using two different approaches differing on the dominance given to heavy or light particles in the energy of the system.

- With all the information above, we have obtained the radiative ages of the radio sources associated with the BAL QSOs in the RBQ sample. The derived spectral ages have been found to range between 1 and 50 kyr in the case of dominating protons and heavy particles. These ages could be even smaller in case the electrons are dominating the system, because the equipartition magnetic field increases accordingly. In any case, the derived ages are consistent with those found in other samples of CSS/GPS radio sources, and much smaller than typical ages of more evolved radio sources (with about 10^7 years). This is in agreement with an scenario where BAL QSOs could be objects at the first stages of their evolution.

- The main sources of uncertainty in these calculations have been discussed, stressing the importance of improving the information about the geometry and physical extension of these radio BAL QSOs.

These are the conclusions from Chapter 7

- We have presented VLBA observations at 5.0 and 8.4 GHz of 5 radio bright BAL QSOs. For these sources previous observations allowed us to determine their radio spectra, polarisation characteristics, and precise radio coordinates.

- Three out of the five sources show an unresolved or barely resolved morphology with projected extensions of a few parsecs. Our previous VLA observations of these sources reveal that these are not polarised, which is not consistent with a blazar-like nature of these sources. Alternatively these objects could be very young radio sources, which would explain their low polarisation.

- The unusual BAL QSO 1624+37 show a compact core-jet morphology and we can constrain the orientation of the jet which is at least 37 degrees from the direction of the line of sight. No polarisation information could be extracted from our VLBI observations of this object.

- The luminous BAL QSO 1159+01 has revealed an interesting morphology with the remainders of an inactive jet, and a feature which could be an additional pc-scale jet emerging from the core. These two jets are not aligned but form an angle in the sky of about 50 degrees. The polarisation is more intense in the faint large-scale jet but some polarisation is also found in the emerging jet, with the magnetic field lines being approximately parallel to the advance direction of the jets.

- Merging our list of BAL QSOs with other VLBI observations reported in the literature we end up with a list of 17 radio BAL QSOs and find a variety of morphologies for these objects. The most likely morphologies are either unresolved at mas-scale or core-jet. Only a few sources show compact symmetric or complex structure. We find that those two sources displaying complex morphology show indications of intermittent radio activity and jet realignment, both possibly linked to some merger activity. If this is relatively common among BAL QSOs, this would strongly support an evolutionary scenario to explain the nature of these objects.

These are the conclusions from Chapter 8

- Our 12-h observations with WSRT against the radio BAL QSO J1624+3758 led to a non-detection of H I in absorption. This information was used to get an upper limit for the H I column density of about 1.2×10^{21} cm^{-2} (assuming T_s=140 K). Based on this, we obtained an upper limit for the H I particle density of 2.7 cm^{-3}, which we used together with the RM to obtain a lower limit for the strength of the magnetic field parallel to the line of sight, $B_{||} \gtrsim 60$ µG.

Summarising the previous findings, it seems clear that the analysis of our sample leads to several evidence favouring an evolutionary scheme. In addition, these results are probably difficult to harmonise with the idea of a restricted range of orientations of BAL QSOs. The convex shape of their spectra peaking at MHz frequencies, their radio compactness at pc-scales, the small spectral ages derived, the absence of significant polarisation in most of the objects, and the indications of recurrent radio activity which can be associated to merger events all point to radio BAL QSOs being young sources, probably evolving into normal QSOs.

However, there are still some unknowns to be investigated. For instance, an interesting project that will be developed in the near future will be to measure the presence or not of large amounts of cold dust in radio-loud BAL QSOs. Similar studies in the radio-quiet regime for which the statistics are still not very big, seem to conclude that no differences have been found in terms of dust contents between BAL and non-BAL QSOs. This is, in principle, at odds with the expectations in an evolutionary scenario for the origin of BAL QSOs, and an interesting topic to explore in the radio-loud regime. Observations with current mm and sub-mm telescopes (e.g., IRAM 30-m/MAMBO, APEX/LABOCA-SABOCA, JCMT/SCUBA-2) are being planned for the near future, which will help to shed light on this topic.

And in the classical radio range, further follow-up of the sources studied here will serve to delimit the effect of variability in total flux and also in polarisation. In addition, the analysis of the radio sample of SDSS BAL QSOs defined in Chapter 3 will serve as a test for the conclusions made in this thesis. This larger and more homogeneous sample will allow us to increase the statistics and therefore the significane of the results. Most of the work to be done with this sample will be part of the Ph.D. thesis by Gabriele Bruni at the Istituto di Radioastronomia in Bologna.

A

PypEff: A pipeline to reduce Effelsberg single-dish continuum data

DURING the development of this thesis, several observing runs took place with the 100-m single-dish radio telescope at Effelsberg. Radio continuum observations in full polarisation were collected for this and other projects in those years. The current official reduction tool for this kind of data is the software package TOOLBOX/CONT2[1]. This robust software has been used for decades since it can access the raw data coming from the Effelsberg control system, and allows the user to perform simple reduction and analysis of these data. However, the rigid architecture of CONT2 does not allow to automatise the reduction process when hundreds of sources need to be processed.

With the scope of having reduction and calibration processes less time-consuming and more homogeneous I developed a software package called **PyPEff**, conceived as a pipeline for use with relatively large datasets. PyPEff is based on the Python[2] programming language, and makes use of GLADE[3] which provides it with a graphical user interface (GUI). The lack of documentation about the format of the raw data coming from the Effelsberg system makes it difficult to implement a direct access to the data through Python. For this reason PyPEff makes use of CONT2 to access the original raw data and convert them to easily procesable ASCII files. It is thus a requirement for using PyPEff to have a running version of CONT2 installed in the computer.

A.1 Example of use

In order to run the script one just needs to type:

```
> python PyPEff.py
```

[1] See `http://www.mpifr-bonn.mpg.de/div/hhertz/documents/smtoum/smtoum/node284.html`
[2] See `http://www.python.org`
[3] See `http://glade.gnome.org`

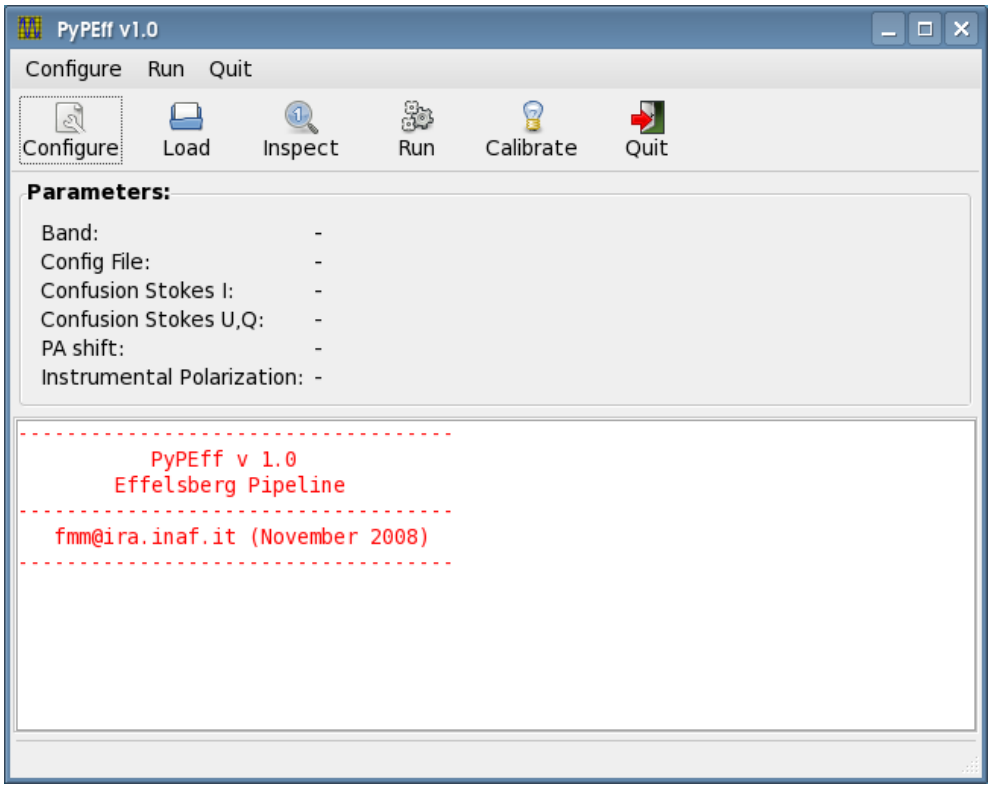

Figure A.1: Main screen of the PyPEff reduction tool for Effelsberg data.

which starts the programme and opens its main window, as shown in Figure A.1. The main window is divided in three regions: the main menu is shown as a series of buttons in the upper part, labeled as *Configure*, *Load*, *Inspect*, *Run* and *Quit*; the second region, labeled as *Parameters*, contains information about the data under analysis. The third region is a white text area where messages can be read at different stages of the data reduction.

The first step is to set those parameters necessary to reduce a certain dataset. Clicking on *Configure* a window appears where such information can be entered (Figure A.2). In practise, only the observing band has to be selected, since the remaining receiver-dependent data appear by default once the band has been selected in the scroll menu. These additional data are the confusion level (in mJy) for each band in total power (Stokes I) and linear polarisation (Stokes Q,U), the offset in the polarisation angle introduced by the directional coupler, and the instrumental polarisation. Once these parameters have been set one has to click *Accept* and these parameters are copied to the corresponding region in the main window.

PyPEff needs a text input file which has to be prepared beforehand in order to start with the reduction (see Section A.2). The next step is thus loading this file from the disk. To do so, one clicks on *Load* which opens a navigation window where the user can select that file. Once selected, PyPEff checks for the syntax of the file and, if this is correct,

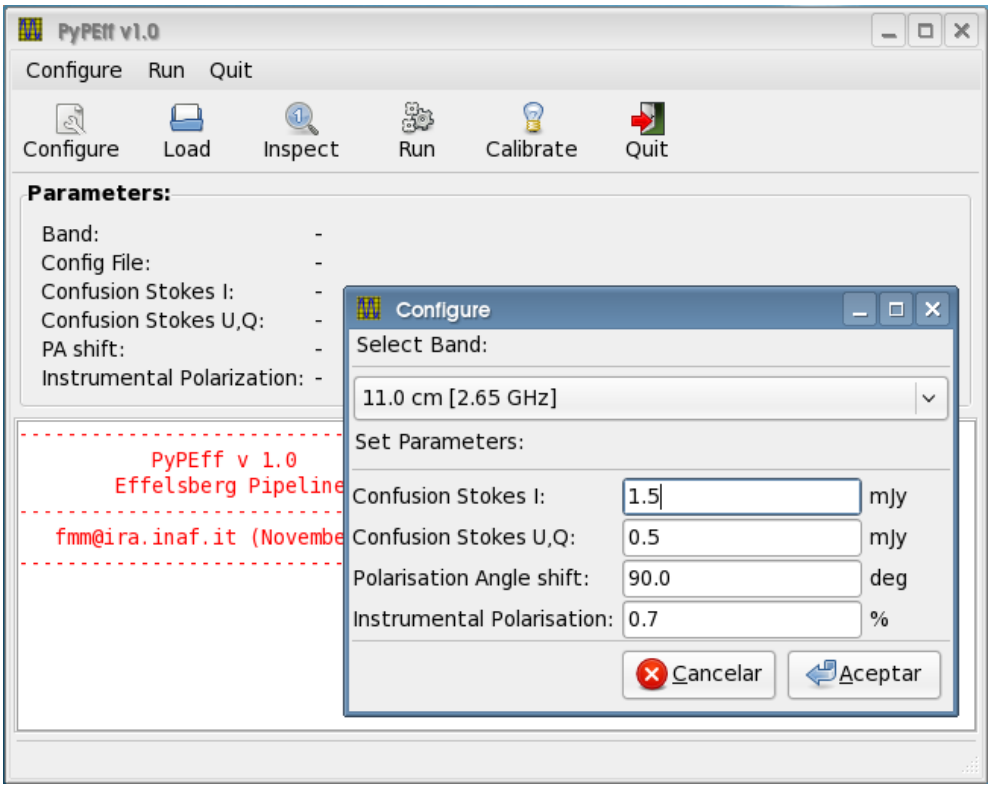

Figure A.2: Configuration window in PyPEff. We select the desired band and the receiver parameters.

the name of the file will also appear in the main window together with the previously set parameters. If the syntax is not correct, the programme notifies it so that the user can correct it.

After this, one presses the *Run* button to start the reduction process. The programme will follow each entry in the input file, processing each scan or group of scans, combining the corresponding subscans, fitting Gaussians to each Stokes channel, obtaining the corresponding fit parameters and writing them to an output file. PyPEff also creates a directory called *png_files* where individual plots for each source are stored showing the quality of the fit and the residuals after subtracting the fitted Gaussian to the original data.

The text area in the main window will show the scan under analysis and a series of warning flags about the quality of each individual fit. This information is also stored in an output file for later inspection in case of problematic sources. A screenshot of the reduction process can be seen in Figure A.3.

Once all the subscans have been processed, the reduction stops and the message *Reduction finished* can be seen in the bottom of the main window.

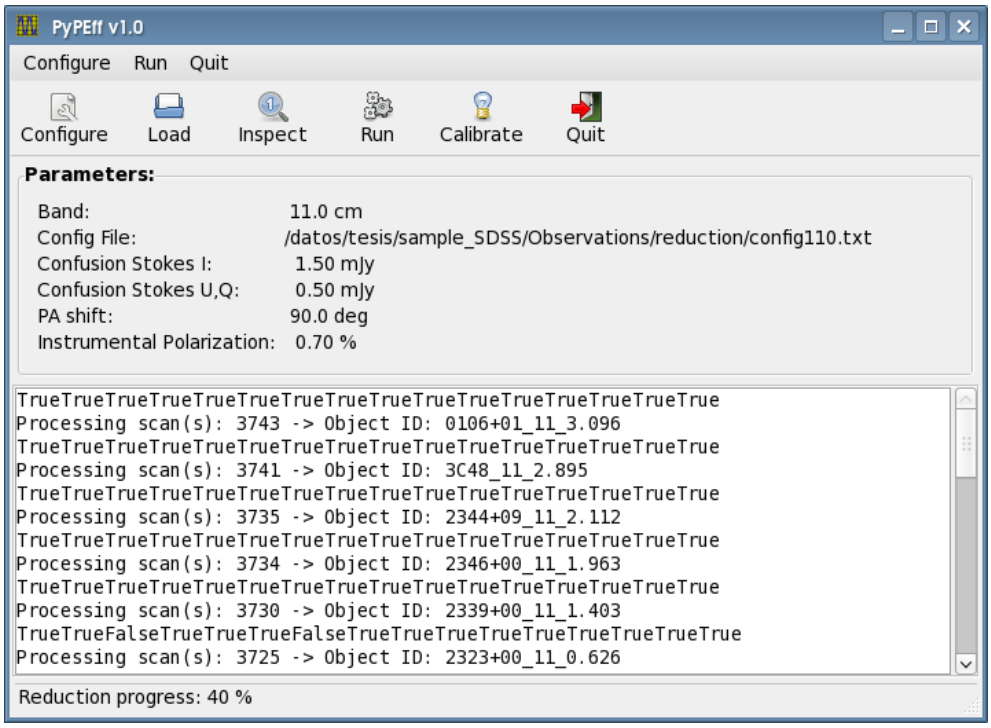

Figure A.3: PyPEff sofware reducing Effelsberg data at 11 cm. The reduction progress is indicated on the bottom-left corner of the window. The main text output shows the scans currently in progress and some flags (True or False) from individual fits.

The text file produced by PyPEff contains uncalibrated flux densities for the different Stokes parameters. In order to convert from arbitrary into physical units a last calibration step has to be done. For PyPEff to do this, the user needs to press the *Calibrate* button. PyPEff looks for all the scans where calibration sources were observed during the observing run. These sources are usually 3C 295 and 3C 286, commonly used as flux density calibrators in single-dish centimetre observations due to their flux density stability and their brightness at these frequencies. The flux densities of these and other sources as a function of frequency were determined by Baars et al. (1977) and their results are the scaling factors that PyPEff uses to calculate the calibrated flux densities of the target sources.

The procedure can be shown in Figure A.4, which was produced by PyPEff. The programme calculates the ratio between the observed and the Baars flux densities for all scans of calibration sources in the run. These are plotted as a function of time. The simplest approach is to get an overall calibration factor for all sources in the run, performing a zeroth-order fit to these data, which is shown as a horizontal dashed black line in Figure A.4. The global error of the calibration is estimated as the standard deviation of the data with respect to this mean value. The 1-σ error can be seen in the plot as two grey dashed lines at both sides of the black line.

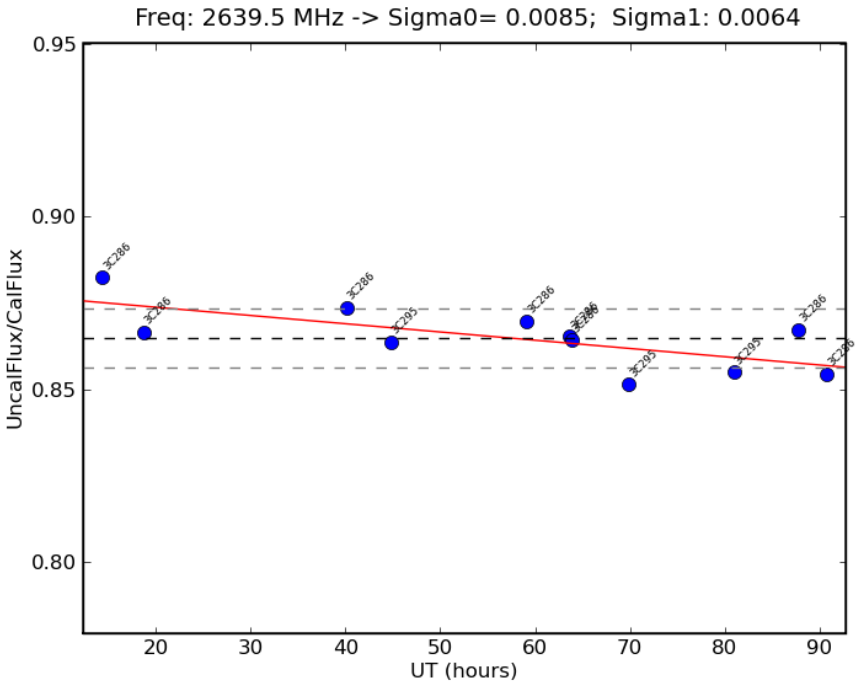

Figure A.4: PyPEff produces a calibration plot with the different calibration sources along the observing run. The horizontal axis shows UT time and the vertical axis shows the ratio between the uncalibrated and calibrated (according to the Baars scale) flux densities. The calibration factor can be determined either by a zeroth- or a first-order fit to the data, with the calibration error being estimated as the standard deviation of the data with respect to this fit.

In some occasions the user might want to perform a first-order fit to the data. The antenna gain can monotonically decrease or increase in certain periods, principally due to variable weather. PyPEff can also perform this fit and calculates the standard deviation of the data with respect to it. Usually both the zeroth- and first-order approaches do not give too different results and for this reason the default is to apply the zeroth-order calibration factor.

Once the calibration has been applied, the calibrated flux densities are written in a second output text file (see Section A.3).

A.2 The input file

PyPEff needs an input text file that specifies the location of the raw data and the list of scans to combine for a given source. This file is loaded into PyPEff to later perform the automatic processing. However, some additional work has to be done in order to prepare this input file.

Each scan is composed by a series of subscans that are later combined to give an im-

proved signal to noise ratio. However, some of these individual subscans can be affected by various problems, like particularly bad weather conditions, occasional baseline instabilities or radio frequency interference. These problematic subscans should be identified and marked in order to exclude them from the final average. The ideal would be to perform this inspection in a way as automatic as possible. In the future, PyPEff will do (at least part of) this work implementing some quality criteria to evaluate every single subscan. However, for the time being this information has to be collected by the user by visual inspection and later included into the input file.

This input file contains two kinds of sentences. Those text lines starting with the word *file* indicate the location of the E-files where the observations are stored as raw data. On the other hand, those lines starting with a number make reference to one or more scan numbers to be averaged. After the scan number(s), the identified subscans to be excluded should be written.

This is an example of this configuration file:

```
------------------------------------------------------------------------
file ../Efiles/E14
3418 X
3429 6,7,8,9,10,11,12
3449 X
3467 12
3478 X
3532 X
3544 X
3562,3563 X X
3566 X
3569 X
3570,3571 X 10
3574 X
3580,3581,3583,3584 X X X X
3588,3589 X X
3595 X
3606,3607 X 1
3613 7,8,9,10,11,12
3638 X
3653 7,8,9,10,11,12
3704 3,4,7,8,9,11
3708 X
3710 1,2,3,4,5,6,7,8
3725 X
3730 X
3746 2,4,7,8,9,10,11,15
3749 X
3750 X
3753 2
3756 1,2,3,4,5,6,7,8,9,10,11,12
3757 X
3766 X
3771 1
file ../Efiles/E15
```

```
3786 X
3787 1,3,4,5
3826 1,2,3,4,5,6
3857 1,4
3866,3867 X X
3876 7,8,9,10,11,12
3930 X
3932 X
3999 X
4004 6,7,8,9,10,11,12
4010 3,5,6,8,9,11
4023 X
4024 1
4025 4,7,8,9,10,11,12
4033,4034 7,8,9,10,11,12 5,6,7,8
--------------------------------------------------------------------------
```

The programme performs the reduction sequentially following the scans in this file. This means that scan number 3418 will be processed first, followed by 3429 immediatly afterwards. After processing scan number 3771 the programme needs to open file E15, since the next scan (3786) and the remaining ones are included in this new file.

When there are two or more scans containing data from the same source which should be combined together, the two scan numbers appear at the beginning of the line separated by a comma, like e.g. scans 3866 and 3867. If there is only one scan to combine, there will be only one scan, like e.g. scan number 3730. In this particular case, there is an 'X' symbol after it (separated by a blank space), which means that all subscans in the scan should be combined. However, when reducing scan number 4024, the subscan number 1 should be excluded. Similarly, subscans 4, 7, 8, 9, 10, 11 and 12 should be excluded when combining the data in scan 4025.

When there are various scans to average like in the following line:

```
3580,3581,3583,3584 X X X X
```

there must be as many blocks (separated by blank spaces) of comma-separated lists of subscans as the number of scans to combine. In this particular case there are four scans, and there are four blocks (separated by spaces) which are all of them composed by a single 'X'. However provided that subscans 4 and 5 from scan 3581 and subscans 1, 2 and 3 from scan 3584 had a problem, the same line would appear:

```
3580,3581,3583,3584 X 4,5 X 1,2,3
```

A.3 The output files

Every scan or group of scans to be combined corresponds to a single source. For each source a fit is performed to the signal in Stokes I, Q and U parameters. The fitted functions are Gaussians with the form:

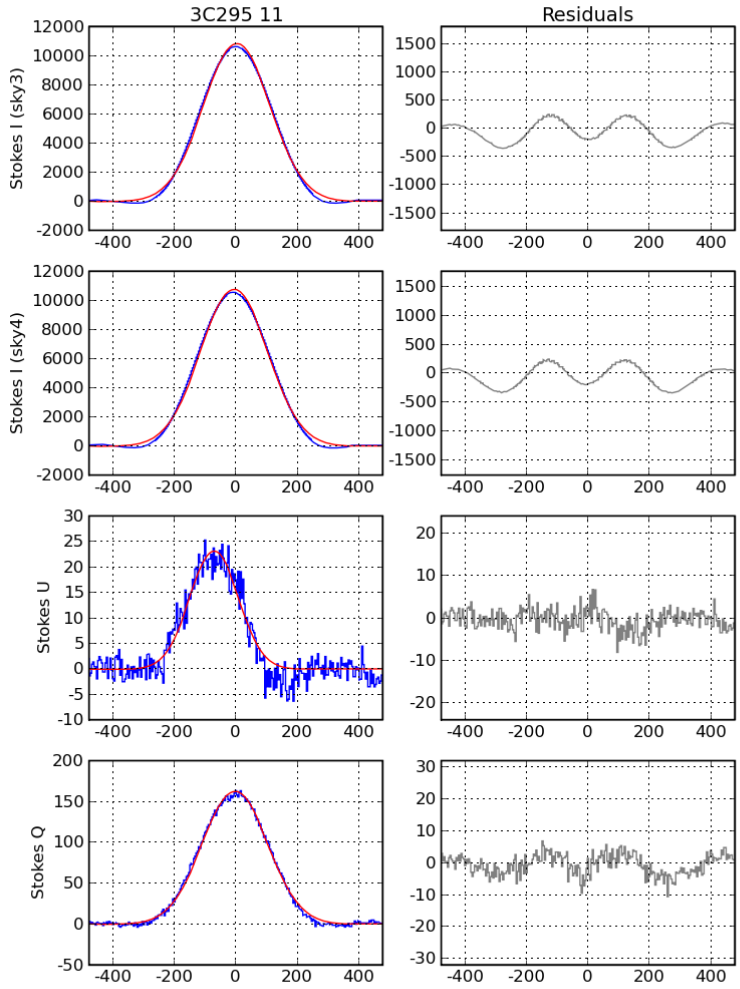

Figure A.5: For each scan or group of scans, PyPEff makes a Gaussian fit in Stokes I, Q and U. The result of the fit and the residuals after subtracting the fit to the data are shown in a plot. Both upper plots correspond to Stokes I and are usually the same. However in some multi-horn receivers it is possible to have different results when subtracting from the "on-source" the "off" sky signal from different horns. The vertical scale is arbitrary since these are uncalibrated data. The horizontal scale is in channels.

$$f(A, x_0, \sigma; x) = A \cdot e^{\left(\frac{x-x_0}{2\sigma}\right)^2} \tag{A.1}$$

and the fitted parameters are the amplitude (A), the central abscissa of the Gaussian

(x_0) and the full-width at half-maximun (σ). All these parameters and their uncertainties are determined by a least-square fit. The most relevant parameter is the amplitude A, which is called S_I, S_Q or S_U following the terminology in Chapter 5. These values are identified with the (uncalibrated) flux densities of the source. From these quantities, it is possible to derive other important information like the degree of polarisation, m, or the polarisation angle, χ, both mentioned in Chapter 5. The expressions for these quantities and their associated uncertainties are described in Klein et al. (2003).

Figure A.5 shows an example of the output plot for a particular scan of the source 3C 295. The two upper rows correspond to Stokes I, while the two lower rows correspond to Stokes U and Stokes Q. The right column shows the residuals after subtracting the fits from the data. The wave pattern that can be seen there, especially when having strong signal, is due to the fact that the shape of the beam is not perfectly described by a Gaussian function. However, the error introduced with this assumption is small as compared to other sources of error like, for instance, the calibration error.

After the PyPEff has reduced all the scans specified in the input file, an output text file is created, named *ffluxes11.txt*, where the 11 accounts for the observing wavelength. This file contains the following information:

```
     name      UT       SI       err_SI    rmsI   SNRI dI    SU     err_SU    rmsU   SNRU dU
-------------------------------------------------------------------------------------------
     3C138   12.018  5016.63      5.8     32.5  154.4 1   454.33      0.8      3.2  143.5 1
     3C138   12.193  4939.40      7.6     44.9  110.1 1   468.04      0.8      3.3  140.8 1
     3C286   17.653  9130.18     14.8     81.3  112.2 1  -774.60      1.0      5.2  149.2 1
  1212+389   17.800    53.67      0.4      2.4   22.8 1    -2.11      0.5      1.0    2.0 0

   SQ      err_SQ    rmsQ   SNRQ dQ PolDg(%) errPolDg upp_Pol paralac  chi    errchi
-------------------------------------------------------------------------------------
 -157.17      0.8     3.5   45.5 1    9.58     0.06      0.3    19.5   164.1      0.3
 -116.07      0.7     2.2   53.4 1    9.76     0.09      0.2    21.8   163.8      0.2
  694.07      1.0     4.2  164.0 1   11.39     0.10      0.2   -30.2    35.7      0.2
    0.00   -999.0     1.3    0.0 0 -999.00  -999.00      9.3     5.8  -999.0   -999.0
```

In this previous example only four sources are shown. The columns indicate: (1) name of the source; (2) time of the observation in UT hours; (3-7) uncalibrated flux density, associated error, rms, signal-to-noise ratio and detection flag (1 if $\mathrm{SNR}_I > 3$, 0 otherwise) for the Stokes I channel; (8-12) Idem for Stokes Q; (13-17) Idem for Stokes U; (18-19) degree of polarisation in percentage and its associated uncertainty; (20) maximum reliable degree of polarisation considering rms_U and rms_Q; (21) parallactic angle of the observation; (22-23) polarisation angle and its associated uncertainty.

After performing the calibration, a similar file is produced, called *calfluxes11.txt*, which includes the same information, but after the calibration factor has been applied.

B

Instrumental Polarisation on the 100-m Radiotelescope Receivers

THE motivation to make this study was to understand the anomalous behaviour of the polarisation measurements in some calibration sources. These sources seemed to present different degrees of polarization when observed at different parallactic angles. This effect was stronger at 2.65 GHz, as can be noted inspecting Table B.1 where several polarization measurements of 3C 286 are shown. These observations were collected in several observing runs for calibration purposes. The collected scientific data were used for different projects including the polarimetric observations of BAL QSOs, presented in the previous chapters of the thesis.

This behaviour was present in all individual observing runs. It is clearly an instrumental effect and nothing related to the calibration sources themselves. In order to understand whether any problem was present in any of the channels Stokes U (S_U) or Stokes Q (S_Q), a chart showing the ratio S_U/S_I as a function of S_Q/S_I was made. Figure B.1 shows such a plot including measurements from several runs.

Ideally, this diagramme should show a section of the Poincaré sphere, i.e., a circle centred in the origin of coordinates and with a radius equal to the degree of polarisation of the source. The reason is that the Stokes parameters are not independent but follow the equation:

$$S_I^2 = S_Q^2 + S_U^2 + S_V^2 \tag{B.1}$$

where S_V accounts for the amount of circular polarization and can be neglected in most extragalactic sources (Weiler & de Pater 1983; Komesaroff et al. 1984).

As can be seen from Figure B.1, the observed points seem to dispose on the graph following a circle, but a clear offset of its origin with respect to the coordinate centre seems to be present. The effect is also visible at higher frequencies although there it appears less evident.

Table B.1: Different polarization measurements of 3C 286 at 2.65 GHz taken during several observing runs in 2005, 2006 and 2007.

Name	S_U (mJy)	U_{RMS} (mJy)	S_Q (mJy)	Q_{RMS} (mJy)	m (%)	$m^{(rms)}$ (%)	PA (deg)	χ (deg)
3C286	−1091.9	5.8	81.2	1.5	10.16 ± 0.09	0.2	−11.4	35.7 ± 0.2
3C286	−533.9	3.3	−808.1	3.8	8.98 ± 0.07	0.2	16.7	33.4 ± 0.2
3C286	−103.7	1.6	−949.8	4.8	8.90 ± 0.07	0.2	28.6	31.7 ± 0.2
3C286	444.9	1.7	−859.8	4.2	9.07 ± 0.07	0.1	43.3	209.6 ± 0.2
3C286	583.8	3.2	−777.7	4.0	9.19 ± 0.07	0.2	47.5	209.0 ± 0.2
3C286	581.0	2.7	−783.9	4.1	9.19 ± 0.06	0.2	47.4	209.1 ± 0.2
3C286	526.8	2.7	−805.0	3.9	9.16 ± 0.07	0.2	45.7	209.1 ± 0.2
3C286	−1089.9	6.0	65.8	1.2	10.15 ± 0.09	0.2	−11.1	35.7 ± 0.2
3C286	−140.4	1.7	−939.6	4.5	8.86 ± 0.07	0.2	27.6	31.8 ± 0.2
3C286	207.5	1.4	−930.3	4.9	8.91 ± 0.08	0.2	36.6	210.4 ± 0.2
3C286	587.0	2.6	−783.2	4.2	9.23 ± 0.07	0.2	47.5	209.1 ± 0.2
3C286	584.3	2.6	−782.2	4.2	9.23 ± 0.07	0.2	47.4	209.0 ± 0.2
3C286	−904.0	5.2	810.1	4.2	11.39 ± 0.10	0.2	−30.2	35.7 ± 0.2
3C286	108.3	1.4	−940.4	5.4	8.88 ± 0.08	0.2	34.6	211.3 ± 0.2
3C286	192.8	1.7	−929.1	5.2	8.89 ± 0.07	0.2	36.8	210.9 ± 0.2
3C286	545.3	3.2	−791.8	4.7	9.11 ± 0.08	0.2	46.5	209.2 ± 0.2
3C286	528.3	3.1	−791.4	5.1	9.08 ± 0.08	0.2	46.1	209.3 ± 0.2
3C286	144.1	1.7	−935.3	5.4	8.86 ± 0.08	0.2	35.6	211.2 ± 0.2
3C286	216.3	2.3	−929.4	6.0	8.90 ± 0.08	0.2	37.5	211.0 ± 0.2
3C286	240.2	1.6	−926.2	4.6	8.90 ± 0.07	0.2	38.1	210.8 ± 0.2
3C286	574.1	2.7	−784.6	4.7	9.14 ± 0.07	0.2	47.2	209.1 ± 0.2
3C286	−885.4	3.9	802.9	3.7	11.38 ± 0.08	0.2	−30.4	35.7 ± 0.2
3C286	−984.9	5.3	694.2	3.4	11.19 ± 0.09	0.2	−26.6	36.0 ± 0.2
3C286	−760.7	3.7	986.4	4.6	11.60 ± 0.09	0.2	−35.9	35.3 ± 0.2

I explain in this appendix how this offset has been determined in the different bands, and how this information has been taken into account in order to correct the observed data used for the thesis. These corrections have been included in the PyPEff reduction package.

There are a few works in the literature which illustrate some methods to calibrate the instrumental polarization introduced by radio receivers. As an example, Turlo et al. (1985) describe a calibration scheme based on the determination of the instrumental Müller matrix, with repeated observations of calibration sources like 3C 48 or 3C 286. They apply their results to the MPIfR 5-GHz three channel receiver. A similar approach has more recently been taken by van Straten (2004) who calibrates the centre element of the Parkes multibeam receiver by observing a pulsar and a radio galaxy.

Here I will follow a similar procedure as the one used by Turlo et al. (1985), making

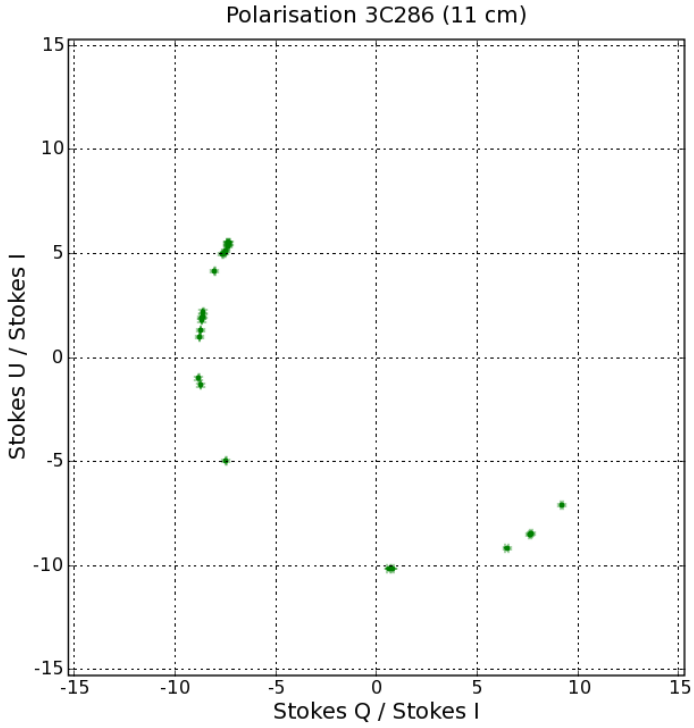

Figure B.1: Stokes diagramme showing the measurements of 3C 286 from Table B.1. The axis are S_U/S_I and S_Q/S_I, but all values have been multiplied by 100, because then the radius of the circle directly gives the percentage of linear polarisation.

use of repeated observations of the sources 3C 48 or 3C 286 taken during several campaigns. However, these observations were not done *ad hoc* and are thus not optimized for this issue. As a consequence, a detailed analysis like that mentioned before will not be done here. The main interest is therefore the determination of the shift that affects the centre of the Stokes circle.

The radio sources 3C 286 and 3C 48 were among the first quasars to be optically identified (Matthews & Sandage, 1963). The quasar 3C 286 is a strong radio source which is known to have a secular stability in flux density (Ott et al. 1994) and has an almost constant degree of polarization, which makes it a reference source for calibration purposes. It is used also to calibrate the polarisation angle which is relatively constant (Taylor & Myers, 2000). This source is also quite compact, which means that can be used as an interferometer flux density calibrator, except at relatively high frequency where it starts to be resolved for some interferometers and in particular configurations (e.g., VLA in A configuration). The Compact Steep Spectrum source 3C 48 has a relatively simple radio spectrum peaking at about 100 MHz. Because its spectrum is quite stable at MHz/GHz frequencies (Baars et al. 1977) and its morphology is quite compact, it is used as interferometer flux density

calibrator. However, Ott et al. (1994) showed that 3C 48 presents some secular variations, so it can be better used as a secondary calibrator, with regular checks of its flux density with that of 3C 286.

B.1 Procedure

The procedure consists of fitting circles to the points in the S_U/S_I vs S_U/S_I representation for both calibration soures. A first consideration is that, since all three Stokes parameters are measured simultaneously, any possible gain instability present in any particular observation (for instance due to bad weather) will affect all of them in the same way. Thus, these two ratios will remain unchanged and the points will appear in the correct position on the plot.

The approach I followed was to make several "best fits" choosing each time a different position for the circle centre. At a first stage an approximate location of the best centre was guessed by eye, and around this position a grid of points was built following both axes. The separation of two adjacent points was chosen to be about 0.01 in each direction. A fit was then done with a circle centred in every point of the grid.

The symmetry of the problem allows one to use polar coordinates where the fitting procedure becomes trivial because only the radius has to be determined. I took as the best radius the weighted average of the distances from the points to the central point, as shown in Equation B.2. The weights were computed from the error estimates of S_I, S_Q and S_U. In other words, ΔS_I, ΔS_Q and ΔS_U were translated into polar coordinates following Equation B.3. The degree of polarisation has been called m and is defined in Equation B.4.

$$M_{best} = \frac{1}{N} \sum_i m_i \cdot w_i \tag{B.2}$$

$$w_i = \Delta m = \sqrt{\left(\frac{\partial m}{\partial U}\right)^2 \Delta S_U^2 + \left(\frac{\partial m}{\partial Q}\right)^2 \Delta S_Q^2 + \left(\frac{\partial m}{\partial I}\right)^2 \Delta S_I^2} \tag{B.3}$$

$$m = 100 \cdot \frac{\sqrt{S_Q^2 + S_U^2}}{S_I} \tag{B.4}$$

For each fit the residuals were then computed, and with those the χ^2 was obtained as an estimate of the goodness of the fit (see Equation B.5).

$$\chi^2 = \sum_i \frac{m_i - M_{best}}{M_{best}} \tag{B.5}$$

The computation of χ^2 for every point in the grid defines a surface of χ^2, of which the minimum will in principle identify the best location for the centre of the circle. This

method was done for both, 3C 286 and 3C 48, in all bands, giving each source a slightly different best solution for the circle centre. As a compromise, the averaged position was chosen between both centres, weighting each position with the χ^2 of the fit. Since 3C 286 is more strongly polarised, this calibrator usually gives a better χ^2, which is then taken into account in the weighted final result.

Table B.2: Final positions determined for the origin of the Stokes circles in each frequency.

Band	3C 286 fit			3C 48 fit			Final results	
	$(Q/I)_c$ (%)	$(U/I)_c$ (%)	χ^2	$(Q/I)_c$ (%)	$(U/I)_c$ (%)	χ^2	$(Q/I)_c$ (%)	$(U/I)_c$ (%)
11 cm	1.66	0.20	0.046	1.60	0.08	0.358	1.65	0.19
6.0 cm	0.00	0.60	1.644	−0.50	0.10	1.802	−0.24	0.36
3.6 cm	−40.30	−0.12	0.270	−0.30	0.06	0.733	−0.30	−0.10
2.8 cm	−0.40	−0.20	4.173	−0.20	−0.40	0.755	−0.23	−0.37

The obtained shifts are given in Table B.2. Figures B.2, B.3, B.4 and B.5, show the Stokes diagrammes with the best fitted circles centred in the determined positions. In addition, the contours indicating constant values of the χ^2 surface are shown for 3C 286 and 3C 48.

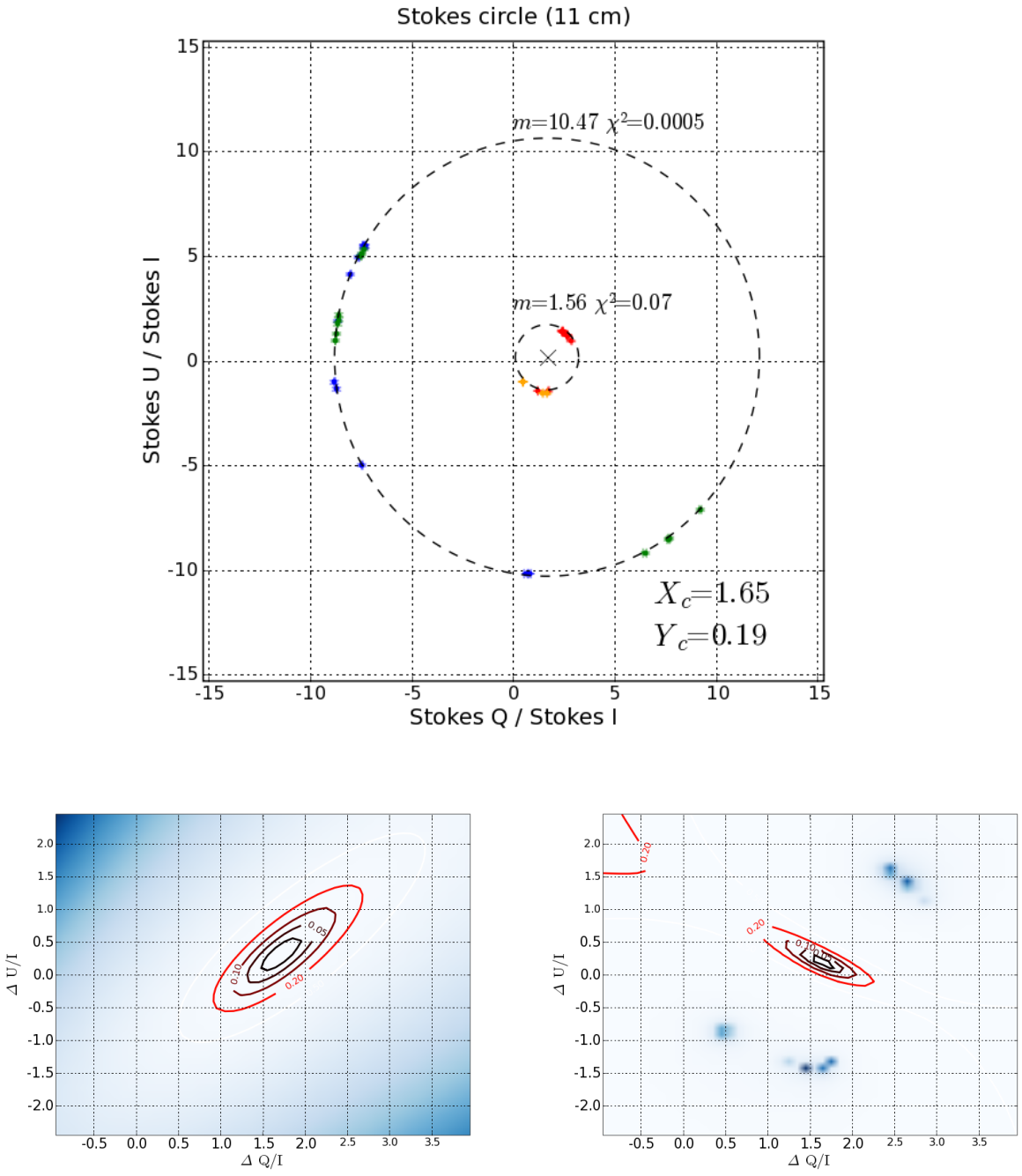

Figure B.2: *T*op: Stokes diagramme at 11.0 cm showing the best fitted circles for 3C 286 and 3C 48. Different colours represent different observing runs. The cross marks the "weighted" best circle centre. *B*ottom: Coloured representation of the χ^2 surfaces with stronger blue meaning higher χ^2. The contour levels indicate values of constant χ^2. The left plot corresponds to 3C 286 and the right one to 3C 48

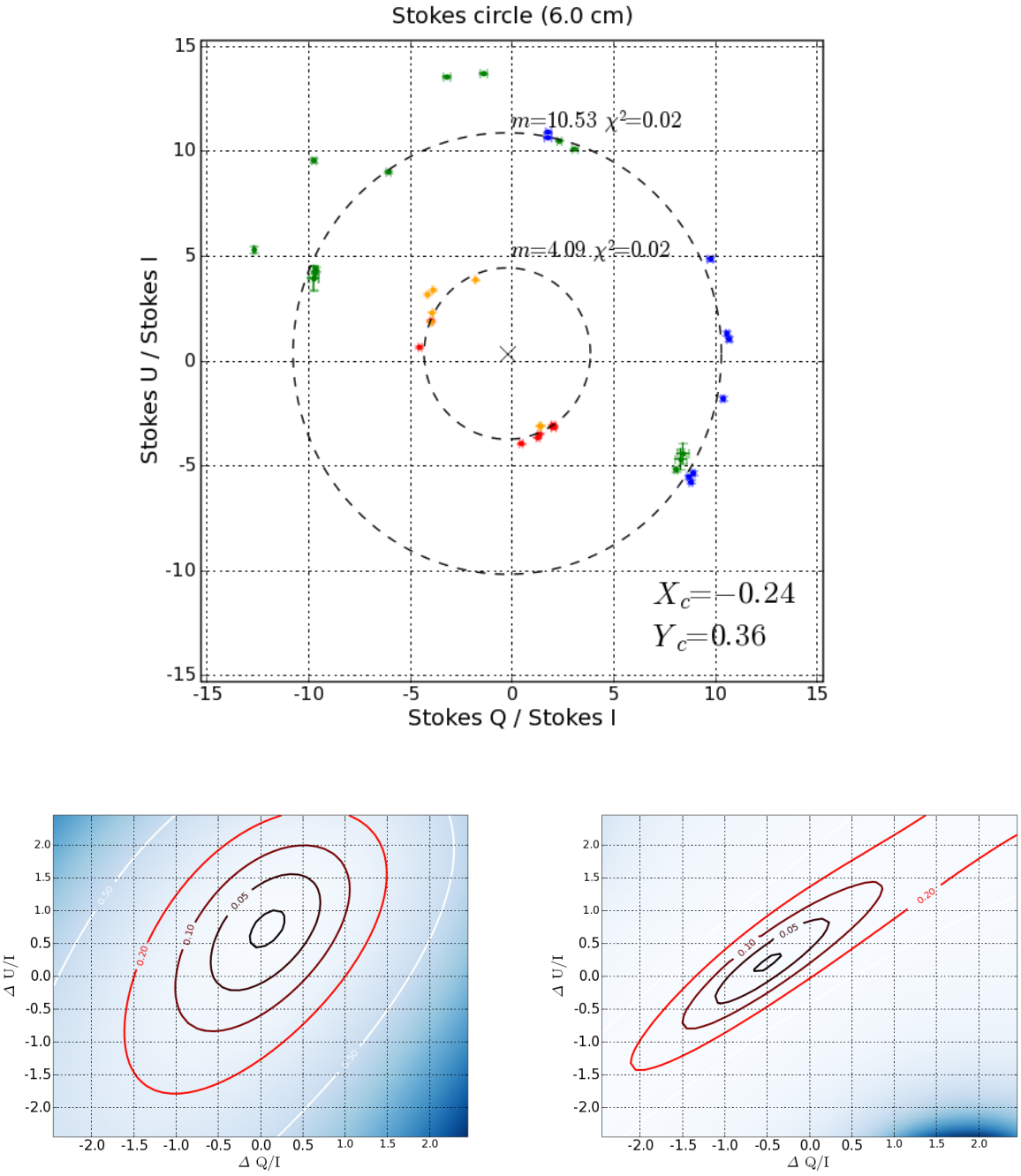

Figure B.3: Idem as in Figure B.2 but at 6.0 cm. The four green points and the two yellow ones in the upper left side of the corresponding circle were considered outliers and were not considered in any fit.

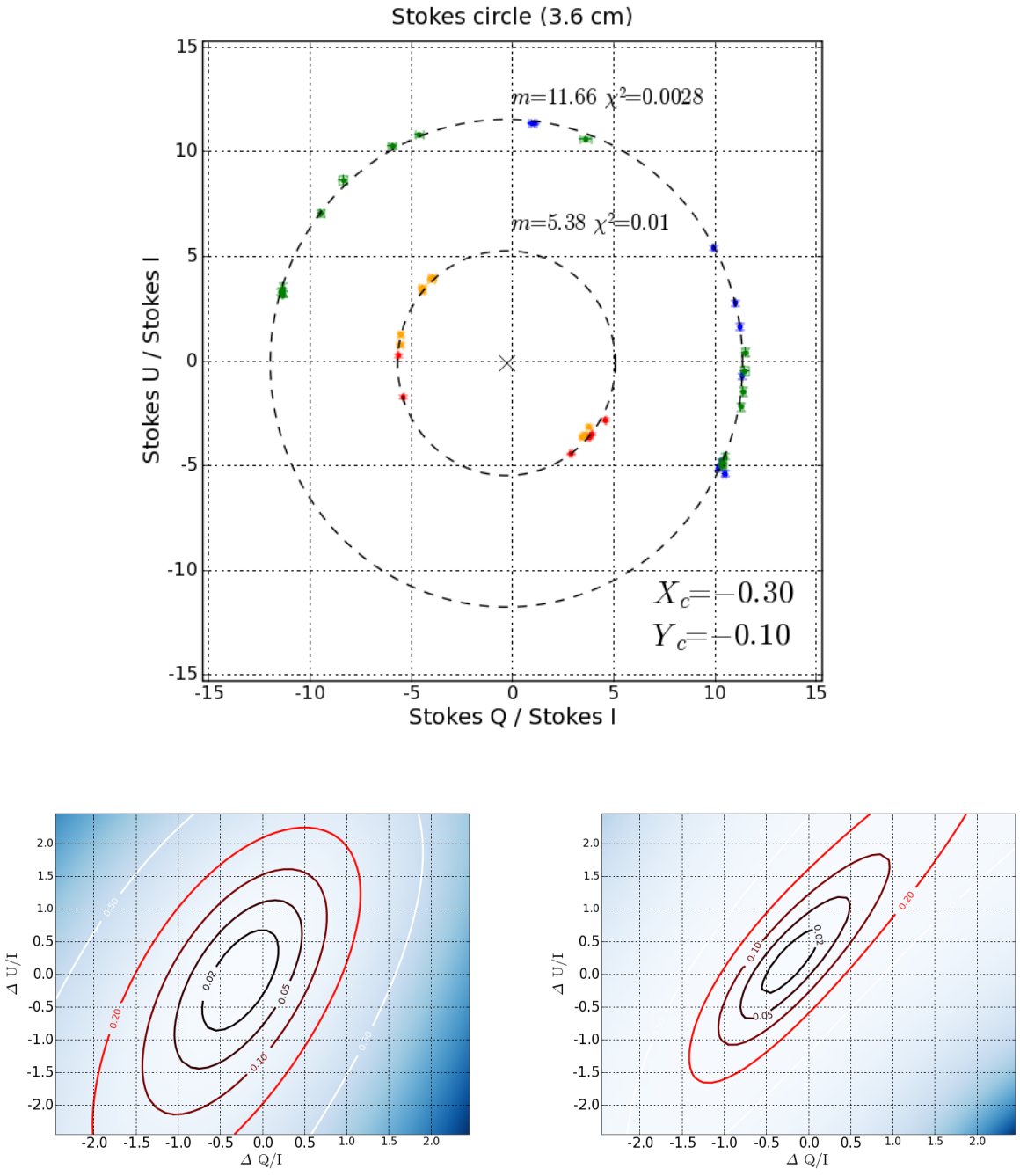

Figure B.4: Idem as in Figure B.2 but at 3.6 cm.

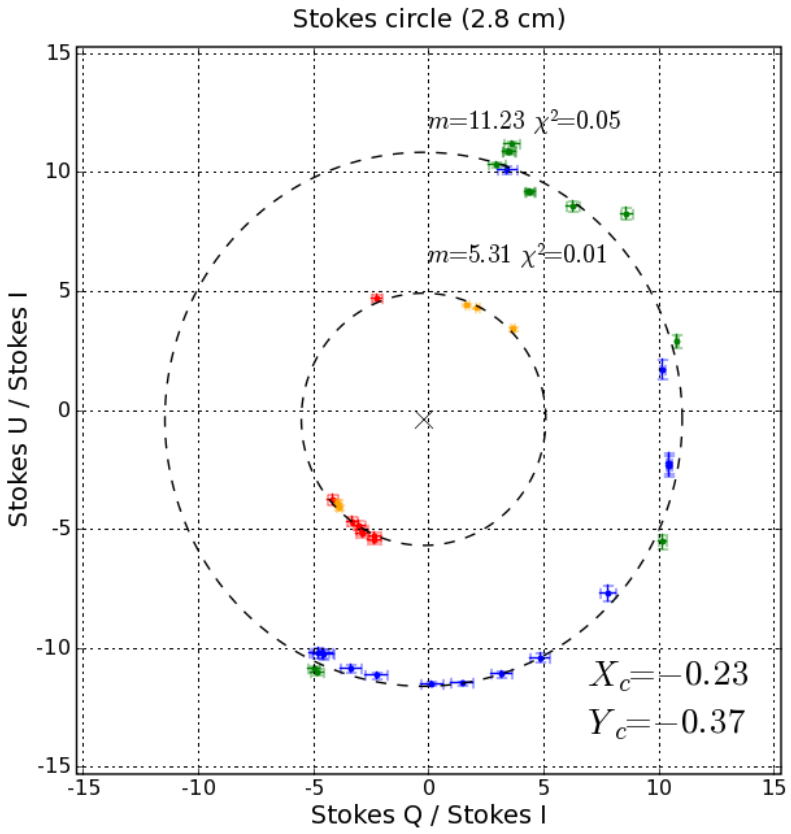

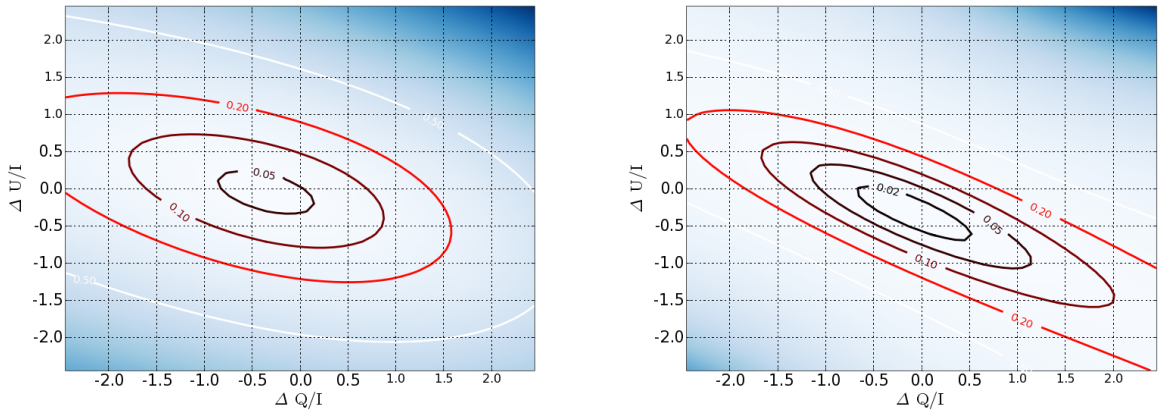

Figure B.5: Idem as in Figure B.2 but at 2.8 cm.

C

List of Acronyms used in this text

In this appendix the list of acronyms used in this work has been summarised for an easy reference. They are listed in alphabetical order:

2MASS – 2-Micron All Sky Survey
AI – Absorption Index
AGN – Active Galactic Nucleus
APM – Automate Plate Measurement facility
ASCA – Advanced Satellite for Cosmology and Astrophysics
BAL – Broad Absorption Line
BAL QSO – Broad Absorption Line Quasar
BI – Balnicity Index
BLR – Broad Line Region
CSO – Compact Symmetric Object
CSS – Compact Steep Spectrum
DI – Detachment Index
DLA – Damped Lyman α
FBQS – FIRST Bright Quasar Survey
FeLoBAL – Fe (iron) Low-ionisation Broad Absorption Line
FIRST – Faint Images of the Radio Sky at Twenty centimeters
FR I – Fanaroff & Riley (galaxy) of type I
FR II – Fanaroff & Riley (galaxy) of type II
GPS – Gigahertz-Peaked Spectrum
GUI – Graphical User Interface
HiBAL – High ionisation Broad Absorption Line
HPQ – Highly Polarised Quasar
HVO – High Velocity Outflow
IR – InfraRed
IRAC – InfraRed Advanced Camera
IRAS – InfraRed Astronomical Satellite
ISO – Infrared Space Observatory

IXO – International X-ray Observatory
LBQS – Luminous Bright Quasar Survey
LLS – Lyman Limit System
LoBAL – Low-ionisation Broad Absorption Line
LVQ – Learning Vector Quantization
MIPS – Multiband Imaging Photometer for Spitzer
NAL – Narrow Absorption Line
NED – NASA Extragalactic Database
NLR – Narrow Line Region
NRAO – National Radio Astronomy Observatory
NVSS – NRAO VLA Sky Survey
PG – Palomar-Green (survey)
PHL – Palomar-Haro-Luyten (stellar object)
POSS – Palomar Observatory Sky Survey
PSPC – Position Sensitive Proportional Counter
QSO – Quasi Stellar Object or Quasar. Some authors distinguish between these two terms but in this work they are considered as equivalent.
RASS – ROSAT All Sky Survey
RM – Rotation Measure
ROSAT – ROetgen SATellite
SDSS – Sloan Digital Sky Survey
SDSS-DRn – Sloan Digital Sky Survey - Data Release n
TNG – Telescopio Nazionale Galileo
UKIRT – United Kingdom InfraRed Telescope
UKIDSS – UKIRT Infrared Sky Survey
ULIRG – UltraLuminous InfraRed Galaxy
UV – UltraViolet
VIPS – VLBA Imaging and Polarimetry Survey
VLA – Very Large Array
VLBA – Very Long Baseline Array
VLBI – Very Long Baseline Interferometry
WENSS – WEsterbork Northern Sky Survey

D

Optical spectra of the radio BAL QSOs

In this appendix, the 66 radio BAL QSOs selected from the SDSS-DR5 QSO catalogue are shown in Figure D.1. The selection criteria for this sample are explained in Chapter 4 and Table 4.8 shows the whole list.

The plots do not show the complete optical spectrum but only the regions where the BAL features are present, always either in Mg II λ 2799 Å or in C IV λ 1549 Å. The plots are similar to those shown in Figure 2.4 and sketch the calculation of the BI, which is written in the upper part of each panel. The green area below the continuum represents the contribution to the BI. However, unlike in Figure 2.4, the continuum was computed fitting a low-order polynomial to the spectrum, selecting by eye the regions where no absorptions or emission features are present. The resulting continuum used in the calculations is presented in the figures as a blue dashed line.

Finally, in Figure D.2, the optical spectrum of the radio BAL QSO 1537+58 studied in Chapter 7 is shown.

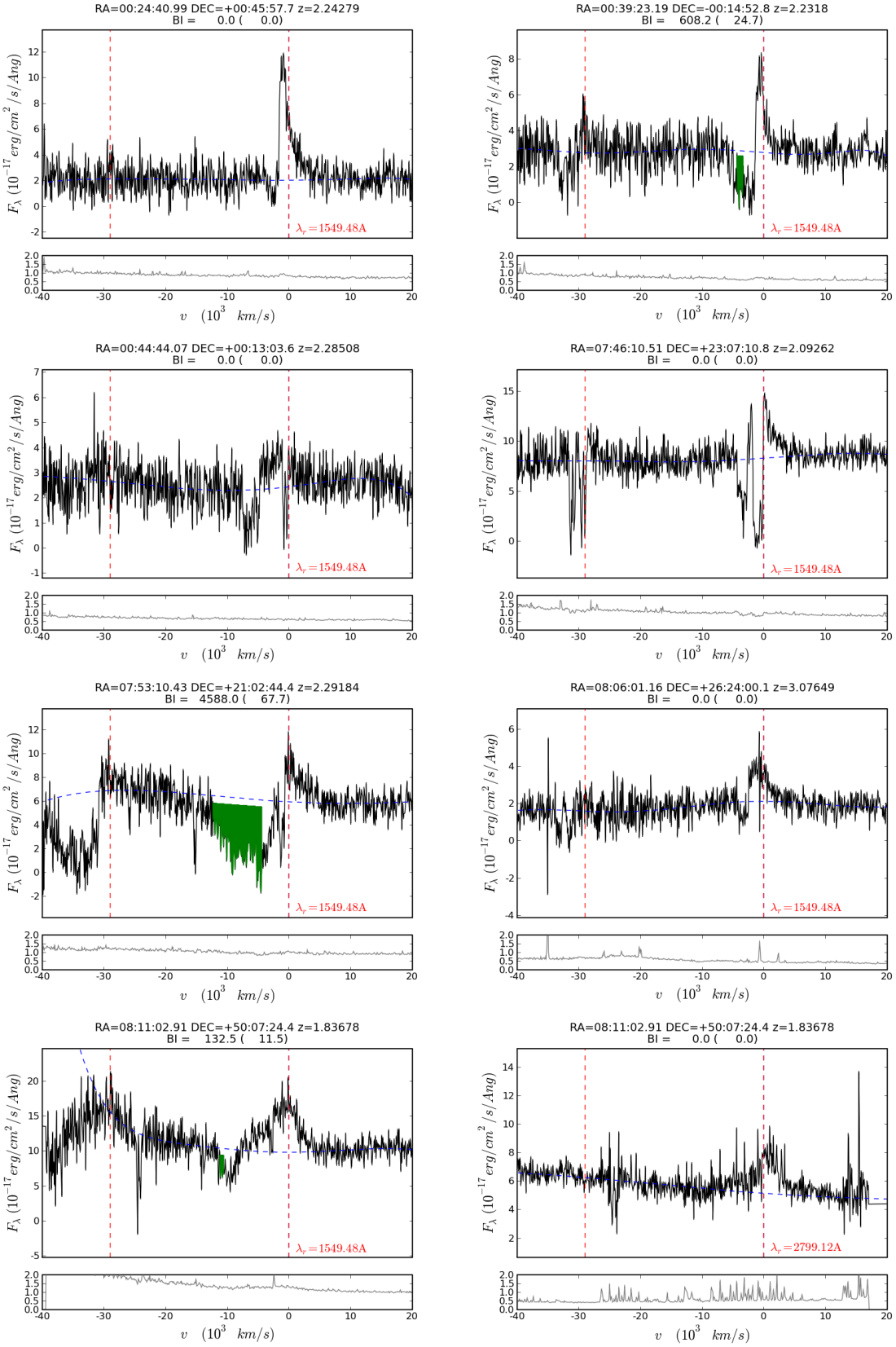

Figure D.1: Plots with the BAL features found in the radio BAL QSO sample selected from the SDSS-DR5.

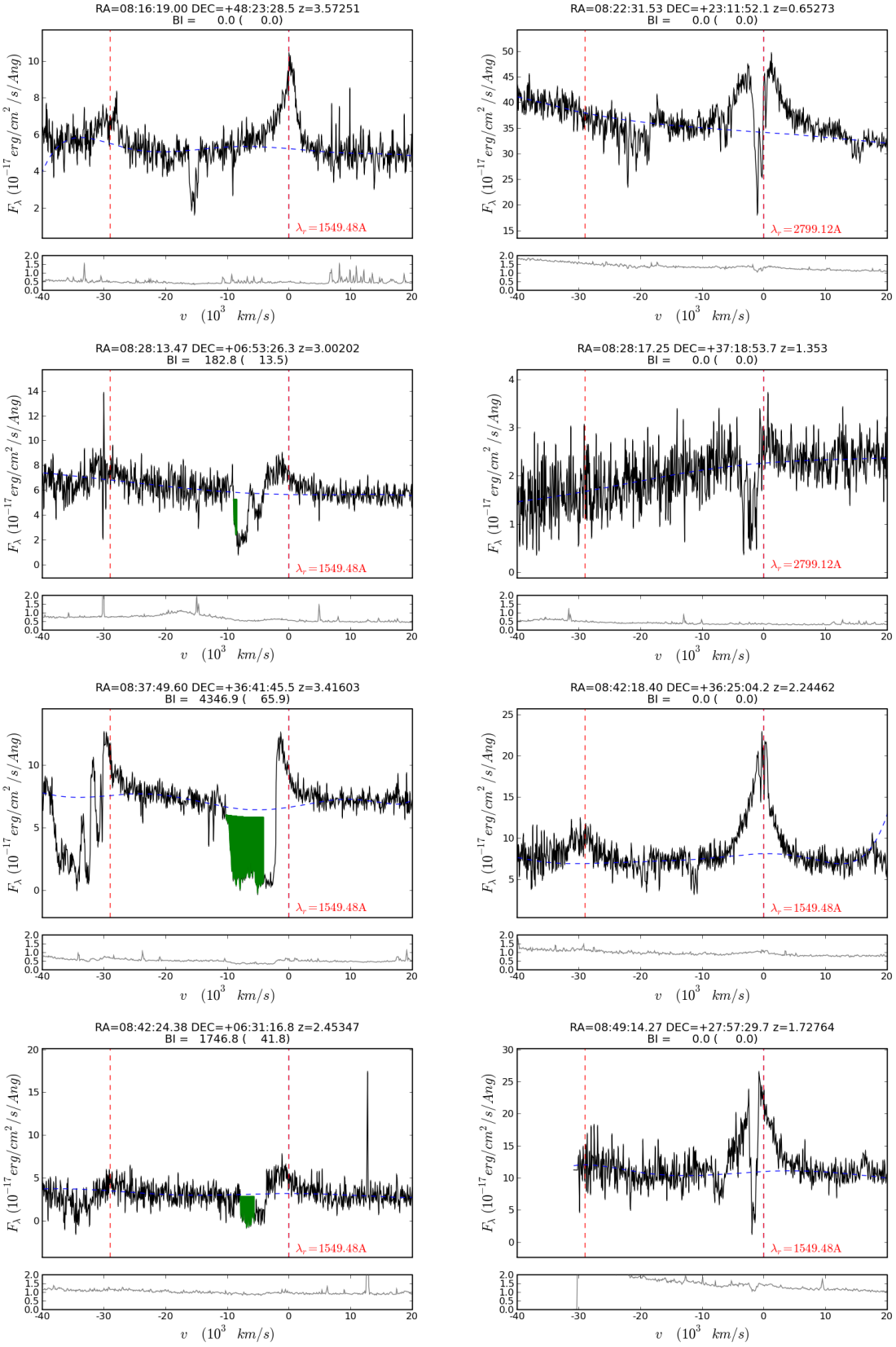

Figure D.1 - Continued

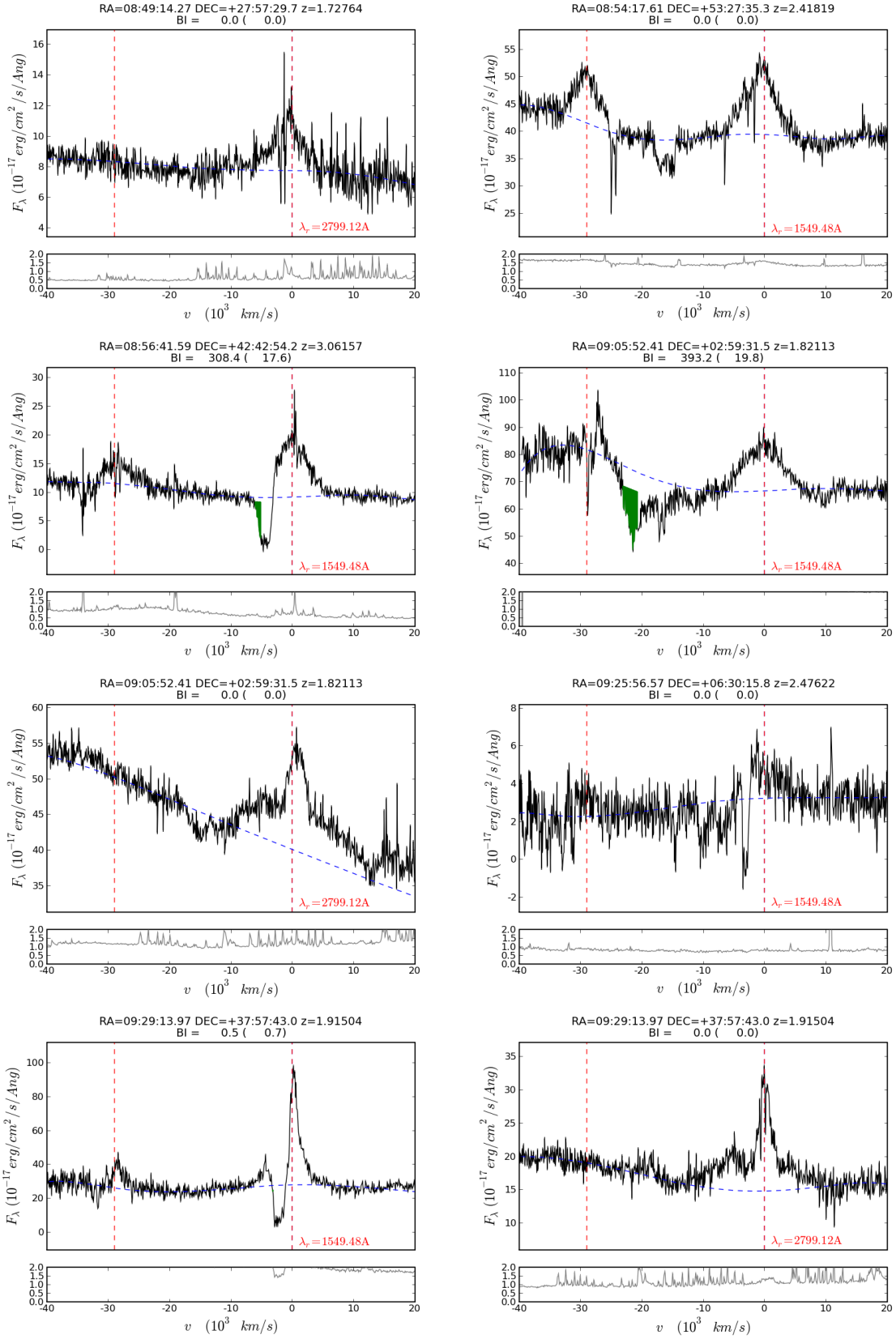

Figure D.1 - Continued

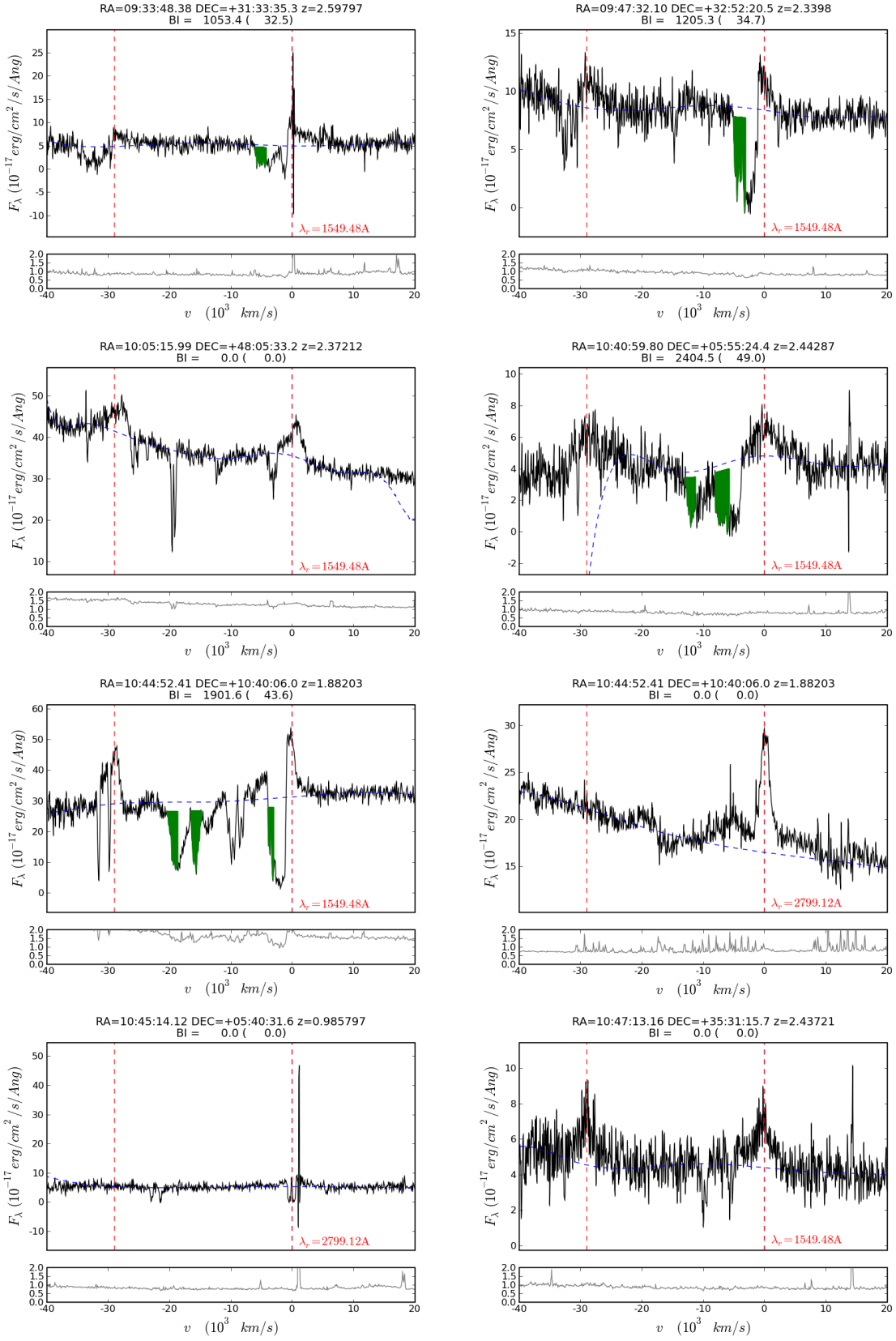

Figure D.1 - Continued

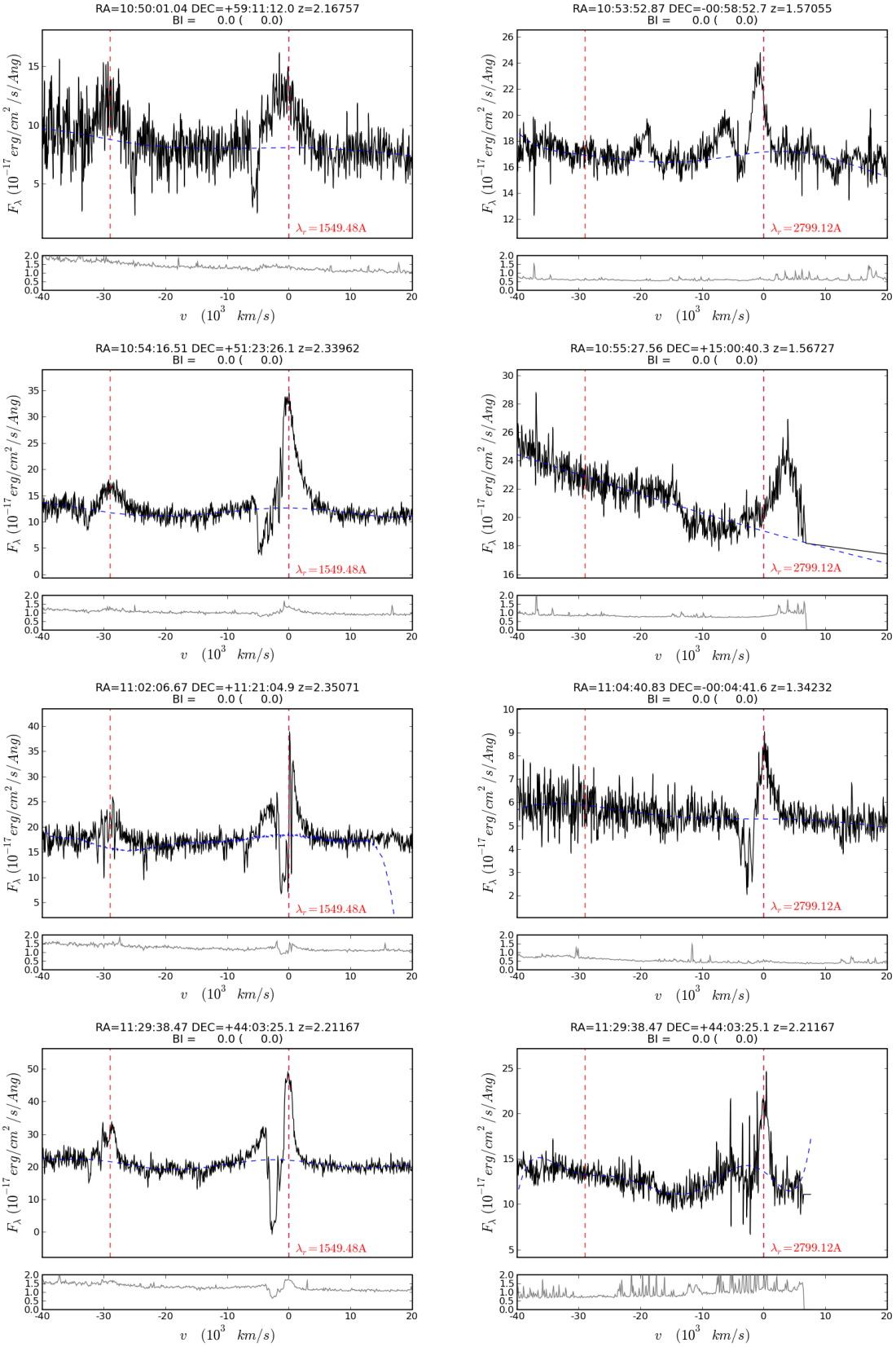

Figure D.1 - Continued

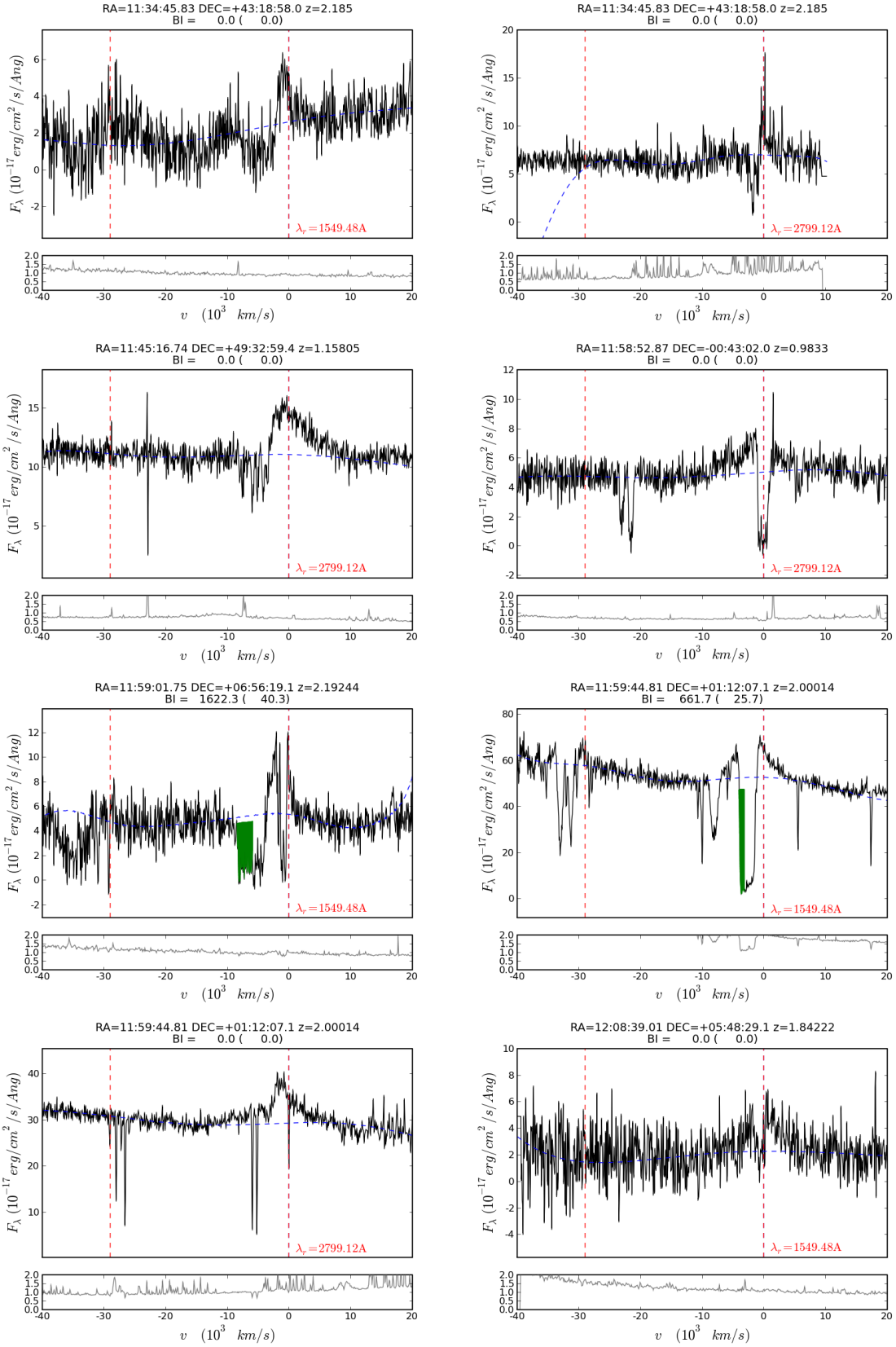

Figure D.1 - Continued

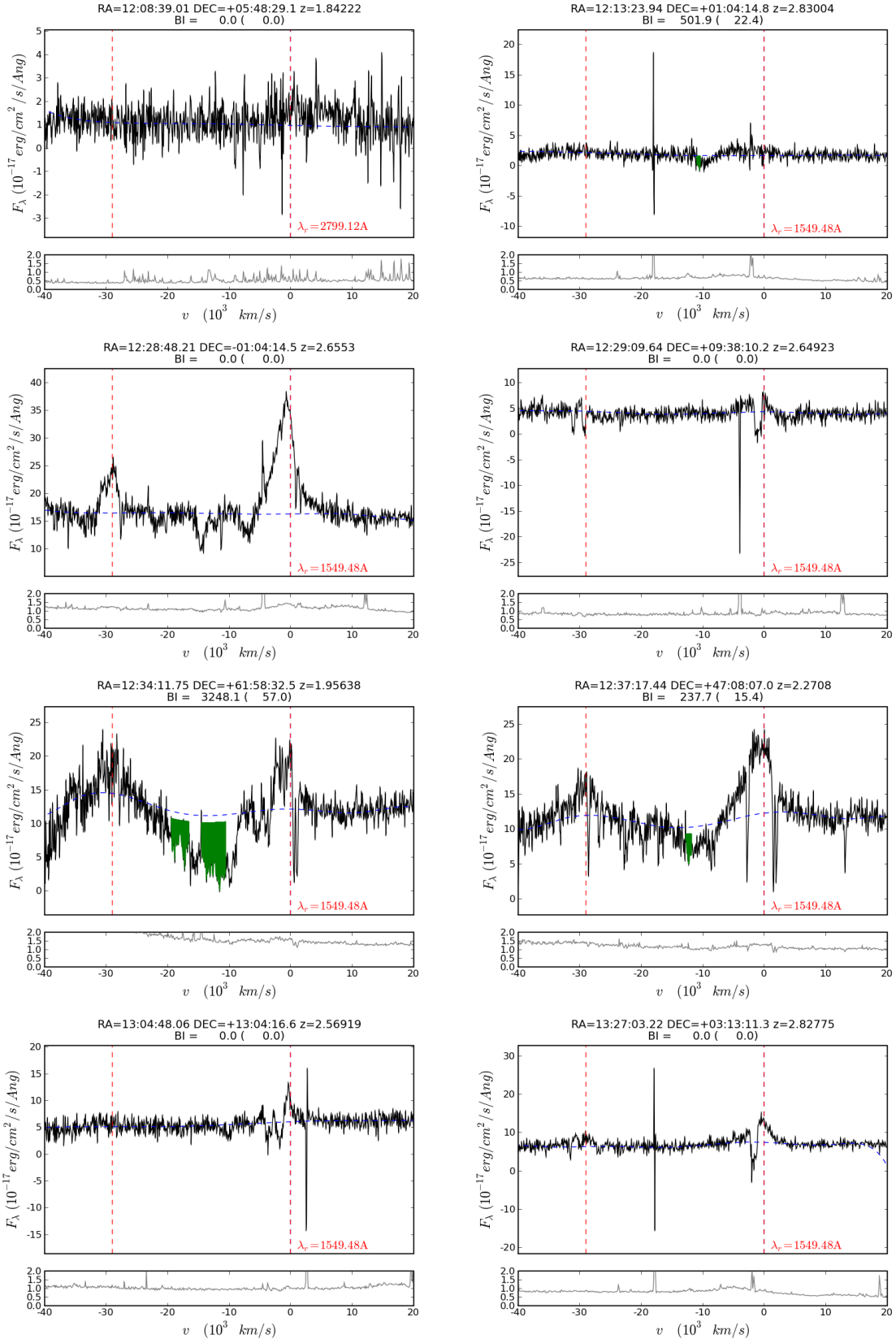

Figure D.1 - Continued

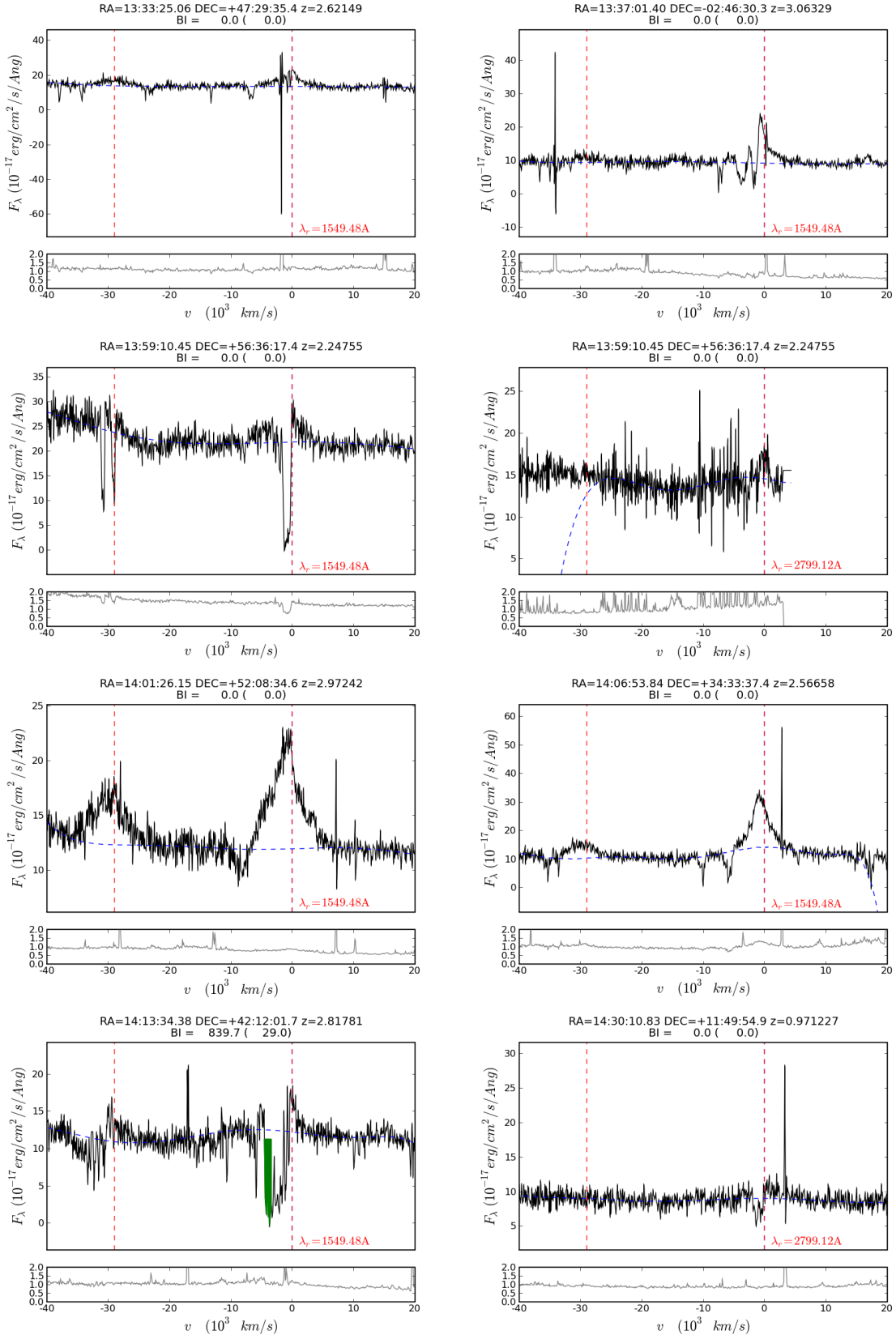

Figure D.1 - Continued

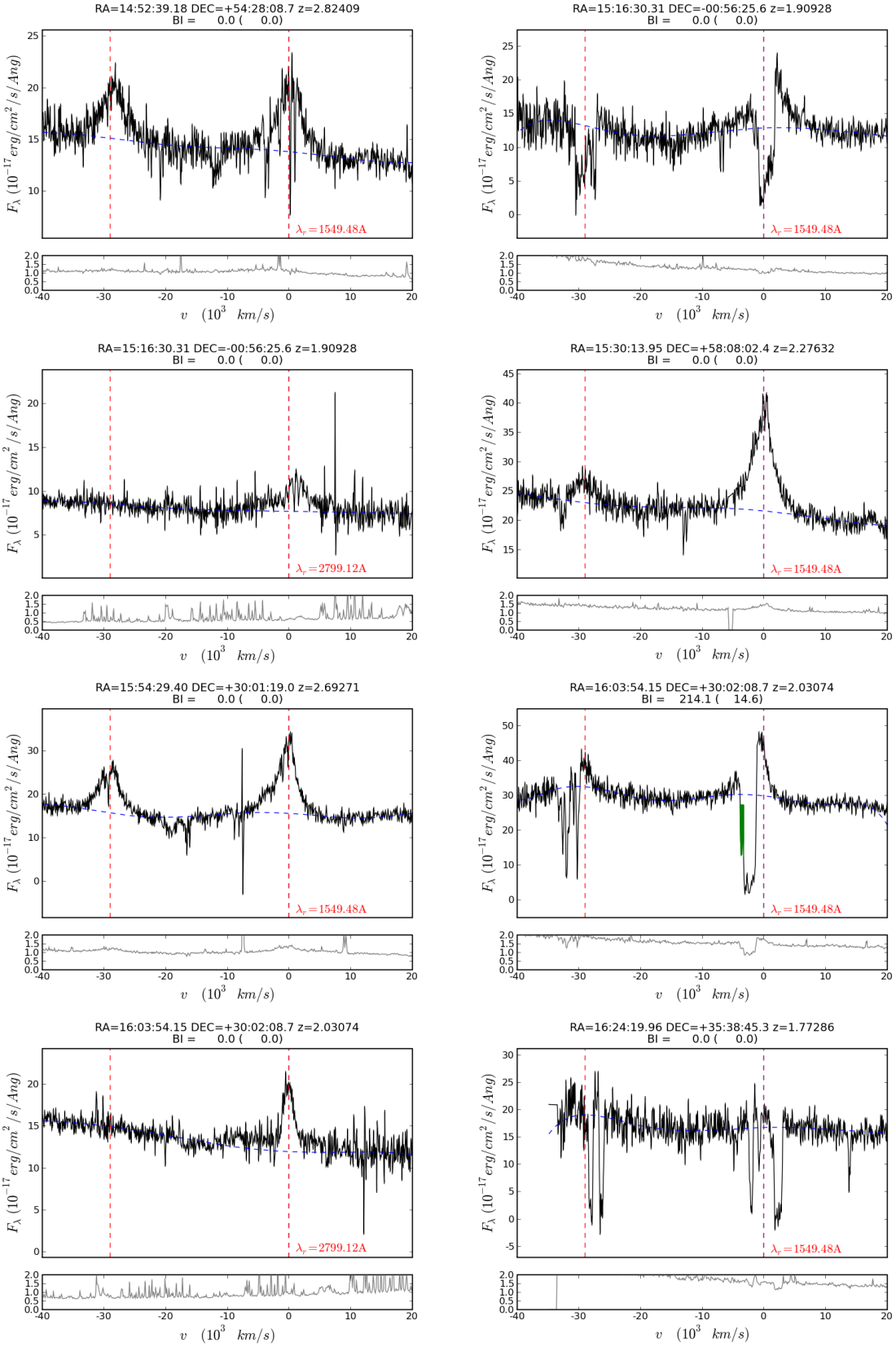

Figure D.1 - Continued

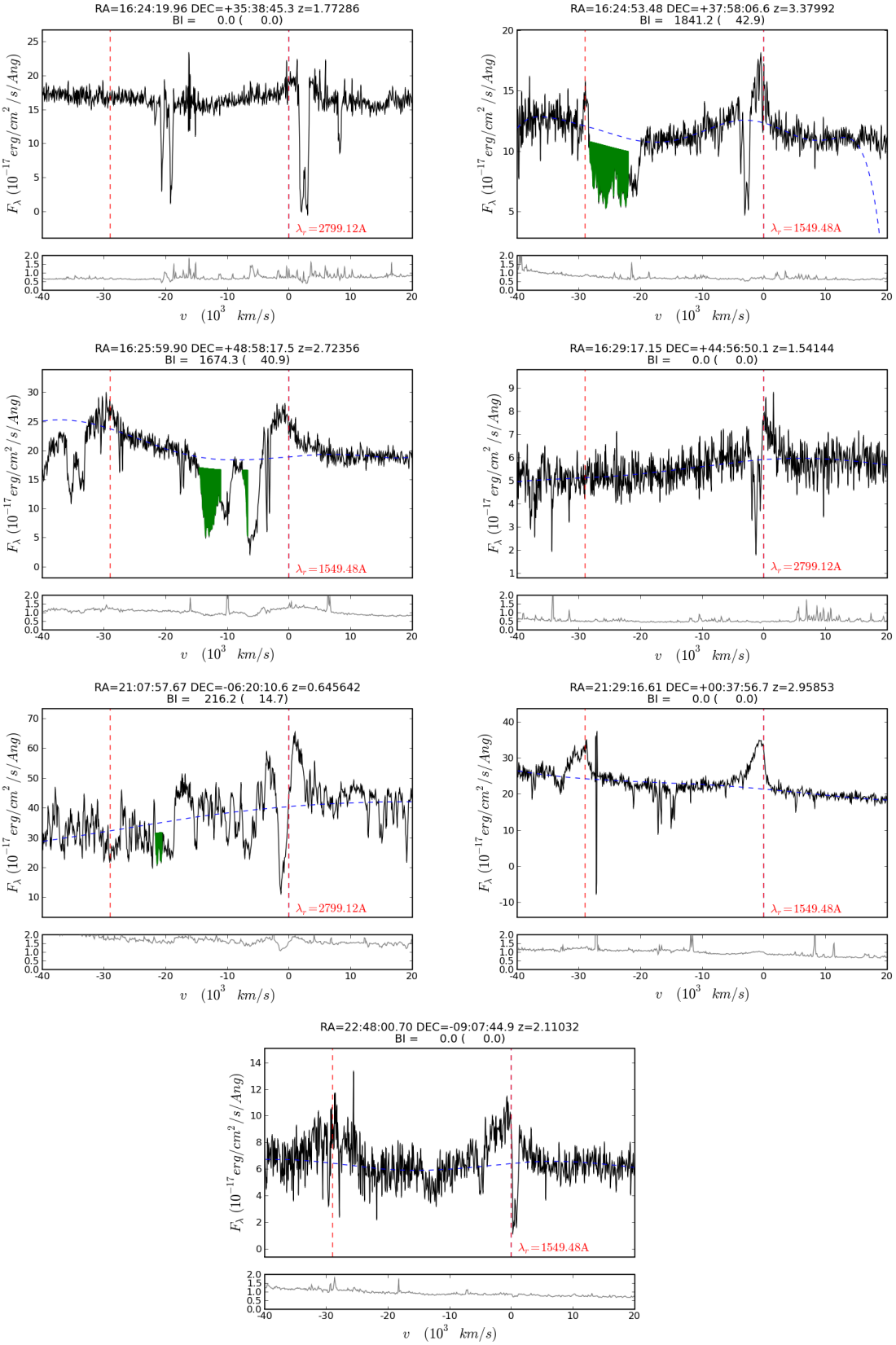

Figure D.1 - Continued

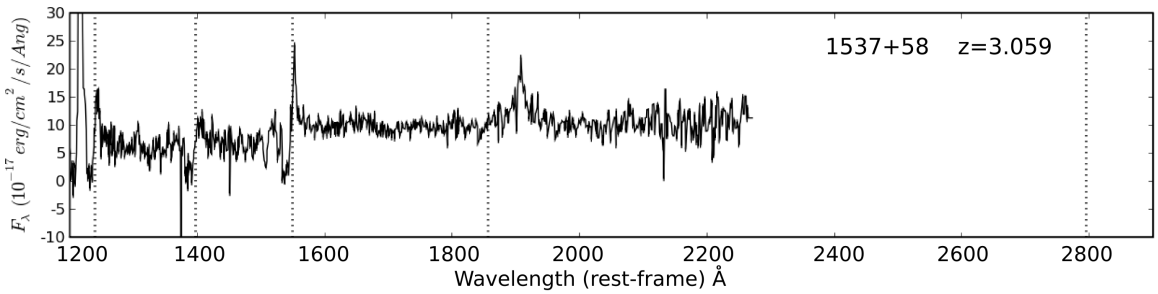

Figure D.2: Rest-frame UV spectra of LoBAL QSO 1537+58. This was not included in the RBQ sample for being slightly fainter than the flux density threshold that defines the sample, although it shares similar characteristics with those BAL QSOs in the RBQ sample. The VLBA map of this source as well as its radio spectrum are shown in Chapter 7 of this thesis. Vertical dotted lines in the optical spectrum mark the positions of the most typical emission lines where BALs can be found: Mg II λ 2799 Å, Al III λ 1857 Å, C IV λ 1549 Å, Si IV λ 1400 Å and N V λ 1240 Å.

Bibliography

Aller M. F., Aller H. D., Hughes P. A., 2003, ApJ, 586, 33

Anderson S. F., Weymann R. J., Foltz C. B., Chaffee Jr. F. H., 1987, AJ, 94, 278

Aoki K., Iwata I., Ohta K., Ando M., Akiyama M., Tamura N., 2006, ApJ, 651, 84

Aoki K., Iwata I., Ohta K., Tamura N., Ando M., Akiyama M., Kiuchi G., Nakanishi K., 2007, in Ho L. C., Wang J.-W., eds, The Central Engine of Active Galactic Nuclei Vol. 373 of Astronomical Society of the Pacific Conference Series, Balmer Absorption Lines in FeLoBALs. pp 337–+

Arav N., 1996, ApJ, 465, 617

Arav N., Korista K. T., Barlow T. A., Begelman M. C., 1995, Nature, 376, 576

Baars J. W. M., Genzel R., Pauliny-Toth I. I. K., Witzel A., 1977, A&A, 61, 99

Baker J. C., Hunstead R. W., Brinkmann W., 1995, MNRAS, 277, 553

Barlow T. A., Hamann F., Sargent W. L. W., 1997, in Arav N., Shlosman I., Weymann R. J., eds, Mass Ejection from Active Galactic Nuclei Vol. 128 of Astronomical Society of the Pacific Conference Series, Partial Coverage and Time Variability of Narrow-Line Intrinsic QSO Absorption Systems. pp 13–+

Barlow T. A., Junkkarinen V. T., Burbidge E. M., Weymann R. J., Morris S. L., Korista K. T., 1992, ApJ, 397, 81

Barlow T. A., Sargent W. L. W., 1997, AJ, 113, 136

Beasley A. J., Conway J. E., 1995, in Zensus J. A., Diamond P. J., Napier P. J., eds, Very Long Baseline Interferometry and the VLBA Vol. 82 of Astronomical Society of the Pacific Conference Series, VLBI Phase-Referencing. pp 328–+

Beck R., Krause M., 2005, Astronomische Nachrichten, 326, 414

Becker R. H., Gregg M. D., Hook I. M., McMahon R. G., White R. L., Helfand D. J., 1997, ApJ, 479, L93+

Becker R. H., White R. L., Gregg M. D., Brotherton M. S., Laurent-Muehleisen S. A., Arav N., 2000, ApJ, 538, 72

Becker R. H., White R. L., Gregg M. D., Laurent-Muehleisen S. A., Brotherton M. S., Impey C. D., Chaffee F. H., Richards G. T., Helfand D. J., Lacy M., Courbin F., Proctor D. D., 2001, ApJS, 135, 227

Begelman M., de Kool M., Sikora M., 1991, ApJ, 382, 416

Benn C. R., Carballo R., Holt J., Vigotti M., González-Serrano J. I., Mack K.-H., Perley R. A., 2005, MNRAS, 360, 1455

Benn C. R., Vigotti M., Pedani M., Holt J., Mack K.-H., Curran R., Sánchez S. F., 2002, MNRAS, 329, 221

Bennett C. L., Lawrence C. R., Burke B. F., Hewitt J. N., Mahoney J., 1986, ApJS, 61, 1

Bicknell G. V., Dopita M. A., O'Dea C. P. O., 1997, ApJ, 485, 112

Blandford R. D., Payne D. G., 1982, MNRAS, 199, 883

Boissier S., Péroux C., Pettini M., 2003, MNRAS, 338, 131

Boroson T. A., Meyers K. A., 1992, ApJ, 397, 442

Briggs F. H., Turnshek D. A., Wolfe A. M., 1984, ApJ, 287, 549

Brotherton M. S., van Breugel W., Smith R. J., Boyle B. J., Shanks T., Croom S. M., Miller L., Becker R. H., 1998, ApJ, 505, L7+

Brunetti G., Setti G., Comastri A., 1997, A&A, 325, 898

Burbidge E. M., 1968, ApJ, 152, L111+

Carballo R., González-Serrano J. I., Benn C. R., Jiménez-Luján F., 2008, MNRAS, pp 1151–+

Carballo R., González-Serrano J. I., Montenegro-Montes F. M., Benn C. R., Mack K.-H., Pedani M., Vigotti M., 2006, MNRAS, 370, 1034

Catinella B., 2008, in Minchin R., Momjian E., eds, The Evolution of Galaxies Through the Neutral Hydrogen Window Vol. 1035 of American Institute of Physics Conference Series, Pushing Arecibo to the Limit: Detection of HI Emission from Galaxies at Redshift z˜0.2. pp 186–189

Chartas G., 2000, ApJ, 531, 81

Cohen A. S., Lane W. M., Cotton W. D., Kassim N. E., Lazio T. J. W., Perley R. A., Condon J. J., Erickson W. C., 2007, AJ, 134, 1245

Cohen M. H., Ogle P. M., Tran H. D., Vermeulen R. C., Miller J. S., Goodrich R. W., Martel A. R., 1995, ApJ, 448, L77+

Condon J. J., Cotton W. D., Greisen E. W., Yin Q. F., Perley R. A., Taylor G. B., Broderick J. J., 1998, AJ, 115, 1693

Cotton W. D., Dallacasa D., Fanti C., Fanti R., Foley A. R., Schilizzi R. T., Spencer R., Saikia D. J., Garrington S., 2003, Publications of the Astronomical Society of Australia, 20, 12

Crenshaw D. M., Kraemer S. B., Boggess A., Maran S. P., Mushotzky R. F., Wu C.-C., 1999, ApJ, 516, 750

Dai X., Shankar F., Sivakoff G. R., 2008, ApJ, 672, 108

Dallacasa D., 2003, Publications of the Astronomical Society of Australia, 20, 79

Dallacasa D., Stanghellini C., Centonza M., Fanti R., 2000, A&A, 363, 887

Dallacasa D., Stanghellini C., Centonza M., Furnari G., 2002, New Astronomy Review, 46, 299

de Bruyn G., Miley G., Rengelink R., Tang Y., Bremer M., Rottgering H., Raimond R., Bremer M., Fullagar D., 2000, VizieR Online Data Catalog, 8062, 0

de Vries W. H., Becker R. H., White R. L., 2006, AJ, 131, 666

de Vries W. H., O'Dea C. P., Baum S. A., Sparks W. B., Biretta J., de Koff S., Golombek D., Lehnert M. D., Macchetto F., McCarthy P., Miley G. K., 1997, ApJS, 110, 191

Dennett-Thorpe J., Scheuer P. A. G., Laing R. A., Bridle A. H., Pooley G. G., Reich W., 2002, MNRAS, 330, 609

Dickey J. M., Lockman F. J., 1990, ARA&A, 28, 215

Djorgovski S., Thompson D. J., Vigotti M., Grueff G., 1990, PASP, 102, 113

D'Odorico V., Cristiani S., Romano D., Granato G. L., Danese L., 2004, MNRAS, 351, 976

Douglas J. N., Bash F. N., Bozyan F. A., Torrence G. W., Wolfe C., 1996, AJ, 111, 1945

Edge D. O., Shakeshaft J. R., McAdam W. B., Baldwin J. E., Archer S., 1959, MmRAS, 68, 37

Egami E., 1999, in Barnes J. E., Sanders D. B., eds, Galaxy Interactions at Low and High Redshift Vol. 186 of IAU Symposium, Low-Ionization BalQSOS: Warm Ultraluminous Galaxies at High Redshifts. pp 475–+

Elvis M., 2000, ApJ, 545, 63

Emmering R. T., Blandford R. D., Shlosman I., 1992, ApJ, 385, 460

Fanaroff B. L., Riley J. M., 1974, MNRAS, 167, 31P

Fanti C., Branchesi M., Cotton W. D., Dallacasa D., Fanti R., Gregorini L., Murgia M., Stanghellini C., Vigotti M., 2004, A&A, 427, 465

Fanti C., Fanti R., Dallacasa D., Schilizzi R. T., Spencer R. E., Stanghellini C., 1995, A&A, 302, 317

Fanti C., Pozzi F., Dallacasa D., Fanti R., Gregorini L., Stanghellini C., Vigotti M., 2001, A&A, 369, 380

Fanti R., Fanti C., Schilizzi R. T., Spencer R. E., Nan Rendong Parma P., van Breugel W. J. M., Venturi T., 1990, A&A, 231, 333

Farrah D., Lacy M., Priddey R., Borys C., Afonso J., 2007, ApJ, 662, L59

Ficarra A., Grueff G., Tomassetti G., 1985, A&AS, 59, 255

Foltz C. B., Chaffee F. H., Hewett P. C., Weymann R. J., Morris S. L., 1990, BAAS, 22, 806

Foltz C. B., Chaffee Jr. F. H., Hewett P. C., MacAlpine G. M., Turnshek D. A., Weymann R. J., Anderson S. F., 1987, AJ, 94, 1423

Foltz C. B., Weymann R. J., Morris S. L., Turnshek D. A., 1987, ApJ, 317, 450

Francis P. J., Hooper E. J., Impey C. D., 1993, AJ, 106, 417

Frey S., Gurvits L. I., Paragi Z., É. Gabányi K., 2008, A&A, 484, L39

Fukugita M., Ichikawa T., Gunn J. E., Doi M., Shimasaku K., Schneider D. P., 1996, AJ, 111, 1748

Gallagher S. C., Brandt W. N., Chartas G., Priddey R., Garmire G. P., Sambruna R. M., 2006, ApJ, 644, 709

Gallagher S. C., Brandt W. N., Sambruna R. M., Mathur S., Yamasaki N., 1999, ApJ, 519, 549

Gallagher S. C., Hines D. C., Blaylock M., Priddey R. S., Brandt W. N., Egami E. E., 2007, ApJ, 665, 157

Ganguly R., Brotherton M. S., 2008, ApJ, 672, 102

Ganguly R., Brotherton M. S., Cales S., Scoggins B., Shang Z., Vestergaard M., 2007, ApJ, 665, 990

Ganguly R., Sembach K., Charlton J., Eracleous M., Palma C., Tripp T., 2004, in Richards G. T., Hall P. B., eds, AGN Physics with the Sloan Digital Sky Survey Vol. 311 of Astronomical Society of the Pacific Conference Series, Instrinsic Narrow Absorption Lines in the HST/STIS Echelle Archive. pp 243–+

Gelderman R. F., 1994, PhD thesis, AA(Virginia Univ. Hospital, Charlottesville, VA.)

Ghosh K. K., Punsly B., 2007, ApJ, 661, L139

Gibson R. R., Brandt W. N., Schneider D. P., Gallagher S. C., 2008, ApJ, 675, 985

Giroletti M., 2004, PhD thesis, Dipartimento di Astronomia, Università di Bologna

Giustini M., Cappi M., Vignali C., 2008, ArXiv e-prints, 809

Goodrich R. W., 1997, ApJ, 474, 606

Green P. J., Aldcroft T. L., Mathur S., Wilkes B. J., Elvis M., 2001, ApJ, 558, 109

Green P. J., Mathur S., 1996, ApJ, 462, 637

Green P. J., Schartel N., Anderson S. F., Hewett P. C., Foltz C. B., Brinkmann W., Fink H., Truemper J., Margon B., 1995, ApJ, 450, 51

Gregg M. D., Becker R. H., de Vries W., 2006, ApJ, 641, 210

Gregg M. D., Becker R. H., White R. L., Helfand D. J., McMahon R. G., Hook I. M., 1996, AJ, 112, 407

Gregorini L., Vigotti M., Mack K.-H., Zoennchen J., Klein U., 1998, A&AS, 133, 129

Greisen E. W., 2003, in Heck A., ed., Astrophysics and Space Science Library Vol. 285 of Astrophysics and Space Science Library, AIPS, the VLA, and the VLBA. pp 109–+

Gugliucci N. E., Taylor G. B., Peck A. B., Giroletti M., 2005, ApJ, 622, 136

Gupta N., Saikia D. J., 2006, MNRAS, 370, 738

Gupta N., Salter C. J., Saikia D. J., Ghosh T., Jeyakumar S., 2006, MNRAS, 373, 972

Haehnelt M. G., Steinmetz M., Rauch M., 1998, ApJ, 495, 647

Hall P. B., 2007, AJ, 133, 1271

Hall P. B., Anderson S. F., Strauss M. A., York D. G., Richards G. T., Fan X., Knapp G. R., Schneider D. P., et al., 2002, ApJS, 141, 267

Hamann F., Barlow T. A., Beaver E. A., Burbidge E. M., Cohen R. D., Junkkarinen V., Lyons R., 1995, ApJ, 443, 606

Hamann F., Murdin P., 2000, Encyclopedia of Astronomy and Astrophysics

Hamann F., Sabra B., 2004, in Richards G. T., Hall P. B., eds, AGN Physics with the Sloan Digital Sky Survey Vol. 311 of Astronomical Society of the Pacific Conference Series, The Diverse Nature of Intrinsic Absorbers in AGNs. pp 203–+

Helmboldt J. F., Taylor G. B., Tremblay S., Fassnacht C. D., Walker R. C., Myers S. T., Sjouwerman L. O., Pearson T. J., Readhead A. C. S., Weintraub L., Gehrels N., Romani R. W., Healey S., Michelson P. F., Blandford R. D., Cotter G., 2007, ApJ, 658, 203

Henstock D. R., Browne I. W. A., Wilkinson P. N., McMahon R. G., 1997, MNRAS, 290, 380

Hewett P. C., Foltz C. B., 2003, AJ, 125, 1784

Hewett P. C., Foltz C. B., Chaffee F. H., 1995, AJ, 109, 1498

Hines D. C., Wills B., 1990, in Bulletin of the American Astronomical Society Vol. 22 of Bulletin of the American Astronomical Society, The Optical Polarization of IRAS QSO's. pp 806–+

Holt J., Benn C. R., Vigotti M., Pedani M., Carballo R., González-Serrano J. I., Mack K.-H., García B., 2004, MNRAS, 348, 857

Holt J., Tadhunter C. N., Morganti R., 2008, MNRAS, 387, 639

Hooimeyer J. R. A., Schilizzi R. T., Miley G. K., Barthel P. D., 1992, A&A, 261, 25

Hopkins P. F., Hernquist L., Martini P., Cox T. J., Robertson B., Di Matteo T., Springel V., 2005, ApJ, 625, L71

Hutsemekers D., Lamy H., Remy M., 1998, A&A, 340, 371

Jaffe W. J., Perola G. C., 1973, A&A, 26, 423

Jansky K. G., 1932 Vol. 20 of IRE Proceedings, Directional Studies of Atmospherics at High Frequencies. pp 1920–+

Jiang D. R., Wang T. G., 2003, A&A, 397, L13

Kaiser C. R., Schoenmakers A. P., Röttgering H. J. A., 2000, MNRAS, 315, 381

Kameno S., Inoue M., Wajima K., Sawada-Satoh S., Shen Z.-Q., 2003, Publications of the Astronomical Society of Australia, 20, 134

Kanekar N., Carilli C. L., Langston G. I., Rocha G., Combes F., Subrahmanyan R., Stocke J. T., Menten K. M., Briggs F. H., Wiklind T., 2005, Physical Review Letters, 95, 261301

Kanekar N., Chengalur J. N., Lane W. M., 2007, MNRAS, 375, 1528

Kardashev N. S., 1962, Soviet Astronomy, 6, 317

Kato T., Tabara H., Inoue M., Aizu K., 1987, Nature, 329, 223

Klein U., Mack K.-H., Gregorini L., Vigotti M., 2003, A&A, 406, 579

Klein U., Mack K. H., Saripalli L., 1996, in Ekers R. D., Fanti C., Padrielli L., eds, Extragalactic Radio Sources Vol. 175 of IAU Symposium, General Properties of Giant Radio Galaxies. pp 311–+

Knigge C., Scaringi S., Goad M. R., Cottis C. E., 2008, MNRAS, 386, 1426

Kohonen T., 2001, Self-Organizing Maps. Self-organizing maps. 3rd ed. Berlin: Springer, 2001, xx, 501 p. Springer series in information sciences, ISBN 3540679219

Komesaroff M. M., Roberts J. A., Milne D. K., Rayner P. T., Cooke D. J., 1984, MNRAS, 208, 409

Korista K. T., Voit G. M., Morris S. L., Weymann R. J., 1993, ApJS, 88, 357

Kunert-Bajraszewska M., Marecki A., 2007, A&A, 469, 437

Kunert-Bajraszewska M., Marecki A., Thomasson P., Spencer R. E., 2005, A&A, 440, 93

Labiano A., 2006, PhD thesis, Space Telescope Science Institute and Kapteyn Astronomical Institute

Lahulla J. F., Merighi R., Vettolani G., Vigotti M., 1991, A&AS, 88, 525

Lamy H., Hutsemekers D., 2004, A&A, 427, 107

Lane W. M., Briggs F. H., 2002, in Mulchaey J. S., Stocke J., eds, Extragalactic Gas at Low Redshift Vol. 254 of Astronomical Society of the Pacific Conference Series, Damped Lyα Absorbers: The 21cm Story. pp 189–+

Lanzetta K. M., McMahon R. G., Wolfe A. M., Turnshek D. A., Hazard C., Lu L., 1991, ApJS, 77, 1

Lanzetta K. M., Wolfe A. M., Turnshek D. A., 1995, ApJ, 440, 435

Lara L., Márquez I., Cotton W. D., Feretti L., Giovannini G., Marcaide J. M., Venturi T., 1999, A&A, 348, 699

Leahy J. P., Parma P., 1992, in Roland J., Sol H., Pelletier G., eds, Extragalactic Radio Sources. From Beams to Jets Multiple outbursts in radio galaxies.. pp 307–308

Lewis G. F., Chapman S. C., Kuncic Z., 2003, ApJ, 596, L35

Lípari S., Terlevich R., Zheng W., Garcia-Lorenzo B., Sanchez S. F., Bergmann M., 2005, MNRAS, 360, 416

Lípari S. L., Terlevich R. J., 2006, MNRAS, pp 390–+

Liu Y., Jiang D. R., Wang T. G., Xie F. G., 2008, MNRAS, 391, 246

Longair M. S., 1981, High energy astrophysics. Cambridge and New York, Cambridge University Press, 1981. 420 p.

Longair M. S., 1994, High energy astrophysics. Vol.2: Stars, the galaxy and the interstellar medium. Cambridge: Cambridge University Press, —c1994, 2nd ed.

Low F. J., Cutri R. M., Kleinmann S. G., Huchra J. P., 1989, ApJ, 340, L1

Lu L., Wolfe A. M., 1994, AJ, 108, 44

Lundgren B. F., Wilhite B. C., Brunner R. J., Hall P. B., Schneider D. P., York D. G., Vanden Berk D. E., Brinkmann J., 2007, ApJ, 656, 73

Lynds C. R., 1967, ApJ, 147, 396

Mack K.-H., Vigotti M., Gregorini L., Klein U., Tschager W., Schilizzi R. T., Snellen I. A. G., 2005, A&A, 435, 863

Maddox N., Hewett P., 2008, in Angelakis E., ed., The Central kiloparsec: AGN and their Hosts Vol. 79 of Memorie de la Società Astronomica Italiana, Investigating Broad Absorption Line Quasars with SDSS and UKIDSS. p. ???

Maddox N., Hewett P. C., Warren S. J., Croom S. M., 2008, MNRAS, 386, 1605

Maiolino R., Oliva E., Ghinassi F., Pedani M., Mannucci F., Mujica R., Juarez Y., 2004, A&A, 420, 889

Marecki A., Thomasson P., Mack K.-H., Kunert-Bajraszewska M., 2006, A&A, 448, 479

Marr J. M., Taylor G. B., Crawford III F., 2001, ApJ, 550, 160

Matthews T. A., Sandage A. R., 1963, ApJ, 138, 30

McMahon R. G., Irwin M. J., 1992, in MacGillivray H. T., Thomson E. B., eds, Digitised Optical Sky Surveys Vol. 174 of Astrophysics and Space Science Library, APM Surveys for High Redshift Quasars. pp 417–+

Menou K., Vanden Berk D. E., Ivezic Z., Kim R. S. J., Knapp G. R., Richards G. T., Strateva I., Fan X., Gunn J. E., Hall P. B., Heckman T., Krolik J., Lupton R. H., Schneider D. P., York D. G., Anderson S. F., Bahcall N. A., Brinkmann J., et al. 2001, ApJ, 561, 645

Miley G., 1980, ARA&A, 18, 165

Misawa T., Charlton J. C., Eracleous M., Ganguly R., Tytler D., Kirkman D., Suzuki N., Lubin D., 2007, ApJS, 171, 1

Momjian E., Carilli C. L., McGreer I. D., 2008, ArXiv e-prints

Montenegro-Montes F. M., Mack K.-H., Vigotti M., Benn C. R., Carballo R., González-Serrano J. I., Holt J., Jiménez-Luján F., 2008, MNRAS, 388, 1853

Morganti R., 2008, in Rector T. A., De Young D. S., eds, Extragalactic Jets: Theory and Observation from Radio to Gamma Ray Vol. 386 of Astronomical Society of the Pacific Conference Series, The Interplay Between Radio Jets and ISM in Sub-kpc Radio Sources. pp 210–+

Morris S. L., Weymann R. J., Foltz C. B., Turnshek D. A., Shectman S., Price C., Boroson T. A., 1986, ApJ, 310, 40

Murdoch H. S., Hunstead R. W., Pettini M., Blades J. C., 1986, ApJ, 309, 19

Murgia M., Fanti C., Fanti R., Gregorini L., Klein U., Mack K.-H., Vigotti M., 1999, A&A, 345, 769

Murray N., Chiang J., Grossman S. A., Voit G. M., 1995, ApJ, 451, 498

Mutoh M., Inoue M., Kameno S., Asada K., Kenta F., Uchida Y., 2002, PASJ, 54, 131

North M., Knigge C., Goad M., 2006, MNRAS, 365, 1057

O'Dea C. P., 1998, PASP, 110, 493

O'Dea C. P., Baum S. A., 1997, AJ, 113, 148

O'Dea C. P., Stanghellini C., Baum S. A., Charlot S., 1996, ApJ, 470, 806

Ogle P. M., Cohen M. H., Miller J. S., Tran H. D., Goodrich R. W., Martel A. R., 1999, ApJS, 125, 1

Orienti M., Dallacasa D., Stanghellini C., 2007, A&A, 475, 813

Orienti M., Dallacasa D., Tinti S., Stanghellini C., 2006, A&A, 450, 959

Orr M. J. L., Browne I. W. A., 1982, MNRAS, 200, 1067

Osmer P. S., Porter A. C., Green R. F., 1994, ApJ, 436, 678

Ott M., Witzel A., Quirrenbach A., Krichbaum T. P., Standke K. J., Schalinski C. J., Hummel C. A., 1994, A&A, 284, 331

Owsianik I., Conway J. E., Polatidis A. G., 1999, New Astronomy Review, 43, 669

Pacholczyk A. G., 1970, Radio astrophysics. Nonthermal processes in galactic and extragalactic sources. Series of Books in Astronomy and Astrophysics, San Francisco: Freeman, 1970

Perley R. A., 1982, AJ, 87, 859

Pihlström Y., Conway J., Vermeulen R., 2003, Publications of the Astronomical Society of Australia, 20, 62

Polatidis A. G., Conway J. E., 2003, Publications of the Astronomical Society of Australia, 20, 69

Popping A., Braun R., 2007, New Astronomy Review, 51, 24

Priddey R. S., Gallagher S. C., Isaak K. G., Sharp R. G., McMahon R. G., Butner H. M., 2007, MNRAS, 374, 867

Prochaska J. X., Wolfe A. M., 1998, ApJ, 507, 113

Proga D., Stone J. M., Kallman T. R., 2000, ApJ, 543, 686

Punsly B., 1999, ApJ, 527, 624

Punsly B., 2006, ApJ, 647, 886

Reichard T. A., Richards G. T., Hall P. B., Schneider D. P., Vanden Berk D. E., Fan X., York D. G., Knapp G. R., Brinkmann J., 2003, AJ

Reichard T. A., Richards G. T., Schneider D. P., Hall P. B., Tolea A., Krolik J. H., Tsvetanov Z., Vanden Berk D. E., York D. G., Knapp G. R., Gunn J. E., Brinkmann J., 2003, AJ

Rengelink R. B., Tang Y., de Bruyn A. G., Miley G. K., Bremer M. N., Roettgering H. J. A., Bremer M. A. R., 1997, A&AS, 124, 259

Richards G. T., Fan X., Newberg H. J., Strauss M. A., Vanden Berk D. E., Schneider D. P., Yanny B., Boucher A., Burles S., Frieman J. A., Gunn J. E., Hall P. B., Ivezić Ž., Kent S., et al. 2002, AJ, 123, 2945

Rodriguez Hidalgo P., Hamann F., Nestor D., Shields J., 2007, in Ho L. C., Wang J.-W., eds, The Central Engine of Active Galactic Nuclei Vol. 373 of Astronomical Society of the Pacific Conference Series, High-velocity Outflows in Quasars. pp 287–+

Rossetti A., Dallacasa D., Fanti C., Fanti R., Mack K.-H., 2008, A&A, 487, 865

Rottmann H., 2001, PhD thesis, Universität Bonn

Rybicki G. B., Lightman A. P., 1986, Radiative Processes in Astrophysics. Radiative Processes in Astrophysics, by George B. Rybicki, Alan P. Lightman, pp. 400. ISBN 0-471-82759-2. Wiley-VCH , June 1986.

Saikia D. J., Salter C. J., 1988, ARA&A, 26, 93

Saikia D. J., Singal A. K., Cornwell T. J., 1987, MNRAS, 224, 379

Sanders D. B., Soifer B. T., Elias J. H., Neugebauer G., Matthews K., 1988, ApJ, 328, L35

Schaye J., 2001, ApJ, 559, L1

Scheuer P. A. G., Wills D., 1966, ApJ, 143, 274

Schlegel D. J., Finkbeiner D. P., Davis M., 1998, ApJ, 500, 525

Schmidt G. D., Hines D. C., 1999, ApJ, 512, 125

Schneider D. P., Fan X., Hall P. B., Jester S., Richards G. T., Stoughton C., Strauss M. A., SubbaRao M., Vanden Berk D. E., Anderson S. F., Brandt W. N., Gunn J. E., Gray J., Trump J. R., Voges W., Yanny B., Bahcall N. A., Blanton M. R., et al. 2003, AJ, 126, 2579

Schneider D. P., Hall P. B., Richards G. T., Strauss M. A., Vanden Berk D. E., Anderson S. F., Brandt W. N., Fan X., Jester S., Gray J., Gunn J. E., SubbaRao M. U., Thakar A. R., Stoughton C., Szalay A. S., Yanny B., York D. G., Bahcall N. A., et al. 2007, AJ, 134, 102

Schneider D. P., Hall P. B., Richards G. T., Vanden Berk D. E., Anderson S. F., Fan X., Jester S., Stoughton C., Strauss M. A., SubbaRao M., Brandt W. N., Gunn J. E., Yanny B., Bahcall N. A., Barentine J. C., Blanton M. R., Boroski W. N., et al. 2005, AJ, 130, 367

Schneider D. P., Richards G. T., Fan X., Hall P. B., Strauss M. A., Vanden Berk D. E., Gunn J. E., Newberg H. J., Reichard T. A., Stoughton C., Voges W., Yanny B., Anderson S. F., Annis J., Bahcall N. A., Bauer A., Bernardi M., et al. 2002, AJ, 123, 567

Schoenmakers A. P., de Bruyn A. G., Röttgering H. J. A., van der Laan H., Kaiser C. R., 2000, MNRAS, 315, 371

Scoville N., Norman C., 1995, ApJ, 451, 510

Shankar F., Dai X., Sivakoff G. R., 2008, ArXiv e-prints

Shen Z.-Q., Shang L.-L., Cai H.-B., Chen X., Jiang D. R., Chen Y.-J., Liu X., Yang R., Kameno S., Hirabayashi H., 2005, ApJ, 622, 811

Shepherd M. C., 1997, in Hunt G., Payne H., eds, Astronomical Data Analysis Software and Systems VI Vol. 125 of Astronomical Society of the Pacific Conference Series, Difmap: an Interactive Program for Synthesis Imaging. pp 77–+

Simard-Normandin M., Kronberg P. P., Button S., 1981, ApJS, 45, 97

Skrutskie M. F., Cutri R. M., Stiening R., Weinberg M. D., Schneider S., Carpenter J. M., Beichman C., Capps R., Chester T., Elias J., Huchra J., Liebert J., Lonsdale C., Monet D. G., Price S., et al. 2006, AJ, 131, 1163

Snellen I. A. G., Mack K.-H., Schilizzi R. T., Tschager W., 2003, Publications of the Astronomical Society of Australia, 20, 38

Snellen I. A. G., Röttgering H. J. A., Barthel P. D., Best P. N., Brüggen M., Conway J. E., Jarvis M. J., Lehnert M. D., Miley G. K., Morganti R., 2009, Astronomische Nachrichten, 330, 297

Snellen I. A. G., Schilizzi R. T., Bremer M. N., Miley G. K., de Bruyn A. G., Röttgering H. J. A., 1999, MNRAS, 307, 149

Snellen I. A. G., Schilizzi R. T., Miley G. K., de Bruyn A. G., Bremer M. N., Röttgering H. J. A., 2000, MNRAS, 319, 445

Sprayberry D., Foltz C. B., 1992, ApJ, 390, 39

Srianand R., Petitjean P., Ledoux C., Hazard C., 2002, MNRAS, 336, 753

Stanghellini C., 1992, PhD thesis, PhD thesis, University of Bologna, (1992)

Stanghellini C., 2003, Publications of the Astronomical Society of Australia, 20, 118

Stanghellini C., O'Dea C. P., Dallacasa D., Baum S. A., Fanti R., Fanti C., 1998, A&AS, 131, 303

Stanghellini C., O'Dea C. P., Dallacasa D., Cassaro P., Baum S. A., Fanti R., Fanti C., 2005, A&A, 443, 891

Stickel M., Kühr H., 1993, A&AS, 101, 521

Stocke J. T., Morris S. L., Weymann R. J., Foltz C. B., 1992, ApJ, 396, 487

Stockman H. S., Moore R. L., Angel J. R. P., 1984, ApJ, 279, 485

Tabara H., Inoue M., 1980, A&AS, 39, 379

Taylor G. B., 2000, ApJ, 533, 95

Taylor G. B., Myers S. T., 2000, NRAO Memo, 26

Tolea A., Krolik J. H., Tsvetanov Z., 2002, ApJ, 578, L31

Torniainen I., Tornikoski M., Lähteenmäki A., Aller M. F., Aller H. D., Mingaliev M. G., 2007, A&A, 469, 451

Torniainen I., Tornikoski M., Teräsranta H., Aller M. F., Aller H. D., 2005, A&A, 435, 839

Tribble P. C., 1993, MNRAS, 261, 57

Trump J. R., Hall P. B., Reichard T. A., Richards G. T., Schneider D. P., Vanden Berk D. E., Knapp G. R., Anderson S. F., Fan X., Brinkman J., Kleinman S. J., Nitta A., 2006, ApJS, 165, 1

Turlo Z., Forkert T., Sieber W., Wilson W., 1985, A&A, 142, 181

van Breugel W., Miley G., Heckman T., 1984, AJ, 89, 5

van Straten W., 2004, ApJS, 152, 129

Vermeulen R. C., Pihlström Y. M., Tschager W., de Vries W. H., Conway J. E., Barthel P. D., Baum S. A., Braun R., Bremer M. N., Miley G. K., O'Dea C. P., Röttgering H. J. A., Schilizzi R. T., Snellen I. A. G., Taylor G. B., 2003, A&A, 404, 861

Vigotti M., Gregorini L., Klein U., Mack K.-H., 1999, A&AS, 139, 359

Vigotti M., Grueff G., Perley R., Clark B. G., Bridle A. H., 1989, AJ, 98, 419

Vigotti M., Vettolani G., Merighi R., Lahulla J. F., Pedani M., 1997, A&AS, 123, 219

Vilkoviskij E. Y., Irwin M. J., 2001, MNRAS, 321, 4

Voit G. M., Weymann R. J., Korista K. T., 1993, ApJ, 413, 95

Wang H.-Y., Wang T.-G., Wang J.-X., 2005, ApJ, 634, 149

Wang H.-Y., Wang T.-G., Wang J.-X., 2007, ApJS, 168, 195

Wang J., Jiang P., Zhou H., Wang T., Dong X., Wang H., 2008, ApJ, 676, L97

Weiler K. W., de Pater I., 1983, ApJS, 52, 293

Weymann R. J., Morris S. L., Foltz C. B., Hewett P. C., 1991, ApJ, 373, 23

Weymann R. J., Morris S. L., Gray M. E., Hutchings J. B., 1997, ApJ, 483, 717

White R. L., Becker R. H., Gregg M. D., Laurent-Muehleisen S. A., Brotherton M. S., Impey C. D., Petry C. E., Foltz C. B., Chaffee F. H., Richards G. T., Oegerle W. R., Helfand D. J., McMahon R. G., Cabanela J. E., 2000, ApJS, 126, 133

White R. L., Becker R. H., Helfand D. J., Gregg M. D., 1997, ApJ, 475, 479

White R. L., Helfand D. J., Becker R. H., Glikman E., de Vries W., 2007, ApJ, 654, 99

Widrow L. M., 2002, Reviews of Modern Physics, 74, 775

Wielebinski R., Krause F., 1993, A&A Rev., 4, 449

Wilkinson P. N., Polatidis A. G., Readhead A. C. S., Xu W., Pearson T. J., 1994, ApJ, 432, L87

Willott C. J., Rawlings S., Grimes J. A., 2003, ApJ, 598, 909

Wills B. J., Netzer H., Wills D., 1985, ApJ, 288, 94

Wolfe A. M., Briggs F. H., 1981, ApJ, 248, 460

York B. A., Kanekar N., Ellison S. L., Pettini M., 2007, MNRAS, 382, L53

York D. G., Adelman J., Anderson Jr. J. E., Anderson S. F., Annis J., Bahcall N. A., Bakken J. A., Barkhouser R., Bastian S., Berman E., Boroski W. N., Bracker S., Briegel C., Briggs J. W., et al. 2000, AJ, 120, 1579

Yuan M. J., Wills B. J., 2003, ApJ, 593, L11

Zheng W., Tsvetanov Z. I., Schneider D. P., Fan X., Becker R. H., Davis M., White R. L., Strauss M. A., Anderson Jr. J. E., Annis J., Bahcall N. A., Connolly A. J., et al. 2000, AJ, 120, 1607

Zhou H., Wang T., Wang H., Wang J., Yuan W., Lu Y., 2006, ApJ, 639, 716

List of publications

- *Effelsberg 100-m polarimetric observations of a sample of compact steep-spectrum sources.* Mantovani, F., Mack, K.-H., **Montenegro-Montes, F. M.**, Rossetti, A., & Kraus, A. 2009, A&A 502, 61.

- *Mid-infrared spectroscopy of infrared-luminous galaxies at $z \sim 0.5$-3.* Hernán-Caballero, A., Pérez-Fournon, I., Hatziminaoglou, E., Afonso-Luis, A., Rowan-Robinson, M., Rigopoulou, D., Farrah, D., Lonsdale, C. J., Babbedge, T., Clements, D., Serjeant, S., Pozzi, F., Vaccari, M., **Montenegro-Montes, F. M.**, Valtchanov, I., González-Solares, E., Oliver, S., Shupe, D., Gruppioni, C., Vila-Vilaró, B., Lari, C. & La Franca, F. 2009, MNRAS 395. 1695.

- *VLBA imaging of radio-loud Broad Absorption Line QSOs.* **Montenegro-Montes, F. M.**, Mack, K. -H., Benn, C. R., Carballo, R., Dallacasa, D., González-Serrano, J. I., Holt, J. & Jiménez-Luján, F. *Proceedings of Science: "The 9th European VLBI Symposium on The Role of VLBI in the Golden Age of Radioastronomy and EVN Users Meeting".* 2009, arXiv:0903.5119

- *Are radio-loud Broad Absorption Line Quasars young sources?* **Montenegro-Montes, F. M.**, Mack, K.-H., Benn, C. R., Carballo, R., González-Serrano, J. I., Holt, J. & Jiménez-Luján, F. 2009, AN 330, 157.

- *Polarimetric observations of a sample of Compact Steep-Spectrum sources.* Mantovani, F., Mack, K.-H., **Montenegro-Montes, F. M.**, Rossetti, A., & Kraus, A. 2009, AN 330, 133.

- *Radio spectra and polarization properties of radio-loud broad absorption-line quasars.* **Montenegro-Montes, F. M.**, Mack, K. -H., Vigotti, M., Benn, C. R., Carballo, R., González-Serrano, J. I., Holt, J. & Jiménez-Luján, F. 2008, MNRAS 388, 1853.

- *A 15 micron Selected Sample of High-z Starbursts and AGNs.* Hernán-Caballero, A., Pérez-Fournon, I., Rowan-Robinson, M., Rigopoulou, D., Afonso-Luis, A., Hatziminaoglou, E., González-Solares, E., **Montenegro-Montes, F. M.**, Vila-Vilaró, B., Farrah, D., Lari, C., Vaccari, M., Babbedge, T., Oliver, S., Clements, D., Serjeant, S., Pozzi, F., La Franca, F., Gruppioni, C., Valtchanov, I. & Lonsdale, C. J. *The Second Annual Spitzer Science Center Conference: Infrared Diagnostics of Galaxy Evolution.* 2008, ASPC 381. 367.

- *Compact radio-loud Broad Absorption Line Quasars.* **Montenegro-Montes, F. M.**, Mack, K. -H., Vigotti, M., Benn, C. R., Carballo, R., González-Serrano, J. I., Holt, J. & Jiménez-Luján, F. 2008, Memorie della Società Astronomica Italiana, 79, 1221.

- *A Search for Molecular Gas in Low-Luminosity Radio Galaxies.* Prandoni, I., Laing, R. A., Parma, P., de Ruiter, H. R., **Montenegro-Montes, F. M.**, & Wilson, T. L. *From Z-Machines to ALMA: (Sub)Millimeter Spectroscopy of Galaxies.* 2007, ASPC 375, 271.

- *A molecular gas study of low luminosity radio galaxies* Prandoni, I., Laing, R. A., Parma, P., de Ruiter, H. R., **Montenegro-Montes, F. M.**, & Wilson, T. L. 2007, NewAR 51, 43.

- *A FIRST-APM-SDSS survey for high-redshift radio QSOs* Carballo, R., González-Serrano, J. I., **Montenegro-Montes, F. M.**, Benn, C. R., Mack, K.-H., Pedani, M., & Vigotti, M. 2006, MNRAS 370, 1034.

- *Morphological studies of the SWIRE survey galaxy population in the UGC 10214 HST/ACS field* Hatziminaoglou, E., Cassata, P., Rodighiero, G., Pérez-Fournon, I., Franceschini, A., Hernán-Caballero, A., **Montenegro-Montes, F. M.**, Afonso-Luis, A., Jarrett, T., Stacey, G., Lonsdale, C., Fang, F., Oliver, S., Rowan-Robinson, M., Shupe, D., Smith, H. E., Surace, J., Xu, C. K. & González-Solares, E. A. 2005, MNRAS 364, 47.

- *SDSS Quasars in the SWIRE ELAIS N1 Field: Properties and Spectral Energy Distributions* Hatziminaoglou, E., Pérez-Fournon, I., Polletta, M., Afonso-Luis, A., Hernán-Caballero, A., **Montenegro-Montes, F. M.**, Lonsdale, C., Xu, C. K., Franceschini, A., Rowan-Robinson, M., Babbedge, T., Smith, H. E., Surace, J., Shupe, D., Fang, F., Farrah, D., Oliver, S., González-Solares, E. A. & Serjeant, S. 2005, AJ 129, 1198.

- *A study of the 15-μm quasars in the ELAIS N1 and N2 fields* Afonso-Luis, A., Hatziminaoglou, E., Pérez-Fournon, I., González-Solares, E. A., Rowan-Robinson, M., Vaccari, M., Lari, C., Serjeant, S., Oliver, S., Hernán-Caballero, A. & **Montenegro-Montes, F. M.** 2004, MNRAS 354, 961.